

# Superconductor Magnetization Modeling for the Numerical Calculation of Field Errors in Accelerator Magnets

vorgelegt von  
Diplom-Ingenieurin  
**Christine Völlinger**

an der Fakultät IV – Elektrotechnik und Informatik  
der Technischen Universität Berlin  
zur Erlangung des akademischen Grades

Doktorin der Ingenieurwissenschaften  
– Dr.-Ing. –

genehmigte Dissertation

**Vorsitz der wissenschaftlichen Aussprache:**

- **Prof. Dr.-Ing. Dr.h.c. H.G. Wagemann**  
am Institut für Hochfrequenz- und Halbleiter-Systemtechnologien, Fakultät IV – Elektrotechnik und Informatik, Technische Universität Berlin

**Berichter:**

- **Prof. Dr.-Ing. H. Henke**  
am Institut für Technische Informatik und Mikroelektronik, Fakultät IV – Elektrotechnik und Informatik, Technische Universität Berlin
- **Prof. Dr. L. Rossi**  
Fakultät für Mathematik, Physik und Naturwissenschaften, Universität Mailand, Leiter der Gruppe Magnete und Supraleiter, CERN Europäisches Labor für Teilchenphysik, Genf

Tag der wissenschaftlichen Aussprache: 25.10.2002

Berlin 2003

D 83



# Superconductor Magnetization Modeling for the Numerical Calculation of Field Errors in Accelerator Magnets

submitted by  
Diplom-Ingenieurin  
**Christine Völlinger**

at the Faculty IV – Electrical Engineering and Computer Science  
of the Technical University of Berlin  
in order to receive the academic grade

**Doktorin der Ingenieurwissenschaften  
– Dr.-Ing. –**

**approved dissertation**

**Chairperson of the Scientific Rehearsal:**

- **Prof. Dr.-Ing. Dr.h.c. H.G. Wagemann**  
at the Institute of Radiofrequency and Technology of Semiconductor-systems, Chairholder  
of Semiconductor Devices, Technical University of Berlin

**Scientific Board:**

- **Prof. Dr.-Ing. H. Henke**  
at the Institute for Technical Computer Science and Microelectronics, Chairholder of  
Theoretical Electrical Engineering, Technical University of Berlin
- **Prof. Dr. L. Rossi**  
at the Faculty of Mathematics, Physics and Natural Science, University of Milan, Head  
of Main Magnet and Superconductors Group, CERN European Laboratory for Particle  
Physics, Geneva

**date of the Scientific Rehearsal: 25.10.2002**

**Berlin 2003**

**D 83**



# Contents

<b>1</b>	<b>Introduction</b>	<b>1</b>
1.1	Why Superconducting Magnets? . . . . .	1
1.2	Field Errors in Superconducting Magnets . . . . .	4
1.3	Outline of Works on the Calculation of Superconductor Magnetization and Compensation Methods . . . . .	6
1.4	Scope of the Thesis . . . . .	9
<b>2</b>	<b>The Basics of Superconductivity</b>	<b>11</b>
2.1	Models of the Superconducting State . . . . .	11
2.1.1	The Static Model of Superconductivity . . . . .	12
2.1.2	The BCS-Theory . . . . .	13
2.2	Type I and Type II Superconductors . . . . .	14
2.2.1	Type I Superconductors . . . . .	14
2.2.2	Type II Superconductors . . . . .	16
2.3	The $J_c(\mathbf{B}, \mathbf{T})$ -dependence . . . . .	20
<b>3</b>	<b>Superconductor Models for Filaments</b>	<b>27</b>
3.1	The Critical State Model . . . . .	29
3.2	The Wilson Model . . . . .	33
<b>4</b>	<b>The Nested Ellipse Model</b>	<b>39</b>
4.1	Solution for Changes of a Homogeneous External Field . . . . .	40
4.1.1	Principle of Intersecting Circles . . . . .	42
4.1.2	Principle of Intersecting Ellipses . . . . .	44
4.1.3	Magnetic Induction from Intersecting Ellipses . . . . .	46
4.1.4	Geometry of Nested Circles or Ellipses . . . . .	48
4.1.5	$J_c$ -dependence in the filament cross-section . . . . .	50
4.1.6	Correction Factor for the Current-free Triangles . . . . .	51
4.1.7	Magnetic Induction in the Filament After a Sweep of a Homogeneous External Field . . . . .	54
4.1.8	Comparison to the Wilson Model . . . . .	55
4.1.9	The Hysteresis in the Superconductor Magnetization . . . . .	57
4.1.10	Continuous Course of the Magnetization . . . . .	58

4.1.11	Magnetization Resulting from a Change of a Homogeneous External Field . . . . .	60
4.1.12	Initial State Curve and Fully Penetrated State . . . . .	63
4.1.13	Calculation of $B_{p1}$ . . . . .	65
4.2	The Nested Ellipse Model for Rotating Fields . . . . .	67
4.2.1	Magnetic Induction in Case of a Rotating Field Sweep . . . . .	68
4.2.2	Parameterizing the Problem . . . . .	69
4.2.3	Equations for the Relative Penetration Depth . . . . .	73
4.3	Influence of Arbitrarily Shaped Filaments . . . . .	74
4.3.1	Change of Filament Size . . . . .	74
4.3.2	Hollow Filaments . . . . .	75
4.3.3	Influence of Deformed Filaments . . . . .	77
<b>5</b>	<b>Magnet Calculation and Repercussion on the External Field</b>	<b>81</b>
5.1	The M(B)-Iteration . . . . .	82
5.2	Fixed Point Iteration . . . . .	83
5.3	General Termination Criterion for the Iteration . . . . .	85
5.4	The Relaxation Method . . . . .	85
5.5	The ROXIE Interface . . . . .	86
5.5.1	The Combination with the BEM-FEM Coupling Method . . . . .	88
5.5.2	The Combination with the Finite Element Method . . . . .	89
5.6	Implementation and Conversion in ROXIE . . . . .	91
5.6.1	The Iteration Function . . . . .	93
5.6.2	Termination Criterion in ROXIE . . . . .	93
5.6.3	Local and Global Method of the Relaxation . . . . .	93
5.7	Test Results from the Relaxation Methods . . . . .	96
5.7.1	Comparison of Local and Global Methods . . . . .	96
5.7.2	Onset of the Relaxation . . . . .	97
5.8	Multipole Results with and without Repercussion . . . . .	99
5.8.1	The Limits of the Application of the Imaging Method . . . . .	103
<b>6</b>	<b>Field Calculations for the LHC Magnets</b>	<b>107</b>
6.1	The LHC Project . . . . .	107
6.2	Lattice and Magnet System . . . . .	108
6.3	The LHC Main Dipole Magnet . . . . .	109
6.3.1	The Dipole Magnet Geometry . . . . .	110
6.3.2	Technical Requirements . . . . .	110
6.3.3	The Cables of the LHC Main Dipole and Quadrupole Magnets . . . . .	112
6.3.4	Results . . . . .	113
6.4	The LHC Main Quadrupole Magnet . . . . .	117
6.4.1	Results . . . . .	117
6.5	Calculation of the MCBX Orbit Corrector Magnet . . . . .	121

<b>7</b>	<b>Field Errors from Persistent Currents</b>	<b>125</b>
7.1	Multipole Expansion from the Magnetic Moment . . . . .	125
7.2	Resulting Field of Neighboring Strands . . . . .	129
7.3	Influence of the Ramp Cycle on the Induced Field Errors . . . . .	130
7.4	Hysteresis Losses in Strands . . . . .	133
<b>8</b>	<b>Compensation of Persistent Current Induced Multipole Errors</b>	<b>137</b>
8.1	Ferromagnetic Coil Protection Sheet . . . . .	138
8.1.1	Investigating the Sheet Covering Angle . . . . .	140
8.1.2	Tuning Possibility by Varying the Sheet Thickness . . . . .	142
8.2	Influence of a Ferromagnetic Sheet Inside the Magnet Aperture . . . . .	143
8.3	Ferromagnetic Shims Inside the Superconducting Cable . . . . .	145
<b>9</b>	<b>Conclusion</b>	<b>147</b>
<b>A</b>		<b>151</b>
A.1	The RRR-Value of Normal Conductors . . . . .	151
A.2	Fourier Expansion of the Radial Field Component . . . . .	153
A.3	The Thermodynamic Potential of Superconductors . . . . .	154
A.4	Using the Hypergeometric function . . . . .	156





# Chapter 1

## Introduction

### 1.1 Why Superconducting Magnets?

In the framework of this thesis, carried out at CERN<sup>1</sup>, the subject of superconducting magnets, as used in particle accelerators, will be treated, with the main focus on bending magnets. The use of superconductor technology is a standard procedure in all new large particle accelerators, today. Nevertheless, the construction of superconducting magnets with a very high bending field for circular accelerators is still a great challenge.

In this work, a special emphasis is put on the magnet system of the Large Hadron Collider (LHC<sup>2</sup> [1]), mostly for illustration of the calculated results and also to verify the outcome by means of comparison with measurements taken at CERN. The magnet system of the LHC can be considered as exemplary.

When accelerating heavy particles, energy loss due to synchrotron radiation is no longer the main problem, since in this case energy loss due to this radiation only occurs at considerably higher energies than for  $e^+e^-$ -accelerators, as for example, LEP<sup>3</sup>. The comparison between the radiation of an electron ( $m_e c^2 = 0.511$  MeV) and the radiation of a proton with the same energy ( $m_p c^2 = 938.19$  MeV) yields a ratio of  $(m_p c^2 / m_e c^2)^4 = 1.13 \cdot 10^{13}$  [2].

Hence, for the LHC proton ring, as for all hadron accelerators, the maximum particle energy is limited by the obtainable strength of the magnetic field keeping the particles in their orbit. Since the guiding dipole field has to increase with the particle energy (synchrotron principle), the main bending magnets are the crucial elements of the LHC.

The use of superconducting magnets instead of conventional magnets with copper coils has unique advantages. First of all, the vanishing electrical resistance of superconducting coils opens the way to higher currents while at the same time the operating costs are reduced. Secondly, very high bending fields are produced, allowing for higher particle energies.

Superconductors for applications have been produced from the late 1960s on and are still under development today. At the moment it is possible to manufacture wires that can carry extremely high electric current densities (up to  $1000$  A/mm<sup>2</sup>) in the presence of high magnetic fields (10 T and greater) [3]. For the NbTi cables of the LHC, the aim is to reach a current density of  $3000$  A/mm<sup>2</sup> at a field of 5 T and a temperature of 4.2 K. Superconductors do this with little power dissipation; this is one of the main reason for their usefulness

---

<sup>1</sup>CERN, the European Laboratory for Particle Physics, Geneva, Switzerland.

<sup>2</sup>LHC, the Large Hadron Collider, currently under construction at CERN.

<sup>3</sup>LEP, the Large Electron Positron Collider, has been decommissioned at CERN in November 2000.

in manufacturing high-field electromagnets. The consumption of energy for the LHC, for instance, will be extremely small compared to accelerators using conventional magnets: the LHC with 22 times the collision energy of the SPS<sup>4</sup> will not consume more power than the SPS machine. Furthermore, a superconducting magnet of the same field strength is much smaller than a conventional magnet with copper coils and carries only a fraction of its weight. The savings in power, size and weight are therefore substantial. Additionally, in case of the LHC, the required high bending fields of the main dipoles are impossible to produce with conventional magnets.

However, the advantages of using superconducting coils are reduced by one main flaw: Any field variation induces magnetization currents in the superconducting material which disturb the current distribution in the coil and deteriorate the field quality in the aperture. At a first glance, these currents are similar to commonly known eddy currents in conventional conductors. However, they do not decay exponentially but persist due to the lack of resistivity. Therefore they are often denoted as *persistent currents*.

Persistent currents become a major problem: once induced during magnet ramp, they flow as bipolar currents in the superconducting filaments and are a source of superconductor magnetization in the coil. This magnetization causes field distortions that are small compared to the main field in case of nominal current but are non-negligible at low excitation field.

Additionally, the multipole fields caused by persistent currents depend on the field amplitude as well as on local changes in field direction and have opposite signs for increasing and decreasing main field, respectively. From this, a hysteresis arises in the resulting induced magnetization.

The reduction of the influence of persistent currents and the development of compensation methods, by incorporating them into the magnet design process, for example, requires a careful modeling of the superconducting material. Since persistent currents arise only in individual filaments, the response of a *superconductor filament* on an external field change has to be modeled. This task composes a main item of this thesis. For magnetic field calculation, however, determining the filament magnetization is not sufficient. The following necessary procedure is therefore derived:

Starting from the development of a persistent current model of an individual filament, a procedure is launched which firstly accounts for the applied history and incorporates the filament hysteresis into the calculation. In this step, all possible states are considered including the initial state curve and the so-called minor looping which arises from very small field sweeps. Further, an algorithm is derived which calculates and superposes the induced currents of each filament in the coil cross-section depending on the local field with the source currents. The change of the field distribution in the cross-section due to the repercussion of the persistent current field on the original field is then computed iteratively. Finally, the model is combined with numerical field-solving methods for the calculation of the non-linear magnetic regions in the magnet (such as the ferromagnetic iron yoke, for instance). In some cases, the use of the imaging method substituting the iron yoke is possible. However, in most magnets the inner yoke structure is not of circular shape, or the effects from the non-linear yoke saturation have to be considered. In these cases, imaging is not possible. In addition, the imaging method cannot provide solutions for thin ferromagnetic layers or shims in the aperture of a magnet – as used for persistent current compensation. Depending on the vicinity of ferromagnetic regions and source currents, the local field distribution can change, demanding a re-iteration of the already computed persistent currents. A re-calculation of

---

<sup>4</sup>SPS, the **S**uper **P**roton **S**ynchrotron; accelerator at CERN.

superconductor magnetization and ferromagnetic magnetization is inevitable in these cases.

Superconducting cables for magnet applications consist of a composite structure, where thin superconducting filaments are embedded in a normal-conducting metal matrix, usually commercial copper or aluminum. The first superconducting magnets were made of mono-filamentary (bulk) superconductors and showed a disappointing behavior in such a way that they did not reach the expected current-carrying limit of the cable [4]. The reason for this is the local spontaneous transition from superconducting to normal state due to small perturbations as, for example, variations of temperature or magnetic field which cause a local heat rise and a normal-conducting spot. Current passing through this resistive region then generates additional Joule heat and raises the temperature of the adjoining material, leading to more heating and eventually the entire superconductor is driven into the normal conducting state. One possibility to prevent this superconductor-to-normal transition is the so-called cryogenic stabilization [5]. Cryogenic stabilization denotes the increase of the cross-section area of the normal-conducting metal with respect to the superconducting material which can be realized by using multi-filamentary superconductors. At low temperatures, the resistivity of normal metal is two or three orders of magnitude below the normal-state resistivity of the superconductor. As a result, most of the current flows out of the superconductor and into the normal-conducting area in case the superconductor performed a superconductor-to-normal transition (so-called current sharing principle). This leads to a decrease of self-heating and a decrease of stationary temperature of the composite superconductor. Since the normal conducting region in the superconductor can only exist as long as the rate of generation of Joule heat is equal to, or exceeds, the rate at which heat can be transported away by the surroundings, the superconductor will recover. Usually, superconductors are poor thermal conductors, thus the cooling capability of the surrounding matrix material is higher than that of the superconductor. This works in favour of the recovery effect.

It should be mentioned here, that the electrical (and also the thermal) conductivity of normal conducting materials also depends on the applied temperature and the magnetic induction. The electrical conductivity of normal conductors thus also of the matrix material is expressed in terms of the so-called RRR-value. The RRR-value is explained in the appendix A.1 in detail.

For NbTi superconductors the typical filament diameters are in the range of about 5-10  $\mu\text{m}$ , whereas for Nb<sub>3</sub>Sn superconductors, the filaments are considerably thicker with a diameter of about 20-25  $\mu\text{m}$ . Figure 1.1 (right) shows the cross-section of a superconducting strand of NbTi filaments embedded in a copper matrix. The filaments are twisted in longitudinal direction, in order to reduce inter-filament coupling effects. For the LHC main dipoles and quadrupoles, a cable of Rutherford type is used which consists of 28 to 36 individual strands made of thousands of superconducting filaments (6500 in the dipole outer layer cable and 8900 in the dipole inner layer cable). The strands are grouped together for the cable and then also twisted in order to reduce flux linkages.

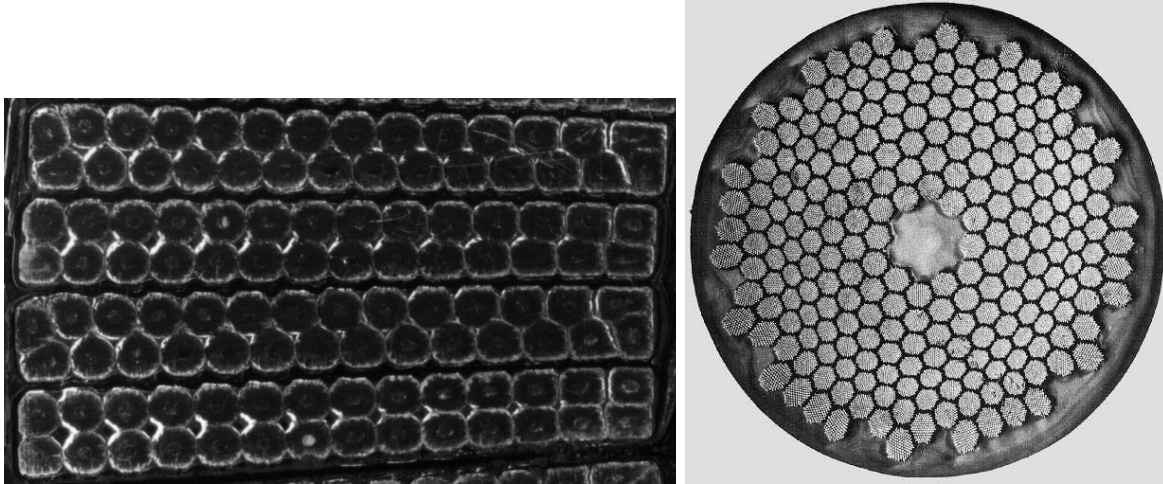


**Figure 1.1:** Left: Cut-through a Rutherford type cable of four windings for the LHC main dipoles and quadrupoles. The cable is made of individual strands and is insulated by different layers of polyimide tape. Right: Typical NbTi strand cross-section showing superconducting filaments in groups of about 50 filaments and embedded in a copper matrix.

Also shown in Fig. 1.1 (left) is a cut through an LHC Rutherford type cable. The cable possesses a trapezoidal outer shape – the so-called key-stoning – in order to give a good circular approximation while being put closely around the circular aperture of the magnet. The Rutherford cable is the most frequently used cable in all superconducting accelerators today. The main advantage of this cable type is that it can be compacted to a high density of 88-94% of the material in the cross-section without damaging the strands [6].

## 1.2 Field Errors in Superconducting Magnets

The expression *magnetic field errors* in the aperture of a magnet denotes all the field components that are different from the main field component. Field errors are expressed in so-called multipoles,  $B_n$ , which are the coefficients of the Fourier series expansion of the radial field component at a certain reference radius in the aperture, obtained after harmonic analysis (see appendix A.2 for details). The multipoles are usually normalized to the main field component and expressed in units of  $10^{-4}$ . It is convention to start the multipole numbering with 1 for the dipole field, 2 for the quadrupole and so on. The entity  $b_3$ , calculated for a dipole magnet, for instance, then denotes the relative deviation of the sextupole field with respect to the main (dipole) field component given in units of  $10^{-4}$ :  $b_3 = B_3/B_1 \cdot 10^4$ .

Since an extremely high field quality is required for the storage of an intense particle beam for many hours, the relative deviation from the ideal field in the aperture of a magnet should not exceed a few parts in units of  $10^{-4}$ . This is no particular problem in case of conventional magnets whose field distributions are governed by accurately shaped iron yokes. However, in superconducting magnets, the field quality in the aperture is determined by the coil arrangement and the position of the conductors. Even small deviations in current

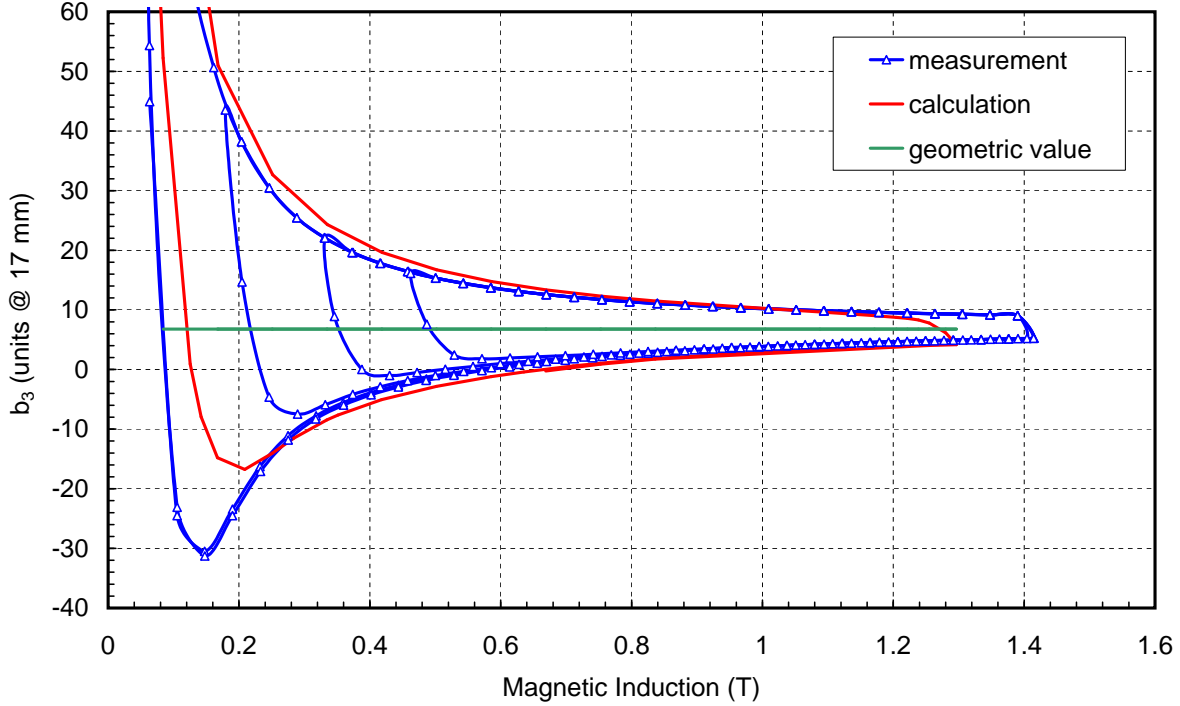


**Figure 1.2:** Multipole  $b_3$ : relative deviation of the sextupole field with respect to the main dipole field component calculated at a reference radius of 17 mm and expressed in units of  $10^{-4}$ . Red curve: Calculated values; blue curve: Measured values [7]; green curve: Geometric value.

positions will cause a considerable loss of field quality in the aperture.

Field errors in superconducting magnets can be divided into random and systematic errors. Random errors arise, for instance, from the manufacturing tolerances of individual parts of the magnet and will not be considered here. Systematic errors, however, arise from the coil geometry, for example, which is only an approximation to the ideal so-called  $\cos(m\theta)$  current distribution<sup>5</sup> or from the surrounding yoke structure. Also persistent current induced field errors are systematic errors. Usually, the field errors show a great variation resulting from persistent currents which dominates the low field range. In addition a comparatively small variation with increasing current exists, which is due to the gradual saturation of the ferromagnetic yoke material. At medium field level, a remaining constant multipole value exists, which is denoted as the *geometric* value. The geometric value is obtained from calculations without considering the persistent current effect. In order to give an idea of the amount of field errors in the LHC dipole, for instance, Fig. 1.2 shows the calculated field error  $b_3$  including the influence of persistent currents (red curve). Also indicated in the plot is the geometrical value (green curve) resulting from the calculation without persistent currents and the measured value (blue curve) [7].

When calculating a superconducting magnet, the vicinity of non-linear magnetic regions

<sup>5</sup>Besides the geometry of intersecting ellipses and circles, introduced in section 4.1, the  $\cos(m\theta)$  current distribution is the only geometry which produces a pure multipole field. See, for example, [8] or [9] for details.

and the source currents determine whether the sources of the total field error can be directly identified or not. The local yoke magnetization depends on the strength and the position of the coil currents. Assuming the inner yoke contour in the immediate vicinity to the coil causes an induction of strong persistent ‘mirror’ currents in the yoke. Thus, at intermediate and high currents when the magnetic features of the yoke change, the yoke starts to saturate on several regions along the inner yoke contour. This way, saturation effects of the iron parts may change the *magnetically effective* inner yoke contour. Such local saturation effects can yield an asymmetry which results in additional field errors even for a mechanically perfectly round inner yoke contour. In general, it can be said, that the smaller the distance between the inner yoke contour and the outer coil radius, the stronger are the saturation induced field errors.

In the case of the LHC main dipole magnet, for instance, where the distance between the inner yoke shape and the outer coil radius is large (minimum distance is 40 mm), the identification of the geometric value is straightforward, since the saturation produces only little variation in multipoles. For a corrector magnet, however, where the yoke is close to the outer coil radius, the identification is far more difficult and can often only be accomplished by splitting the calculation of the total operating cycle into a great number of individual steps.

### 1.3 Outline of Works on the Calculation of Superconductor Magnetization and Compensation Methods

This section is meant to provide a (non-exhaustive) overview on different works carried out on superconductor modeling and persistent current calculation in superconducting magnets. The first part presents several approaches to filament magnetization models which usually differ in their covering range, this means, the models often lack the field dependence of the critical current density, or do only consider a one-dimensional change in the applied field instead of giving a expressions for rotating fields. Rotating fields, in this context denote a change in the external magnetic induction which can be the amount or the exercising angle or a combination of both in the plane of the filament cross-section. This way, a vectored expression for the description of the external field and the resulting magnetization is necessary.

Besides this models, approximate solutions for the magnetization of the complete coil exist which have been carried out by the use of methods which require field maps and without the attempt to model individual filaments.

A general theory for the description of Type II superconducting material has been introduced in 1962 by C.P. Bean [10], [11] and is known today as the Critical State Model. The model describes the behavior of Type II superconductors such that there is a finite value of current density induced in case the material is exposed to a magnetic field, however small. This current density is called *critical current density*  $J_c$ . The orientation of  $J_c$  results from the right-hand law. The Critical State Model has been applied to a slab of superconducting material whose extension in direction of the applied field is infinitely long. This way, no end effects have to be considered and a simple contour (in form of a straight line) of the distribution of the current density in the cross-section can be found in the case of one-directional field changes<sup>6</sup>. Today, the Critical State Model is still the basis of most macroscopic superconductor models. It is therefore described in detail in section 3.1.

---

<sup>6</sup>The inner current contour defines the shape of the current-free region in the non-fully penetrated case and the boundary between different current layers after a change in external field orientation.

The Critical State Model has been applied to cylindrical wires with circular cross-sections exposed to a perpendicular magnetic field, for example, by C. Pang [12] (1980), who calculated AC losses. The determination of the current contour in the cylindrical wire cross-section is considerably more difficult compared to the slab with an assumed infinitely long extension parallel to the applied field. Therefore Pang discretized the cross-section into thin slices perpendicular to the applied field for its determination. The filament magnetization is calculated from the found current distribution for the cases of a change of a homogeneous field as well as for applied rotating fields. The critical current density is assumed to be constant in the filament cross-section.

A more detailed description of a superconducting filament in an applied field is given by M. Wilson [8] (1983), who derived an approximate solution by assuming the inner current contour as elliptically shaped. The same method is presented in the book of K.-H. Mess, P. Schmüser and S. Wolff [9] (1996). The Wilson Model is the most frequently used approximation for the inner current contour in order to calculate elementary persistent current effects. It is therefore presented in detail in section 3.2. It should be noted that the resulting current contour from the model of Pang assumes no elliptical shape – a result which is remarkable, since it is in contradiction to the later developed Wilson Model.

The inner current contour of a superconducting filament exposed to changing fields has been determined numerically by R.A. Hartmann [13] (1989), for the calculation of AC losses in multi-filamentary wires. The filament/wire magnetization is calculated for the fully penetrated state. A  $J_c(B)$ -dependence is considered by applying the Kim-Anderson<sup>7</sup> current fit [14], resulting in a merely 5% deviation in magnetization loss compared with calculations carried out with a constant  $J_c$ . Results on the calculation of losses for not only circular but arbitrarily shaped filament cross-sections were considered by re-scaling with geometric scaling factors.

The works of K.V. Bhagwat and P. Chaddah give numerical evaluations for the magnetization of superconductors of various shapes exposed to an applied magnetic field. In [15] (1991), an infinitely long superconducting cylinder is presented, however the critical current density is assumed to be constant. The cylinder is a generalization of expressions given in [16] (1990) for a sphere (also no  $J_c(B)$ -dependence considered). In [17] (1994), the authors presented the field response and the magnetization of the same geometries including a  $J_c(B)$ -dependence where  $J_c$  decreases exponentially with increasing  $B$ , and in [18] (1997), the same principle is shown including the Kim-Anderson fit for the critical current density. Rotating fields are not considered.

A combination of the Wilson Model with the Kim-Anderson current fit for the  $J_c(B)$ -dependence is given by Y.N. Zhilichev [19] (2000). There, a piece-wise continuous current distribution is used after dividing the cylinder cross-section into various layers and the magnetization of a superconducting cylinder exposed to a uniform transverse magnetic field is calculated for changes of a homogeneous field. Also included is a hysteresis consideration by calculating the branches in the first and second quadrants and then imaging the results into the third and fourth quadrant in order to complete a full hysteresis loop.

In addition to the examples above, several numerical models with a discretized filament cross-section for the calculation of filament magnetization exist, for example, the models of E.H. Brandt [20] (1996) or L. Prigozhin [21] (1994). The models usually derive the inner

---

<sup>7</sup>The Kim-Anderson current fit describes the dependence of  $J_c(B)$  of hard superconductors expressed in a simple formula. This fit is shown in greater detail in section 3.2, whereas the current fit function applicable for NbTi superconducting material is introduced in section 2.3.

contour of the current numerically. In case of the Brandt model, the magnetization is derived by solving an integral equation and in such a way, the critical current density is determined in the vortices of a regular discretizing mesh in the filament cross-section. The model has been applied recently by Haverkamp et al. [22], [23], for example, for the calculation of the magnetic decay and the snap back in LHC magnets [24]. In this application, filaments in a fully penetrated state exposed to a change of a homogeneous field and to rotating fields are investigated. The critical current density  $J_c(B)$  is assumed to be constant. The model of Prigozhin uses a regular finite element discretization in the filament cross-section where the cross-section has to have an axial-symmetry. Then, a variational problem is derived in order to determine the free-boundary of the current profile in the filament. In case of two-dimensional problems – such as rotating fields in the plane, the solution of the derived variational problem corresponds to finding a minimum in the discretized equation. The critical current density is held constant along the individual finite elements and during each solution step.

Approximate calculations of persistent current effects in magnets have been carried out, for example, by R. Wolf [25] (1974), [26] (1992) for the LHC dipole magnets and in a similar way by H. Brück et al. [27] (1989) for the calculation of the HERA dipole magnet. In both cases, computer programs were developed which are based on a field mapping in the magnet cross-section and then calculate the persistent current distribution by applying the Wilson Model, for example, or a similar one. The calculations of Wolf are restricted to the fully penetrated state. The influence of the iron yoke has in both cases been considered by means of the imaging method and consequently iron saturation effects are not considered. The  $J_c(B)$ -dependence is incorporated by an estimated fit curve whereas the repercussion of the persistent current field is not included. The method of Brück et al. has later been extended by M. Pekeler et al. [28] (1992) to an approximate calculation of rotating fields in a plane on a single filament and has also been compared with measurements taken on a strand.

M.A. Green calculated persistent current effects already in 1972 [29] by assuming a rough current distribution in the filament according to the Critical State Model. Together with others they also considered compensations for persistent current effects, for example, by means of passive superconductors in the aperture [30] (1988), [31] (1990), [32] (1991) as well as ferromagnetic material in the composite superconducting strands [33] (1991).

V.V. Kashikhin and A.V. Zlobin calculated persistent current compensations without modeling the single filament compensation. They linearly superimposed calculations with and without persistent current influence with magnet geometries which included compensatory elements [34] (1999), [35] (1999), [36] (2001) in the framework of the VLHC<sup>8</sup> studies. The application of compensatory elements and their calculation is discussed in chapter 8, where also examples for the reduction and partial compensation of persistent current effects are presented.

Some of the above-mentioned models are introduced in detail later-on and compared with the outcome of the model and the calculations derived in this thesis in case it is deemed appropriate.

---

<sup>8</sup>VLHC, the **V**ery **L**arge **H**adron **C**ollider; post-LHC accelerator studies.



## 1.4 Scope of the Thesis

The major part of this thesis concerns the development of a magnetization model for superconducting filaments such that it can be combined with advanced numerical field solving methods, in order to calculate the influence of induced persistent currents on the magnetic field inside the aperture of the coils of superconducting magnets.

The thesis consists of the following main parts:

### Basics on Superconductivity and Existing Superconductor Models:

In chapter 2, a short introduction into superconductivity and a description of the superconducting state is given, followed by an introduction of the electromagnetic features of Type I and Type II superconductors. The emphasis is put on the response of the different superconductor types on an externally applied field. The critical current density  $J_c$  – the decisive parameter for Type II superconductors – is introduced and the features of this parameter are explained in detail. Different current fit functions are investigated for superconducting materials and the fit function as used for the LHC cable is presented. Already existing superconductor magnetization models (Bean [10], [11], Wilson [8], Schmüser [9]) are discussed and the hysteretic persistent current effect is explained.

### Superconductor Modeling:

In a first step, a semi-analytical model for the calculation of the magnetization in individual filaments in case of a change of a *homogeneous* external field is developed. Expressions are derived which fully describe the response of a superconducting filament on the changing external magnetic induction. The distribution of the screening field in the filament cross-section and the induced magnetization are given. The model considers the source of the filament hysteresis by physical means avoiding an artificial hysteresis model. Emphasis is set on the fact that no material data from measurements is needed excepting values for the critical current density  $J_c$ , which are usually available from the cable manufacturer. This distinguishes the model from others which, for example, are performing an M(B)-fit and therefore depend on magnetization measurements to be carried out over the complete field range of interest. The outcome is compared with existing magnetization models.

### Rotating Fields:

In the second part of chapter 4, the induced filament magnetization resulting from an applied rotating field is calculated. Based on the one-dimensional model of a sweep of a homogeneous field, an analytic expression for the magnetic induction in the filament cross-section due to an applied rotating field is derived and the resulting magnetization from induced persistent currents is determined. Again, the only input parameter is the critical current density  $J_c$ . Further on, the difference in the resulting magnetization between the case of an applied rotating external field and an applied change of a homogeneous external field is discussed.

### Combining the Model with ROXIE:

For the computation of complete coil magnetizations in a magnet and the resulting induced field errors, the magnetization model has been combined with advanced numerical field meth-

ods as the FEM-method and the BEM-FEM-coupling method [37], [38], respectively. Both numerical principles are available in the field computation program ROXIE<sup>9</sup>, which has been used to compute the contribution of non-linear iron regions to the total magnetic field in the aperture. The interface to the ROXIE program and the application of the hysteresis model on each filament in the magnet cross-section is presented.

### **The M(B)-Iteration:**

In order to consider the reactive effect of the coil magnetization on the applied field (repercussion of the magnetic induction), an M(B)-iteration based on the principle of a fixed point iteration has been worked out and programmed. An over-relaxation principle is used to accelerate the convergence velocity and stabilize the convergence. The remaining error after the iteration has been estimated. The principle of the M(B)-iteration is presented and the general necessity of the iteration is shown by means of case studies. Depending on the vicinity of superconductor and ferromagnetic regions in the magnet cross-section, the necessary frequency of re-computing the iron regions in order to derive exact field computations is discussed.

### **Magnet Calculation:**

The magnetization model has been used for the calculation of field errors in the LHC magnets. In chapter 6, the LHC project and its magnet system are introduced and results are presented for the LHC main dipoles, main quadrupoles and an orbit corrector magnet. The results have been compared with measurements taken from magnet prototypes. The influence of changes in the magnet ramp cycle on the induced field errors is presented exemplary for the LHC main dipole.

### **Compensation of Persistent Currents:**

A practical application of the developed method for the computation of superconductor magnetization is the incorporation of compensation principles in the design process for superconducting magnets. In the framework of this thesis, different compensation principles for persistent current induced field errors are calculated such as thin ferromagnetic shims in the magnet aperture or the insertion of passive superconductors. The computed results are discussed and the limitations in the use of intrinsic compensation of persistent currents are shown.

### **Hysteresis Loss Calculation:**

Hysteresis losses can be calculated from the filament magnetization very precisely. As an additional application, the calculation of hysteresis losses arising from the superconductor magnetization of the filaments in general and the result for the LHC main dipole magnet are presented.

---

<sup>9</sup>ROXIE, the **R**outine for the **O**ptimization of magnet **X**-sections, **I**nverse field calculation and coil **E**nd design has been created by Stephan Russenschuck at CERN.

## Chapter 2

# The Basics of Superconductivity

### 2.1 Models of the Superconducting State

Superconductivity was discovered by Kamerlingh Onnes in 1911 and denotes the loss of resistivity of a material below a certain temperature  $T_c$ , the so-called critical temperature of the material. The change from normal to superconducting state is characterized by an abrupt drop in the resistivity of the material from a relatively high value (about  $10 \mu\Omega \cdot \text{cm}$  [3]) to a very low value (smaller than  $1 \text{ f}\Omega \cdot \text{cm}$ ). The remaining resistivity is consequently considered to be null. The graph of the original measurement of Kamerlingh Onnes is shown in Fig. 2.1. In contrast to some of the other superconductor properties, the critical temperature

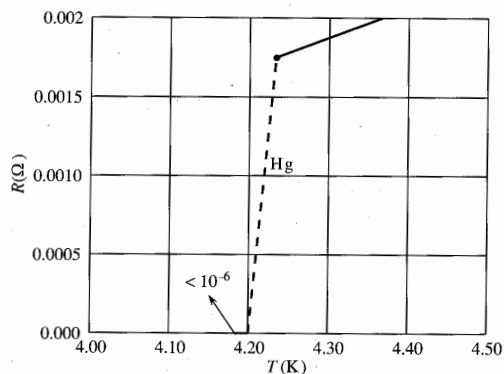


**Figure 2.1:** Superconducting resistance transition as discovered by Kamerlingh Onnes. Picture taken from [39].

is an intrinsic material property, determined mainly by chemical composition and crystal structure. In alloy materials as NbTi, it is relatively unaffected by metallurgical treatments. The effort to reach higher critical temperatures momentarily focuses on third- and fourth-element additions to already known high-temperature superconductors<sup>1</sup>. The development

---

<sup>1</sup>One useful way to distinct between high- and low-temperature superconductors is their cooling medium: Low-temperature superconductors use liquid helium for cooling while high-temperature superconductors operate with liquid nitrogen operating on a far more economic level. Nitrogen liquefies at a temperature of 77 K [40].

of a superconductor with a significantly high  $T_c$ -value does not only result in the obvious advantage of savings in cryogenic, but also the other superconductor properties, namely the critical current and the critical field scale with  $T_c$ . Therefore, even in cases where the operational temperature is kept low, materials with a higher  $T_c$  offer, for example, enhanced stability.

The superconducting materials that are technically relevant today (with respect to magnet applications) differ fundamentally from the first generation of superconductors. Onnes used pure soft metals, such as lead, tin and mercury, all of which are materials that are classified as Type I superconductors, today. Together with their obvious property of zero resistivity at low temperatures, Type I superconductors display the feature of flux expulsion (see section 2.2.1). A completely different situation arises for Type II superconductors as is shown in section 2.2.2 after a brief introduction on models of superconductivity.

### 2.1.1 The Static Model of Superconductivity

In the static model of superconductivity [41], the superconductor is considered to be a lattice of atomic residues with elastic properties in which the electrons, as the conducting party, are moving freely. Due to the assumed elasticity, the atomic residues are not rigidly fixed in resting positions, but can be displaced and in such a way are considered to be statistically oscillating around their resting positions.

Now two negative charges are introduced into this lattice of atomic residues while all the other electrons are neglected. If the first electron passes between the positively charged atoms of the lattice, the atoms are attracted towards its negative charge. Consequently, the electron is creating a distortion of the lattice and thus a region of enhanced positive charge that attracts the second electron to that area of positively charged concentration. This way, the model describes an attracting interaction between two electrons which are then indirectly bound<sup>2</sup>, resulting in a reduction of the repulsive force between the electrons (see Fig. 2.2) due to the enhanced positive charge of the lattice around them.

#### Limitations of the model:

- The assumption of two single insulated negative charges presents a drastic simplification that is somewhat unrealistic, and
- the moving electrons in the lattice of atomic residues experience high velocities and can therefore not produce a *static* polarization of the lattice.

In spite of the fact that the electrons cannot produce a static polarization of the lattice, the model holds qualitatively since the interaction between two electrons can be considered as a polarization along their trajectory. The strength of the polarization now depends on how fast the lattice of residues is able to follow the attracting effect of the moving electrons. Hence the polarization depends on the eigen-frequencies of the lattice and therefore on the total mass of the atomic residues at rest. Low frequencies correspond to heavy isotopes that fulfill slow vibrations; the lattice residues are only able to slowly follow the polarizing influence. Hence in the case of heavy isotopes, only a weak interaction and a small effect takes place.

---

<sup>2</sup>A mechanical analogue of the above described static attracting interaction can be given by two small spheres on an elastically deformable membrane, such as a thin rubber sheet [41].

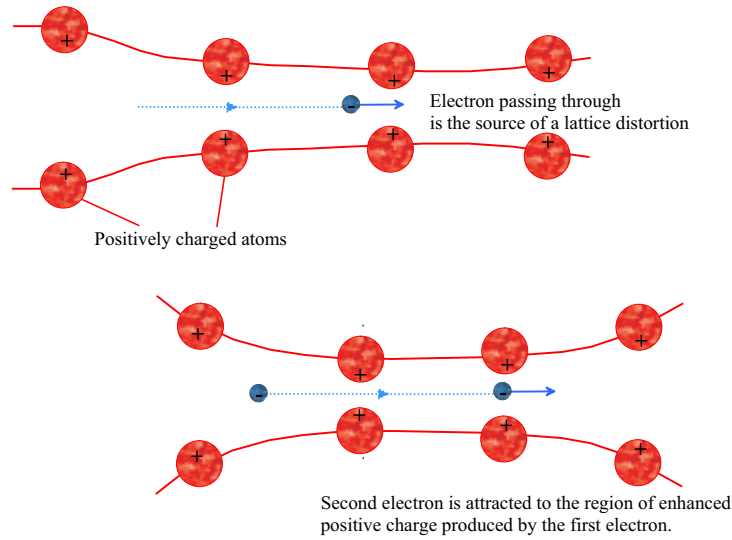


**Figure 2.2:** Static model of the superconducting state. As electrons pass between the lattice's positively charged atoms, these are attracted inwards, creating a region of enhanced positive charge that attracts a second electron to that area.

This also corresponds to the BCS-theory [39] (which is briefly explained in the next section), where the interaction of the electrons with the lattice by polarizing effects is explained by an energy reduction seen by the second electron. One can imagine, that the second electron follows the polarization track of the first and therefore lowers its energy because it finds the lattice in an already polarized state. This means, the correlation of two electrons by distorting the lattice of residues presents an energetically preferred state, what is exactly the effect which is described by the BCS-theory.

### 2.1.2 The BCS-Theory

The central idea of the BCS-theory is the combination of single free electrons to so-called Cooper-pairs<sup>3</sup>. BCS is an abbreviation and stands for the initials of the three persons, who developed this theory: Bardeen, Cooper and Schrieffer. A Cooper-pair consists of two electrons with equal and opposite momenta ( $\mathbf{p}_1 = -\mathbf{p}_2$ ) which correlates them uniquely by anti-correlation. Since single free electrons are fermions, the joining electrons of a Cooper-pair must have opposite intrinsic rotational momenta and merge to a zero-spin particle<sup>4</sup>. The existence of Cooper-pairs in the lattice can be understood by using the principle of exchange interaction: The exchange of a third particle, a phonon, results in an attraction and leads to a binding of the particles and pair-formation of a Cooper-pair. The exchanged phonons are said to be virtual because they only exist during the exchange, but do not have the possibility of passing away from the electrons into the lattice and cannot exist as real phonons.

The tendency of integral spin particles, called bosons, to preferably occupy a state which is already occupied by other bosons yields *one single quantum-mechanical state* which means

<sup>3</sup>Cooper was first to prove that one of the features of a superconducting electron pair (Cooper-pair) is to cause a reduction of energy of the system and therefore is an energetically preferred state.

<sup>4</sup>Then the Cooper-pair itself is a boson.

that all Cooper-pairs are identical in their physical properties. The existence of one single quantum state for the unity of the Cooper-pairs is supported by the great correlation between single pairs. A coherence length  $\zeta_{co}$  exists, which denotes the mean separation distance at which a pair correlation becomes effective. This distance holds between 100 and 1000 nm for a pure superconductor. Intuitively one can say that  $\zeta_{co}$  can be considered as the average size of a single Cooper-pair. This size is large compared with the mean distance between two conduction electrons which amounts to a few  $10^{-1}$  nm. Hence the Cooper-pairs overlap heavily. In the region of one pair, there are  $10^6$  to  $10^7$  other electrons which are themselves correlated into pairs. Under the influence of an external electric field the Cooper-pairs are accelerated and get a momentum since they are charged with  $-2e$ , where  $e$  is the elementary electric charge. It is important to note that all Cooper-pairs acquire the same momentum while staying in the same quantum state. A fact, that makes it impossible for *single* Cooper-pairs to change to another quantum state. Therefore an interaction of single Cooper-pairs with the lattice by momentum exchange cannot take place and a non-resistive transport of charge builds up.

The transition from one quantum state to another is possible for the unity of Cooper-pairs only when the Cooper-pair-relation is broken; in this case the external energy must exceed the binding energy of the pairs. This corresponds to an increase in momentum to a critical value. The principle demonstrates the existence of a critical current density in superconductors, where the excess of this critical current density yields the break up of the Cooper-pairs and the onset of interaction between the now free electrons and the lattice residues. For details see [41], [42], for instance.

## 2.2 Type I and Type II Superconductors

Superconducting materials can be separated into two general groups by identifying the way an externally applied magnetic field penetrates the material. As will be shown in the next section, the first group (the so-called Type I superconductors) completely expel any externally applied magnetic field, whereas Type II superconductors allow the field to enter in quantized flux tubes. In this section, the main difference between this two groups is explained.

### 2.2.1 Type I Superconductors

In 1933, Meissner and Ochsenfeld discovered that a superconductor exposed to a magnetic field and cooled below its critical temperature expels the magnetic flux which tries to penetrate the material (so-called Meissner-Ochsenfeld-effect). They also showed that this flux expulsion arises regardless of whether the material is already in a superconducting state when the field is applied or if it is cooled down in a pre-existing magnetic field configuration. Their experiment confirmed for the first time the existence of *one single* superconducting state denoted as the Meissner phase. Superconductors inherent of the behavior of field expulsion are called Type I superconductors. They act as perfect diamagnets in such a way as surface currents are induced that precisely cancel any magnetic field inside the material. These screening currents penetrate up to a certain depth, known as the London penetration depth<sup>5</sup>

---

<sup>5</sup>The value of the London penetration depth of Type I superconductors is usually measured; numbers can be found in textbooks as, e.g., [43]. The calculation of the London penetration depth requires the knowledge of the charge concentration in the material. From the penetration depth and the critical current density in this layer, the absolute value of the magnetization resulting from this current layer can be determined. However, the value is the equivalent to the critical screening field  $B_c$ , which can as well be measured directly. For NbTi, the London penetration depth is measured to be  $\lambda_L = 39$  nm.

$\lambda_L$ . They can be considered the source of a magnetic moment  $\mathbf{m}$  and a magnetization  $\mathbf{M}$  can be introduced such as  $\mathbf{M} = \mathbf{m}/V$ , where  $V$  is the volume of the sample. Ignoring the finite thickness of the surface current layer and considering an integral unit of the sample then makes the magnetization correspond to that of an ideal diamagnet with a susceptibility  $\chi = -1$ . The magnetization increases proportionally to the applied field until the applied field exceeds a certain value (the so-called critical field  $B_c$ ) which causes a jump back of the superconductor into the normal conducting state. Above  $B_c$ , in the normal conducting state, the applied field fully penetrates the material. The shielding capacity is therefore limited.

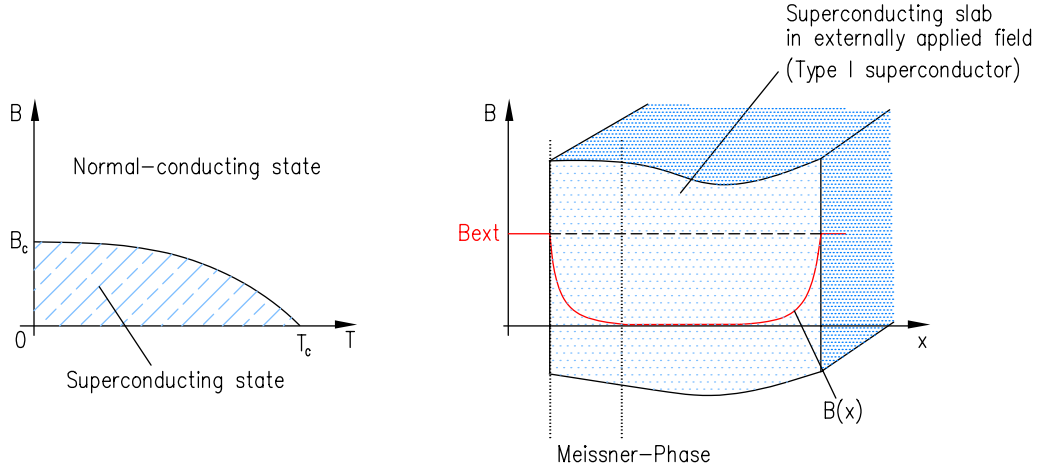


**Figure 2.3:** Left: Phase diagram of Type I superconductors. The superconducting and the normal conducting state are separated by the  $B_c(T)$  curve. Right: Course of the magnetic induction after applying an external field to a Type I superconducting slab. The Meissner phase is penetrating the superconductor while the interior remains field free.

The superconducting state of Type I superconductors is characterized by zero magnetic flux within the material (except for the thin layer of screening current). Figure 2.3 (left) shows the  $B/T$ -plane of the phase diagram of Type I superconductors where the  $B_c(T)$ -curve separates the superconducting from the normal conducting area. On the right-hand side of Fig. 2.3, the decrease of the magnetic field in the  $x/y$ -plane by means of a screening current in the Meissner phase is shown qualitatively for an infinitely long superconducting slab. This way, no end effects have to be considered. The applied external field  $B_{\text{ext}}$  is oriented in the  $y$ -direction.

Macroscopically a magnetization arises due to the induced current. However, from the outside it cannot be decided whether the magnetization results from diamagnetism (hence atomistic currents) or from supercurrents in the Meissner phase. Therefore, the magnetization can be calculated by assuming the susceptibility of an ideal diamagnet:

$$M = \chi \frac{B}{\mu_0} = -\frac{B}{\mu_0}. \quad (2.1)$$

As long as the critical field is not reached, the magnetization stays fully reversible as indicated by the arrows in Fig. 2.4. Table 2.1 shows the critical field values of typical Type I superconductors.

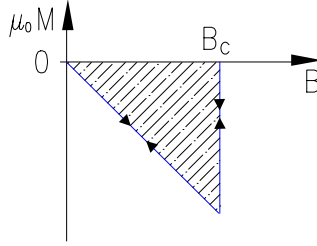


**Figure 2.4:** Magnetization of a Type I superconductor as function of the applied magnetic induction  $B$ . The magnetization stays fully reversible for an applied magnetic inductions below the critical field  $B_c$ . For the example of the superconducting slab, no end effects have to be considered.

**Table 2.1:** Critical field values  $B_c$  of some typical Type I superconductors (values taken from [3]).

Element	$T_c$ (K), $B = 0$ T	$B_c$ (T), $T = 0$ K
Pb	7.19	0.0803
Sn	3.72	0.0305
Ti	0.40	0.0056
Nb	9.25	0.2060

The fact that there is no magnetic field inside a Type I superconductor excludes the existence of a current in the interior as well; therefore no transport current is possible in these superconductors, limiting their utility. Today, all the technically relevant materials which are used for cables in superconducting magnets, including high temperature superconductors, are Type II materials.

### 2.2.2 Type II Superconductors

The main difference between Type I and Type II superconductors is that a Type II superconductor allows flux penetration while remaining in the superconducting state. This flux penetration starts at a value denoted as the lower critical field  $B_{c1}$  of Type II superconductors. The  $B_{c1}$  value is usually considerably smaller than the critical field  $B_c$  of a Type I superconductor whereas the material remains superconducting up to a much higher field value, the so-called upper critical field  $B_{c2}$  of Type II superconductors.

For applied fields below  $B_{c2}$ , however, the flux does not enter continuously but by means of quantized flux tubes, so-called vortices. These vortices are able to move freely inside the material and possess a normal conducting core, while the surrounding area stays superconducting. Each flux tube is surrounded by circular supercurrents that screen the magnetic field in the core from the rest of the superconducting material. Due to the co-existence of superconducting and normal conducting regions, this state is called the mixed state.

Figure 2.5 shows the  $B/T$ -plane of the phase diagram for Type II superconductors, indicating qualitative values. Also shown in the plot is a typical  $B_c(T)$ -curve of Type I super-



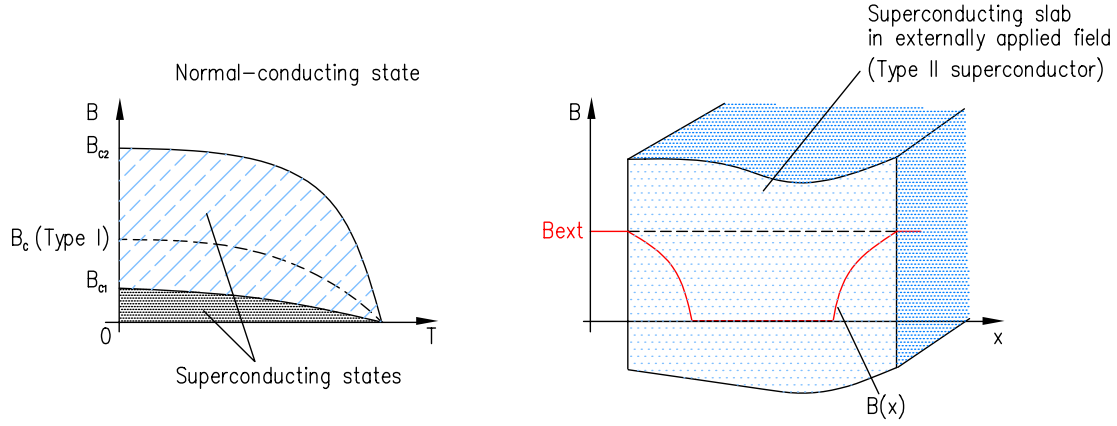


**Figure 2.5:** Left: Phase diagram of Type II superconductors. The superconducting and the normal conducting state are separated by the  $B_{c2}(T)$  curve. Right: Progression of the magnetic induction after applying an external field to a Type II superconducting slab. The external field is raised from 0 to a value  $B_{\text{ext}}$  in the range  $B_{c1} < B_{\text{ext}} < B_{c2}$ , and kept small enough to let the interior stay field free.

conductors for comparison.

The normal conducting core of a flux tube contains exactly one quantum of magnetic flux  $\Phi_0$ , the so-called flux quantum. The value of such a flux quantum is an universal constant and equals:

$$\Phi_0 = \frac{h}{2e} \approx 2.0679 \cdot 10^{-15} \text{ Vs},$$

where  $e$  denotes the charge of an electron and  $h$  is the Planck's constant.

The flux tubes are oriented parallel to the applied field, as illustrated in Fig. 2.6, and they exist for field values in the range  $B_{c1} < B < B_{c2}$ . Any increase of external field within this range yields an increase in the number of flux tubes penetrating the material until  $B_{c2}$  is reached.

In case the Type II superconductor did not undergo any further treatment, the vortices are able to move freely in the material arranging themselves in a triangular flux pattern as is shown in Fig. 2.6 (assuming the absence of transport currents). This triangular flux pattern was first recognised by Essman and Träuble [44] who decorated the surface of a superconductor with metallic powder (evaporated iron) after applying an external magnetic induction. The powder, being attracted by the strongest magnetic field, illustrated the remanent flux pattern.

The magnetization of a Type II superconductor is qualitatively shown in Figure 2.7. Here, the magnetization increases until the lower critical field  $B_{c1}$  is reached at which the superconductor goes into the mixed state. Further increase in the magnetic induction results in a decreasing magnetization which becomes zero when the upper critical field  $B_{c2}$  is reached and the superconductivity vanishes. The difference in the behavior compared to Type I superconductors is the gradual transition from the maximum magnetization at  $B_{c1}$  to the zero value reached for  $B_{c2}$ . The shape of the curve in the range of  $B_{c1} < B_{\text{ext}} < B_{c2}$  can be

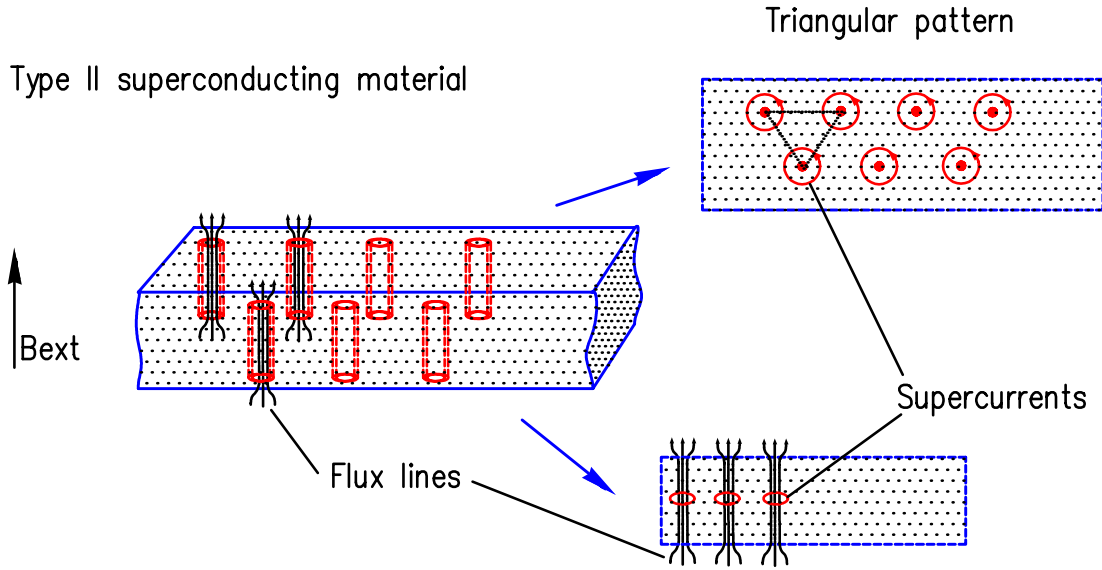


**Figure 2.6:** Type II superconducting plate with externally applied field. The flux penetrates in quantized flux tubes arranged in a triangular pattern. The side view shows the magnetic flux channeled through the tube and the induced surrounding screening currents. For the example of the superconducting slab, no end effects have to be considered.

explained by thermodynamic considerations as is shown in the appendix A.3.

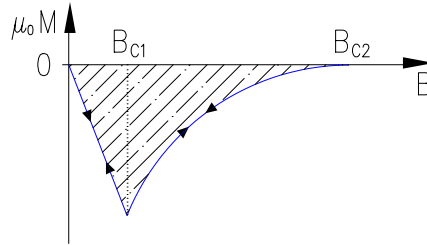


**Figure 2.7:** Magnetization of a Type II superconductor as a function of  $B$ . The magnetization stays fully reversible for applied magnetic inductions below the critical field  $B_{c2}$ . Note that the value of  $B_{c1}$  is much smaller than  $B_{c2}$ .

An externally applied transport current can be carried in the material by reshaping the vortex distribution and adding up the circulating supercurrents of the flux tubes. This allows a Type II superconductor to keep a transport current as long as the total current does not locally exceed the critical current  $I_c$ .

However, the applied transport current exerts a Lorentz force on the flux tubes causing them to move. The movement of flux lines under this force dissipates energy, which is heating the superconductor, raising the temperature above  $T_c$  and driving it into normal conducting state. Therefore, flux movement has to be avoided, a fact, that means a restriction in the

use of superconducting material. Metallurgical treatment is required which changes the characteristics of an untreated Type II superconductor by producing certain defects, for instance in form of deformations in the atomic lattice. These defects act as *pinning centers*, preventing the movement of the flux tubes. In general, one distinguishes two different types of defects: The substitutional type where the atoms of the solute substitute the solvent at random points of the lattice and the interstitial type of solution where the atoms of the solute are present in the interstices of the solvent lattice. Most common in superconducting alloys is the precipitation of  $\alpha$ -Ti as is used in NbTi, for example. Ti in the  $\alpha$ -phase<sup>6</sup> is not superconducting and hence builds flux pinning sites [45], [46]. Further, the movement of flux lines being not pinned explicitly is reduced due to their interaction with flux lines that are actually pinned.

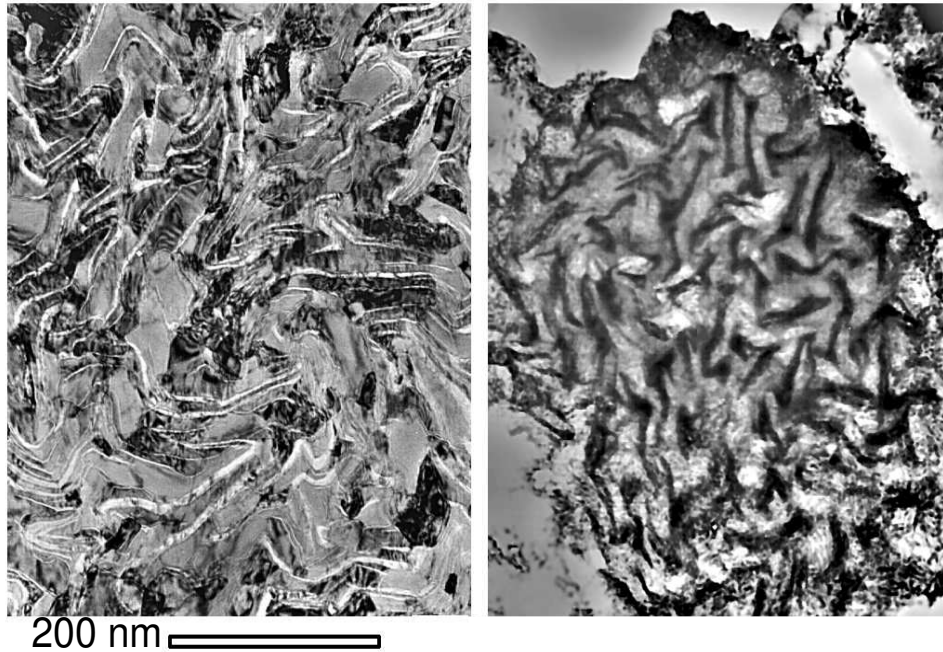


**Figure 2.8:** Micro-photographs of superconductors showing the pinning centers. Left: Conventional pinning centers which consist of  $\alpha$ -titanium (white parts); Right: Artificial pinning centers made of pure niobium (black parts). The picture gives an idea of the difficulties arising when a microscopic modeling is attempted. Pictures with the courtesy of D.C. Larbalestier (University of Wisconsin, USA).

In some cases, special impurities are additionally implanted (so-called artificial pinning centers) in order to increase the pinning, but this method is not used except in laboratory studies, so far [45].

During the strand/cable production process, the material undergoes a series of hard work-

---

<sup>6</sup>The  $\alpha$ -phase denotes a terminal solid solution that has the structure of one of their component metals, Nb in this case. Nb is a body-centered cubic (bcc) metal and since Ti undergoes a transition from a hexagonal close-packed (hcp) lattice to a bcc lattice, the solid solution alloy is a preferred state. See, e.g., [45] for details.

ing such as drawing and rolling and as a result these materials finally become hard, hence those superconductors are sometimes denoted as hard superconductors.

Figure 2.8 shows a micro-photograph of a structure of pinning centers: Conventional pinning centers are indicated by the white domains (left side) and artificial pinning centers are shown on the right-hand side. The maximum pinning strength of the material keeping the flux lines from moving is the key factor in determining the maximum of current that can be carried by the material. However, in the framework of this thesis the interesting point is not the optimal distribution and size of the pinning centers, but to develop a model which works on a macroscopical level. From the structure presented in Fig. 2.8 it is obvious that any microscopical modeling must be considered as extremely difficult, if not impossible and therefore was not pursued any further.

In this thesis, when superconductivity is mentioned, hard superconducting materials are referred to, if not indicated otherwise.

## 2.3 The $J_c(B, T)$ -dependence

In order to describe the behavior of a Type II superconductor in an applied field, not only the magnetic induction  $B_{\text{ext}}$  and the operating temperature  $T$  have to be given, but also the critical current density  $J_c$ . The critical current density  $J_c$  of a Type II superconductor is the maximum current density a superconductor can keep without migrating into normal conducting state. Different functions for expressing the critical current density  $J_c$  are introduced in this section.

The dependence of  $J_c$  on the other parameters is best characterized by its critical surface, presenting  $J_c$  as a function of  $T$  and  $B$ . From material science, it is known that the total magnitude of the critical current density depends on the upper critical field  $B_{c2}$  and the critical temperature  $T_c$ , entities which are *intrinsic* properties of the alloy. Further,  $J_c$  is also a function of the applied strain  $\varepsilon$  and of metallurgical properties (such as the amount of pinning centers resulting from a metallurgical treatment like cold working, etc). The latter are *extrinsic* properties of the alloy and depend on the metallurgical *state*. In the following, a fit function for the critical current density of NbTi is derived which can be incorporated into the magnetization model, reproducing the dependencies on the temperature and the applied magnetic induction.

The strain dependence of the critical current density  $J_c(\varepsilon)$  has been investigated by J.W. Ekin [47] (1981) who developed a strain scaling law for a variety of superconducting materials, including NbTi and Nb<sub>3</sub>Sn. He derived the following expressions for the upper critical field and the temperature as a function of the strain  $\varepsilon$ :

$$B_{c20}(\varepsilon) = B_{c20m}(1 - a|\varepsilon|^{1.7}), \quad T_{c0}(\varepsilon) = T_{c0m} \left(1 - a|\varepsilon|^{1.7}\right)^3. \quad (2.2)$$

Here, the entity  $B_{c20}$  denotes the upper critical field at  $T=0$  K, and  $T_{c0}$  the critical temperature for  $B=0$  T. The parameters  $B_{c20m}$  and  $T_{c0m}$  denote the maximum values of the upper critical field  $B_{c20}$  and the critical temperature  $T_{c0}$  at zero intrinsic strain whereas the parameter  $a$  is a constant whose value depends on the considered strain interval<sup>7</sup>.

A direct temperature dependence of the critical current density  $J_c(T)$  is given by

---

<sup>7</sup>Two intervals are distinguished:  $a \approx 900$  for  $\varepsilon$  below zero and  $a \approx 1250$  for positive values of  $\varepsilon$ .

M.S. Lubell [48] (1983):

$$J_c(T) \sim \left(1 - \left(\frac{T}{T_{c0}}\right)^n\right).$$

Lubell also gives an expression for the upper critical field dependence to:

$$B_{c2}(T) = B_{c20} \left(1 - \left(\frac{T}{T_{c0}}\right)^n\right), \quad (2.3)$$

setting the exponent  $n$  in both equations to 1.7.

The results of Ekin and Lubell are combined by Summers [49] (1991), in order to derive a general equation for the determination of the critical surface of Nb<sub>3</sub>Sn, which besides the strain- and temperature dependence also considers a radiation damage dependence<sup>8</sup>. Following Summers, the expression of  $J_c$  for Nb<sub>3</sub>Sn reads:

$$J_c(B, T, \varepsilon) = C(\varepsilon) (B_{c2}(T, \varepsilon))^{-1/2} \left(1 - t^2\right)^2 b^{-1/2} (1 - b)^2, \quad (2.4)$$

$$\text{where } b = B/B_{c2}(T, \varepsilon), \quad t = T/T_{c0}(\varepsilon). \quad (2.5)$$

Neglecting the strain dependence and inserting Eqs. (2.5) allows a re-formulation of Eq. (2.4) and yields a  $J_c(B, T)$ -dependence:

$$J_c(B, T) \sim B_{c2}^{1/2}(T) \frac{1}{B} \left(\frac{B}{B_{c2}(T)}\right)^{1/2} \left(1 - \frac{B}{B_{c2}(T)}\right)^2 \underbrace{\left(1 - \left(\frac{T}{T_{c0}}\right)^2\right)^2}_{f(T)}. \quad (2.6)$$

Note that the resulting dependence of the  $J_c$ -function on the temperature is two-fold: First explicitly by means of the last term  $f(T)$  and then also indirectly by the definition of the critical field  $B_{c2}$  according to Eq. (2.3).

Equations (2.4) and (2.6) are applied by L. Bottura [50] (1999) as a basis to replace the function of the critical current density with a current fit  $j_c(B, T) = J_{c,\text{ref}} f(B, T)$ . Bottura introduces four fit parameters into the equation for the fit function  $f(B, T)$  that results in a dimensionless fit which reads:

$$j_c(B, T) = J_{c,\text{ref}} f(B, T) = J_{c,\text{ref}} \frac{C_0}{B} \left(\frac{B}{B_{c2}}\right)^\alpha \left(1 - \frac{B}{B_{c2}}\right)^\beta \left(1 - \left(\frac{T}{T_{c0}}\right)^n\right)^\gamma. \quad (2.7)$$

The fit parameters are set to be:

			fit parameters
$B_{c20} =$	14.5 T	(upper critical field)	$C_0 =$ 27.04 T
$T_{c0} =$	9.2 K	(critical temperature)	$\alpha =$ 0.57
$n =$	1.7	(number from Eq. (2.3))	$\beta =$ 0.9
			$\gamma =$ 2.32

**Table 2.2:** Parameters of the fit function  $f(B, T)$  according to Bottura.

---

<sup>8</sup>Summers accounted for radiation damages by changing the expressions for  $T_{c0}$  and  $B_{c0}$ . Since radiation damages are not considered here, these expressions have been omitted.

The fit function  $f(B, T)$  has to be multiplied with the reference value  $J_{c,\text{ref}} = J_c(5 \text{ T}, 4.2 \text{ K})$  to obtain the current fit.

This way, a  $j_c(B, T)$ -surface for NbTi cables could be plotted by applying this fit function  $f(B, T)$ , and an expression could be given for the NbTi cables that are used in the LHC main dipole and quadrupole magnets. In any case, the dependencies of  $J_c(B, T)$  on strain- and radiation damages are neglected. The entity  $B_{c2}$  follows from Eq. (2.3).

Figure 2.9 shows the critical surface that results from Eq. (2.7) with the above-mentioned fit parameters. Note that the function for the critical current density is given by small letters if the current density is expressed by a fit function (instead of capitals). In Figure 2.10, the dependence of  $j_c$  on the magnetic induction and on the temperature are presented explicitly.

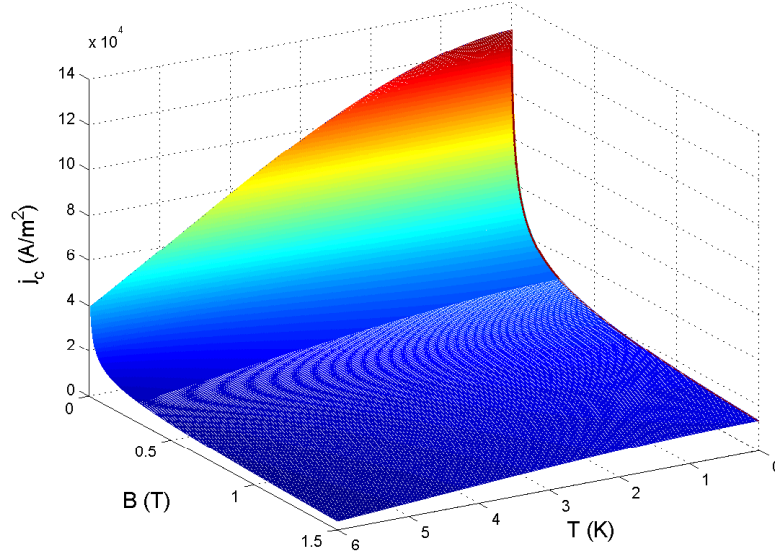


**Figure 2.9:** Surface of critical current density for NbTi resulting from the current fit function  $j_c(B, T)$  which is given in Eq. (2.7). Included are the fit parameters which are given in the table 2.2.

As can be seen from the curves in Fig. 2.10 (left), the current fit for the critical current density possesses a pole at  $B = 0$  and shows a sharp decline with increasing magnetic induction. Only little variation can be observed in the  $j_c(B)$ -dependence for different temperatures (indicated in the legend). Almost no changes can be seen for fields above 0.8 T with varying temperature and also for the extreme low field range (below 0.05 T), only a small variation exists. A change in the slope of the curve can be observed in the range of 0.05 to 1.5 K for the presented temperature values between 1.9 and 4.2 K. All curves approach the same  $j_c$  value for high fields independent of the actual temperature as long as the temperature remains in the cryogenic range.

Figure 2.10 (right) presents the variation of  $j_c(T)$  for different values of the magnetic induction  $B$ . Here, a strong dependence on the applied field is observed. As expected, the critical current density increases with decreasing applied magnetic induction (indicated in the legend) for all temperatures in the cryogenic temperature range. Also an increase in the variation of  $j_c$  over the presented temperature range can be observed for lower magnetic in-

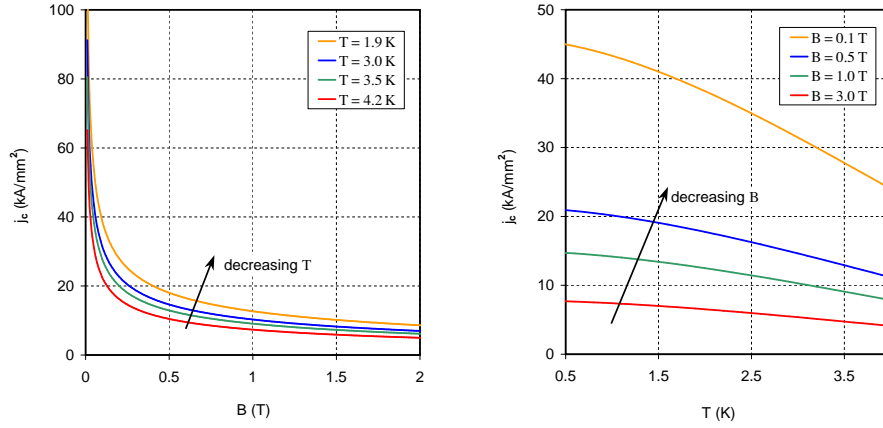


**Figure 2.10:** Left: Critical current density  $j_c$ , expressed by a fit function, versus the total magnetic induction  $B$  for different temperatures  $T$ . The function shows a pole for  $B = 0$  that, however, cannot be reached in practice, due to the self-field of a superconducting filament; Right:  $j_c$  versus the operating temperature  $T$  for different values of the total applied magnetic induction  $B$ . For the calculation of the magnetization that is shown in chapter 4,  $T$  is assumed to be held constant at 1.9 K (red curve in left plot).

ductions. However, the  $j_c(T)$ -dependence resulting from such a strong temperature variation is not critical since  $T$  usually stays stable in the range of  $\Delta T < 0.3 \text{ mK}$ . Note that in Fig. 2.10 (right),  $T$  covers a great range from 0.5 K to 4 K.

The current fit,  $j_c(B, T)$ , of Bottura is used in the framework of this thesis for the calculation of superconductor magnetization effects in the LHC main dipole and quadrupole magnets which are both wound from NbTi cables. A strain dependence is not considered whereas the temperature dependence is kept in the function and the temperature is assumed to be held constant at 1.9 K. The outcome of these calculations is presented in section 6. The ranges for the fit parameters  $\alpha, \beta, \gamma$  are given by Bottura as:  $\alpha$  in the range of 0.5 to 0.8,  $\beta$  around 1 and  $\gamma$  in the range of 2. The Figures 2.11, (left, middle, right) present the critical current density  $j_c$  (from the fit function) versus the magnetic induction  $B$  as a function of the dependencies on the fit parameters  $\alpha, \beta$  and  $\gamma$ . As can be seen from the plots, the extreme low field range is determined mainly by the fit parameter  $\alpha$ , whereas  $\gamma$  defines the bending of the increasing slope as a function of decreasing field. The fit parameter  $\beta$  dominates the medium and high field range and therefore influences the width of the resulting magnetization curve, which is also responsible for the amount of hysteresis losses, especially at high field (see section 7.4 for details). Note that the ranges of  $j_c(B)$  and  $B$  vary in the three plots.

The main flaws to be found in most models of filament magnetization are not only the non-physical negligence of the dependence of the critical current density on the externally applied magnetic induction  $B$ , moreover, most of the models also neglect the variation of  $J_c$  inside the

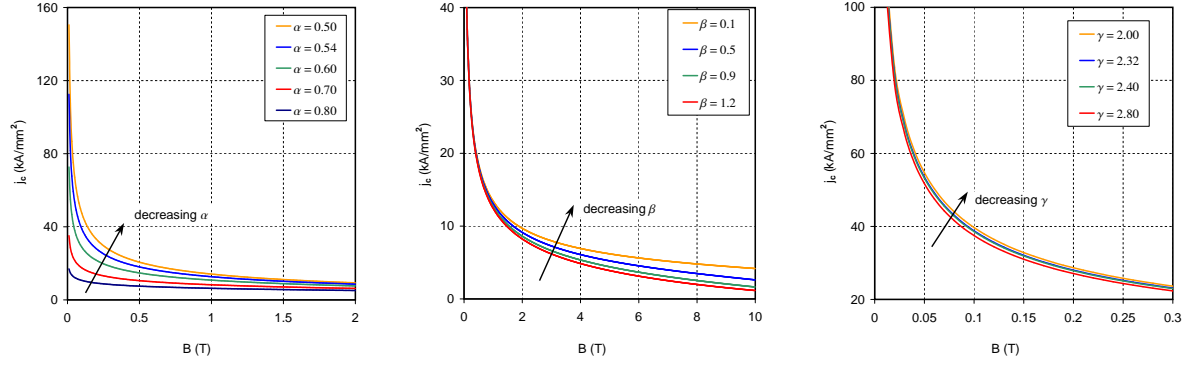


**Figure 2.11:** Fit function of critical current density  $j_c$  versus the magnetic induction  $B$  depending on the dimensionless fit parameters  $\alpha$ ,  $\beta$  and  $\gamma$ .

material<sup>9</sup>. Due to the screening properties of Type II superconductors, the magnetic induction in the filament cross-section decreases from the outer filament border to the interior and is a function of the filament radius. Since  $J_c$  increases as is shown in Fig. 2.11, (left) according to the fit function given in Eq. (2.7), any decrease in  $B(r)$  corresponds to an increase of  $J_c(r)$ . This local variation of  $J_c(r)$  in the filament cross-section is self-included in the magnetization model, in case a of direct consideration of the  $J_c(B)$ -dependence. However, Zhilichev [19], for example, considered a piece-wise continuous distribution of critical currents in a discretized filament cross-section such that the  $J_c(B)$ -dependence indirectly enters the expressions for the resulting magnetic induction and the superconductor magnetization of the filament. The above-mentioned direct consideration of the  $J_c$ -dependence in the magnetization model will become more clear from the derived formulas presented in chapter 4.1, where also the behavior of  $B(r)$  is described in detail. As can then be seen in the Figs. 3.7 and 3.8, the surface fit for  $J_c$  versus  $B$  determines the shape of the magnetization curve in the quadrants.

The main advantage of the fit curve presented above, is that it applies to a field range from 0 T to 9 T and hence covers the total operating range of most magnets<sup>10</sup>. It also applies to very low fields. However, no analytical solution could be found for the integration of the fit function. The fit function has therefore been approximated locally around the actual value of the applied magnetic induction by means of an inverse square root dependence. The approximation reads:

$$j_c(B, T) = j_c(B_{\text{ext}}, T) \frac{\sqrt{B_{\text{ext}}}}{\sqrt{B}}, \quad (2.8)$$

where  $j_c(B_{\text{ext}}, T)$  is the value of the current fit curve which is hereby approximated by a square-dependence in each point in order to obtain integrable equations.

For the sake of completeness, also the current fit function of Kim and Anderson [14] is described here. Kim and Anderson suggested a  $J_c(B)$ -dependence following a power series

<sup>9</sup>As is shown in section 3.1, the Critical State Model does not consider any  $J_c$ -dependence at all, whereas the model of Wilson, described in section 3.2, considers the dependence of  $J_c$  on the external field, but not the local variation of the field in the filament cross-section.

<sup>10</sup>The fit will be used for the calculation of the LHC main magnets being powered up to a main field of 8.5 T, for instance. See chapter 6 for details.



expansion of

$$\frac{\alpha}{J_c} = B_0 + B + a_2 B^2 + a_3 B^3 + \dots,$$

which results in the known expression for the critical current density

$$j_c(B) = \frac{\alpha}{B_0 + B}$$

assuming the coefficients  $a_2, a_3, \dots$  to be sufficiently small. The remaining fit parameters are  $B_0$  and  $\alpha$ ,  $B$  denotes the external magnetic induction. Due to its simplicity the Kim-Anderson current fit function is very often used for the calculation of superconductor magnetization. However, as shown in section 3.2 where the Wilson Model is applied, in case of the LHC dipole magnet, which is taken as exemplary, the fit function only moderately reproduces the measurements taken on the superconducting strand.

It should be emphasized here that for the magnetization model presented in chapter 4 the geometrical data of filament and strand are needed. Besides this values, only the current fit function has to be chosen in order to determine the strand magnetization. The fit function can usually be derived by critical (transport) current measurements (for instance, by means of the ‘hairpin-method’ [3], [8]). Critical current measurements are the most frequently performed measurements of superconductor properties. Measurements of this kind are carried out routinely from both sides, by the cable manufacturers as well as the magnet producers in the framework of the cable quality control. They are therefore mostly easily available. Since the samples are usually tested by means of applying a magnetic field at right angles to the strand longitudinal axis, the situation well covers the applications in magnet construction. At CERN, there are four test stations for critical currents that regularly test strands from all cables for the LHC. Values for critical currents can also be received indirectly from magnetization measurements. In this case, only the results from the measurement from one up-ramp cycle<sup>11</sup> is needed.

---

<sup>11</sup>The up-ramp cycle received from magnetization measurements should ideally be a non-initial state curve, in order to get fit values of the low field range. However, this is no stringent condition. A fit function can be received from initial state curve data as well.



## Chapter 3

# Superconductor Models for Filaments

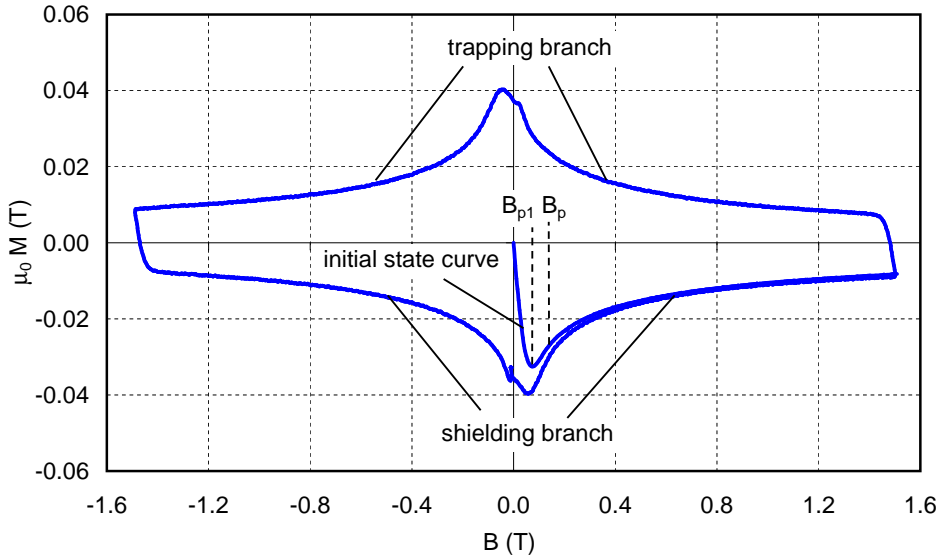
In this chapter, the Critical State Model and the Wilson Model for the determination of superconductor magnetization are described. The two models as well as the magnetization model which is developed in the framework of this thesis express superconductivity macroscopically, which means finding global parameters for its description. Therefore all models admittedly lack microscopic rigor. In this way, the models approach superconductivity from an engineering point of view, keeping in mind that the aim is to calculate and predict the behavior of superconducting magnets, rather than finding a theory to be used by material scientists. Hence, the aim is the development of a model which can be derived from reasonable assumptions and which shows a good agreement with the experimental situation.

Figure 3.1 shows the magnetization curve as measured on a superconducting NbTi strand which is designed for the outer coil layer of the LHC main dipole. The resulting magnetization curve is already here presented in order to give an idea of the expected response if a superconducting filament or strand is exposed to an externally applied magnetic field. The plot shows a sweep in applied magnetic induction from  $0 \text{ T} \rightarrow 1.5 \text{ T} \rightarrow -1.5 \text{ T} \rightarrow 0 \text{ T}$  for a strand with 8900 filaments of radius  $3.5 \mu\text{m}$  yielding a Cu/Sc-ratio<sup>1</sup> of 1.95. Starting from zero, the magnetization follows the initial state curve. The superconducting filaments shield their interior against the applied magnetic induction. The magnetization follows the so-called shielding branch. A change in the direction of the applied magnetic induction raises a reversely oriented current layer penetrating the filament from the outside. The hysteresis arises due to the already existing currents in the interior which remain and are therefore denoted *trapped currents*. The magnetization follows the so-called trapping branch. The decrease of magnetization with increasing field results from the dependence of the critical current density on the field. This effect and the hysteresis behavior can be well observed in the measurements.

In order to determine field errors in a superconducting magnet, any calculated filament/strand magnetization has to be combined with general field calculation programs for the computation of a magnet cross-section. This allows to consider the properties of the materials used in magnet construction. Hence, an additional objective is to derive a model for superconductor magnetization which can easily be incorporated into the field computation

---

<sup>1</sup>The Cu/Sc-ratio denotes the volume ratio of the matrix material (copper (Cu)) and the superconducting material (niobium titanium (NbTi)).



**Figure 3.1:** Measured magnetization curve for a superconducting NbTi strand of an LHC main dipole magnet [51]. Starting from zero, the magnetization first follows the initial state curve. Each filament shields its interior against the applied magnetic induction (shielding branch). Due to the non-reversible properties of Type II superconductors, the magnetization produces a hysteresis by raising a reversely oriented current layer, when the direction of the applied magnetic induction changes. The hysteresis arises due to trapped currents in the interior and the magnetization follows the so-called trapping branch.

program ROXIE [52] in order to combine it with finite element solvers for magnet calculation. ROXIE is an abbreviation for **R**outine for the **O**ptimization of magnet **X**-sections, **I**nverse field calculation and coil **E**nd design and has been created by Stephan Russenschuck at CERN. The program is used for the electromagnetic design of the superconducting main magnets for the LHC. One important key factor in the ROXIE program is the use of advanced numerical solvers which avoid the meshing of the superconducting coil. This is advantageous, since any coil modeling in finite elements has to be carried out with extreme accuracy due to the fact that the field quality in the aperture of a superconducting magnet is dominated by the source current distribution. The magnetization model to be developed here has to be such as to not violate this principle.

Further, the model should rely only on some characteristic input parameters in order to avoid the calculation of the magnetization by means of curve fits based on measurements. As will be shown in this chapter, the developed model calculates the magnetization from one input function only (which describes the critical current density) and the geometrical data of the filament.

In principle, three decisive parameters exist that define the difference in the models introduced in this chapter:

- The function for the critical current density  $J_c$  and its field dependence. The critical current density is the maximum current density a superconductor can keep before

transition to the normal conducting state,

- the critical field  $B_{c2}$  which is a function of temperature, and
- the penetration field  $B_p$  which denotes the value of applied magnetic induction at which the superconductor reaches full penetration.

In addition, all three models give different expressions for the entity  $B_{p1}$ , which presents the value of the external magnetic induction when the modulus of the filament magnetization passes through its first maximum during up-ramp on the initial state curve (see also Fig. 3.1).  $B_{p1}$  therefore gives a measure of the total maximum value of magnetic flux that can be shielded by the superconductor on the initial state curve. Also the parameter  $T_c$ , denoting the critical temperature of a superconductor is of importance due to its influence on the critical current density, as is already shown in chapter 2. In the framework of the studies carried out here, local temperature distributions, along the cable cross-section, for example, will not be considered, rather a constant operating temperature is assumed. For the LHC, for instance, the operating temperature is set to 1.9 K.

### 3.1 The Critical State Model

The Critical State Model was developed by C.P. Bean (1964) **for a slab** of hard superconductor material. Bean [10], [11] treated the superconductor macroscopically, considering only two possible states of current density: The density is either zero or equal to the maximum current density  $\pm J_c$  which is then called the critical current density. The orientation of  $J_c$  follows from the right-hand law. The Meissner phase and the dependence of the current density on the position in the superconductor cross-section, as well as on the magnetic induction, are not considered although Bean qualitatively described these dependencies in his publications. In case the critical current density  $J_c$  flows everywhere in the specimen, it is said to be in the critical state. Figure 3.2 follows from Bean's publication [11], showing a superconducting slab of width  $D$ .<sup>2</sup> The slab experiences an applied magnetic field  $H$ , where  $H^*$  denotes the maximum screenable field which is reached when the material gets fully penetrated. The magnetic field  $H^*$  then corresponds to the magnetic induction  $B_p/\mu_0$  for a filament (see also section 4.1). In case of a slab with a constant critical current density, the maximum screenable field is reached at full penetration ( $B_p = B_{p1}$ ). However, as will be shown later, this is not necessarily the case and the resulting calculated screening field depends on the superconductor model. The maximum screenable field, for example, is dependent on the course of the  $J_c$ -function at low field and therefore its evolution depends on the method of how the critical current density is included into the model. It is obvious, that the value of the computed maximum of the screening field depends on whether  $J_c$  is held constant or considered as field-dependent.

In the Critical State Model, the relationship  $J_c(B)$  is determined by the magnetic field only insofar as the critical current density  $J_c$  follows a step function which is reached even for small variations and does not change for different  $H$ -values as long as they are different from zero. Thus,  $J_c$  is constant along the cross-section of the superconductor and only the penetration depth varies if the external field changes.

---

<sup>2</sup>Note, that Bean used the magnetic field  $H$  instead of the magnetic induction  $B$  in his publications – this principle is followed for the explanation of the Critical State Model, only.

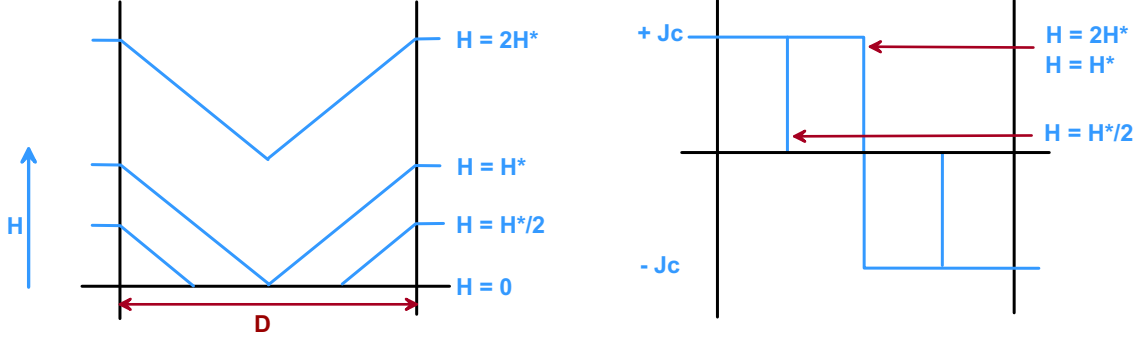


**Figure 3.2:** Application of the Critical State Model: Left: Superconducting slab of width  $D$  with an external magnetic field  $H$  applied on the outside according to Bean. The magnetic field constantly rises from  $0 \rightarrow H^*/2 \rightarrow H^* \rightarrow 2H^*$ . Right: Associated distribution of the critical current density  $J_c$  with respect to the  $H$  distribution shown on the left. The plots are taken from [11].

The plots in Fig. 3.2 qualitatively show the magnetic field distribution inside a slab of width  $D$  (left) for three different values starting from  $H = 0$ . The associated current density  $J_c$  is shown in the right plot of Fig. 3.2. The external magnetic field  $H$  is increased from  $0 \rightarrow H^*/2 \rightarrow H^* \rightarrow 2H^*$ . In the more general case, when the applied magnetic field changes orientation, additional current layers are generated as shown in Fig. 3.3, state (e).

Thus the magnetic field in the interior of the slab which is extended infinitely in the  $y$ - and  $z$ -direction, derives from Maxwell's Equation for magnetostatics,  $\nabla \times \mathbf{H} = \mathbf{J}_c$ , by solving the simple differential equation:

$$\frac{\partial H_y}{\partial x} = J_c. \quad (3.1)$$

If the applied field is oriented into the  $y$ -direction of the coordinate system, the critical current density will point into the  $z$ -direction, according to the right-hand law for a slab with the width  $D$  in the  $x$ -direction. Eq. (3.1) is valid in the plane of the slab cross-section and the critical current density  $J_c = J_z$  is constant, according to the model. Thus the magnetic field inside the slab results to:

$$H_y = J_c |x| + H_0.$$

Here, the integration constant  $H_0$  represents the offset of the  $H$ -curve with respect to the null value, in case the external field exceeds the maximum screenable field of the slab. The penetration field  $B_p = \mu_0 H_p$ , defined as the value which is reached when the superconductor gets fully penetrated, reads:

$$B_p = \mu_0 J_c \frac{D}{2}.$$

As already mentioned, the maximum screening field is identical to  $B_p$  for the Critical State Model. It will be shown in section 4.1.13 that for the more general case of a superconducting cylinder, when a  $J_c(B(r))$ -dependence is considered, the maximum screening field is reached **before** the cylinder is fully penetrated. It should be noted that the above given equations are describing one upramp cycle, only. In Fig. 3.3, the field and current distribution for an upramp and down-ramp cycle are shown.

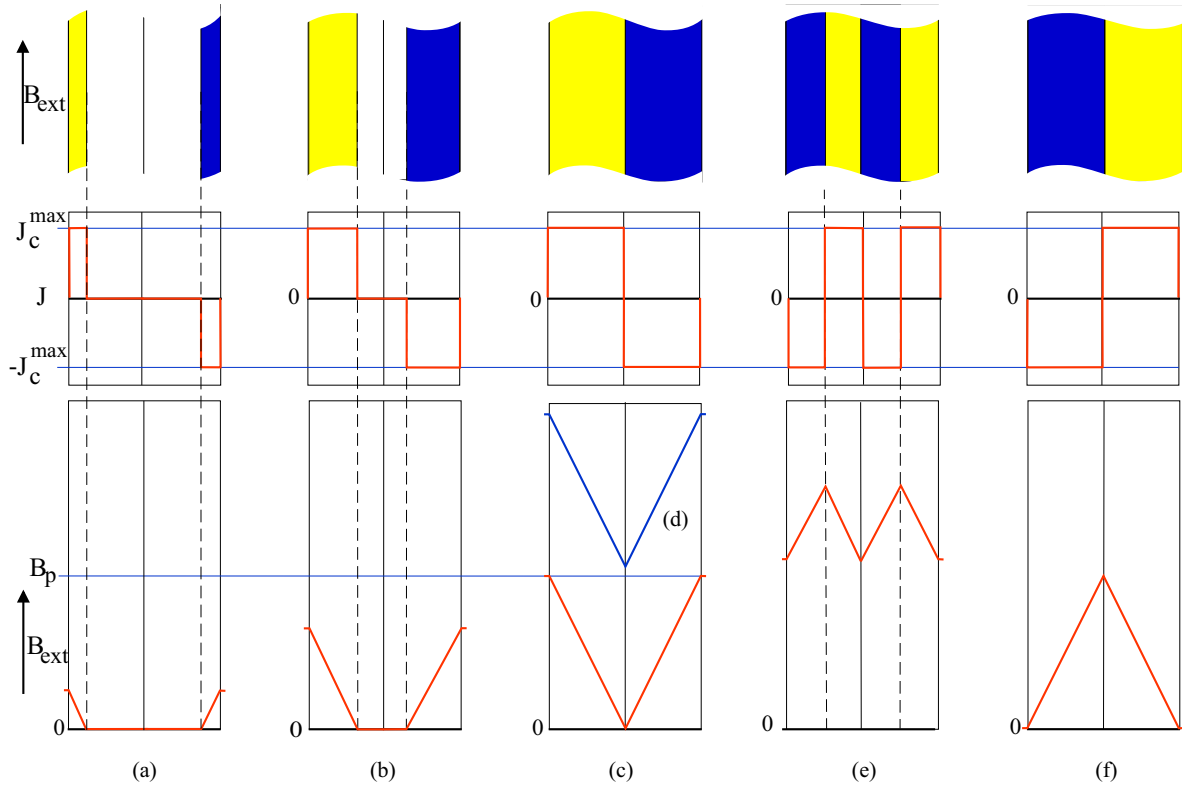


**Figure 3.3:** Superconducting slab which is exposed to a one-dimensional external field for different penetration states as derived from the Critical State Model. The slab dimension parallel to the orientation of the applied field extends to infinity. Top:  $J_c$ -profiles in the slab cross-section; middle and bottom: Distribution of critical current density  $J_c$  and magnetic induction  $B = \mu_0 H$  along the slab axis in the cross-section. The axis is perpendicular to the applied field orientation. Note, that due to the field independent current density in the slab, the penetration field always presumes the same slope.

Figure 3.3 shows the cross-section of a superconducting slab being exposed to a sweep of a homogeneous external field which results in different penetration states according to the Critical State Model:

- (a), (b) Initial state curve, not fully-penetrated. The external field is raised from zero to a value below  $B_p$ , leaving a field free region inside the filament.
- (c) Initial state curve, fully penetrated. The external field assumes the value  $B_p$ .
- (d) Initial state curve, fully penetrated. The external field assumes a value  $\geq B_p$ .
- (e) Reduction of external field when the field previously has been increased from zero to a value  $\geq B_p$  once before. This results in the development of an additional layer. In the magnetization curve, a hysteresis arises due to the remaining current distribution in the center of the filament.
- (f) Fully penetrated state (the external field assumes a value  $\geq B_p$ ) after reducing the external field.

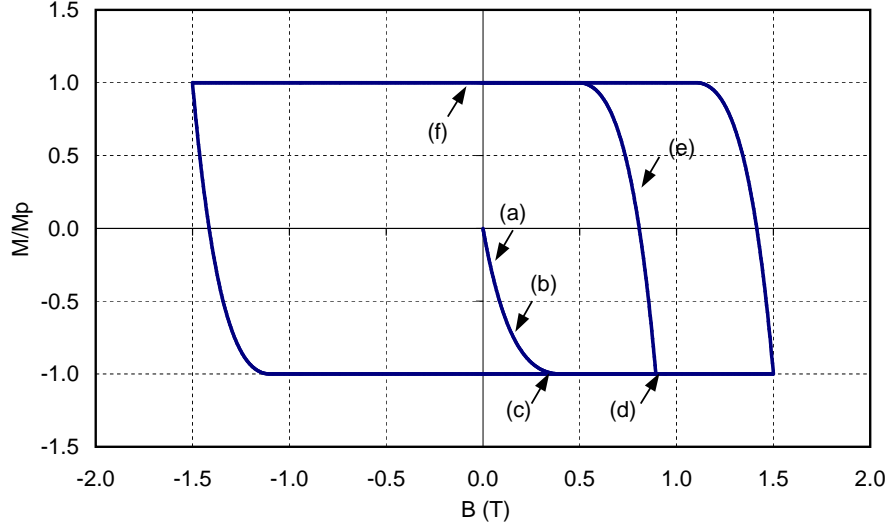


**Figure 3.4:** Normalized superconductor magnetization  $M/M_p$  of a NbTi filament versus the external magnetic induction according to the Critical State Model.  $M_p$  indicates the magnetization at maximum screening field  $B_{p1} = B_p$ . The magnetization of the different states [(a)-(e)] described in Fig. 3.3 are indicated in the plot.

Although Bean merely considered a slab, the behavior of a superconducting cylinder can now be described by adopting this model to the cylindric shape of the superconducting filament we are interested in. In this case, an equation for the inner  $J_c$  distribution in the filament cross-section has to be assumed and is chosen to be an ellipse here. The fixed value of  $J_c$  can be considered as an intrinsic property of the material. The entity  $B_p$  then also has a fixed value, only depending on the constant  $J_c$  and the filament radius  $r_f$  and such can be determined by:

$$B_p = f(J_c, r_f) = \frac{2\mu_0}{\pi} J_c r_f.$$

This equation has to be adopted to a cylinder with circular cross-section which is exposed to an external field perpendicular to the longitudinal axis of the cylinder. This way, the magnetic induction is obtained after integration of two half circles which are carrying the current densities  $\pm J_c$ , respectively. This idea has been taken from the model of Wilson (to be seen in Fig. 3.5, state (c)). It represents the so-called fully penetrated state of the filament. In this way, the model has been programmed in FORTRAN in order to obtain the plot in Fig. 3.4. By omitting the  $J_c(B)$ -dependence, the computation of the response of a superconducting filament on the external field by means of this very simple model yields a magnetization as displayed in Fig. 3.4. As can be seen, the curve differs considerably from the measured values presented in Fig. 3.1 and the results given in section 4.1. However, a rough scheme of the general behavior including the hysteresis is displayed and the results also show the limitations of the Critical State Model. Note that the approximate model of an ellipse as inner contour of  $J_c$  has been introduced originally by Wilson [8]. Applying this approximation, an initial state curve and different curves of up-down-ramp can be calculated, but expressions for minor loops have not been given by Bean.



## 3.2 The Wilson Model

For the calculation of the magnetization of superconducting filaments, M. Wilson [8] developed an approximate model which assumes the inner boundary of the current distribution of a round superconducting cylinder to approximately match an ellipse, whose ellipticity changes in order to screen any external field change. Although the screening field produced by this arrangement will not produce a perfectly uniform dipole field, Wilson expected the deviations with respect to the real current distribution to be small. Just as for the slab in the Critical State Model, Fig. 3.5 qualitatively shows a cylinder with circular cross-section in the  $x/y$ -plane in different states of externally applied fields. Again, the critical current density and the magnetic induction inside the superconductor are presented. As can be seen, the resulting distribution of critical current density  $J_c$  considers a dependence on the total amount of applied field. However, any change of  $J_c$  or  $B$  as a function of penetration depth is not part of the model. Wilson determined the resulting magnetic induction and the magnetization in the center of the filament, only, although for the assumed current distribution, the field is not exactly zero within the current free core of the filament. Compared with the Critical State Model, the Wilson Model differs in the distribution of the critical current density insofar, as a general dependence is considered, and a round cylindrical filament is treated. The radial dependence of  $J_c$  in the filament cross-section, however, is not considered.

Applying the Biot-Savart's Law on an assumed current distribution as is shown in Fig. 3.5, where the current is homogeneously distributed in the two areas and pointing in the  $\pm z$ -direction, allows to determine the resulting magnetic induction in the center of the filament<sup>3</sup> to:

$$\mathbf{B} = \frac{\mu_0 J_c}{\pi} \int_F \frac{y}{x^2 + y^2} \mathbf{e}_x - \frac{x}{x^2 + y^2} \mathbf{e}_y \, dF. \quad (3.2)$$

Here, the total area  $F$  consists of the two current carrying surfaces.

Let  $r_f$  be the filament radius. Then the elliptic inner contour of the current density is determined by the two entities  $r_f$  and  $a$ , the semi-major axis and the semi-minor axis of the ellipse, respectively (as indicated in the Figs. 3.5, 3.6). In this way, the current-carrying surface  $F$  in the filament cross-section is determined. Applying Eq. (3.2), the integrals for the components of the magnetic induction in the center of the superconducting cylinder read:

$$\begin{aligned} B_x &= 0, \\ B_y &= -\frac{\mu_0 J_c}{\pi} \int_{-r_f}^{r_f} \int_{f_1(y)}^{f_2(y)} \frac{x}{x^2 + y^2} \, dx \, dy, \end{aligned} \quad (3.3)$$

where the integral borders resulting from the inner ellipse and the outer circular contour are

$$\begin{aligned} f_1(y) &= a \sqrt{1 - \left(\frac{y}{r_f}\right)^2} \\ \text{and} \\ f_2(y) &= \sqrt{r_f^2 - y^2}. \end{aligned} \quad (3.4)$$

---

<sup>3</sup>The origin of the coordinate system is positioned in the filament center for this calculation.

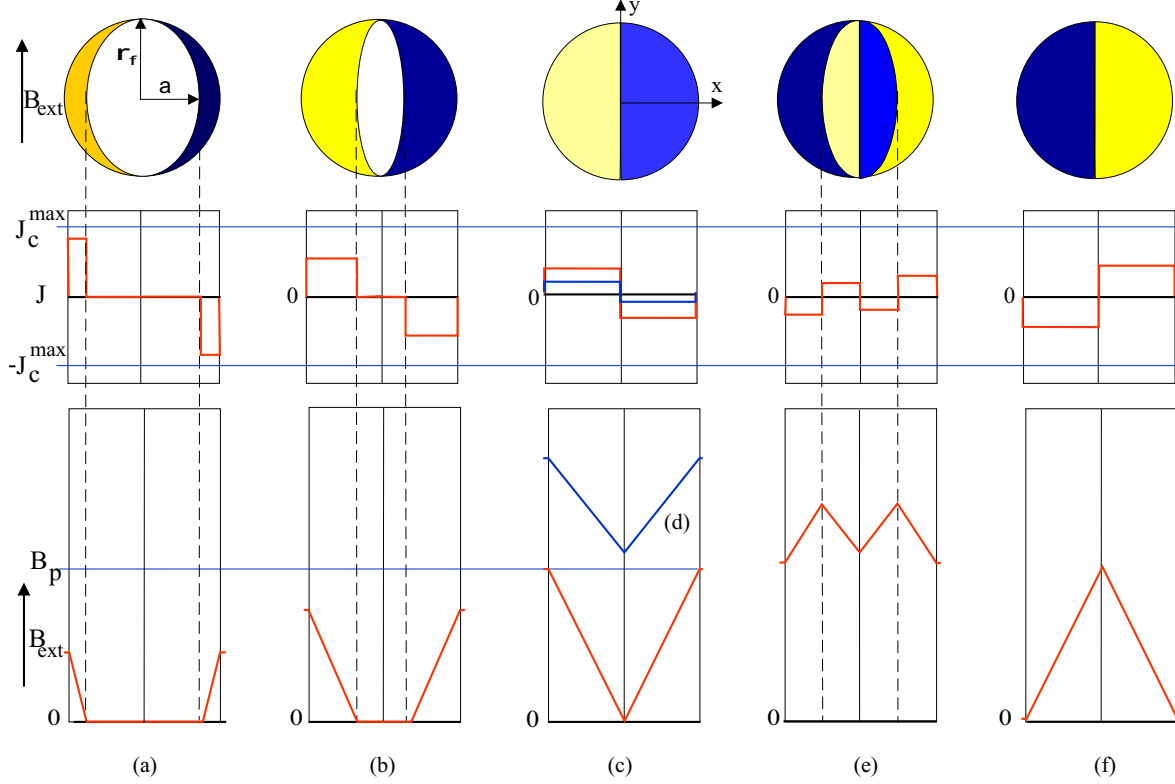


**Figure 3.5:** Round superconducting cylinder in a homogeneous external field for different penetration states according to the Wilson Model. Top:  $J_c$ -profiles in the cylinder cross-section; middle and bottom: Distribution of critical current density  $J_c$  and  $B$ -distribution in the cylinder cross-section, respectively. The Wilson Model considers a dependence of  $J_c$  on the value of the applied magnetic induction  $B$ . Thus, the slopes of the resulting magnetic inductions vary, depending on the state of the filament. The different penetration states correspond to those of the Critical State Model, shown before. Note that, when going from state (c) to state (d), the critical current density reduces to a lower value, due to the dependence on the changing external magnetic induction  $B_{\text{ext}}$  (blue curve).

Integration of Eq. (3.3) with the integral boundaries given in the Eqs. (3.4) yields the magnetic induction in the center of the filament:

$$B_y = -\frac{2\mu_0 J_c r_f}{\pi} \left[ 1 - \frac{a}{r_f} \frac{\arcsin\left(\sqrt{1 - \left(\frac{a}{r_f}\right)^2}\right)}{\sqrt{1 - \left(\frac{a}{r_f}\right)^2}} \right]. \quad (3.5)$$

According to Eq. (3.5), the maximum screenable magnetic induction (in case of  $J_c = \text{const.}$ ) is reached, for  $a=0$ , when the ellipse in the interior is shrunk to a line (corresponding to the states (c) and (f) in Fig. 3.5):

$$B_y = -\frac{2\mu_0 J_c r_f}{\pi} \quad (3.6)$$

In all states, the critical current density is oriented parallel to the  $z$ -axis according to a right-hand coordinate system.

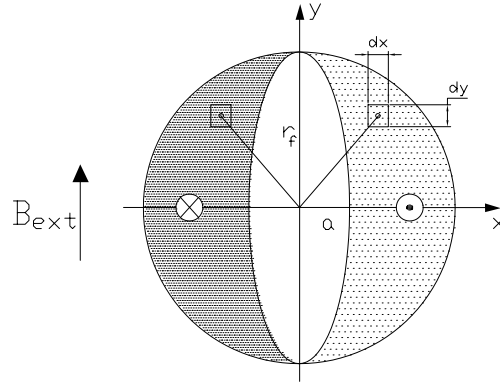


**Figure 3.6:** Calculation of the magnetization from the model of Wilson. The model integrates the surface of equivalent induced currents. The currents are oriented in  $\pm z$ -direction.

Using the same principle, the magnetization can be calculated. Starting from the magnetic moment of two infinitely small currents applied symmetrically around the ordinate axis as indicated in Fig. 3.6, the magnetic moment in the center of the filament results from:

$$dm_f = J_c 2x l_f \, dx dy, \quad (3.7)$$

$$m_f = 2J_c l_f \int_{-r_f}^{r_f} \int_{a\sqrt{1-(\frac{y}{r_f})^2}}^{\sqrt{r_f^2 - y^2}} x \, dx dy = \frac{4}{3} J_c l_f r_f^3 \left( 1 - \frac{a^2}{r_f^2} \right)$$

where  $2x$  denotes the distance between the two currents and  $l_f$  the length of the filament along the  $z$ -axis.

The magnetization  $M$ , given in (A/m) is defined as the magnetic moment per unit volume and can be found by division by the filament volume  $\pi r_f^2 l_f$ :

$$M = \frac{4}{3\pi} J_c r_f \left( 1 - \left( \frac{a}{r_f} \right)^2 \right), \quad (3.8)$$

where the only remaining parameter is the term for the critical current density  $J_c = j_c(B)$  which includes the fit function. The expression for the magnetization reaches a maximum for the ellipse shrunk to a line, when  $a = 0$ . The magnetization is then only depending on the filament radius and the current density:

$$M_p = \frac{4}{3\pi} J_c r_f. \quad (3.9)$$

Several fit functions for the critical current density exist which differ considerably, even for the same alloy material. The importance of choosing the  $J_c$ -fit function has already been discussed in section 2.3. Wilson suggested the use of either the Kim-Anderson current fit [14]

as a fair approximation or an extended current fit function derived from the Kim-Anderson fit as follows:

$$J_c(B) = A_0 + A_1 B + \frac{J_0 B_0}{B + B_0}.$$

Here,  $A_0, A_1, B_0$  are the available fit parameters. However, a current fit for the LHC cables has been developed at CERN by L. Bottura [50] which gives a good agreement with measured and calculated values. The magnetization can now be calculated from Eq. (3.8) and allows to consider the dependence  $J_c(B_{\text{ext}})$ , where  $B_{\text{ext}}$  denotes the applied field on the outer filament border (but neglect the dependence of  $B$  on the radial coordinate in the cross-section). The Wilson Model has been programmed in FORTRAN, in order to compare the outcome with the measurements. The calculation results in a magnetization which is shown in Fig. 3.7. Also presented in this plot is a measurement performed on an LHC cable [51], which has already been introduced at the beginning of this chapter, for comparison.

The two curves show a good agreement in the region of moderate and higher fields. However, the offshift of the measured curve with respect to the ordinate axis is not reproduced. Also an artificial hysteresis model has to be set up in order to compute the different branches, since the superconductor hysteresis does not occur by physical means in this model. Reverse current layers are assumed to keep a current density of  $2J_c$ , which is superimposed on the original shielding current, and expressions for minor looping have not been given by Wilson. The question of how in general the current surface in the superconductor cross-section with respect to  $B$  actually looks, still remains. The Wilson Model has also been used by Mess, Schmüser and Wolff [9] for magnetization calculation. For comparison, a calculation of the magnetization by means of the Kim-Anderson current fit [14], (which has not been specially developed for the LHC cables) is shown as well in Fig. 3.8.

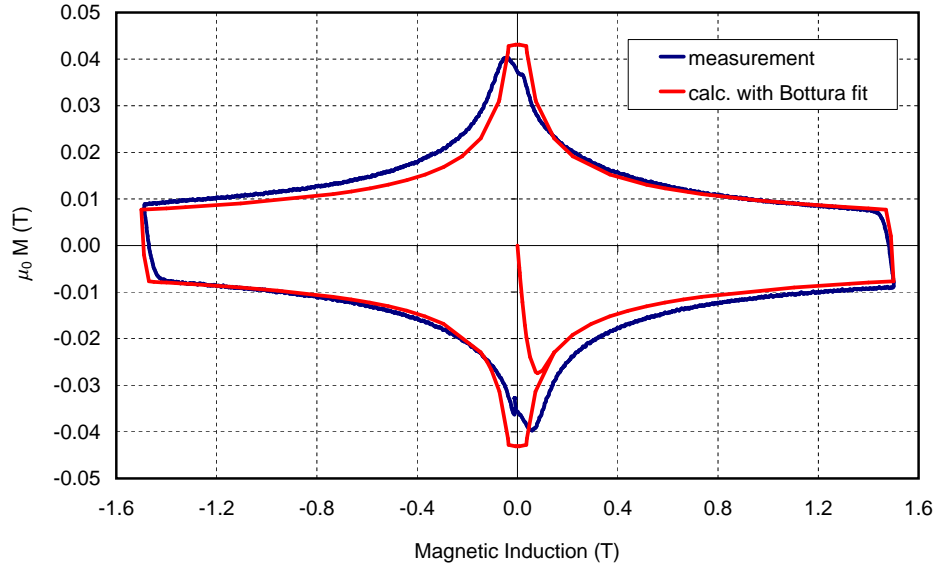


**Figure 3.7:** Magnetization versus magnetic induction of a superconducting filament with  $3.5 \mu\text{m}$  filament radius (computed with the current fit of Bottura) and measurements taken on an LHC strand. The magnetization has been calculated by means of the magnetization model of Wilson and has been combined with a hysteresis model in order to calculate the individual branches and the initial state curve.

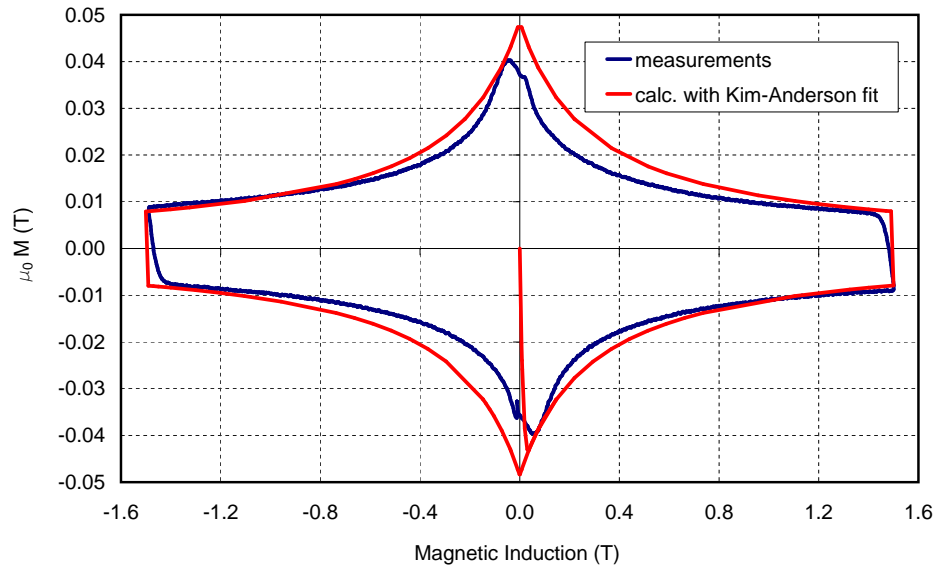


**Figure 3.8:** Magnetization versus magnetic induction of a superconducting filament with  $3.5 \mu\text{m}$  filament radius (computed with the Kim-Anderson current fit) and measurements taken on an LHC strand. The magnetization has been calculated by means of the same magnetization model of Wilson and has also been combined with a hysteresis model in order to calculate the individual branches and the initial state curve.



## Chapter 4

# The Nested Ellipse Model

As already explained in the sections 3.1 and 3.2, a screening current distribution is induced in all superconducting filaments if exposed to an external magnetic field. This current is of bipolar type and is the source of a screening field in the interior of the superconductor which results in a superconductor magnetization on a macroscopic range. In order to calculate the field inside the superconductor and its magnetization, the current-carrying area and the field dependent value of the local current have to be determined. The screening field in the interior is directed opposite to the external magnetic field, thus it can be considered as one-dimensional in a first approach. The coordinate system can be chosen such that the applied field is always directed parallel to the positive  $y$ -axis without loss of generality. According to the right-hand law, the induced current density is then only oriented in the  $\pm z$ -direction, and takes the value of the critical current density  $J_c$  – which in general depends on the local distribution of the magnetic induction  $B(r)$ . Due to its screening behavior, a superconducting filament exposed to an externally applied magnetic induction produces a pure dipole field from the induced current distribution in the filament cross-section. Since the filament tries to screen its interior, the pattern of the produced screening field will always be inverse to that of the originally applied field. Further, the field pattern will always follow the principle of minimal energy. Thus, no unnecessary field harmonics will be produced by the filament if these do not contribute to the screening behavior. Since on the level of filament sizes, it is a very good assumption to expect a one-dimensional field at the position of each filament during one field step, the screening currents which are induced within one step will produce a dipolar field – independently of the chosen magnet geometry.

The magnetization model presented in this chapter is derived from the principle of two intersecting ellipses – a structure, where the current transporting surface is defined by two identical partially overlapping ellipses – carrying currents with opposite orientations. Such an arrangement has the advantage that it precisely produces the desired pure dipole field in the current-free core area in the filament cross-section. The ellipses degenerate to the special case of intersecting circles if the ellipse axes are chosen to be identical.

The derived method is such that pairs of intersecting ellipses are inserted serially one into another. This will be denoted *Nested Ellipses* in order to distinguish it from the result of two (single) intersecting ellipses. The resulting magnetic field is obtained by superposition of the contribution of all individual ellipse pairs. The sum can be transferred into an integral expression by taking the limiting value where the thickness of the current transporting area of one pair of ellipses approaches zero. Solving the resulting integral gives an analytic equation for the magnetic induction in the filament cross-section as has been shown already in [53].

The dependence of the critical current density on the applied field and the field variation in the interior of the superconducting material have been taken into account by applying a current fit function in order to express  $J_c(B, r)$  (see section 2.3 for details on the current fit function). Here,  $B$  means the magnetic induction and  $r$  indicates the local coordinate inside the filament which accounts for the variation of  $B$  in the filament cross-section.

## 4.1 Solution for Changes of a Homogeneous External Field

In this section, the Nested Ellipse Model is introduced for a sweep of a homogeneous external field. The result for rotating fields is shown in section 4.2. The Nested Ellipse Model fully reproduces the response of a Type II superconducting cylinder on an externally applied field. It is tested for verification by calculating field errors in the superconducting magnets for the LHC which are presented in chapter 6.

As before for the Critical State Model and the Wilson Model, respectively, Fig. 4.1 qualitatively shows the distribution of the critical current density and the magnetic induction in the interior of a superconducting filament being exposed to an externally applied magnetic induction  $B_{\text{ext}}$ . The applied homogeneous magnetic induction undergoes a sweep. Note that the intersecting ellipses in the filament cross-sections are drawn qualitatively, with only a finite thickness. Hence, they do not precisely correspond to the contours which are finally obtained after taking a limiting value. The Nested Ellipse Model assumes the number of inserted ellipses to go to infinity and in this way allows a continuous course of the applied critical current density as is explained in detail in the following sections.

The individual steps in the sequence of Fig. 4.1 are:

- (a), (b) Initial state curve, non-fully penetrated. The external field is raised from zero to a value below  $B_p$ , where  $B_p$  denotes the state when the filament is fully penetrated.
- (c) Initial state curve, fully penetrated. The external field assumes the value  $B_p$ .
- (d) Initial state curve, fully penetrated. The external field assumes a value  $\geq B_p$ . The plot of the  $J_c$ -profile in the filament cross-section corresponds to state (c) (red curve).
- (e) Reduction of external field when the field previously has been increased from zero to a value  $\geq B_p$  once before. This results in the development of an additional current layer. In the magnetization curve, a hysteresis arises due to the remaining current distribution (so-called trapped currents) in the center of the filament.
- (f) Fully penetrated state after a change in external field orientation. The external field equals zero. The resulting magnetization is close to its maximum value on the trapping branch. The plot of the  $J_c$ -profile in the filament cross-section corresponds to state (g) (blue curve).
- (g) Distribution after a change in external field orientation which went from a high positive external field value to a negative one ( $B_{\text{ext}} < 0$ ).

As can be seen from the plots, the magnetic induction gradually decreases with the penetration depth, whereas (depending on the total amount of applied field) the critical current density rises with increasing superconductor penetration. The maximum critical current density is reached at the point in the filament cross-section, where the external field is sufficiently screened and the field inside equals zero. This can be seen in the cases (a), (b)



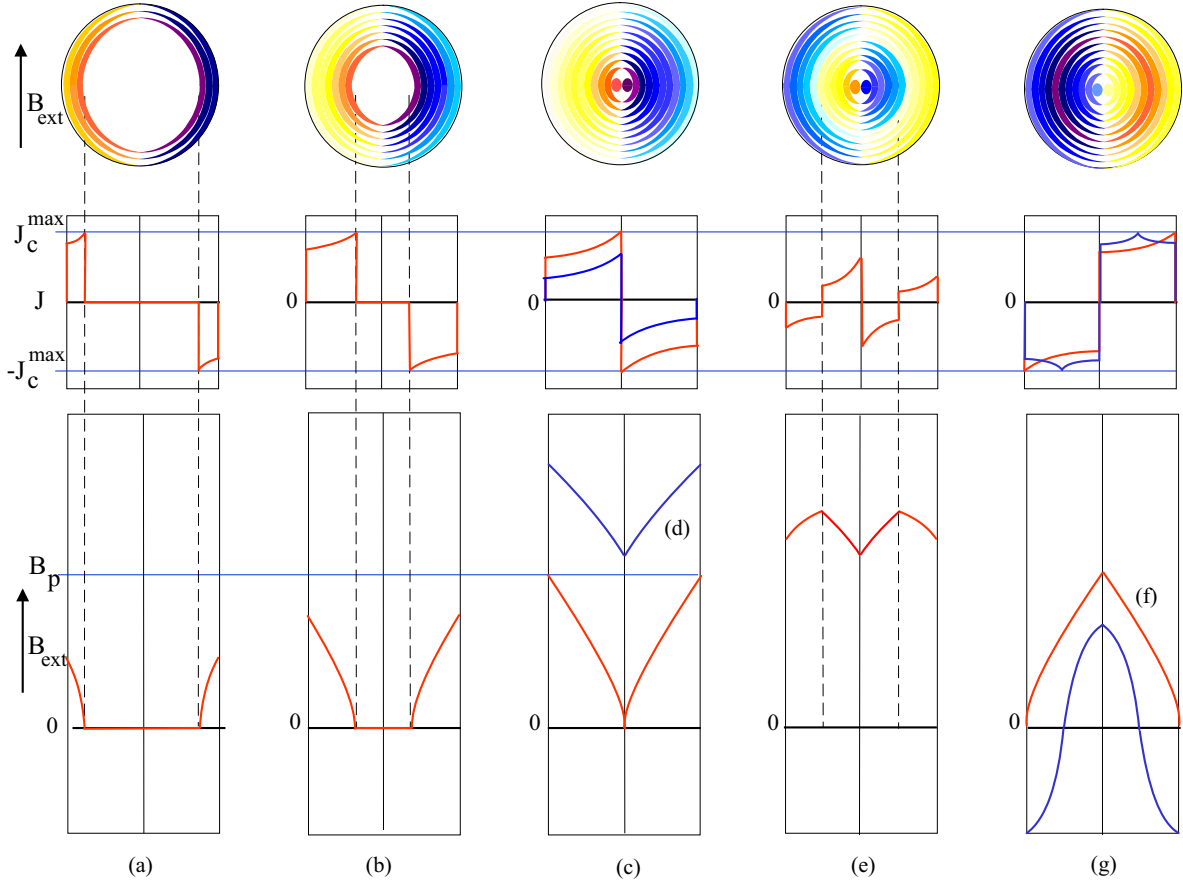


**Figure 4.1:** Round superconducting cylinder in a homogeneous external magnetic induction  $B_{\text{ext}}$  for different penetration states according to the Nested Ellipse Model. Top:  $J_c$ -profiles in the cylinder cross-section; middle and bottom: Distribution of critical current density  $J_c$  and magnetic induction  $B$  along the cylinder axis in the cross-section, respectively. The Nested Ellipse Model distinguishes from the Critical State and the Wilson Model by considering the dependence of the critical current density  $J_c$  both on the applied magnetic induction as well as its variation in the filament cross-section due to the screening effect. In addition, by using the correct current profile inside the filament, non-fully penetrated states can be calculated as well.

and (c). Note, that the critical current density decreases on the outer filament border due to the increase in the external magnetic induction, when going from case (a) to the cases (b) and (c). Consequently,  $J_c$  reduces in the filament center when the screening capacity of the filament is exceeded (see case (d)), while the slope of the magnetic induction inside the filament reduces when going from case (c) to case (d). As will be shown, the outcome for the magnetic induction and the resulting induced superconductor magnetization differs considerably from both the Critical State and the Wilson Model. The field and current distributions which are shown in case (e) are reached after reducing the external field which

was applied in case (d). The distributions of  $J_c$  and  $B$  after a further decrease of the external field are shown in the cases (f) and (g). In case (f), the external field value equals zero, whereas in case (g) the field is even further decreased and goes to negative values.

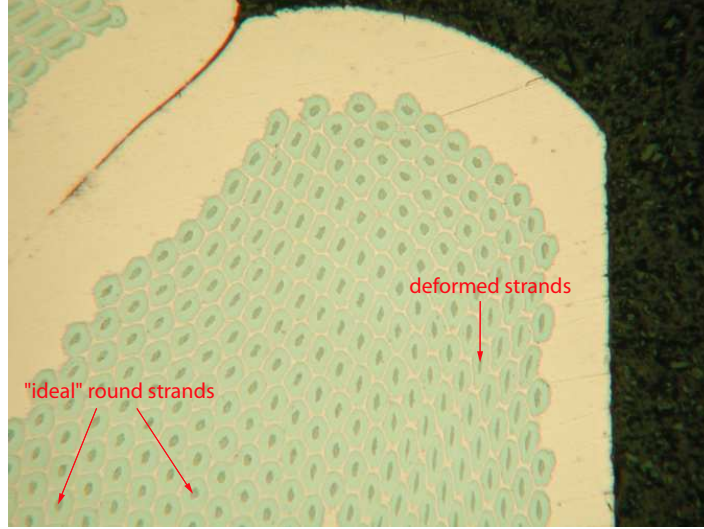


**Figure 4.2:** Cut-through a Nb<sub>3</sub>Sn strand showing filaments with non-uniform cross-sections of various shapes. Deformed filaments are expected to show an increased superconductor magnetization compared to the ideal (round) ones. Pictures with the courtesy of G. Kirby (CERN).

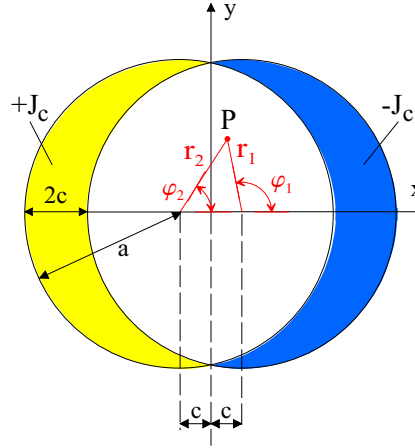
The superconductor magnetization can be calculated, if the current profile in the filament cross-section is determined. Filaments may be round in the ideal case, however, more general, the current distribution which results in a filament with an elliptically shaped cross-section is of interest, since filaments are sometimes the object of unwanted deformations. In these cases, their outer shape can be approximated by an ellipse and an estimation about the expected changes in superconductor magnetization for these filaments depending on the level of deformation can be given. In addition, filaments can be hollow, depending on their manufacturing process – a feature which has to be considered additionally when the current profile in the filament cross-section is determined.

Figure 4.2 shows the cut through a Nb<sub>3</sub>Sn strand with filaments of different shapes, where deformations can be seen especially on those filaments which are close to the outer strand border. As can be seen, these filaments are all hollow. It should be noted, that the deviation in the value of the induced magnetization, compared to the ideally shaped (round) ones also depends on the orientation of the elliptic filament with respect to the applied field (see section 4.3 for details).

#### 4.1.1 Principle of Intersecting Circles

For a better understanding, the principle of the intersecting circles (a special case of the intersecting ellipse structure which is used for the derivation of the model) is briefly explained here. It is then also shown that an intersecting circle structure produces a pure dipole field in the current-free region. In the next section it is shown that this principle applies for circles

as well as ellipses.



**Figure 4.3:** Intersecting circles with constant current distribution in the cross-section. Geometries of overlapping circles or ellipses are producing pure dipole fields in the resulting current-free region. The radius of the circle is  $a$ .

Figure 4.3 schematically shows two intersecting circles which are carrying a current density  $J_c$  of the same amount but with opposite orientation. According to the right-hand law, this current density only has components oriented in the  $\pm z$ -direction of the coordinate system. The current density is considered to be positive, if its orientation points in the direction of the positive  $z$ -axis. Additionally,  $J_c$  is considered constant and homogeneously distributed in the areas of the circles and the geometries of the circles are identical. Such two intersecting circles are of interest, since they produce a current-free region in their intersection in which the resulting field configuration of the magnetic induction is of pure dipole type.

Integrating the first Maxwell equation and applying Stokes' integral theorem, results in  $\oint_C H_\varphi ds = \int_F J_c dF$ , where  $C$  denotes the surrounding contour of the current transporting area  $F$ , and  $J_c$  is the critical current density. From this, the magnetic induction of two single circular cylinders calculated at the radial positions  $r_1, r_2$  with respect to the filament centers reads:

$$B_{\varphi 1} = \frac{-\mu_0 J_c}{2} r_1, \quad B_{\varphi 2} = \frac{\mu_0 J_c}{2} r_2.$$

The resulting  $B$ -field from these two identical circular cylinders with  $r > c$  being shifted out of the origin along the  $x$ -axis by the value  $\pm c$  as shown in Fig. 4.3 can be derived by superposition. From

$$\mathbf{e}_{\varphi_{1/2}} = -\sin \varphi_{1/2} \mathbf{e}_x + \cos \varphi_{1/2} \mathbf{e}_y, \quad \mathbf{B} = \frac{-\mu_0 J_c}{2} [r_1 \mathbf{e}_{\varphi 1} - r_2 \mathbf{e}_{\varphi 2}]$$

the magnetic induction is found to be:

$$\mathbf{B} = \frac{\mu_0 J_c}{2} [-r_1 (-\sin \varphi_1 \mathbf{e}_x + \cos \varphi_1 \mathbf{e}_y) + r_2 (-\sin \varphi_2 \mathbf{e}_x + \cos \varphi_2 \mathbf{e}_y)],$$

and the components result with  $r_1 \sin \varphi_1 = r_2 \sin \varphi_2$  (see Fig. 4.3) to:

$$\begin{aligned} B_x &= \frac{\mu_0 J_c}{2} (r_1 \sin \varphi_1 - r_2 \sin \varphi_2) = 0 \\ \text{and } B_y &= \frac{\mu_0 J_c}{2} (-r_1 \cos \varphi_1 + r_2 \cos \varphi_2) = \mu_0 J_c c. \end{aligned} \quad (4.1)$$

It is now easy to understand, that such a geometry can merely produce a pure dipole field in the current-free region. In addition, it can be seen from Eq. (4.1) that the  $y$ -component of the magnetic induction is independent of the position in the current-free area of the circle overlap, which indicates a homogeneous field distribution.

#### 4.1.2 Principle of Intersecting Ellipses

The same principle as for filaments with a circular cross-section can be applied on those with elliptical ones. As is already mentioned at the beginning of this chapter, the calculation of an elliptical cross-section is of interest, since filaments are sometimes the object of unwanted deformations. In these cases their outer shape can be approximated by an ellipse more precisely than with a circle. The calculation of the magnetic induction inside a long conductor with elliptically shaped cross-section which is transporting a constant current density  $J_z$  can be carried out by solving the Poisson's Equation  $\Delta A_z = -\mu_0 J_z$  for the vector potential  $A_z$ . Since the problem is treated in the plane, the vector potential and the transported current possess only a  $z$ -component as indicated by their indices. Further, they are independent of the variable  $z$ .

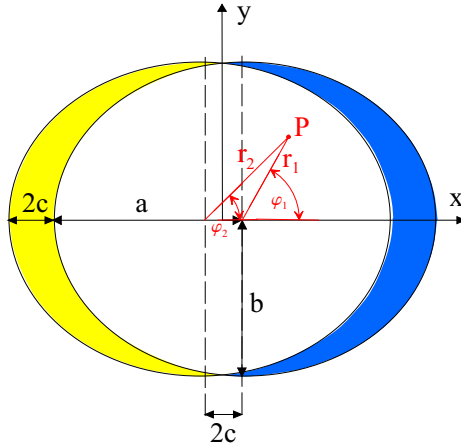


**Figure 4.4:** Intersecting ellipses with constant current distribution in the cross-section. Geometries of overlapping circles or ellipses are producing pure dipole fields in the resulting current-free region. The semi-axes of the ellipse are  $a$  and  $b$ .

Consequently, the magnetic induction of such an overlapping ellipse structure has a  $y$ -component only and reads:

$$B_y = \frac{2\mu_0 J_c}{4} (-r_1 \cos \varphi_1 + r_2 \cos \varphi_2) \frac{2b}{a+b},$$

as is derived below.

Following [54], the expression of this vector potential resulting from a homogeneously distributed current which is pointing in the positive  $z$ -direction and determined at an arbitrary evaluation point with distance  $r$  from the ellipse center, but inside the elliptic boundary, reads:

$$A_z = -\frac{\mu_0 J_z r^2}{4} \left( 1 - \frac{a^2 - b^2}{(a + b)^2} \cos(2\varphi) \right).$$

From this, the magnetic induction can be calculated by  $\mathbf{B} = \nabla \times A_z \mathbf{e}_z$ , and reads:

$$\mathbf{B} = \mathbf{e}_r \left( \frac{1}{r} \frac{\partial A_z}{\partial \varphi} \right) + \mathbf{e}_\varphi \left( -\frac{\partial A_z}{\partial r} \right),$$

and the components result to:

$$\begin{aligned} B_r &= -\frac{\mu_0 J_z r}{4} \left( 2 \frac{a^2 - b^2}{(a + b)^2} \sin(2\varphi) \right) \quad \text{and} \\ B_\varphi &= \frac{2\mu_0 J_z r}{4} \left( 1 - \frac{a^2 - b^2}{(a + b)^2} \cos(2\varphi) \right). \end{aligned}$$

Considering the local coordinate systems of the two shifted ellipses, which are shown in Fig. 4.4,

$$\mathbf{e}_{\varphi_{1/2}} = -\sin \varphi_{1/2} \mathbf{e}_x + \cos \varphi_{1/2} \mathbf{e}_y, \quad \mathbf{e}_{r_{1/2}} = \cos \varphi_{1/2} \mathbf{e}_x + \sin \varphi_{1/2} \mathbf{e}_y,$$

gives a magnetic induction which origins from these two intersecting ellipses. As before in the case of the intersecting circle model, the magnetic induction is calculated at an arbitrary evaluation point with the distances  $r_1$  and  $r_2$  from the two ellipse centers. The transported current density  $J_z$  equals  $J_c$ , the critical current density. The contribution of the two ellipses can be superimposed and thus the  $r$ - and  $\varphi$ -component of  $B$  read:

$$\begin{aligned} \mathbf{B} &= \frac{2\mu_0 J_c (a - b)}{4(a + b)} (\mathbf{e}_{r_1} r_1 \sin(2\varphi_1) - \mathbf{e}_{r_2} r_2 \sin(2\varphi_2)) \\ &+ \frac{2\mu_0 J_c}{4} \left( \mathbf{e}_{\varphi_1} \left( -r_1 + \frac{a - b}{a + b} r_1 \cos(2\varphi_1) \right) + \mathbf{e}_{\varphi_2} \left( r_2 - \frac{a - b}{a + b} r_2 \cos(2\varphi_2) \right) \right). \end{aligned} \quad (4.2)$$

Expressing the components of  $\mathbf{B}$  from Eq. (4.2) in cartesian coordinates, it can be shown, that such an arrangement produces a pure dipole field in the  $y$ -direction, while the  $B_x$ -component vanishes. Further, the  $B_y$ -component has to be independent of the local coordinates over the whole current-free surface in order to show that the resulting field is homogeneous.

In cartesian coordinates, the terms of Eq. (4.2) read:

$$\begin{aligned} B_x &= \frac{2\mu_0 J_c}{4} \left[ \frac{a - b}{a + b} r_1 \sin(2\varphi_1) \cos \varphi_1 - \frac{a - b}{a + b} r_2 \sin(2\varphi_2) \cos \varphi_2 \right. \\ &\quad \left. + \sin \varphi_1 \left( r_1 - \frac{a - b}{a + b} r_1 \cos(2\varphi_1) \right) + \sin \varphi_2 \left( -r_2 + \frac{a - b}{a + b} r_2 \cos(2\varphi_2) \right) \right] \end{aligned} \quad (4.3)$$

and

$$\begin{aligned} B_y &= \frac{2\mu_0 J_c}{4} \left[ -r_1 \cos \varphi_1 + r_2 \cos \varphi_2 + \frac{a - b}{a + b} (r_1 \sin(2\varphi_1) \sin \varphi_1 + r_1 \cos(2\varphi_1) \cos \varphi_1 \right. \\ &\quad \left. - r_2 \sin(2\varphi_2) \sin \varphi_2 - r_2 \cos(2\varphi_2) \cos \varphi_2) \right]. \end{aligned} \quad (4.4)$$

From Eq. (4.3), it can be seen that the  $B_x$ -component vanishes, if the following expression holds:

$$\begin{aligned} & \frac{a-b}{a+b} r_1 \sin(2\varphi_1) \cos \varphi_1 - \frac{a-b}{a+b} r_2 \sin(2\varphi_2) \cos(\varphi_2) \\ & r_1 \sin \varphi_1 - \frac{a-b}{a+b} r_1 \sin \varphi_1 \cos(2\varphi_1) - r_2 \sin \varphi_2 + \frac{a-b}{a+b} r_2 \sin \varphi_2 \cos(2\varphi_2) \stackrel{!}{=} 0, \end{aligned}$$

which means, that

$$r_1 \sin \varphi_1 - r_2 \sin \varphi_2 \stackrel{!}{=} 0$$

and

$$r_1 \sin(2\varphi_1) \cos \varphi_1 - r_2 \sin(2\varphi_2) \cos \varphi_2 - r_1 \sin \varphi_1 \cos(2\varphi_1) + r_2 \sin \varphi_2 \cos(2\varphi_2) \stackrel{!}{=} 0.$$

Both conditions are fulfilled and this way it is shown that no  $B_x$ -component exists in the current-free region of an intersecting ellipse structure. The  $y$ -component of the magnetic induction,  $B_y$ , which is given by Eq. (4.4), can be written as:

$$\begin{aligned} B_y &= \frac{2\mu_0 J_c}{4} \left[ -r_1 \cos \varphi_1 + r_2 \cos \varphi_2 + \frac{a-b}{a+b} (r_1 \cos \varphi_1 - r_2 \cos \varphi_2) \right] \\ &= \frac{2\mu_0 J_c}{4} (-r_1 \cos \varphi_1 + r_2 \cos \varphi_2) \frac{2b}{a+b}. \end{aligned} \quad (4.5)$$

Since the term

$$-r_1 \cos \varphi_1 + r_2 \cos \varphi_2 = 2c$$

stays constant in the current-free area of the ellipse overlap, the homogeneity of the  $B_y$ -component is demonstrated. This proof will be applied in the next section. It shows that it is sufficient to determine the magnetic induction in an arbitrary point in the current-free area of the ellipse overlap. Note, that in the case of setting the ellipse axes to be equal ( $a = b$ ), the geometry degenerates to intersecting circles and Eq. (4.5) gives the identical expression that has already been found in Eq. (4.1):

$$B_y = \frac{\mu_0 J_c}{2} (-r_1 \cos \varphi_1 + r_2 \cos \varphi_2) = \mu_0 J_c c.$$

### 4.1.3 Magnetic Induction from Intersecting Ellipses

In case of the intersecting circle or ellipse geometry, carrying a uniform current, it has now been shown in the previous sections, that only the  $B_y$ -component of the magnetic induction is different from zero, whereas  $B_x$  vanishes. In addition, a geometry of two intersecting circles or ellipses produces a homogeneous dipole field in the current-free region of their overlap, allowing the determination of the field at any arbitrary point of the current-free region, without loss of generality. An expression for the magnetic induction has been given, however a more intuitive approach is presented here by calculating the magnetic induction directly by means of an integration. Starting from Biot-Savart's Law, the magnetic induction of a homogeneous current distribution of arbitrary shape  $F$  in the origin of a coordinate system can be calculated to be:

$$\mathbf{B} = \frac{\mu_0 J_c}{\pi} \int_F \frac{y}{x^2 + y^2} \mathbf{e}_x - \frac{x}{x^2 + y^2} \mathbf{e}_y \, dF,$$

and so, the  $y$ -component of the magnetic induction reads:

$$B_y = -\frac{\mu_0}{\pi} \int_F J_c \frac{x}{x^2 + y^2} dx dy.$$

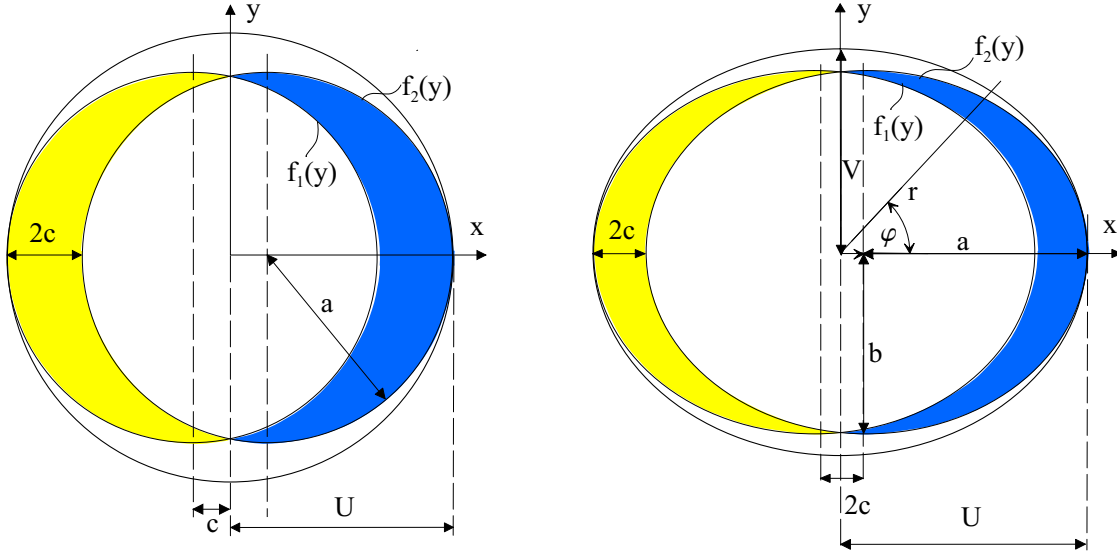


**Figure 4.5:** Intersecting circles and ellipses in the cross-section of a circular (left) or elliptic filament (right). Let  $a, b$  be the semi-major axis and the semi-minor axis of the ellipses, respectively and  $\pm c$  the ellipse shifts with respect to the ordinate axis. The current-carrying surface is limited by the contours  $f_1(y)$  and  $f_2(y)$ . The outer filament shape can be round or elliptical with the semi-axes  $U, V$  (or radius  $U$ , respectively). In case of intersecting circles (left),  $a = b$ .

The current-carrying surface consists of the two intersecting ellipses as is shown in Fig. 4.5. Thus, the resulting magnetic induction can be calculated by integrating along the contours of the two intersecting ellipses in order to get the current-transporting profile. For solving the integral, the equation is transformed into cylindrical coordinates and reads after the transformation:

$$\begin{aligned} B_y &= \frac{\mu_0 J_c}{2\pi} \int_{-\pi/2}^{\pi/2} \int_{f_1(\varphi)}^{f_2(\varphi)} \frac{\cos \varphi}{r} r dr d\varphi \\ &= \frac{\mu_0 J_c}{2\pi} \int_{-\pi/2}^{\pi/2} (f_2(\varphi) - f_1(\varphi)) \cos \varphi d\varphi, \end{aligned}$$

where

$$f_1(\varphi) = \frac{-b^2 c \cos \varphi + ab \sqrt{b^2 \cos^2 \varphi + a^2 \sin^2 \varphi - c^2 \sin^2 \varphi}}{b^2 \cos^2 \varphi + a^2 \sin^2 \varphi}, \quad (4.6)$$

$$f_2(\varphi) = \frac{b^2 c \cos \varphi + ab \sqrt{b^2 \cos^2 \varphi + a^2 \sin^2 \varphi - c^2 \sin^2 \varphi}}{b^2 \cos^2 \varphi + a^2 \sin^2 \varphi}. \quad (4.7)$$

The integral boundaries in cylindrical coordinates result from the points of intersection of the radial vector  $r$  with the two shifted ellipses. From this, the resulting magnetic induction in the current free filament core reads:

$$B_y = 2\mu_0 J_c c \frac{b}{a+b}, \quad (4.8)$$

where  $\pm c$  again denotes the shift of the two ellipses with respect to the filament center (origin of the coordinate system). Note that the expression given in Eq. (4.8) accounts for the backwards current by a factor of two. The expression is identical to the one derived from the magnetic vector potential, Eq. (4.5). In addition, in the case of inscribed circles, where  $a = b$ , the result is identical to Eq. (4.1). The sign of the magnetic induction depends on the orientation of source currents and therefore on the direction of the externally applied field.

#### 4.1.4 Geometry of Nested Circles or Ellipses

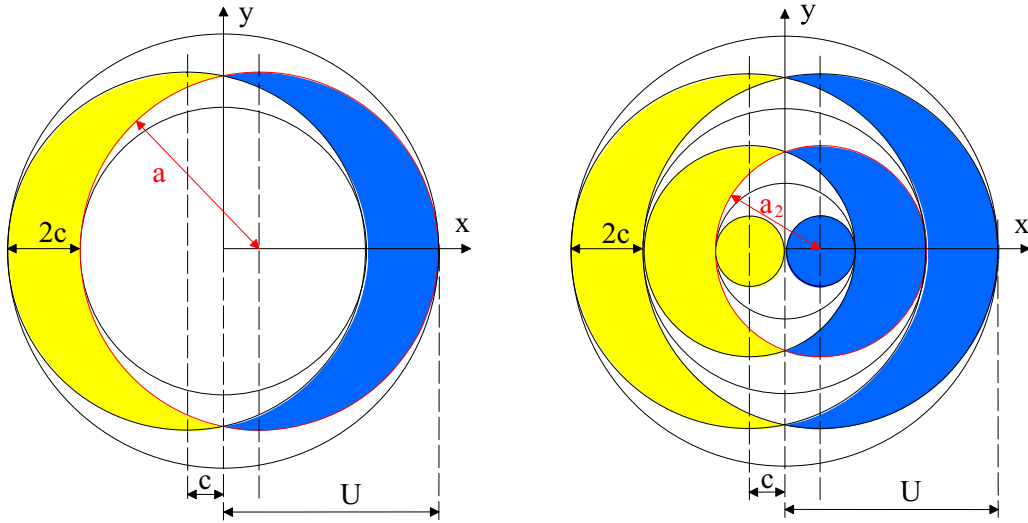


**Figure 4.6:** Principle of nested circles. Left: one set of nested circles with inscribed circle in the current-free area. Right: set of three nested circles for illustration ( $n = 3$ ). In the final model,  $n \rightarrow \infty$ .

Figure 4.6 (left) shows a filament with a circular cross-section of radius  $U$  where a current-carrying surface which results from two shifted circles is inscribed. In the current-free region of the overlap, another circle is placed. Let  $c$  be the shifts of the intersecting circles with respect to the ordinate axis and  $a$  be the radii of the circles, as is indicated in the plot. Then this radius  $a$  is determined by:

$$\begin{aligned} 2a + 2c &= 2U \\ \Rightarrow a &= U - c, \end{aligned}$$



and the inscribed circle in the remaining area has a diameter of  $(2U - 4c)$ . Now another couple of intersecting circles is inscribed into the remaining area of the first inscribed circle and so on as indicated in Fig. 4.6 (right), until a chosen total number  $n$  of inscribed circles in the filament cross-section is reached. The value for  $n$  can be set to an arbitrary number, and for illustration,  $n = 3$  in Fig. 4.6 (right), whereas in the final model,  $n \rightarrow \infty$ . Following this, the radii  $a_1, a_2, \dots, a_i, \dots, a_n$  of the 1<sup>st</sup>, 2<sup>nd</sup>, ...,  $i^{\text{th}}$ , ...,  $n^{\text{th}}$  etc. circle are determined by:

$$\begin{aligned} \Rightarrow 2a_2 + 2c &= 2U - 4c \\ a_2 &= U - 3c. \end{aligned}$$

Consequently, the third semi-minor axis reads:  $a_3 = U - 5c$ , and therefore, more generally:

$$\Rightarrow a_i = U - (2i - 1)c.$$

From this, one gets with  $2c = U/n$  for the  $i^{\text{th}}$  set of circles:

$$\Rightarrow c = \frac{U}{2n} \quad (4.9)$$

$$\begin{aligned} a_i &= U - (2i - 1)\frac{U}{2n} \\ &= U \frac{2n - 2i + 1}{2n}, \end{aligned} \quad (4.10)$$

Thus, an approximation of the current-carrying surface is found in such a way that the individual sets of intersecting circles can be integrated and the results superimposed. This way, an expression for the magnetic induction in the filament cross-section can be obtained, as is shown in the next section.

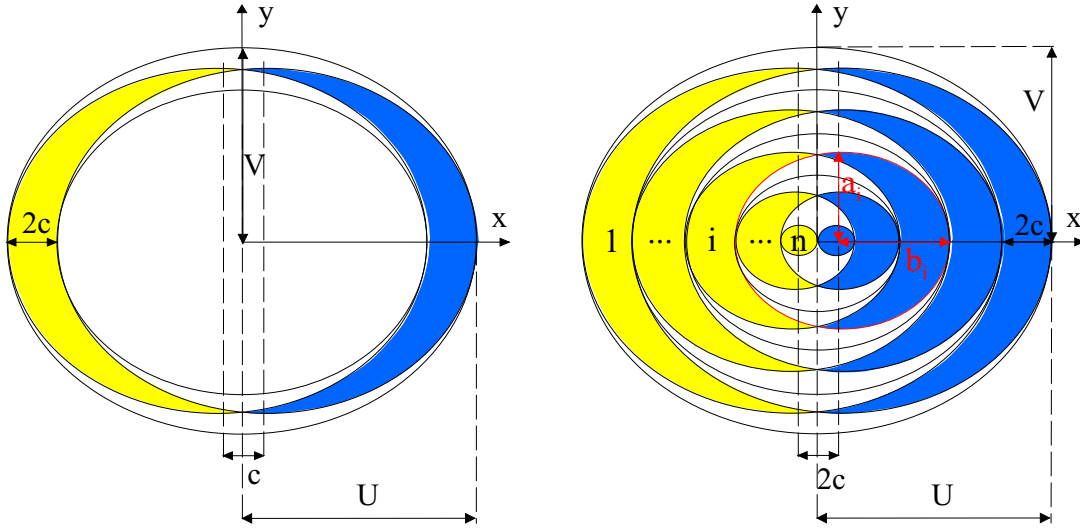


**Figure 4.7:** Principle of nested ellipses. Left: one set of nested ellipses with inscribed ellipse in the current-free area. Right: set of five nested ellipses for illustration ( $n = 5$ ). In the final model,  $n \rightarrow \infty$ .

The same principle can be applied to a filament with an elliptical cross-section, as is shown in Fig. 4.7 for an elliptically shaped filament where  $U$  is the semi-major axis and  $V$

denotes the semi-minor axis, as indicated in the plot. For illustration, the filament is shown with  $n = 5$  inscribed ellipse pairs. In this case, an ellipse (which has the same ratio between the semi-minor and the semi-major axes as the outer ellipse shape) is inscribed into the current-free region of the overlap. Hence, the ratio of the axes of the inscribed ellipses and those of the filament surface stays constant and so the semi-minor axis  $b_i$  results to:

$$b_i = V \frac{2n - 2i + 1}{2n}, \quad (4.11)$$

where  $U, V$  are the semi-axes of the outer filament shape. The special case of round filaments is implicitly covered for  $U = V = r_f$ .

#### 4.1.5 $J_c$ -dependence in the filament cross-section

In order to consider the  $J_c(B(r))$ -dependence, each ellipse pair carries a constant current density depending on the position and the local field in the filament cross-section (indicated by the index  $i$ ). This accounts for the fact that ellipse pairs in the outer region have a screening effect on the inscribed pairs which are closer to the filament center. With increasing vicinity to the filament center, this results in a successively increasing current density for each predecesing inscribed ellipse pair. The magnetic induction in the center of the filament can be calculated as the sum of all inscribed ellipse pairs.

$$B = 2\mu_0 c \sum_{i=1}^n J_{c,i} \frac{b_i}{a_i + b_i} \quad (4.12)$$

$$= \frac{\mu_0}{n} \sum_{i=1}^n J_{c,i} \frac{UV}{U + V} \quad (4.13)$$

#### Continuous Course of the Magnetic Induction $B$

By means of the Eq. (4.13), an expression for the magnetic induction resulting from a geometry of  $n$  inscribed ellipses (or circles, in the special case) has been derived which allows to set an individual constant current in each layer. This accounts for the screening effect of the outer ellipses on the inner ones, which can, due to the lower total field which they experience, carry a higher current density. The total field can be expressed by a superposition of all layer contributions and results in a sum which is given in Eq. (4.12). In order to get a continuous course of the magnetic induction along the filament cross-section, the limiting value  $n \rightarrow \infty$  is applied on Eq. (4.13). This changes the sum in the equation to an integral expression with the integration constant  $q$  such that

$$q = i/n. \quad (4.14)$$

This way, an analytic term for the magnetic screening field which is produced by two intersecting ellipses for a slice of current between the contours  $U q_i$  and  $U q_{i+1}$  is found:

$$B_i = \mu_0 \int_{q_i}^{q_{i+1}} J_{c,i} \frac{UV}{U + V} dq. \quad (4.15)$$

This allows to give a resulting expression for the magnetic induction which is contributed by the current on an infinitely thin slice  $dq$  in the filament cross-section:

$$dB = \mu_0 J_c(B(q)) \frac{UV}{U + V} dq. \quad (4.16)$$

The expression is independent from the actual shape of the filament as long as its cross-section can be approximated by an ellipse with arbitrary values for the semi-axes  $U, V$ . In the case that intersecting circles are inscribed, the relation simplifies to:

$$dB = \mu_0 J_c(B(q)) \frac{1}{2} r_i dq. \quad (4.17)$$

It also precisely produces a dipole field, where the only source of error is the current-free triangle which remains between the individual pairs of ellipses. In the next section, a correction factor for this current-free triangles, applicable for the case of intersecting ellipses is derived.

#### 4.1.6 Correction Factor for the Current-free Triangles

In the sections above, it has been described how to implement the nested ellipse model in order to determine the current-profile in the cross-section of the filament. As has been shown, the individual ellipse pair is chosen in such a way as to keep the ellipticity of all progressively inscribed ellipses identical. This way, the semi-minor and the semi-major axes are resulting as given in the Eqs. (4.10) and (4.11), allowing to derive the equations for the magnetic induction and the magnetization. Keeping the ellipticity constant is, however, chosen at will and not compulsory. In fact, by keeping the ratio of the ellipse axes of each inscribed ellipse pair constant, an error is produced due to the fact that the remaining triangles between the individual ellipse pairs stay current-free (see, e.g. Fig. 4.7, for illustration)<sup>1</sup>. In order to correct for this error, a dimensionless correction factor  $\mathcal{H}$  is derived from the fully penetrated case as follows: The inscription of an individual sets of ellipses can be done in such a way that the radii of curvature of the  $i^{th}$  and the  $i - 1^{th}$  ellipses are equal. This means, the idea of keeping the ellipticity constant is abandoned and the ellipse axes are calculated for each set of inscribed ellipses individually. This correction is illustrated by Fig. 4.8, showing the optimized, individually adopted ellipse shapes for a set of five nested ellipses and the resulting triangles. This picture can be compared with the nested ellipses with constant ellipticity, Fig. 4.7, or for the inscribed circles, Fig. 4.6.

A general expression for the radius of curvature  $R(x_0, y_0)$ , determined at an arbitrary position  $(x_0, y_0)$  of an ellipse with semi-axes  $a$  and  $b$  is given by the formula [55]:

$$R = a^2 b^2 \left( \frac{x_0^2}{a^4} + \frac{y_0^2}{b^4} \right)^{3/2}.$$

Hence, the radius of curvature  $R_i$  of the inscribed  $i^{th}$  ellipse determined on the abscissa (where  $y_0 = 0$  and  $x_0 = a_i$ ) results to:

$$R_i = \frac{b_i^2}{a_i}$$

whereas  $R_{i-1}$  of the  $i - 1^{th}$  ellipse reads:

$$R_{i-1} = \frac{b_{i-1}^2}{a_{i-1}}.$$

---

<sup>1</sup>In the case that the semi-axes are identical, the ellipses degenerate to circles. The considerations shown here, however, are the same and an error from the current-free triangles occurs in both cases.

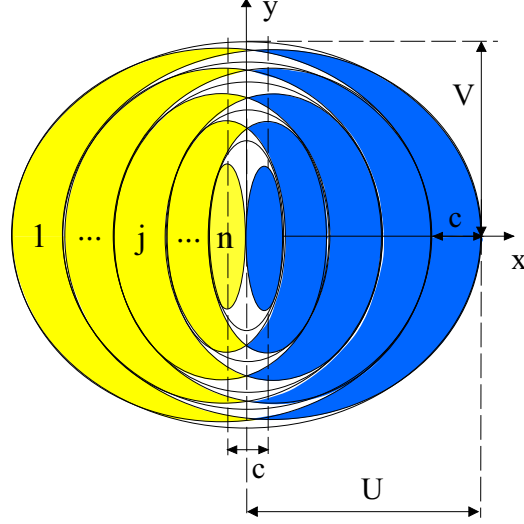


**Figure 4.8:** Principle of nested ellipses where the sets of inscribed ellipses have different ellipticities in order to reduce the error which results from the current-free triangles of each slice of induced current. In this case, the semi-axes of the newly inscribed ellipse pair has to be calculated individually. The current-free triangles get minimal, if the radii of curvature along the filament axis of the newly inscribed ellipses and that of the last ellipse are identical. The example illustrated here is shown for a set of five nested ellipses and this way can be compared to the right picture in Fig. 4.7.

From this, the ratio of the semi-axes  $a_i$ ,  $b_i$  changes to:

$$\frac{b_i^2}{a_i} \equiv \frac{b_{i-1}^2}{a_{i-1}},$$

and the semi-minor axis  $b_i$  can be expressed by:

$$b_i = V \sqrt{\frac{2n - 2i + 1}{2n}}. \quad (4.18)$$

The correction factor  $\mathcal{H}$  for the remaining triangles derives from the comparison to a fully penetrated filament calculated from the ideal field of two intersecting circles. Using the geometry of intersecting circles for comparison allows the resulting correction factor to be applied on the rotating field model that is shown in section 4.2, as well. Therefore, Eq. (4.18) has to be inserted into Eq. (4.12), whereas the major semi-axis  $a_i$  remains according to Eq. (4.10). The resulting magnetic induction including the correction reads:

$$\begin{aligned} B_{\text{corr}} &= 2\mu_0 c \sum_{i=1}^n J_{c,i} \frac{b_i}{a_i + b_i} \\ &= 2\mu_0 c \sum_{i=1}^n J_{c,i} \frac{V}{U \sqrt{\frac{2n-2i+1}{2n}} + V}. \end{aligned} \quad (4.19)$$

Since  $c = U/2n$ , Eq. (4.9), the sum in Eq. (4.19) changes to an integral expression for  $n \rightarrow \infty$ , and  $q = i/n$ , where:

$$\frac{2n - 2i + 1}{2n} = 1 - \frac{2i}{2n} - \underbrace{\frac{1}{2n}}_0 = 1 - q. \quad (4.20)$$

The result is integrated from  $q_1 = 0$  to  $q_2 = 1$ , yielding:

$$\begin{aligned} B_{\text{corr}} &= \mu_0 J_c \int_0^1 \frac{UV}{U\sqrt{1-q} + V} dq \\ &= 2\mu_0 J_c \frac{V(U + V \ln(\frac{V}{U+V}))}{U}. \end{aligned} \quad (4.21)$$

In the special case of round filaments, where  $U = V = r_f$ , the equation simplifies to:

$$B_{\text{corr}} = 2\mu_0 J_c r_f \left( 1 + \ln \left( \frac{1}{2} \right) \right). \quad (4.22)$$

The expression for the fully penetrated filament is achieved from Eq. (4.15), which also has to be integrated from 0 to 1, and yields in the case of round filaments:

$$B = \frac{1}{2} \mu_0 J_c r_f. \quad (4.23)$$

Comparison of Eq. (4.22) with Eq. (4.23) yields a resulting correction factor for round filaments of:

$$\mathcal{H} = 4 \left( 1 + \ln \left( \frac{1}{2} \right) \right) \approx 1.227, \quad (4.24)$$

where  $r_f$  denotes the filament radius. This way, the solution for the magnetic induction resulting from Eq. (4.16) can be expressed as:

$$dB(q) = \mu_0 \mathcal{H} r_f J_c(B(q)) dq,$$

making the correction factor applicable in the expression of the magnetic induction  $dB(q)$  and allowing to derive a closed term, which results from an infinitely thin slice  $dq$  that is carrying a constant current density  $J_c(B(q))$ . This current density is a function of the local field  $B(q)$ , where  $q$  denotes a relative penetration depth in the filament cross-section. The absolute value of the penetration depth (in  $\mu\text{m}$ ) reads:  $qU$ . Consequently,  $q$  equals zero on the outer filament border, which corresponds to no penetration, whereas  $q$  equals 1 in the filament center, corresponding to the case of full penetration, when the absolute value of the penetration depth equals  $U$  (see also Fig. 4.9 and section 4.1.8, where the application of  $q$  is explained by means of exemplary values).

As can be seen from Eq. (4.24), the correction factor causes an increase of the magnetic induction of about 22% which is produced by the additional current compared to the magnetic induction which is due to the non-corrected current distribution shown in the Figs. 4.6 and 4.7. Note, that this increase is only valid for the fully penetrated case, whereas in the case of non-fully penetrated filaments, this correction factor would yield a too high increase of the resulting magnetic induction. This can easily be adopted by a re-scaling with the actual penetration depth.

#### 4.1.7 Magnetic Induction in the Filament After a Sweep of a Homogeneous External Field

From the expression of a slice of constant current, the magnetic induction as a function of the relative penetration depth can be found by integration. It has already been mentioned in section 2.3 that no analytical solution could be found for the integration of the fit function given in Eq. (2.7). The fit function has therefore been approximated locally around the actual value of the applied magnetic induction by means of an inverse square root dependence. This approximation is motivated by the fact that for small values of the magnetic induction  $B$ , where the influence of the persistent currents on the field quality is of interest, the critical current density strives for infinity: Since  $\alpha = 0.57$ ,  $B^{\alpha-1} = B^{-0.43} \propto 1/\sqrt{B}$  for  $B \rightarrow 0$ . Considering now the dependence of  $J_c$  on  $B$  by means of this approximation, a differential equation for  $B(q)$  is found which can be solved including the known boundary condition for  $B(q=0) = B_{\text{ext}}$  to:

$$\begin{aligned} dB(q) &= \mu_0 \mathcal{H} r_f j_c(B_{\text{ext}}, T) \frac{\sqrt{B_{\text{ext}}}}{\sqrt{B(q)}} dq, \\ \Rightarrow \int \sqrt{B(q)} dB(q) &= \int \mu_0 \mathcal{H} r_f j_c(B_{\text{ext}}, T) \sqrt{B_{\text{ext}}} dq, \\ B(q) &= \left( B_{\text{ext}}^{3/2} + \frac{3}{2} \xi \mu_0 \mathcal{H} r_f j_c(B_{\text{ext}}, T) \sqrt{B_{\text{ext}}} q \right)^{2/3}. \end{aligned} \quad (4.25)$$

Here, the parameter  $\xi$  indicates the branch of the hysteresis curve, in the case of ramping up,  $\xi$  equals  $-1$  and for ramping down,  $\xi = 1$ . In the first case ( $\xi = -1$ ), the magnetic moment resulting from the screening current is opposite to the orientation of the outside field  $B_{\text{ext}}$  and the magnetic induction  $B(q)$  decreases inside the filament. For reasons of brevity, a new parameter  $\mathcal{F}$  is introduced which follows Eq. (2.8) and substitutes to:

$$\mathcal{F} = j_c(B_{\text{ext}}, T) \sqrt{B_{\text{ext}}}. \quad (4.26)$$

This way, a closed expression for the magnetic induction in the interior of the filament can be given as:

$$B(q) = \left( B_{\text{ext}}^{3/2} + \frac{3}{2} \xi \mu_0 \mathcal{H} r_f \mathcal{F}(B_{\text{ext}}) q \right)^{2/3}. \quad (4.27)$$

Equation (4.27) depends on the external field  $B_{\text{ext}}$  and gives a description of the magnetic induction in the filament cross-section. Figure 4.9 shows  $B(q)$  according to Eq. (4.27) together with the dependence of the critical current density<sup>2</sup>  $J_c(B(q))$  on the relative penetration depth  $q$ . The curves are not normalized and so the magnetic induction at  $q = 0$  equals the externally applied field  $B_{\text{ext}}$ . In general, the magnetic induction in the interior of a filament can become negative. This case is implicitly included in Eq. (4.27) and is considered in the programmed code by expressing the equation as:

$$B(q) = \left( |B_{\text{ext}}^{3/2} + \frac{3}{2} \xi \mathcal{H} r_f \mathcal{F}(B_{\text{ext}}) \mu_0 q| \right)^{2/3} \cdot \text{sign}(B_{\text{ext}}^{3/2} + \frac{3}{2} \xi \mathcal{H} r_f \mathcal{F}(B_{\text{ext}}) \mu_0 q).$$

The field distribution shown presents the filament in a fully penetrated state, which is reached for the case of increasing the external field from negative field values to  $B_{\text{ext}} = 0.08$  T. As

<sup>2</sup>As introduced in section 2.3, the critical current density  $J_c$  is written in capitals for the general case, whereas small letters as  $j_c$  indicate the use of an explicit current fit function.

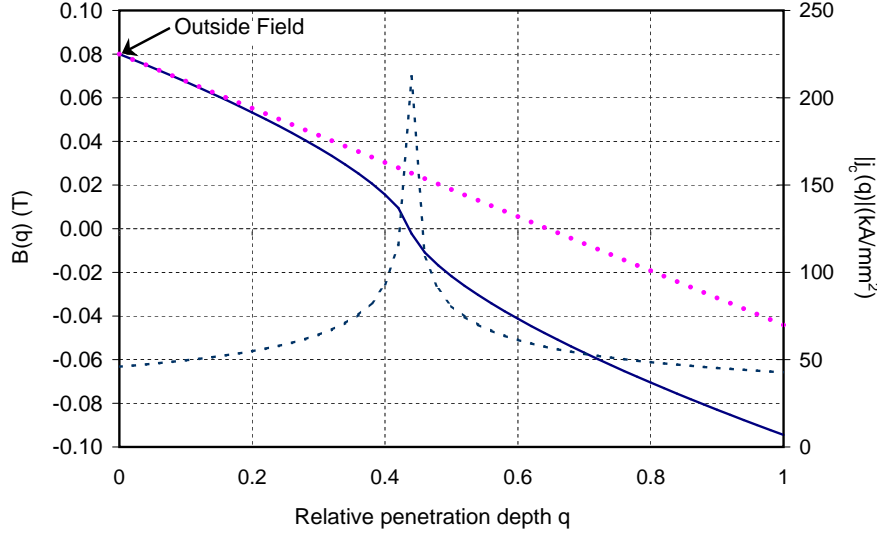


**Figure 4.9:** Magnetic induction  $B(q)$  as a function of the relative penetration depth  $q$  (continuous line) in the cross-section of a NbTi-filament. Here,  $q = 0$  denotes the outer filament border, whereas  $q = 1$  is the center of the filament. Consequently,  $B(q)$  presumes the value of the outside field,  $B_{\text{ext}}$ , for  $q = 0$ . The dark blue dashed line indicates the absolute value of the current density  $|j_c(q)|$  according to this induction whereas the red dotted line indicates the magnetic induction, which results when  $J_c$  is held constant. Note that the scales on the right- and the left-hand side ( $B$  and  $J_c$ ) are not correlated.

can be seen in the plot, this results in a decreasing field  $B(q)$  along the relative penetration depth which produces an increase of  $J_c(B(q))$  along  $q$ . At  $B(q) = 0$ , the critical current density reaches its maximum value and the strong increase of  $j_c$  comes with a sharp decline of  $B(q)$ . Though the fit function would presume a pole for  $B = 0$ , the values are cut to a finite value as can be seen in the plot. It is obvious, that an infinitely high current density has no practical meaning and, in addition, can even theoretically never be reached due to the self-field produced by each individual filament. However, the course of  $j_c(q)$  shows the importance of expressing  $j_c$  as a function of  $q$  in addition to the dependence on  $B_{\text{ext}}$  rather than assuming a constant value.

#### 4.1.8 Comparison to the Wilson Model

In the case of round filaments, the solution for the magnetic induction in the filament cross-section should lead to a similar result as the model of Wilson given in Eq. (3.5), where  $a/r_f = 1 - q$ . The latter expression can be cross-checked by the two cases of full penetration and no penetration: In the Wilson Model, for the case of the non-penetrated filament, there is  $a = r_f$ , which is equivalent to  $q = 0$ , whereas in case of the fully penetrated filament,  $a = 0$ , which is equivalent to  $q = 1$ .

Figure 4.10 shows the difference between the solution of Wilson and Eq. (4.27) for two cases: The case of a filament exposed to a field value below the penetration field  $B_p$  (left

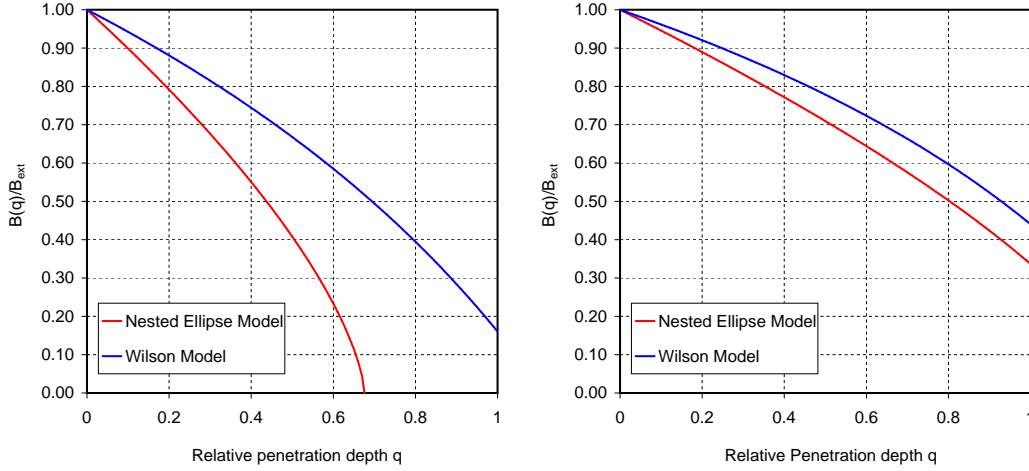


**Figure 4.10:** Comparison between the screening field calculated from Eq. (4.27) and the field resulting from the Wilson Model. Left plot: Applied magnetic induction  $B_{\text{ext}}$  below penetration field  $B_p$ ; right plot:  $B_{\text{ext}} > B_p$ . Note that depending on the model, the value of  $B_p$  varies considerably. Here, the calculated value from the Nested Ellipse Model is taken.

plot) and a fully penetrated filament where  $B_{\text{ext}} > B_p$ , (right plot). For a better comparison, the curves are normalized to the applied external induction  $B_{\text{ext}}$ . It can be seen from the plots that the difference between the Wilson and the Nested Ellipse Model is small in case of field values above the penetration field  $B_p$ , where mainly the shape of the curve and the field value in the filament center at  $q = 1$  differs. However, in the low field range, the difference is significant. It can be seen from the left plot in Fig. 4.10 that there is less penetration of the filament in the Nested Ellipse Model compared to the Wilson Model, resulting in a considerably different course of screening field in the filament cross-section. In case of the Nested Ellipse Model, a field free filament core in the range of  $0.68 < q < 1$  remains, where a complete screening takes place which arises due to the consideration of the  $J_c(B(q))$ -dependence in the Nested Ellipse Model as follows: The currents induced in the outer part of the filament cross-section screen the interior, reducing the applied magnetic induction with increasing penetration depth. This screening effect allows the existence of higher current densities with increasing penetration depth and thus produces a higher screening effect than the Wilson Model. This is due to the fact that the critical current density in the Wilson Model is a function of  $B$ , although constant with the penetration depth ( $J_c = f(B_{\text{ext}})$ , but  $J_c \neq f(B(q))$ ) and hence only considers a dependence of  $J_c$  on the applied field, but not on the varying field in the filament cross-section. It is obvious that the reinforced screening capacity which can be observed in the Nested Ellipse Model results in a stronger decrease of the magnetic induction  $B(q)$  versus  $q$  in the filament cross-section and as such the point of complete screening is reached for less penetration.

In general, the precision with which the dipole screening field of a superconducting filament is reproduced can be used as a measure of the quality of the magnetization model. Due to the fact that each pair of ellipses produces a pure dipole field inside the filament cross-section, the resulting field from the superposition of the current-carrying areas of all ellipses



also remains of dipole type. This means, for instance, in case of the non-fully penetrated state, the derived current distribution from the Nested Ellipse Model precisely produces the field-free core area. Likewise, the resulting magnetic induction outside the filament follows an exact dipole field.

It is shown in the sections 5.1 and 7.2 that the reproduction of an exact dipole field from the induced current distribution is a stringent condition for the determination of the resulting field distribution in the close vicinity of a strand (as is needed in case of the calculation of superconducting magnet cables). Also it is important to precisely determine the actual field shape for the calculation of the repercussion of the magnetic induction which is produced by the screening currents on the originally applied field. In fact, the magnetic induction at the surface of the superconducting filament considerably increases when the induced field is superimposed. It should be noted that the resulting screening field from the Wilson Model, for instance, is of no dipole type and therefore will neither result in a field free core, nor produce a dipole type field outside the filament. Besides the fact that the Nested Ellipse Model considers the dependence of the critical current density on the applied field and the field distribution in the filament cross-section, the generation of a pure dipole field in the interior and the exterior of the filament, is one of the important benefits of the model with respect to the calculation of superconducting magnets.

#### 4.1.9 The Hysteresis in the Superconductor Magnetization

In the sections 3.1 and 3.2, it is shown from the magnetization curve that a hysteretic effect arises when the external field changes its orientation. In order to express a hysteresis function, different mathematical models exist, for example, the Preisach Model [56] which is the most common one. The aim of all hysteresis models is to unequivocally identify the branch on which the effect has to be calculated from the cause. Usually the resulting value is calculated from a constitutive equation like the  $H(B)$ -curve for ferromagnetic materials and has to be associated with the actual branch in the  $H/B$ -plane by checking on the history. In the case of modeling a superconductor magnetization, however, the physical source of the hysteresis is well known and therefore *it is possible to incorporate it into the model* such that the hysteresis arises by physical modeling as is done within the scope of this thesis. This is advantageous since it avoids any artificial hysteresis modeling. In this section, the principle of how superconductor hysteresis arises and the idea of considering a pre-conditioning from a set of applied field values for single filaments is explained.

When calculating a superconducting cylinder exposed to a magnetic induction, the inner contour can be determined from the nested ellipses and the only unknown parameter is the relative penetration depth. Since the resulting magnetization depends on the history experienced by the filament, the very first calculation has to always start with an initial state curve (see also chapter 6). The sequence of the applied field values has to be stored in order to correctly calculate the resulting magnetizations. However, storing the whole history of applied fields for a great number of filaments as in superconducting cables would allocate an unreasonable amount of memory and is unnecessary. From the calculation of the penetration depth one can decide between history-relevant values that have to be kept for a correct calculation and those that can be erased. A successively increasing external field has the feature of wiping out the predessessing field values which then do not have to be stored in the history array, once the higher field value is reached.

In the example given below and illustrated by Fig. 4.11, the value of the magnetic induc-

tion  $B_1$  is wiped out while reaching the value  $B_2$ . Going from value  $B_2$  to value  $B_3$ , however, means that both values have to be stored in the history array in order to be able to produce the resulting field pattern inside the superconductor by considering its history (it is obvious that a different field pattern would arise if the value  $B_3$  is reached on an initial state curve). Both values,  $B_2$  and  $B_3$ , however are wiped out when the field value  $B_4$  is applied. Consequently, in each step the field array that is containing the history values changes, keeping only the history-relevant field values.

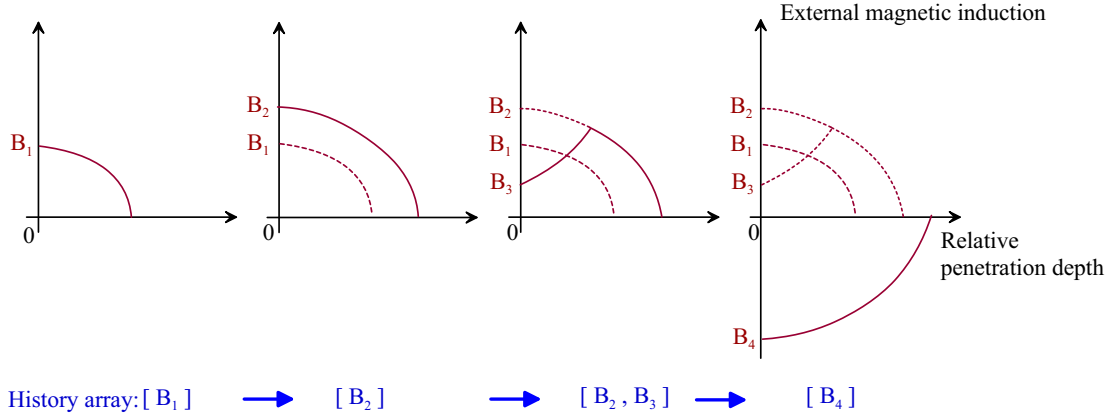


**Figure 4.11:** Setup of a history array for a sweep of a homogeneous external field. The pictures show the distribution of the magnetic induction in the interior of a filament as a function of the relative penetration depths for a field sweep from  $B_1 - B_4$ . The dashed lines show the field profile of the predecing step(s). The values below indicate the corresponding entries in the history array.

Fig. 4.12 shows the resulting magnetization for the indicated low field values of the above described field sweep, where starting from zero, the external field successively assumes the values  $B_1, \dots, B_4$ , of which  $|B_1| < |B_2| > |B_3|$  and  $|B_4| > |B_2|$ . The field orientations of  $B_1, B_2$  opposites those of  $B_3, B_4$ .

As already explained, changes in the orientation of the applied field cause additional current layers of opposite direction in the filament cross-section, whereas the application of the magnetic induction  $B_1$  starting from zero field raises a magnetization which is following the up-ramp branch (shielding branch on the initial state curve) from 0 to  $B_1$ . in this case, the filament is shielding its core from the applied field.

In the application of superconducting magnet calculation, history arrays of individual filaments usually do not contain more than 8 - 10 values due to the repeated wipe out of non history-relevant entries. However, mainly for correction magnets which are powered permanently in up-down-up ramp modes, the history array can become two or three times as large, when strong minor looping arises for individual filaments.

#### 4.1.10 Continuous Course of the Magnetization

In a similar way to the derivation of the analytic expression of the magnetic induction  $B(q)$  inside the filament, the magnetization of such an ellipse formation can be calculated. An expression for the magnetization due to a radial slice of current  $J_c(q)$  between the relative

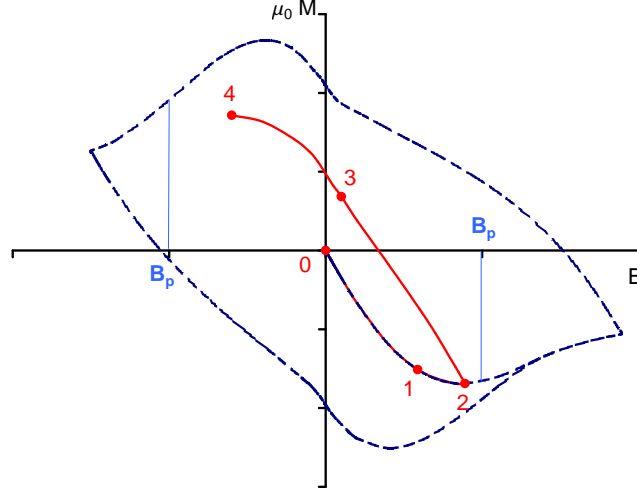


**Figure 4.12:** Resulting magnetization from the field sweep shown in Fig. 4.11. The blue dashed line presents a major magnetization loop as it would result from a field sweep with higher inductions. It is given in order to illustrate the actual position of the example values on the  $M(B)$ -curve.

penetrations  $q_i$  and  $q_{i+1}$  can be derived. Integration over the current-carrying surface leads to the magnetic moment and the magnetization can be found by dividing the result by the superconductor volume. For one set of inscribed ellipses with semi-minor axis  $a$  and semi-major axis  $b$ , the contours are determined by Eqs. (4.6) and (4.7) and the expression for the magnetic moment reads:

$$dm_f = 2J_c l_f \int_F x \, dx dy = 2J_c l_f \int_F r^2 \cos \varphi \, dr d\varphi,$$

in cylindrical coordinates. From this, the magnetization is defined by the magnetic moment per volume of superconducting material, the filament volume  $V_{\text{fil}}$ , here. The filament volume reads  $V_{\text{fil}} = \pi UV l_f$  in the case the filament has an elliptical cross-section with the semi-axes  $U, V$ , and  $V_{\text{fil}} = \pi r_f^2 l_f$  in the case of a circular cross-section with a filament radius  $r_f$ . As before,  $l_f$  denotes the length of the filament.

$$M = \frac{2J_c l_f}{V_{\text{fil}}} \int_{f_1(\varphi)}^{f_2(\varphi)} r^2 \cos \varphi \, d\varphi = \begin{cases} \frac{2J_c abc}{UV} & \text{for elliptical cross-section} \\ \frac{2J_c abc}{r_f^2} & \text{for circular cross-section.} \end{cases}$$

Again, a circle (or an ellipse) is inscribed into the current-free region of the intersection axis shown in the Figs. 4.6, 4.7 (left) and then another couples of intersecting ellipses is inserted into the remaining area of this circle and so on. Summation of the contribution of all  $n$  ellipse pairs reads:

$$\begin{aligned} M &= \frac{2c}{UV} \sum_{i=1}^n J_{c,i} a_i b_i \\ &= 2c \sum_{i=1}^n J_{c,i} \left( \frac{2n - 2i + 1}{2n} \right)^2, \end{aligned}$$

where expressions for the semi-axes of the inscribed ellipses are taken from Eqs. (4.10) and (4.11). The magnetization is given in (A/m). The special case of a circular filament cross-section can be obtained for  $U = V = r_f$ .

Following the argumentation in section 4.1.7 for the calculation of the magnetic induction, a similar expression for the magnetization  $M$  is found. Again, taking the limiting value for  $n \rightarrow \infty$  changes the sum to an integral with the integration constant  $q$  where  $q = i/n$  and  $nc = U/2$ . For the considered slice of current between the contours  $Uq_1$  and  $Uq_2$ , the magnetization reads:

$$M_i = U \int_{q_i}^{q_{i+1}} J_{c,i} (1-q)^2 dq,$$

and for an infinitely thin slice of thickness  $dq$ , where  $dq \rightarrow 0$ , an expression for the magnetization can be given as:

$$dM = \underbrace{J_c(B(q)) U (1-q)^2}_{m(q)} dq. \quad (4.28)$$

As already shown before when deriving the expression for the magnetic induction  $B(q)$ , the result is independent of the actual shape of the filament as long as its cross-section can be approximated by an ellipse with arbitrary values for the semi-axes  $U, V$ . Note, that the expression for  $dM$  only depends on the value of the semi-major axis  $U$ . This is a result of the homogeneous field distribution inside the filament cross-section.

This way, a function  $m(q)$  is introduced which can be considered as a magnetization contribution since the magnetization is obtained from the integral over this function. As is shown in the Figs. 4.15 and 4.16, the magnetization contribution  $m(q)$  can be identified with the curve in the  $m(q)$ -plots, whereas  $M(q)$  is given by the area under the curve. In the next section, only the case of filaments with a circular cross-section and a filament radius  $r_f$  is considered. The solution for arbitrarily shaped filaments can be found in section 4.3.

#### 4.1.11 Magnetization Resulting from a Change of a Homogeneous External Field

In section 4.1.9 it is shown that changes in the external magnetic induction cause current layers with opposite polarities and are the source of the filament hysteresis. Therefore, individual slice magnetizations are needed to describe the hysteresis after changes of the ramp direction. Such a change, where  $\partial B_{\text{ext}}/\partial t$  changes sign, will produce a new layer of screening currents with opposite polarity. This means that the parameter  $\xi$  which is indicating the branch of the hysteresis curve switches sign. The individual layers of different slice magnetizations have to be added up to the total magnetization of one filament as illustrated in detail in section 4.1.9. For small changes the *new* current layer will penetrate the filament only from  $q_1 = 0$  to  $q_2 \leq 1$  while the currents inside persist. The values for  $q_i$  are calculated using Eq. (4.27), following Figure 4.5 (left), where one such layer in the cross-section of a filament for the non-fully penetrated state is presented. For minor excitation loops, the magnetization is obtained from the superposition of  $k$  different layers,

$$M(q) = \sum_{i=1}^k M_i = \sum_{i=1}^k \int_{q_i}^{q_{i+1}} U \underbrace{J_{c,i} (1-q)^2}_{m(q)} dq. \quad (4.29)$$

In Eq. (4.29),  $M_i$  denotes the modulus of the magnetization of the  $i^{th}$  layer of  $M$ . It has a negative value if the resulting orientation is opposite to a positive external field. Its value results from the integration of the function  $m(q)$ . With the expression for the current fit function given in Eq. (2.7), the magnetization for a round filament ( $U = r_f$ ) with radius  $r_f$  results to:

$$M_i = r_f \xi \int_{q_i}^{q_{i+1}} J_c(B(q))(1-q)^2 dq = r_f \xi \mathcal{F} \int_{q_i}^{q_{i+1}} \frac{(1-q)^2}{\sqrt{B(q)}} dq. \quad (4.30)$$

As before in the expression for the magnetic induction, Eq. (4.27), the parameter  $\xi$  indicates the branch of the hysteresis curve, in the case of ramping up,  $\xi$  equals  $-1$  and for ramping down,  $\xi = 1$ . By means of solving the integral given in Eq. (4.30) and including the history parameter  $\xi$ , the current fit function, the parameter  $\mathcal{F}$  from Eq. (4.26), and the expression for the magnetic induction  $B(q)$  which is given in Eq. (4.27), a closed expression is found for the filament magnetization for one slice as follows:

$$M_i = \frac{4 B(q)}{5\pi \mathcal{F}^2 \mu_0^2 \mathcal{H}^3 r_f^2} \left[ B_{\text{ext}}^3 + \xi \mathcal{H} \mathcal{F} \mu_0 \left( \left( 5 - 4q + \frac{5}{4} q^2 \right) \xi \mathcal{H} \mathcal{F} \mu_0 - (q - 4) B_{\text{ext}}^{3/2} \right) \right] \Big|_{q=q_i}^{q=q_{i+1}} \quad (4.31)$$

The total magnetization is calculated by the sum of the individual slices given in Eq. (4.29) and reads:

$$\begin{aligned} M &= \sum_{i=1}^k M_i \\ &= \sum_{i=1}^k \frac{4 B(q)}{5\pi \mathcal{F}^2 \mu_0^2 \mathcal{H}^3 r_f^2} \left[ B_{\text{ext}}^3 + \xi \mathcal{H} \mathcal{F} \mu_0 \left( \left( 5 - 4q + \frac{5}{4} q^2 \right) \xi \mathcal{H} \mathcal{F} \mu_0 - (q - 4) B_{\text{ext}}^{3/2} \right) \right] \Big|_{q=q_i}^{q=q_{i+1}} \end{aligned} \quad (4.32)$$

The parameter  $\xi$  changes the sign for each layer and thus assumes the values  $\pm 1$  depending on the direction of the externally applied field. As before, a correction factor for the remaining triangles is received from the case of a fully penetrated filament containing one single layer of constant current by integrating Eq. (4.30) from  $q_i = 0$  to  $q_{i+1} = 1$ , which yields:

$$M = r_f J_c \int_0^1 (1-q)^2 dq = -r_f J_c \frac{1}{3}. \quad (4.33)$$

Comparison of Eq. (4.33) and the result for a fully penetrated filament with a circular cross-section given in Eq. (3.9) yields a correction factor of  $4/\pi$ . The factor  $\mathcal{H}$  remains in the expression for  $B(q)$  as a correction factor for the ellipse shape when calculating the magnetic induction in the filament cross-section.

Figure 4.13 presents calculations of the filament magnetization derived from Eq. (4.31). The outcome is multiplied with the filling factor  $\lambda$  in order to rescale to the magnetization of a strand which then can be compared with measurements<sup>3</sup>. The initial state curve and

<sup>3</sup>It should be noted that measurements can be carried out on a strand level only. The superconducting alloy is very brittle and has a filament radius of  $6\mu\text{m}$  which would not restrain the mechanical handling – whereas a strand where a bunch of filaments is embedded in a copper matrix can easily be handled mechanically.

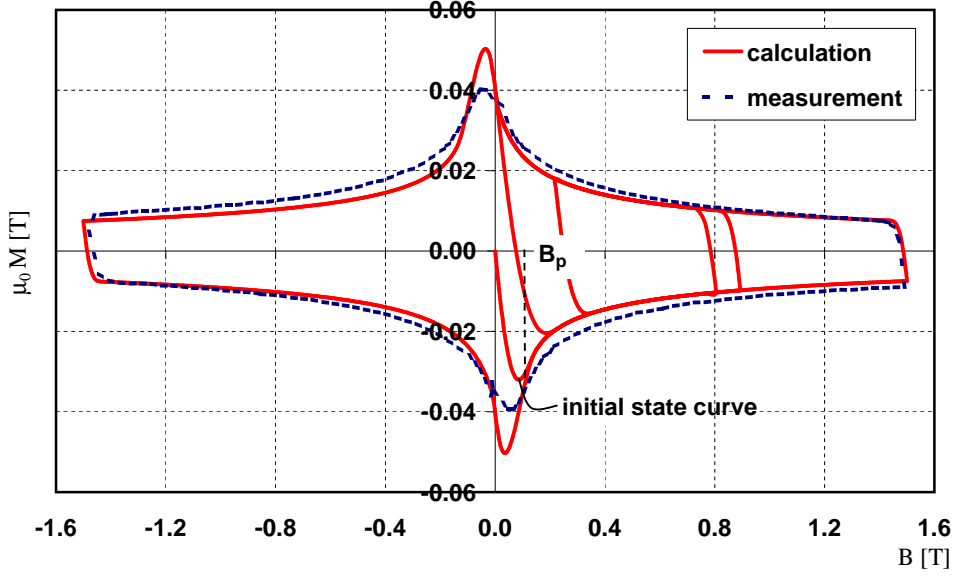


**Figure 4.13:** Computed magnetization curve for one filament ( $r_f = 3.5\mu\text{m}$ ,  $\lambda = 1/2.95$ ,  $T = 1.9\text{ K}$ ) compared to measurements on a superconducting strand [51].

several hysteresis loops are displayed. The comparison of the calculation and the measured magnetization of a superconducting strand (dashed line) shows good agreement apart from the region of  $B$  close to zero. At these points the difference between the magnetizations of one filament and a whole strand becomes significant. Since the outside field for each filament varies slightly due to the position in the strand cross-section and is additionally influenced by the field arising from the screening currents in the neighboring filaments,  $B_{\text{ext}}$  will be different for each filament according to its exact position. This results in a spread of filament magnetizations and hence in a smoothing of the region of  $B$  close to zero. Since the Rutherford cables used in LHC magnets consist of many individual strands, this region will be smoothed out automatically due to the differences of  $B_{\text{ext}}$  at the individual strand positions within the coil.

### Calculation of the Relative Penetration Depths

The equation for the magnetization, Eq. (4.32) can be evaluated, if the values of the penetration depths of the individual layers are known. These relative penetration depths can be calculated from the course of the magnetic induction, Eq. (4.27), by fulfilling an additional condition for the field that is depending on the actual pre-conditioned state of the filament. This can be the screening field condition in the case of the initial state, where  $B(q^{\text{in}}) = 0$ , or the intersecting condition for all other cases.

For the initial state, the magnetic field in Eq. (4.27) vanishes when  $q = q^{\text{in}}$  and the relative penetration depth at initial state  $q^{\text{in}}$  results to:

$$\begin{aligned} B(q^{\text{in}}) &= 0 \\ \Rightarrow q^{\text{in}} &= \left| \frac{2 B_{\text{ext}}^{3/2}}{3\mu_0 \mathcal{H} r_f \mathcal{F}(B_{\text{ext}})} \right|, \end{aligned} \quad (4.34)$$

whereas the relative penetration depth of the general case  $q^{\text{gen}}$  results from the point of intersection between the  $(i-1)^{\text{th}}$  and the  $(i)^{\text{th}}$  applied field value to:

$$\left( (B_{\text{ext}}^{i-1})^{3/2} + \frac{3}{2} \xi^{i-1} \mathcal{H} r_f \mathcal{F}(B_{\text{ext}}^{i-1}) \mu_0 q^{\text{gen}} \right)^{2/3} = \left( (B_{\text{ext}}^i)^{3/2} + \frac{3}{2} \xi^i \mathcal{H} r_f \mathcal{F}(B_{\text{ext}}^i) \mu_0 q^{\text{gen}} \right)^{2/3}.$$

In the latter case, the hysteresis parameters  $\xi^{i-1}$  from the last step and  $\xi^i$  from the actual step always have opposite signs. The relative penetration depth finally reads:

$$q^{\text{gen}} = \left| \frac{(B_{\text{ext}}^{i-1})^{3/2} - (B_{\text{ext}}^i)^{3/2}}{3\mu_0 \mathcal{H} r_f \mathcal{F}} \right|. \quad (4.35)$$

The derivation of the Eqs. (4.34) and (4.35) is illustrated in Fig. 4.14.

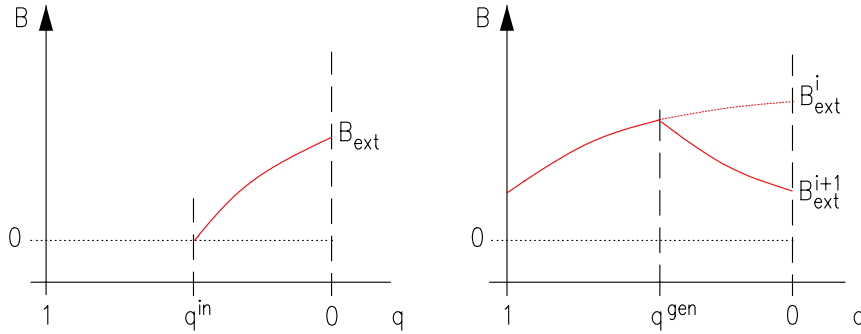


**Figure 4.14:** Calculation of the relative penetration depths  $q^{\text{in}}$  and  $q^{\text{gen}}$  for the initial state curve and the general case, respectively. The dashed line indicates the magnetic induction in the predecing ( $i^{\text{th}}$ ) step.

#### 4.1.12 Initial State Curve and Fully Penetrated State

The derived expressions of the magnetic induction  $B(q)$ , Eq. (4.27), and the magnetization contribution  $m(q)$ , Eq. (4.28), respectively the magnetization  $M$ , Eq. (4.31), can be plotted as a function of the relative penetration depth  $q$ , where the absolute penetration depth (in  $\mu\text{m}$ ) is obtained from the product with the semi-axis  $U$  of the filament  $qU$ . Figure 4.15 (upper plot), shows the result for the magnetic induction  $B(q)$  versus the relative penetration depth in the case of increasing external fields  $B_{\text{ext}}$  ( $\xi = -1$ ) on the initial state curve. The magnetic induction in this case is achieved from one current layer extending from  $q_1 = 0$  to  $q_2(B_{\text{ext}})$ . Depending on  $B_{\text{ext}}$ , the resulting  $B(q)$  decreases according to the screening effect until a certain penetration depth is reached, where complete screening of the external field is obtained. The remaining part of the filament stays field free. In the lower plot the contribution  $m(q)$  of a slice  $dq$  to the total magnetization  $M$  is presented. As shown, the value of the magnetization  $M$  can be obtained by integrating the presented curves (see indication on the plot).

Figure 4.16 illustrates the same quantities as in Fig. 4.15, but for a filament that has already experienced a negative outside field once before (different history) and hence is fully

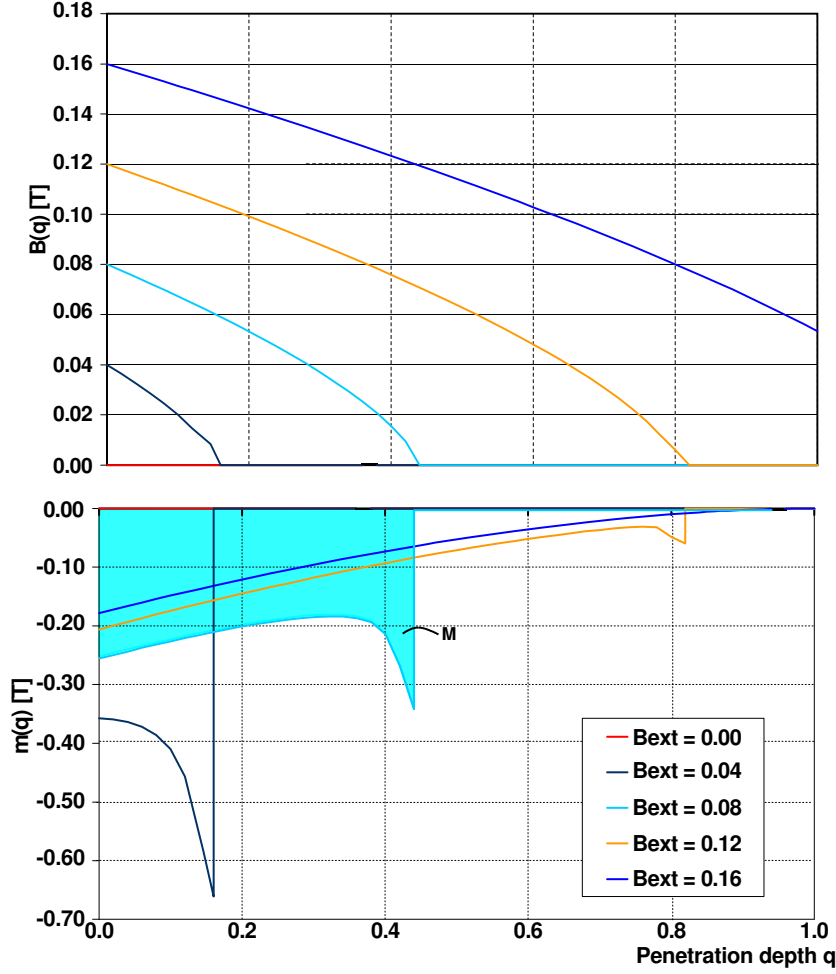


**Figure 4.15:** Course of the magnetic induction  $B(q)$  and the contribution  $m(q)$  as a function of the relative penetration depth  $q$  for the initial state curve. The magnetization is obtained by integrating the value of the magnetic contribution  $m(q)$  and thus corresponds to the blue area under the  $m(q)$ -curve.

penetrated. Since the currents inside the superconductor persist, there is a remaining negative field  $B(q)$  inside, whereas in the case of the initial state curve the field is zero for  $q > q_2(B_{\text{ext}})$ . The lower plot in Fig. 4.16 also explains why the maximum magnetization does not occur at  $B_{\text{ext}} = 0$ : As the magnetization is determined by the integrated area  $M$  under the  $m(q)$  curve, it can be seen that it is biggest for small values of  $B_{\text{ext}} \neq 0$ . This characteristic behavior has already been observed in measurements (see Fig. 4.13), but a theoretical explanation was missing so far. In those cases, where the magnetization model neglects the  $J_c$ -dependence, this effect is not reproduced as can be seen in the case of the Wilson Model, Fig. 3.7, for example.



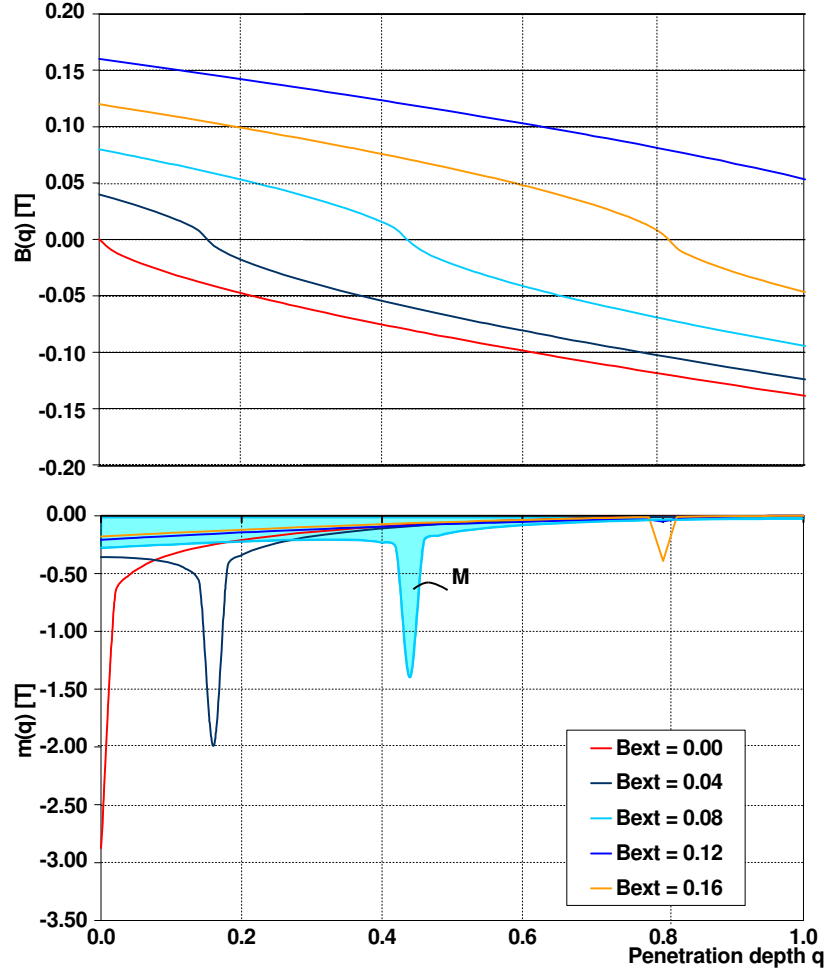


**Figure 4.16:** Course of the magnetic induction  $B(q)$  and the contribution of the magnetization  $m(q)$  as a function of the relative penetration depth  $q$  for a filament already been exposed to a magnetic field before (non-initial state curve). The magnetization is obtained by integrating the value of the magnetic contribution  $m(q)$  and thus corresponds to the blue area under the  $m(q)$ -curve.

#### 4.1.13 Calculation of $B_{p1}$

In the case that the critical current density is held constant, the magnetization reaches its maximum on the initial state curve exactly when the filament is fully penetrated and the outside magnetic induction  $B_{\text{ext}}$  equals  $B_p$ . However, in the case that the field-dependency of the critical current density is considered, the maximum in the magnetization is reached *before* the filament goes into the fully penetrated state. Thus, a magnetic induction  $B_{p1}$  is defined that denotes the value of the outside magnetic induction where the modulus of the filament magnetization passes through its first maximum when ramping up on the initial state curve (see Fig. 4.13). This value of  $B_{p1}$  and the correspondent relative penetration depth are calculated in the following.

The calculation of the maximum magnetization, starts with the closed analytical expres-

sion that has been given in Eq. (4.31). For the initial state curve, the magnetization consists of only one layer, so  $i = 1$ . This single layer penetrates the filament from  $q_1 = 0$ , to a relative penetration depth  $q_2$  which can be calculated from Eq. (4.27), in which  $B(q_2) = 0$  to:

$$q_2 = 2B_{\text{ext}}^{3/2} / (\mathcal{H} r_f \mathcal{F}(B_{\text{ext}}) \mu_0), \quad (4.36)$$

since the field inside the superconductor is fully screened in this case (see also Fig. 4.13 for illustration).

The magnetization given in Eq. (4.31) now only depends on  $B(q)$  and  $B_{\text{ext}}$  and thus, the maximum of the magnetization on the initial state curve can now be derived by solving the equation  $\partial M(B_{\text{ext}}) / \partial B_{\text{ext}} = 0$ . Since the function of the critical current density in the region of very low values is cut to a finite value, an approximation is used when  $B_{\text{ext}} = B_{p1}$ , such that  $j'_c(B_{\text{ext}}) \cong 0$ . This way, the applied field reads:

$$B_{p1} \cong (\mathcal{H} \mathcal{F}(B_{p1}) \mu_0)^{2/3} \frac{(15 - 5\sqrt{5})^{1/3}}{2}, \quad (4.37)$$

$$q_2 \cong \sqrt{\frac{5}{6} - \frac{5\sqrt{5}}{18}} \cong 0.46. \quad (4.38)$$

Equation (4.37) has to be solved recursively and yields a good estimate for the entity  $B_{p1}$  after few iterations. From Eq. (4.38), it can be seen that the maximum modulus of the magnetization does occur at a relative penetration depth of  $q_2 \cong 0.46$  rather than in the fully penetrated state. This fact is illustrated by the lower plot of the Figs. 4.15 and 4.16, where the area under the  $m(q)$ -curve reaches its maxima at  $q \rightarrow 0.46$  (solid blue line). Note that the value of  $q_2$  is independent of the critical current fit, provided  $\partial \mathcal{F}(B_{\text{ext}}) / \partial B_{\text{ext}} \cong 0$  i.e. the critical current diverges with  $1/\sqrt{B_{\text{ext}}}$ , for  $B_{\text{ext}} \rightarrow 0$ , a restraint which is fulfilled as can be seen from Eq. (2.7) and its approximation, Eq. (2.8) for the example of the LHC main dipole and quadrupole cable. Also this can be seen in the Figs. 4.15 and 4.16.

## 4.2 The Nested Ellipse Model for Rotating Fields

In the last section, the field response of a superconducting cylinder on an externally applied magnetic induction exposed to a change of a *homogeneous* external field has been described. In the more general case, the applied magnetic induction rotates in the plane of the filament cross-section. This means that with varying source currents, the magnetic induction which is applied on the strands in the coil cross-section changes not only its value, but also the exercising angle with respect to the local coordinate system of the strand. The amount of local change in applied field depends on numerous parameters as the location of the strand in the coil cross-section, the type of coil, as, dipole, quadrupole or so-called nested coils, for instance, the influence of the iron yoke saturation and such the vicinity of the yoke structure with respect to the coil position, local iron saturation effects, influence of neighboring strands, global displacement effects of the magnetization in the complete coil and influences due to the application of local compensation devices (as ferromagnetic shims or non-powered (passive) superconductors, etc.), if present. All these effects make the determination of the magnetization in the more realistic case of so-called rotating fields far more complicated than in the one-dimensional case. Since it has been shown, for example, in [41], that magnetic fields oriented parallel to the strand axis only have a minor influence on the induced superconductor magnetization, rotating fields in the plane can be considered the general case of interest in the framework of persistent current calculation.

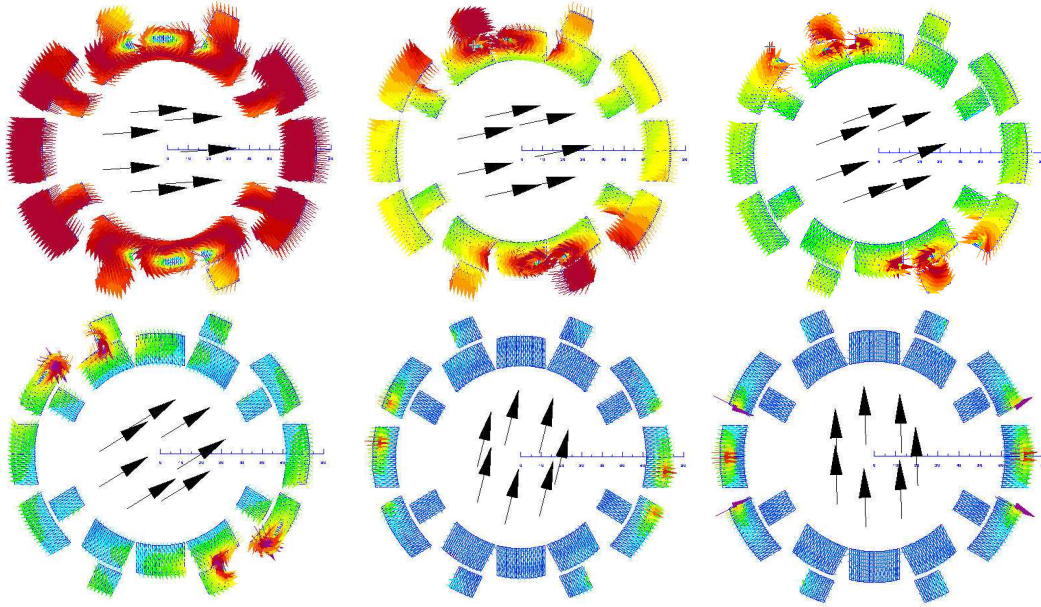


**Figure 4.17:** Coil cross-section of an orbit corrector magnet (LHC MCBX magnet) showing the induced magnetization vectors (in color) and the resulting magnetic induction (in black) for different states in a powering cycle. The pictures show the results for a time-stepping of the source currents from the coil in the top left to the bottom on the right-hand side. The source currents result in an anti-clockwise rotation of the main field. The vectors of the induced magnetization in the superconducting coil change accordingly.

Figure 4.17 shows the coil cross-section of an orbit corrector magnet which is designed for LHC (so-called MCBX magnet). The MCBX magnet is described in detail in section 6.5. The plots have been chosen here in order to illustrate the necessity of the rotating field calculation. The presented magnetic fields have been calculated from source currents, only. The currents are fed in such a way that the resulting inner field distribution rotates in the plane. As can be seen from the field distribution in the cross-section, the vortices which exist within the coil structure, are moving according to the orientation of the main field component. In addition, the radial position of these vortices depends on the total amount of source current in the coil and on the shape and the vicinity of the ferromagnetic iron contour surrounding the coil (not shown in the plot). Strands which are located in the vortex regions experience a rapid change in external field direction with the movement of the field vortices and such react with a strong change in their induced superconductor magnetization. Additionally, the field vortices indicate low field regions (field drains) where the amount of magnetization as well as the magnetization gradient are high.

In the case of rotating fields, the magnetic induction resulting from external field sweeps can no longer be determined by superposition which results in a sum of several scalar terms (as in Eq. (4.32)). Changes in external field orientation do not only produce a new current layer, moreover, different layers can presume arbitrary angular rotations of their local coordinate system. The resulting magnetic induction has then to be calculated by superposition of the vector terms of the fields resulting from the induced currents of the individual layers. Since it is also possible, that the total amount of the applied magnetic induction stays constant while only the angle of the direction of the applied field varies, also the criteria for detecting hysteresis branches have to be adapted and the history array of each strand has to contain an angular information in addition to the amount of the applied field.

#### 4.2.1 Magnetic Induction in Case of a Rotating Field Sweep

The model presented in this section has been derived from the one-dimensional case introduced in section 4.1 and the expressions given there. In a first step, the one-dimensional integral for the magnetic induction in the interior of a filament, Eq. (4.27) has to be modified for the 2D case. This means that the parameter  $\xi$ , which was formerly toggling between  $-1$  and  $+1$  (in case the external field changed orientation), now has to be modified in such a way as to encompass the exercising angle of the applied field instead of merely expressing the external field orientation. Assuming, in a first step, the applied magnetic induction to be oriented in the  $x$ -direction of the local coordinate system of the filament and the origin of local coordinate system to be in the filament center. Then  $\alpha$  may denote the angle between the applied field and the induced screening field. Thus, the entity  $\xi$  can be expressed by the relation

$$\xi = -\cos \alpha. \quad (4.39)$$

In case only one field value has been applied so far,  $\alpha$  equals zero in the first step and the screening field directly opposites the applied field. In case of any change in external field strength *without angular variation*,  $\alpha$  assumes either null or  $\pi$ , corresponding to the one-dimensional cases  $\xi = \pm 1$ . This allows to modify the one-dimensional differential equation  $B' = \pm \mu_0 \mathcal{H} r_f \mathcal{F} / \sqrt{B(q)}$ , (equivalent of Eq. (4.25)), to the set of equations:

$$\begin{aligned} B'_x(q) \sqrt[4]{B_x^2(q) + B_y^2(q)} &= -\cos \alpha \mathcal{H} r_f \mu_0 \\ B'_y(q) \sqrt[4]{B_x^2(q) + B_y^2(q)} &= -\sin \alpha \mathcal{H} r_f \mu_0, \end{aligned} \quad (4.40)$$

where  $q$  denotes the dimensionless relative penetration depth. The absolute penetration depth (in  $\mu\text{m}$ ) is obtained from the product  $q U$ . The equations have to fulfill the boundary conditions on the outer filament border:

$$B_x(0) = B_{\text{ext}} \quad B_y(0) = 0.$$

The amount of resulting magnetization, formerly expressed only for the one-dimensional case, Eq. (4.31), already includes the parameter  $\xi$  which now follows Eq. (4.39) and such the application on a slice  $i$  of current between the relative penetration depths  $q_i \rightarrow q_{i+1}$  remains as derived in section 4.1:

$$M_i = \frac{4 B(q)}{5\pi \mathcal{F}^2 \mu_0^2 \mathcal{H}^3 r_f} \left[ B_{\text{ext}}^3 + \xi \mathcal{H} \mathcal{F} \mu_0 \cdot \left( \left( 5 - 4q + \frac{5}{4} q^2 \right) \xi \mathcal{H} \mathcal{F} \mu_0 - (q - 4) B_{\text{ext}}^{3/2} \right) \right] \Big|_{q=q_i}^{q=q_{i+1}}.$$

The problem is now, to determine the relative penetration depths  $q^i, q^{i+1}$  in the rotating field case. As before in the case of a sweep of a homogeneous external field, a new current layer is induced in case of a general external field change. Consequently, the width of the existing current layer(s) from the previous step(s) changes due to the newly induced currents. Direction and amount of the newly induced currents follow a set of rules: Independent of the (already existing) current distribution which resulted from the previous step, they are oriented according to the right-hand law with respect to the external field direction of the actual step. The amount is such as to screen the change in field from the previous to the actual step (assuming the field change does not exceed the penetration field  $B_p$ ). In case the field change exceeds the maximum screen-able field, the current layer from the previous step is wiped out. In any case, the total field of such a filament results from the superposition of the contribution of all remaining and the actual current layers. The orientation of the magnetization which results from the individual layers has to be taken into account. Therefore, both the direction of total screening field and the direction of the resulting superconductor magnetization decouples from the orientation of the actual applied magnetic induction. For the calculation of rotating fields, only nested circles are used. This way, the individual current slices can be shifted with an arbitrary angle and such the rotation is modelled.

### 4.2.2 Parameterizing the Problem

Generally, the relative penetration depth can be received in a similar way as in the one-dimensional case from the boundary conditions. In order to do so, the set of equations, Eqs. (4.40) is parameterized

$$B'_x(q) = -t'(q) \cos \alpha, \quad B'_y(q) = -t'(q) \sin \alpha. \quad (4.41)$$

This way, the components of the magnetic induction as a function of the relative penetration depth  $q$ , in the general case, result to:

$$\begin{bmatrix} B_x(q) \\ B_y(q) \end{bmatrix} = B_{\text{ext}} \begin{bmatrix} \cos \varphi \\ \sin \varphi \end{bmatrix} - t(q) \begin{bmatrix} \cos(\alpha + \varphi) \\ \sin(\alpha + \varphi) \end{bmatrix}, \quad (4.42)$$

where  $\varphi$  is the angle of the external magnetic induction with respect to the  $x$ -axis. For the special case mentioned before, where the magnetic induction in the first step has only an  $x$ -component ( $\varphi=0$ ), Eq. (4.42) modifies to the easier case of:

$$\begin{bmatrix} B_x(q) \\ B_y(q) \end{bmatrix} = B_{\text{ext}} \begin{bmatrix} 1 \\ 0 \end{bmatrix} - t(q) \begin{bmatrix} \cos \alpha \\ \sin \alpha \end{bmatrix}. \quad (4.43)$$

Equally, if the external magnetic induction has only a  $y$ -component,  $\varphi=\pi/2$  and the equation reads:

$$\begin{bmatrix} B_x(q) \\ B_y(q) \end{bmatrix} = B_{\text{ext}} \begin{bmatrix} 0 \\ 1 \end{bmatrix} - t(q) \begin{bmatrix} \cos \alpha + \frac{\pi}{2} \\ \sin \alpha + \frac{\pi}{2} \end{bmatrix}. \quad (4.44)$$

The function  $t(q)$  can be considered the newly induced screening field in the present step. In order to illustrate this, two successive values of magnetic inductions,  $\mathbf{B}_{\text{ext}}^1$  and  $\mathbf{B}_{\text{ext}}^2$  may be applied to a filament as is shown in Fig. 4.18, where  $|\mathbf{B}_{\text{ext}}^1| = B_{\text{ext}}^1 > B_p$ , the penetration field, and  $B_p > |\mathbf{B}_{\text{ext}}^2| = B_{\text{ext}}^2$ . The superscript indices 1,2 denote the number of the step. If no superscript is given (as, for instance, in Eq. (4.39)), the general case is meant. Without loss of generality,  $\mathbf{B}_{\text{ext}}^1$  may be oriented in the  $+y$ -direction.

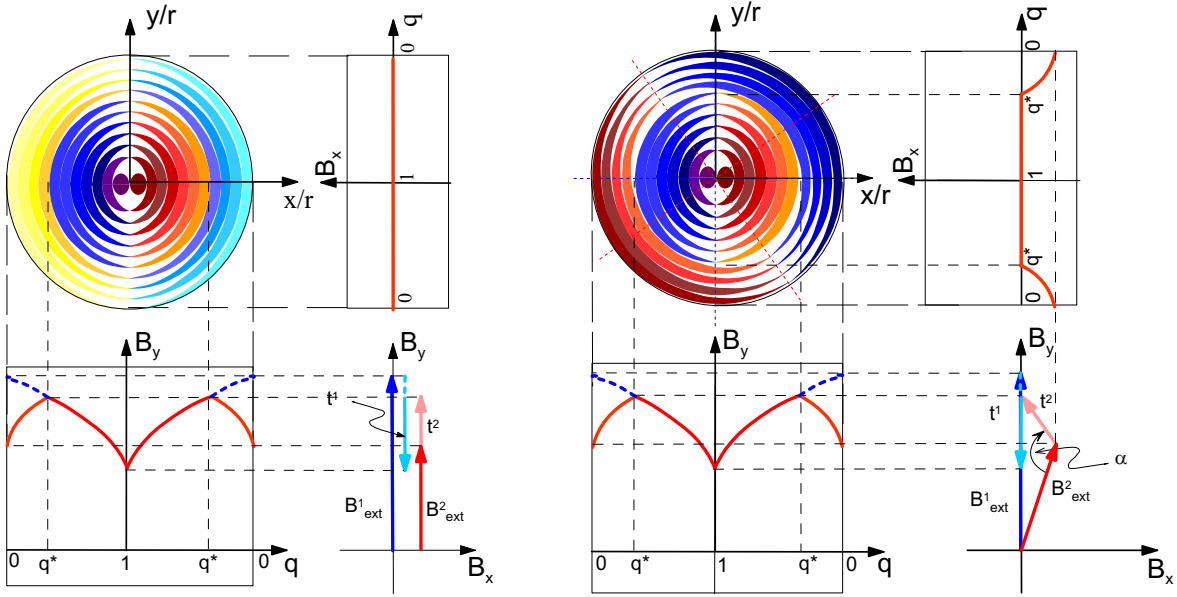


**Figure 4.18:** Cross-sections of a round superconducting filaments exposed to externally applied magnetic inductions  $\mathbf{B}_{\text{ext}}^{1,2}$ . The intersecting circle pairs suggest the induced current profiles. The number of inscribed pairs goes to infinity in the model by applying a limiting value. Left: 1-dimensional change of the applied magnetic inductions  $\mathbf{B}_{\text{ext}}^1, \mathbf{B}_{\text{ext}}^2$ . Right: The magnetic induction  $\mathbf{B}_{\text{ext}}^2$  has changed the exercising angle with respect to the first step. The arrow diagrams show the resulting induced screening vectors  $\mathbf{t}^1, \mathbf{t}^2$  in the respective two steps. Applied cycle, left hand side:  $|B_{\text{ext}}^1 \mathbf{e}_y| > B_p$  (indicated by the dark blue arrow)  $\rightarrow |B_{\text{ext}}^2 \mathbf{e}_y| < B_p$  (indicated by the red arrow). Applied cycle, right hand side:  $|B_{\text{ext}}^1 \mathbf{e}_y| > B_p \rightarrow |\mathbf{B}_{\text{ext}}^2 = B_{\text{ext},x}^2 \mathbf{e}_x + B_{\text{ext},y}^2 \mathbf{e}_y| < B_p$ . The vector  $\mathbf{t}^2$  is the resulting screening vector from the second step. It opposes the *change* in the magnetic induction rather than the induction itself. In the case of the rotating fields, it can be seen that the screening vector de-couples from the orientation of the magnetic induction applied in the second step.

The right plot in Fig. 4.18 shows qualitatively how the two magnetic inductions of the two steps induce two independent current slices of which the outer is rotated by the angle  $\varphi$ . The arrow diagram at the right hand side of this figure is to be read as follows: In the 1st step,  $\mathbf{B}_{\text{ext}}^1$  is applied pointing only in the  $y$ -direction. The induced screening currents fully penetrate the filament, since  $B_{\text{ext}}^1 > B_p$ . They result in a screening field  $\mathbf{t}^1$  with opposite direction to  $\mathbf{B}_{\text{ext}}^1$ . The screening is, however, not complete, thus the length of the arrow of  $\mathbf{t}^1$  is shorter than that of  $\mathbf{B}_{\text{ext}}^1$ . In the 2nd step, the applied field reduces its total amount and – in addition – rotates by the angle  $\varphi$  with respect to the coordinate system of the 1st step. A new current layer is induced. The resulting screening field  $\mathbf{t}^2$  of the second step opposes the *change* in the field with respect to the last step (rather than the total field that is applied in the second step). The resulting total screening is obtained from the superposition of the screening from the 1st step and the screening field produced in the 2nd step (not shown in the arrow diagram). Consequently, the orientation of the total screening field de-couples from the external field direction. This is, of course, equally true for the orientation of the resulting magnetization. In addition, the second current layer reduces the screening capacity of the 1st layer due to the re-distribution of the current: When the second current slice is induced, the newly induced currents are reducing the available area of the currents of the 1st step. Consequently, the length of the arrow of  $\mathbf{t}^1$  has to be shortened when the second step is applied (dashed part of  $\mathbf{t}^1$ ).

The plot on the left hand side of Fig. 4.18 is showing the easier case of a one-dimensional change of the applied field, for comparison. In addition, for both cases shown in Figure 4.18, the resulting distributions of the two components  $B_x(q)$  and  $B_y(q)$  of the induced magnetic inductions in the filament cross-section versus the relative penetration depth  $q$  of the filament are presented. As can be seen from the plots, the  $y$ -component of the screening field is reduced in the second application step and matches the applied magnetic induction  $B^2$  at  $q = 0$  (the dashed line indicates the course of  $B_y(q)$  versus  $q$  after the 1st application step). It should be noted that the amount of  $B_{\text{ext},y}^2$  in the case of rotating fields is chosen to have the same amount as  $B_{\text{ext}}^1$  (thus the distributions of  $B_y$  versus  $q$  are identical).

As has already been mentioned, for rotating fields, the orientation of the induced screening fields (and this way also the resulting magnetization) de-couples from the externally applied field direction. This feature will be further investigated in section 6.5, when a rotating field is applied to the coil of a dipole-orbit corrector magnet and the resulting magnetization is computed.

A similar diagram as the arrow plot for the applied field and the screening fields in the different step can be derived for the correlation between the relative penetration depths and the external fields in the various steps. Figure 4.19 illustrates the development and the boundary conditions which are used to determine the relative penetration depths for the above given example of two consecutive steps with rotating the fields by an angle  $\varphi$ .

In order to calculate the above described penetration of the induced current layers, the relative penetration depth of the actual step has to be calculated by combining the Eqs. (4.40), (4.41). This yields the correlation:

$$t'(q) \sqrt[4]{B_x^2 + B_y^2} = \mathcal{F}\mathcal{H}\mu_0.$$

Including now the components that are given in Eq. (4.43), results in:

$$t'(q) \sqrt[4]{B_{\text{ext}}^2 + t^2(q) - 2B_{\text{ext}}t(q)\cos\alpha} = \mathcal{F}\mathcal{H}\mu_0,$$

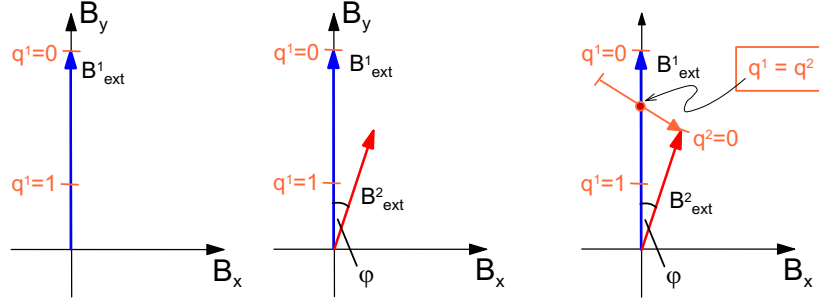


**Figure 4.19:** Diagrams of the applied magnetic induction (blue and red) and the resulting vector for the determination of the penetration depths in the different steps. Applied cycle:  $|B_{\text{ext}}^1 \mathbf{e}_y| > B_p \rightarrow |\mathbf{B}_{\text{ext}}^2 = B_{\text{ext},x}^1 \mathbf{e}_x + B_{\text{ext},y}^2 \mathbf{e}_y| < B_p$ . The penetration depth of the second step, is obtained from two boundary conditions: (1) on the outer border of the filament, where  $q^2 = 0$ , the screening field has to have the value of the external field,  $B_{\text{ext}}^2$ , in the actual step (the two arrowheads of the red and orange arrows meet). (2) At the position, where the two slices of current which result from the two successive steps touch, the value of the penetration depth from the first step and that one from the second step have to be identical. This is indicated by the red point, where  $q^1 = q^2$  and corresponds to the point  $q^*$  in Fig. 4.18.

with the boundary condition  $t(q = 0) = 0$ . Substituting now  $u(q) = t(q) - B_{\text{ext}} \cos \alpha$  gives:

$$u'(q) \sqrt[4]{u^2(q) + B_{\text{ext}}^2 \sin^2 \alpha} = \mathcal{FH}\mu_0 \quad (4.45)$$

and the boundary condition  $u(0) = -B_{\text{ext}} \cos \alpha$ . From Eq. (4.45), the function of the relative penetration depth  $q$  can be determined:

$$\begin{aligned} du(q) \sqrt[4]{u^2(q) + B_{\text{ext}}^2 \sin^2 \alpha} &= \mathcal{FH}\mu_0 dq \\ q &= \frac{1}{\mathcal{FH}\mu_0} \int \sqrt[4]{u^2(q) + B_{\text{ext}}^2 \sin^2 \alpha} du(q) \end{aligned} \quad (4.46)$$

which yields:

$$\begin{aligned} q &= \frac{1}{\mathcal{FH}\mu_0} \left[ \frac{2}{3} u \left( B_{\text{ext}}^2 \sin^2 \alpha + u^2 \right)^{1/4} \right. \\ &+ \frac{1}{3} \frac{B_{\text{ext}}^2 \sin^2 \alpha u \left( 1 + \frac{u^2}{B_{\text{ext}}^2 \sin^2 \alpha} \right)^{3/4}}{(B_{\text{ext}}^2 \sin^2 \alpha + u^2)^{3/4}} {}_2F_1 \left( \frac{1}{2}, \frac{3}{4}, \frac{3}{2}, \frac{-u^2}{B_{\text{ext}}^2} \right) \\ &\left. + \sqrt{|B_{\text{ext}} \sin \alpha|} {}_2F_1 \left( \frac{1}{2}, \frac{3}{4}, \frac{3}{2}, \frac{-(t(q) - B_{\text{ext}} \cos \alpha)^2}{B_{\text{ext}}^2} \right) \right] \end{aligned}$$

This way, the relative penetration depth can be expressed including the boundary condition  $q(-B_{\text{ext}} \cos \alpha) = 0$  as<sup>4</sup>:

$$q(t) = \frac{1}{3\mathcal{FH}\mu_0} \left[ B_{\text{ext}} \cos \alpha (2\sqrt{B_{\text{ext}}} + \sqrt{|B_{\text{ext}} \sin \alpha|}) \right] {}_2F_1 \left( \frac{1}{2}, \frac{3}{4}, \frac{3}{2}, -\cot^2 \alpha \right) +$$

<sup>4</sup>Equation (4.46) has been solved by means of the program package *MATHEMATICA*®.



$$(t - B_{\text{ext}} \cos \alpha) \left( 2(B_{\text{ext}}^2 + t^2 - 2B_{\text{ext}}t \cos \alpha)^{1/4} + \sqrt{|B_{\text{ext}} \sin \alpha|} {}_2F_1 \left( \frac{1}{2}, \frac{3}{4}, \frac{3}{2}, -\frac{(t - B_{\text{ext}} \cos \alpha)^2}{\sin^2 \alpha B_{\text{ext}}^2} \right) \right). \quad (4.47)$$

Where  ${}_2F_1$  denotes the Gauss' hypergeometric function. The input of the hypergeometric function in Eq. (4.47) assumes a pole in its argument if  $\sin \alpha = 0$  or  $B_{\text{ext}} = 0$ . In this case, the function  $q(t)$  can be determined as follows:

$$q(t) = \frac{2}{3\mathcal{F}\mathcal{H}\mu_0} \left[ B_{\text{ext}}^{3/2} \cos \alpha + (t - B_{\text{ext}} \cos \alpha)(B_{\text{ext}}^2 + t^2 - 2B_{\text{ext}}t \cos \alpha)^{1/4} \right] \quad (4.48)$$

For programming purposes, the hypergeometric function is expressed in terms of the Gamma-function [57] as is shown in the appendix A.4.

### 4.2.3 Equations for the Relative Penetration Depth

It is now possible, to determine the function  $t(q)$  of the Eqs. (4.47), (4.48) by means of the Newton algorithm and from this, the components of the induced magnetic induction  $B_x, B_y$  are received by means of Eq. (4.42) as a function of the relative penetration depth for different values of externally applied magnetic induction  $B_{\text{ext}}$ . However, in the general case, where both fields (predessessing and actual step) are applied on the filament with arbitrary angles in the filament cross-section, three unknowns  $t^i, t^{i+1}$  and  $\alpha^{i+1}$  remain. Here,  $i$  denotes the  $i^{\text{th}}$  step (predessessing step),  $i+1$  the  $i+1^{\text{th}}$  step (actual step) hence,  $q(t^i)$  the relative penetration depth in the  $i^{\text{th}}$  step,  $q(t^{i+1})$  the relative penetration depth in the actual step. The entities  $\alpha^i$  and  $\alpha^{i+1}$  denote the angles between the screening vectors  $\mathbf{t}^i$  and the corresponding applied fields  $\mathbf{B}_{\text{ext}}^i$ , and  $\mathbf{t}^{i+1}$  and  $\mathbf{B}_{\text{ext}}^{i+1}$ , respectively (see Fig. 4.20 for the illustration of the entities in the general case).

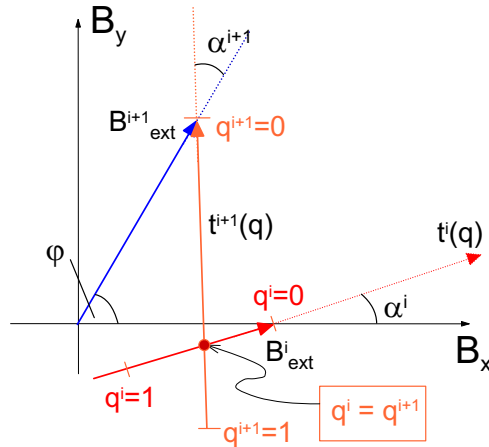


**Figure 4.20:** Diagram of consecutively applied magnetic inductions  $B_{\text{ext}}^i, B_{\text{ext}}^{i+1}$  and the induced screening field vector  $\mathbf{t}^{i+1}(q)$  of the  $i+1$ -th application step.

As already mentioned, the relative penetration depths of two consecutive steps have to be identical since the current layers of two consecutive steps touch. Therefore, the condition

for the relative penetration depths reads:

$$q(t^i) \Big|_{B_{\text{ext}}, \alpha^i} = q(t^{i+1}) \Big|_{B_{\text{ext}}^{i+1}, \alpha^{i+1}} \quad , \quad (4.49)$$

delivering the first stipulative equation for the remaining three unknowns.

The two other stipulative equations result from the fact that the magnetic inductions at the point of intersection from the  $i^{\text{th}}$  and  $i + 1^{\text{th}}$  step are continuous:

$$B_x(q^i) = B_x(q^{i+1}), \quad B_y(q^i) = B_y(q^{i+1}). \quad (4.50)$$

The system of equations Eq. (4.49), (4.50) can be solved by means of the Newton algorithm and delivers the three unknowns  $t^i$ ,  $t^{i+1}$  and  $\alpha^{i+1}$ .

## 4.3 Influence of Arbitrarily Shaped Filaments

### 4.3.1 Change of Filament Size

While investigating the influence of filaments with arbitrarily shaped cross-sections, in a first step, the dependency on the filament radius is considered. Therefore, the magnetization of a filament during a homogeneous field sweep is calculated for different filament radii. The magnetization value is multiplied with the Cu/Sc-ratio in order to obtain the same presentation as in the predecesing chapters. As could be seen from the Eqs. (4.8), (4.22) and (4.33), the magnetic induction and the resulting magnetization have a direct proportionality to the filament radius  $r_f$ .

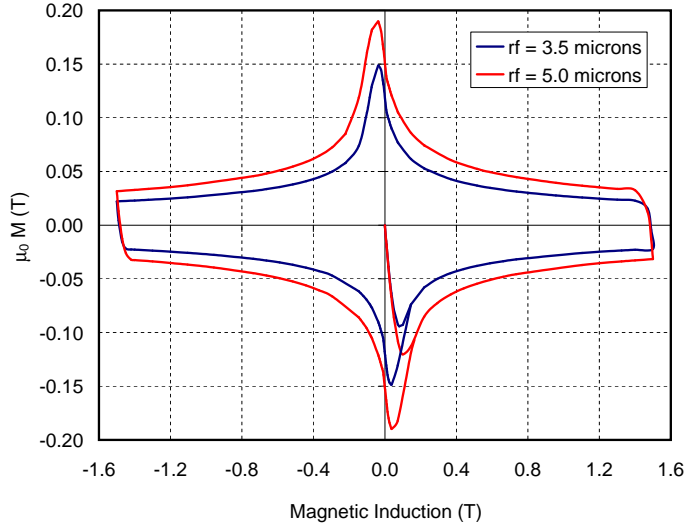


**Figure 4.21:** Calculated magnetization for a NbTi-filament with different filament radii of 3.5  $\mu\text{m}$  and 5.0  $\mu\text{m}$ . As expected, the filament magnetization directly scales with the filament radius and increases accordingly.

Figure 4.21 shows the magnetization calculated for a filament radius of 3.5  $\mu\text{m}$  and 5.0  $\mu\text{m}$ , respectively. As can be seen from the plot, the area that is outlined by the magnetization

curve grows proportionally to the filament radius, but the characteristic shape of the curve is preserved. This is a very good illustration of the fact that the shape of the curve is given by the dependency of the filament on the current fit function and supports the statement given in section 2.3 that the  $j_c$ -function has to be chosen carefully. It can also be seen that the  $B_{p1}$ -value and the  $B_p$ -value change for different radii. As is shown in section 7.4, the area being surrounded by the magnetization curve is directly proportional to the hysteresis losses experienced in the filament. Consequently, the losses during a major loop increase with an increasing filament radius as well.

It should be mentioned here that in the early literature, while treating the subject of magnetization, the filament radius has often been used as a parameter to adjust the calculated values to the measured magnetization curve. In these cases, so-called "effective filament radii" were introduced into the expression for the magnetization. By doing so, the magnetization curve can be adjusted (provided that the current fit function is well chosen), but this method cannot be recommended, since it might also blur other effects which can occur within a magnetization measurement that is taken on a strand.

### 4.3.2 Hollow Filaments

In the framework of the development of conductors for even higher fields that are foreseen for the LHC (e.g. fields up to 10 T in a dipole-type magnet), the material Nb<sub>3</sub>Sn seems to be a promising alternative to NbTi, allowing to carry a higher critical current density. Nb<sub>3</sub>Sn-filaments have a typical filament radius of around 20  $\mu\text{m}$ . They are made by means of a so-called powder-in-tube (PIT) process in which a Nb-tube is embedded into a copper-carrier and filled with Sn-powder. Considerable research in this respect has been carried out, for example, by A. Ouden et al. from the University of Twente (NL) partly in collaboration with CERN [58]. Main objectives in the development of such new Nb<sub>3</sub>Sn-filaments are the reduction of the filament radius and an improvement of the current carrying capacity. The Sn-core is reacting with the Nb-tube to Nb<sub>3</sub>Sn and this way is providing the Type II superconducting material. The center part of the core, however, will not react and stays as pure Sn. This core is measured to be in the range of 6-8  $\mu\text{m}$ , which means that from the point of the magnetization effect, the core part as not being a Type II superconductor will not contribute in carrying the critical current density and thus the filament can be considered to be "hollow". An example of such hollow filaments is presented in the cut through already shown in Fig. 4.2.

Although the main interest in using Nb<sub>3</sub>Sn-filaments is to operate at considerable higher fields than it is currently possible with NbTi, the magnetization that can be observed at low field only, is the part which interests here. Figure 4.22 shows the calculated magnetization for a Nb<sub>3</sub>Sn-filament at an operating temperature of 4.4 K for values of the inner radius of 6 and 8  $\mu\text{m}$ . The outer filament radius is chosen to be 11  $\mu\text{m}$  (green and red curve). The resulting magnetization for a massive filament is presented for comparison (blue curve).

In the same way as for a simple change of the outer filament radius (presented in the last section), different effects can be observed: Firstly, the magnetization reduces if the filament has a hollow core. This is to be expected since the maximum penetration depth which is available to the critical current is smaller in the hollow case. Consequently, the area which is surrounded by the magnetization curve reduces and thus less hysteresis losses are to be expected in the case of a hollow filament *on the major loop*. Running a minor loop, however, the situation is different. As it is explained in section 7.4, the losses are proportional to the

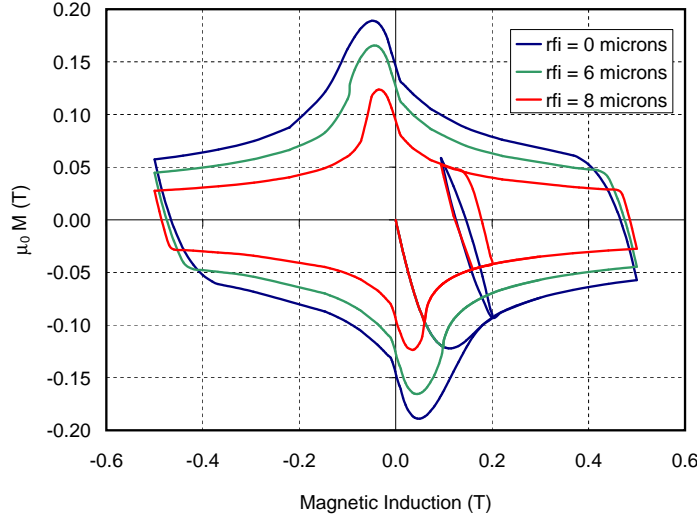


**Figure 4.22:** Calculated magnetization for a hollow  $\text{Nb}_3\text{Sn}$ -filament with different inner radii and identical outer radius. The outer filament radius is chosen to be  $11\ \mu\text{m}$  and the inner is  $6\ \mu\text{m}$  and  $8\ \mu\text{m}$ , respectively (red and green curve). For comparison, a massive filament (inner radius =  $0\ \mu\text{m}$ ) has been calculated as well. Such a filament corresponds to the ones shown in the cut through in Fig. 4.2. In addition, for the massive filament and the hollow filament with inner radius of  $8\ \mu\text{m}$ , a minor loop on the up-ramp branch is calculated.

area which is enclosed by the magnetization curve. Comparing now the minor loop of the blue curve (massive filament) with the minor loop of the red curve (hollow filament with an inner radius of  $6\ \mu\text{m}$ ), it can be seen that the area surrounded by the red curve is slightly larger than that of the blue curve<sup>5</sup>. Thus higher losses *during the minor looping* are to be expected in the second case. This observation is not pursued further, and so the difference between the two loss-values during the minor looping has not been quantified. Nevertheless, it is obvious from the curves that in the case that the magnet ramp contains a minor looping, a re-scaling of the calculated hysteresis losses, (e.g. as a function of the filament radii or the superconductor surface), will not result in correct loss values. Though a re-scaling might work on the loss calculation of an individual filament, calculated for a major loop (as it is suggested, for example, by R. Hartmann in [13]), it is not applicable for a superconducting accelerator magnet.

Finally, a considerable change in the initial state curve is observed. As can be seen from the curves, all initial state curves are identical until  $B_{p1}$  (the maximum value of the magnetization on the initial state curve) is reached. In case of the massive filament,  $B_{p1}$  and  $B_p$  are different, whereas for the two hollow filaments, these values coincide. This is due to the fact, that the hollow part does not carry any critical current and this way, the screening property (and also the resulting magnetization, of course) of the filament is limited by reaching the inner edge of the filament. Thus, the point of maximum penetration is

<sup>5</sup>In order to keep Fig. 4.22 readable, no minor loop has been calculated for an inner radius of  $6\ \mu\text{m}$ .

reached, when the critical current touches the core part of the filament<sup>6</sup>. It is also obvious that, depending on their inner radii, each filament possesses a different value for  $B_{p1}$ .

### 4.3.3 Influence of Deformed Filaments

During the production process, the filaments within one strand are usually more or less deformed, depending on their position within the bundle when they are drawn. The state of their deformation is also used as a measure of the quality of the total billet from which the filaments are taken. In general, it can be said that within one bundle of filaments, their cross-sections are not continuously deformed, thus no uniform type of filament cross-section exists [59]. It is also observed, that the shape of the filament cross-section deteriorates towards the outer border of the bundle [60], (also to be seen in Fig. 4.2). The damage of the filament's cross-sections is detected by a cut through and a micro-photographic inspection.

Deformation of the originally round filament cross-sections results in an increase of the expected magnetization and a widening of the magnetization loop. It is therefore necessary for quality insurance to quantify the expected deformations before the cable to be used in an accelerator magnet is produced.

The application of an elliptically shaped filament cross-section into the calculation of the magnetization in the Nested Ellipse Model is only possible for a homogeneous external field change. In the case of rotating fields, a circle has to be inscribed into the remaining areas (see section 4.2) in order to make the rotation in the cross-section possible within the model and thus the filament cross-section has to be round. Note, that all investigations in this section are carried out for fully penetrated filaments, only (no initial state curve is considered, here).

Though the filament cross-section will not exactly deform from a circular to an elliptic shape, assuming an ellipse shape is a good assumption which gives sufficient flexibility to model even heavily deformed filaments which are presuming a thin, flat shape. In addition, one can assume that the available area of the cross-section does not change. Following now the investigation of S. Le Naour and R. Wolf [60], there are two possible extrema for the positioning of such a deformed filament with respect to the applied field: The semi-major axis is positioned parallel or perpendicular to the external field direction (see Fig. 4.23, case I is the original round filament, in case II the semi-major axis is parallel to the external field and in case III, the semi-major axis is perpendicular to the applied field).

From Equation (3.9), the magnetization of a round, fully penetrated filament depends on the filament radius  $r_f$ , which is – at the same time – the maximum penetration distance that is available for screening. In the case of an elliptically shaped filament, the magnetization depends on the width of the semi-axis *a perpendicular* to the external field orientation (which is the  $x$ -direction in the system shown in Fig. 4.23). Therefore the resulting magnetization in the center of the filament, given in Tesla, for the three cases and in the fully penetrated state read:

$$M = \frac{4\mu_0}{3\pi} J_c \begin{cases} r_f & \text{round filament} \\ b & \text{case II filament} \\ a & \text{case III filament} \end{cases} .$$

Comparing now the magnetization of two ellipses with the same ellipticity, the same area of the cross-section, but one being upright as in case II of Fig. 4.23 and the other one flat as

---

<sup>6</sup>This is valid as long as the inner radius has a certain size; as it typically the case today, due to the production process.

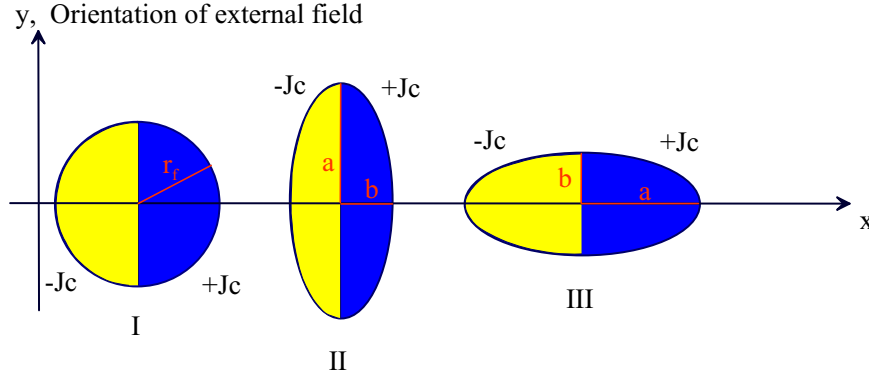


**Figure 4.23:** Deformation of filaments: It is assumed that the deformed filament can be represented by an elliptical shape. Case I: Original round filament, cases II and III: Two extreme possibilities for the positioning of the deformed filament with respect to the orientation of the external magnetic field. All filaments are in the fully penetrated state.

in case III, the differences in their magnetization will not cancel out when they are averaged, and the average results to:

$$M = \frac{4\mu_0}{3\pi} J_c \frac{a+b}{2}.$$

By keeping the cross-sectional area of the round filament for the ellipses constant,  $r_c^2\pi = ab\pi$ , the average magnetization of the two extreme cases II and III reads:

$$M = \frac{4\mu_0}{3\pi} J_c r_f \underbrace{\frac{a^2 + b^2}{2r_f a}}_{>1}.$$

Consequently, the magnetization produced by an elliptical filament will be higher than those of a circular one, if the current density is kept constant. This feature can be easily explained by plotting the screening capacity of the different filaments. Figure 4.24 shows the ratio of the calculated screening field of a filament with elliptical cross-section to the screening field of a filament with a round cross-section versus the width of the semi-axis of the elliptical filament ( $\frac{B_{\text{screen,ellipt.}}}{B_{\text{screen,round}}}$  vs.  $r_f$ , respectively  $a$  in  $\mu\text{m}$ ). The reference filament radius for the round filament is  $3.5 \mu\text{m}$ .

It can be seen from the plot, Fig. 4.24 that the resulting screening field of an elliptical filament of the "upright shape" (shown as case II in Fig. 4.23) is always smaller than the reference value of the round filament. Since the magnetic induction is divergence-free, the field produced by the filament on its outside will therefore also be smaller than the outside field of a round filament. Consequently, the resulting external field of the elliptical filament after superposition to the external source field will be smaller than the resulting field in case of the round filament. This explains, why the magnetic induction in of the elliptical filament is always smaller than that one of the round filament. The same principle is to be applied on the second part of the curve shown in Fig. 4.24, above a semi-axis of approx.  $6 \mu\text{m}$ . In the range between  $3.5 \mu\text{m}$  and approx.  $6 \mu\text{m}$ , however, the screening capacity of the

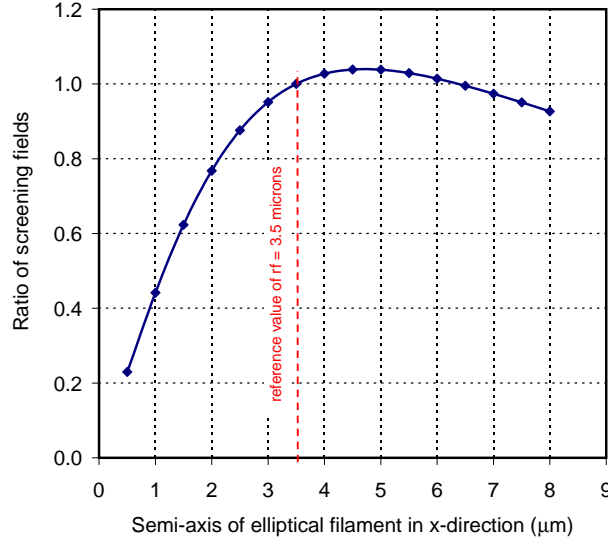


**Figure 4.24:** Screening capacity of an elliptically shaped filament with respect to a filament with a round cross-section (ratio of the calculated screening field of an elliptical filament with respect to the screening field of a round filament). The reference radius of the round filament is  $3.5 \mu\text{m}$ . The ratio is below 1 for all filaments of the case II shown in Fig. 4.23, and equals 1 when the reference radius is reached. For elliptical filaments of the "flat type" (case III in Fig. 4.23), the screening capability first increases above the reference value of the round filament and then reduces to values below.

filament with the elliptical cross-section rises above that of the round filament. In this cases, the resulting magnetization should be **smaller** than the one of the round filament. This, however is not observed from the equations for the magnetization given above. It is to be expected that this behavior is explained when a real  $J_c(B)$ -dependence is included into the equations (instead of the assumption of a constant  $J_c$ , as is taken in this sub-section). However, the aim here is to generally show that a difference in the produced screening field and the resulting magnetization between round and elliptically shaped filaments is to be expected which motivates the use of the model with intersecting ellipses instead of intersecting circles in the case of a homogeneous external field change. Thus, a further investigation is omitted here.





## Chapter 5

# Magnet Calculation and Repercussion on the External Field

In the previous chapter, the response of a superconducting filament or strand on an externally applied field and the calculation of the resulting induced magnetization (persistent currents) is described. In order to calculate the influence of these persistent currents on the field distribution in the superconducting coil of a magnet, the magnetization model has to be evaluated individually for each strand. Therefore, the model is incorporated into the field calculation program ROXIE. The ROXIE package is a numerical field calculation program which has been created by Stephan Russenschuck at CERN. ROXIE stands for the **R**outine for the **O**ptimization of magnet **X**-sections, **I**nverse field calculation and coil **E**nd design. Implementing the persistent current model allows the use of the existing ROXIE subroutines, for example, the routine for the determination of the exact position of the individual strands in the cross-section or the algorithm for the evaluation of the multipoles from a calculated field configuration. Also, the routines for magnet optimization, for the calculation of excitation curves and the graphical packages are used. In addition, the ROXIE program includes advanced numerical field solvers which allow the precise calculation of the contribution of non-linear iron domains to the resulting coil field. Iron domains can be, for example, the yoke structure of a superconducting magnet. All two-dimensional (2D) ROXIE features applicable for the superconducting magnet design can now be carried out including the persistent current calculation. This allows to incorporate the effects from the induced coil magnetization from start on into the design process for superconducting magnets. Due to the repercussion of the persistent current fields on the field which arises from transport currents only, the superposition of these two field contributions has to be solved iteratively. The field distribution in the coil cross-section which results from this M(B)-iteration is then the input value for the calculation of the magnetization of the ferromagnetic parts in the magnet.

At this point, and before the M(B)-iteration can be applied, the user has to decide about which part of the magnet structure has to be incorporated into the iteration and whether the M(B)-iteration influences the magnetization of the ferro-magnetic domains. In the case of magnet geometries, in which the distance between the coil and the inner yoke radius is large, it is often sufficient, to iterate the source currents and the persistent currents in the coil, only. This way, the repercussion of the superconductor magnetization on the field which is resulting only from the source currents, is considered. After convergence in the M(B)-iteration, the yoke contribution can be determined from the fields of this iterated current distribution in

the coil and can then be added in a final step.

However, in the case of coil geometries which include very thin non-linear and highly permeable regions in the cross-section of a magnet, such as tuning shims, for example, their influence can lead to a change in the local field distribution in each step of the iteration of source currents and persistent currents. This change then causes a change in the excitation field of the persistent currents. In such cases, the re-calculation of the iron magnetization has to be carried out in each step of the M(B)-iteration.

In this chapter, first the necessity of the iteration procedure is illustrated by means of calculating the repercussion of the persistent current fields on the source fields. Then the iteration method is presented. The iteration is carried out by means of a fixed point iteration and is combined with a relaxation method in order to accelerate and stabilize the convergence. The relaxation method is investigated and the above-mentioned different possibilities, of applying the M(B)-iteration on a magnet geometry, are discussed.

## 5.1 The M(B)-Iteration

For a precise determination of the field in the coil, an M(B)-iteration is necessary to consider the repercussion of the induced magnetic induction on the external field. From the fact that the field quality in a superconducting magnet is mainly determined by the coil shape and the current distribution in the coil cross-section, it is obvious that the changes in the current distribution in the cross-section which result from the field repercussion have to be considered. As for persistent currents in general, the influence of the repercussion plays an important role especially at very low fields.

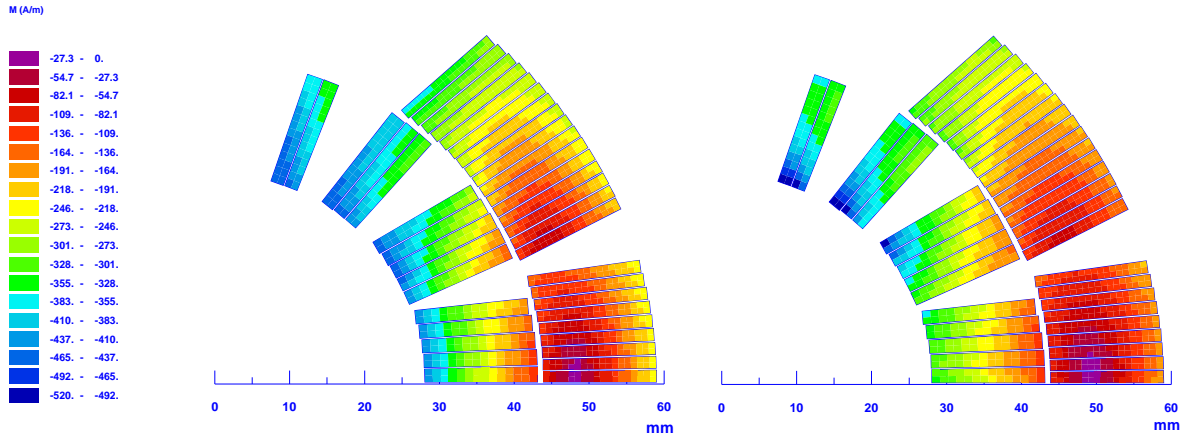


**Figure 5.1:** Magnetization in the first quadrant of the cross-section of a dipole coil computed without M(B)-iteration (left) and with M(B)-iteration (right) at low excitation currents. Without the iteration, the repercussion of the magnetic field produced by the induced persistent currents on the external field cannot be considered.

Figure 5.1 shows the coil magnetization in the first quadrant of a dipole coil arising for low excitation currents. The magnetization has been calculated with and without the field repercussion in order to illustrate the necessity of the iteration. A more detailed evaluation is given in section 5.8 at the end of this chapter.

The plots clearly show the changes in the local distribution of the magnetization in all coil blocks. The calculation has been performed for a very low current *on the initial state curve*. In this case, the amount of induced superconductor magnetization is directly proportional to the applied field and a region of low magnetization is presented by the dark red and purple spot close to the abscissa, where a field drain is located. As is shown in chapter 5.8, exemplery for a superconducting tuning quadrupole (the so-called MQTB), the location of this area of low fields moves with increasing current. Two reasons exist for this behavior. Firstly, small saturation effects occur along the inner yoke structure. Although these have only little influence on the magnetic induction at low field, they make a significant difference for the magnetization since even small changes in the magnetic field result in considerable changes of the magnetization due to the steep slope in the  $J_c(B)$ -curve. For the same reason, the region of low magnetization also moves outwards with respect to the beam center and enlarges if iterations are performed.

Generally, this phenomenon can be described as follows: In a first step, the applied external induction increases when superimposed with the induced field from persistent currents. This results in an increase of the superconductor magnetization in the low field region due to the fact that the initial state curve is calculated. Thus, the area of low magnetization close to the abscissa reduces (illustrated in the plot presented on the left side which is resulting from the calculation without iteration. With the use of the iteration, the increase in the external magnetic induction is considered after each superposition and iteration with the persistent current field. The result is that the external field does not rise with the same amount as it does in the case of no iteration. Therefore, a reduction of induced screening currents is observed. Hence, the magnetic field resulting from these induced (persistent) currents reduces, causing an increase of the region of low induction and therefore also yields in the observed increase of the size of the area of low magnetization, and so on. This process can be derived from considering a single filament and also applies to the entire coil cross-section. It can be accounted for by iterating the field components. These iterations are carried out by means of a fixed point iteration, a numerical principle which is explained in the next section.

## 5.2 Fixed Point Iteration

The iteration is carried out by means of a fixed point iteration and has been implemented into the ROXIE program. Fixed point iterations are generally used for solving systems of non-linear equations. The system is expressed by means of the so-called fixed point notation:

$$\mathbf{x} = \mathbf{F}(\mathbf{x}), \quad (5.1)$$

$$\text{where } \mathbf{x} = \begin{pmatrix} x_1 \\ \vdots \\ x_n \end{pmatrix}, \quad \mathbf{F}(\mathbf{x}) = \begin{pmatrix} f_1(\mathbf{x}) \\ \vdots \\ f_n(\mathbf{x}) \end{pmatrix} \quad (5.2)$$

where  $\mathbf{x}$  denotes the fixed point and  $\mathbf{F}(\mathbf{x})$  the fixed point map which may be non-linear. The solution of this equation maps easily in the  $\mathbb{R}^2$  by searching for the intersection point between  $y(x_i) = x_i$  and  $f_i(\mathbf{x})$ . The method converges due to the self-mapping feature of the function  $y(x) = x$ . The iterative sequence reads:

$$\mathbf{x}^{(i+1)} := \mathbf{F}(\mathbf{x}^{(i)}) \quad \forall i \in \mathbb{N}, \quad (5.3)$$

where the entity  $(i)$  denotes the iteration step.

In general, the exact determination of a fixed point is rare [61]. However, in case an approximate value  $\mathbf{x}^{(i)}$  of the exact solution  $\mathbf{x}^*$  is known, one can calculate a new value by exercising Eq. (5.1). It can then be determined by means of estimating the *distance*, whether the value thus found is closer to the exact solution or not. In the case that the solution is closer, the distance between the function value in the actual step  $\mathbf{F}(\mathbf{x}^{(i)})$  and the true value  $\mathbf{x}^* = \mathbf{F}(\mathbf{x}^*)$  should be smaller than the distance between the function value in the last step  $\mathbf{x}^{(i-1)}$  and the true value  $\mathbf{x}^*$ . The distance is given by means of the mapping

$$d : \mathcal{R} \times \mathcal{R} \rightarrow \mathbb{R}$$

which means that  $d(\mathbf{x}, \mathbf{y})$  can be called the distance function. The distance function has to fulfill the following conditions:

$$\begin{aligned} d(\mathbf{x}, \mathbf{y}) &= 0, \text{ if and only if } \mathbf{x} = \mathbf{y} \\ \text{otherwise, } d(\mathbf{x}, \mathbf{y}) &> 0 \end{aligned} \quad (5.4)$$

$$\text{and } d(\mathbf{x}, \mathbf{y}) \leq d(\mathbf{x}, \mathbf{z}) + d(\mathbf{y}, \mathbf{z}), \quad (5.5)$$

which means that the distance function is fulfilling the triangle inequality. Consequently, the distance  $d$  denotes an unequivocal correlation in space (for example, the length of a vector between two positions). Here, the Euclidean Norm will be used as a distance function:

$$\|\mathbf{x}\| = \sqrt{\sum_{p=1}^n |x_p|^2}.$$

It follows from the triangle inequality, Eq. (5.5) that  $d(\mathbf{x}, \mathbf{y})$  is a continuous function of its arguments, and hence:

$$\begin{aligned} \mathbf{x}_n &\rightarrow \mathbf{x}_0 \text{ and} \\ \mathbf{y}_n &\rightarrow \mathbf{y}_0 \\ \Rightarrow d(\mathbf{x}_n, \mathbf{y}_n) &\rightarrow d(\mathbf{x}_0, \mathbf{y}_0). \end{aligned} \quad (5.6)$$

Applying now the iterative sequence of Eq. (5.3), on an arbitrary starting point  $\mathbf{x}^{(1)}$ , for the determination of a fixed point  $\mathbf{x}^*$ , allows the evaluation of an error for the next value  $\mathbf{x}^{(2)}$ . The use of the distance function yields:

$$d(\mathbf{x}^{(2)}, \mathbf{x}^*) = d(F(\mathbf{x}^{(1)}), F(\mathbf{x}^*)),$$

or, more general:

$$d(\mathbf{x}^{(i+1)}, \mathbf{x}^*) = d(F(\mathbf{x}^{(i)}), F(\mathbf{x}^*)).$$

In any case, if the error is smaller in the new step, the function contracts. With other words: An iterative mapping function  $\mathbf{F}$  is denoted as a contractive mapping function, in case there is a number  $k < 1$ , holding such that:

$$d(\mathbf{F}(\mathbf{x}), \mathbf{F}(\mathbf{y})) \leq k \cdot d(\mathbf{x}, \mathbf{y})$$

or in our case:

$$\|\mathbf{F}(\mathbf{x}) - \mathbf{F}(\mathbf{y})\| \leq k \cdot \|\mathbf{x} - \mathbf{y}\|.$$

This means that the error arising in the actual  $(i + 1)$ -th step is weighted by means of the above explained 'distance' with respect to the true value  $d(\mathbf{x}^{(i+1)}, \mathbf{x}^*) = d(\mathbf{F}(\mathbf{x}^{(i)}), \mathbf{x}^*)$

and is smaller than the error resulting from the last step in case of a contraction mapping (so-called Lipschitz Criterion). In the case of strong contraction mapping, it is possible to perform an error estimation by means of the Contraction Mapping Theorem. The special feature of the distance function of  $d(\mathbf{x}, \mathbf{y}) > 0$ , Eq. (5.5) ensures, together with Eq. (5.6) that the iteration can converge to one fixed point only. Following [62], the existence of an additional fixed point  $\mathbf{y}^*$  would yield (due to the contraction mapping of the function) to  $\|\mathbf{F}(\mathbf{x}^*) - \mathbf{F}(\mathbf{y}^*)\| = \|\mathbf{x}^* - \mathbf{y}^*\| \leq k \|\mathbf{x}^* - \mathbf{y}^*\|$ . However, since  $k \leq 1$ , this equation holds only in case  $\|\mathbf{x}^* - \mathbf{y}^*\| = 0$ , this is  $\mathbf{x}^* = \mathbf{y}^*$ . Thus, no second fixed point can exist if the above-mentioned conditions are fulfilled.

### 5.3 General Termination Criterion for the Iteration

In general, the iteration can be terminated when the changes between the iteration steps are sufficiently small (so-called absolute error estimation or absolute termination decision), which means that the changes are smaller than a certain value  $\varepsilon \in \mathbb{R}$ :

$$\|\mathbf{x}^{(i)} - \mathbf{x}^{(i-1)}\| < \varepsilon. \quad (5.7)$$

It is customary here, to use a relative residual,  $\delta$  for the termination decision:

$$\frac{\|\mathbf{x}^{(i)} - \mathbf{x}^{(i-1)}\|}{\|\mathbf{x}^{(i)}\|} < \delta \quad \text{where } \delta \in \mathbb{R}. \quad (5.8)$$

The precise values for  $\varepsilon$  and  $\delta$  depend on the accuracy that can be obtained in the calculation.

### 5.4 The Relaxation Method

The relaxation method is used to accelerate and stabilize the convergence of the iteration. Figure 5.2 exemplary shows the principle of the relaxation method applied on an oscillating function. There, the relaxation starts when the third iteration step is calculated, hence the function values for the first and the second step are identical for the two cases with/without iteration. When calculating the function value in the actual step, the relaxation causes a displacement of the calculated value towards the (estimated) true value. The individual relaxation methods differ generally in the determination of the relaxation factor, the frequency by which the relaxation is applied and at which iteration step the relaxation starts. Relaxation methods can be applied to all functions presuming a contractive mapping. This means that, during the calculation, the fulfillment of the Lipschitz Criterion has to be provided for.

Two different relaxation methods according to the works of S. Kurz [63] and I. Hantila [64] have been programmed. They mainly differ in the choice between applying the relaxation factor of the iteration in each step or in every second step. For the special case of magnet calculation, the method of Kurz proved to be faster and is therefore implemented in the ROXIE program. The relaxation method consists in the calculation of the relaxation factor  $\omega$  applied to a non-linear system of equations given in fixed point notation:

$$\omega^{(1)} = 1 \quad \text{as starting value} \quad (5.9)$$

$$\begin{aligned} \omega^{(i)} &= \omega^{(i-1)} \left( 1 - \frac{[\mathbf{F}(\mathbf{x}^{(i-1)}) - \mathbf{x}^{(i-1)}] \cdot [\mathbf{x}^{(i-1)} - \mathbf{x}^{(i-2)}]}{[\mathbf{x}^{(i-1)} - \mathbf{x}^{(i-2)}] \cdot [\mathbf{x}^{(i-1)} - \mathbf{x}^{(i-2)}]} \right)^{-1} \\ \mathbf{x}^{(i)} &= \mathbf{x}^{(i-1)} + \omega^{(i)} [\mathbf{F}(\mathbf{x}^{(i-1)}) - \mathbf{x}^{(i-1)}]. \end{aligned} \quad (5.10)$$

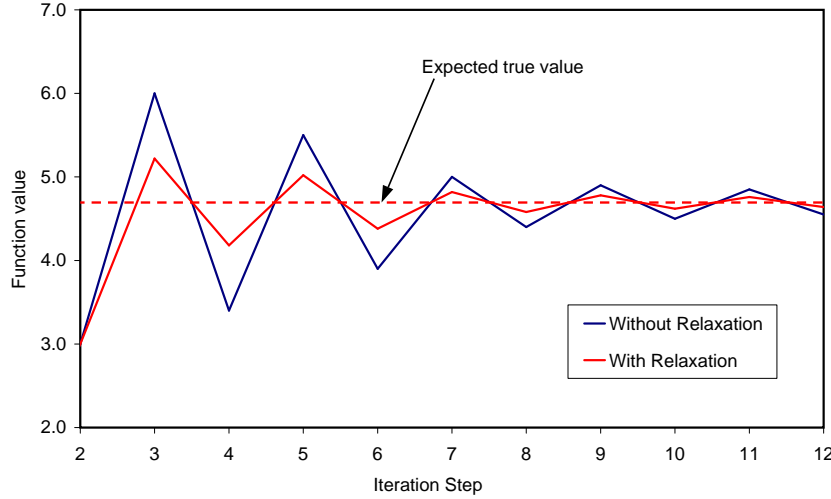


**Figure 5.2:** Principle of the Relaxation method for convergence acceleration and stabilization.

The formula for the calculation of the relaxation factor simplifies considerably in the case of a scalar contractive mapping:

$$\omega^{(i)} = \omega^{(i-1)} \left( 1 - \frac{F(x^{(i-1)}) - x^{(i-1)}}{x^{(i-1)} - x^{(i-2)}} \right)^{-1}. \quad (5.11)$$

As for the case of a global mapping, Eq. (5.10), at least two steps have to be calculated before the first relaxation factor can be determined, thus the earliest application of the relaxation can be carried out in the third step.

## 5.5 The ROXIE Interface

For the calculation of superconducting magnets, different contributions to the main field component and the higher multipole components exist and have to be taken into account by superposition. The main contribution is arising from the source currents in the coil (source field) to which the effect of the magnetization of the non-linear iron yoke has to be added. It is clear that the contribution of the iron yoke to the main field and the field errors is much smaller than that of the source currents and that the value of the iron contribution also depends on the actual current strength in the coil. The non-linear behavior of the iron domains can only be considered by means of numerical field calculation. In the case of the LHC dipole, the contribution of the surrounding iron yoke to the main field component amounts to about 20% of the total field. In addition, the yoke starts to saturate for higher source currents and influences the field errors due to these saturation effects.

The ROXIE program offers the user to chose from various methods for the numerical field calculation, of which two are of special interest in the framework of this thesis. These are the coupled boundary element/ finite element method [65] (the so-called BEM-FEM method) and the classical finite element method [66] (FEM), which, in the ROXIE program, applies a reduced vector potential [67] for the field calculation. All numerical solvers implemented in the ROXIE program have one feature in common that is: They avoid the meshing of the

superconducting coil and restrict the finite element mesh to the iron domains only (as is the case when the BEM-FEM method is used). In the case of the use of the finite element method, also the air domains are meshed, but due to the use of the reduced vector potential, the meshing of the coil geometry can still be avoided.

It has been shown in various publications [38], [68] that it is advantageous, if the coil does not have to be modelled in finite elements, since the field quality in the aperture of a superconducting<sup>1</sup> magnet is dominated by the layout of the coil cross-section and the distribution of the current in the coil. It is this sensitivity to the coil geometry that produces several difficulties (amongst others) in case the coil is to be a part of the finite element mesh:

- The mesh has to be such as to model the coil geometry with an extreme accuracy. Even small geometric effects such as the alignment on the winding mandrel, the exact keystoneing of the cable, the insulation thickness and the shrinking of the coil due to cool down have to be reproduced. This usually results in a very dense mesh in the area of the coil which in turn yields an immense increase in the necessary number of finite elements.
- In case the mesh is adopted dynamically, the change in mesh size from the very small finite elements which are necessary in the coil region to the relatively big elements in the air domain above the outer yoke radius requires an advanced solver for the handling of the resulting system of equations.
- Due to the keystoneing of the cable, the cable compaction changes and so does the current density in the cable. This grading of current density in the radial direction has to be considered and presents a formidable task in using finite elements.
- For the calculation of the coil magnetization and the persistent current effects, the meshing of the cable has to be filament-wise if a numerical method, as listed in chapter 1, is to be used. If a method similar to the Nested Ellipse method is developed, the magnetization results have to be fed back into the finite element mesh of the coil current distribution in order to consider the persistent current effects. This feed-back has to be done iteratively until a steady state solution is reached.
- Compensations of persistent current effects in superconducting magnets are carried out mostly by inserting small ferromagnetic shims or passive (non-powered) superconductors into the coil aperture or close to the coil geometry (as, for instance, attachment of a shim on the outer coil radius). This means that often only a very small gap between the shims and the coil remains (some micrometers), which has to be meshed. In addition, the shim itself has a typical width of some tens of a millimeter.
- Further, a numerical error is also arising from the coil geometry, and not only from the iron yoke calculation (as is the case in the ROXIE program), if the coil is a part of the finite element mesh, and
- the optimization of coil geometries can become difficult, if the mesh has to be changed, since this can result in an additional numerical error.

---

<sup>1</sup>This is one of the main differences between superconducting and conventional magnets, from the field quality point of view. In a conventional magnet, the field quality in the aperture is determined by the shape of the yoke in the magnet cross-section and is relatively insensitive to coil positioning errors. For superconducting magnets, however, the field quality in the magnet aperture is mainly defined by the coil and is less sensitive (but not completely insensitive) to manufacturing errors on the yoke.

It should be emphasized here, that the developed Nested Ellipse model for the superconductor magnetization is semi-analytic and thus follows the ROXIE principle.

### 5.5.1 The Combination with the BEM-FEM Coupling Method

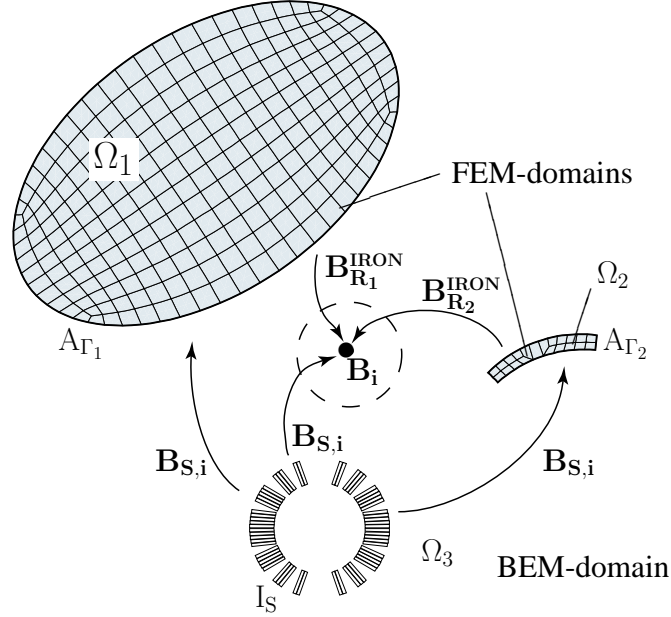


**Figure 5.3:** Elementary model problem for BEM-FEM computation of superconducting magnets. The BEM-FEM area encompasses the air domain  $\Omega_3$  where the superconducting coil and the evaluation point is positioned. The source currents  $I_s$  in the coil act on the different magnetic subdomains  $\Omega_1$  and  $\Omega_2$  (partially non-linear). In the case of computation of superconducting magnets, the evaluation point is located inside the aperture of the magnet in the air domain (symbolized by the dashed circle). The magnetic field in the evaluation point comprises contributions of the non-linear iron yoke (here: subdomain  $\Omega_1$ ), the thin soft magnetic iron sheet (here: subdomain  $\Omega_2$ ) and the superconducting source currents. The magnetic domains may be of arbitrary shape.

Figure 5.3 shows the elementary model problem for the BEM-FEM computation. As can be seen in the figure, the computing area of a superconducting accelerator magnet comprises different domains. In case of the BEM-FEM method, the superconducting coil is positioned inside the non-meshed air domain (boundary element domain)  $\Omega_3$ . Additional magnetic subdomains of different material parameters ( $\Omega_1$  and  $\Omega_2$ ) exist and have to be discretized in finite elements as well. These magnetic subdomains can be arbitrarily shaped and can present a coil protection sheet or tuning shims, for instance. Non-linear material parameters are allowed for all subdomains. The evaluation point is positioned in the boundary element domain, which is free from magnetic material and source currents (symbolized by the dashed circle). During magnet calculation, this is where the radius of the harmonic analysis is



positioned. Only the magnetic domains have to be meshed in finite elements.

The field arising from the superconducting coil can be computed analytically by means of the Biot-Savart's Law, since the coil is positioned in the air subdomain  $\Omega_3$  of the BEM-FEM area. Single currents in the coil are accurately described by single line currents at the position of the superconducting strands in the coil cross-section. From the source currents, the source vector potential  $A_\Gamma$  on the coupling boundary between the FEM domains and the air domain is determined. The resulting vector potentials  $A_{\Gamma_1}$  and  $A_{\Gamma_2}$  are found from the iterative solution of the system of linear equations that results from the BEM-FEM coupling method. In this case, the right-hand side of the system of equations is the vector potential  $A_{\Gamma_S}$ , which can again be calculated by Biot-Savart type integrals [63]. The reduced magnetic inductions  $\mathbf{B}_{R_1}$  and  $\mathbf{B}_{R_2}$  can be computed by means of Kirchhoff-Integrations, once the  $A_\Gamma$  are determined. The magnetic induction at the evaluation point is found by superimposing the source field  $\mathbf{B}_s$  and the iron contributions  $\mathbf{B}_{R_i}$ .

In the case of the LHC main dipoles, about 20% of the total field in the aperture is contributed by the magnetization of the iron yoke structure. Since the BEM-FEM coupling method computes the source fields analytically, the numerical errors are restricted to this numerically computed 20 % of the field arising from the iron yoke.

### 5.5.2 The Combination with the Finite Element Method

The use of a reduced vector potential formulation (which is described in this section) is another possibility besides the BEM-FEM method, that allows the coil to be excluded from the mesh in FEM area. Contrary to the BEM-FEM method, the air domain is meshed in finite elements. In the case of the FEM, the superconducting coil is positioned in the air domain, however, meshing of the coil can be avoided, since that part of the field which is resulting from the source currents, is not determined from a vector-potential, but is calculated by means of the Biot-Savart's Law.

The field which is due to the iron magnetization is then expressed by the curl of a *reduced* vector potential:

$$\mathbf{B} = \mu(\mathbf{B})\mathbf{H} = \mu_0\mathbf{H}_s + \mu_0\mathbf{H}_r = \mu_0\mathbf{H}_s + \nabla \times \mathbf{A}_r \text{ in } \Omega. \quad (5.12)$$

This formulation corresponds to  $\mathbf{B} = \nabla \times \mathbf{A}_{\text{tot}} = \nabla \times (\mathbf{A}_s + \mathbf{A}_r)$ , where  $\mathbf{A}_{\text{tot}}$  denotes the commonly used total vector potential. The magnetic field from the source currents reads:

$$\mathbf{H}_s(\mathbf{r}) = \frac{1}{4\pi} \int_{\Omega_s} \frac{\mathbf{J}(\mathbf{r}_q) \times \mathbf{r}}{r^3} d\Omega. \quad (5.13)$$

The vector  $\mathbf{r}$  is the distance vector from the source point to the field evaluation point. From Equation (5.12), a differential equation for the reduced vector potential  $\mathbf{A}_r$  is derived, which only contains the vector potential and the (known) source field  $\mathbf{H}_s$ .

Apart from that, the field quantities have to fulfil two different types of boundary conditions on the surface  $\Gamma$ . This surface is divided in two sections,  $\Gamma_B$  and  $\Gamma_H$ . On  $\Gamma_B$ , the normal component of the magnetic induction and on  $\Gamma_H$  the tangential component of the magnetic field are prescribed. The boundary  $\Gamma_B$  is often denoted the "Dirichlet-boundary" on which, in many cases, the normal component of the magnetic induction vanishes. This is the case, for instance, on symmetry planes parallel to the field or on the so-called far-field boundary condition on the outer border of the air domain. On the other part of the boundary,  $\Gamma_H$ , the tangential component of the magnetic field also vanishes for some cases. This boundary  $\Gamma_H$

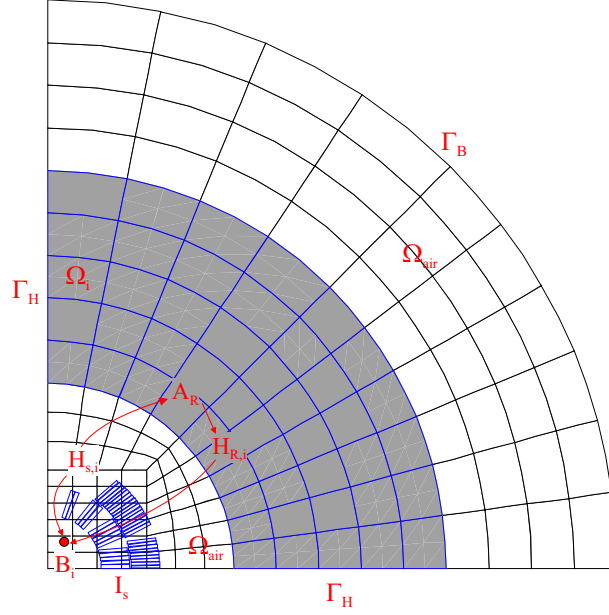


**Figure 5.4:** Elementary model problem for FEM computation of superconducting magnets making use of a reduced vector potential formulation  $\mathbf{A}_r$ . The FEM area encompasses the air domain  $\Omega_{air}$  where the superconducting coil and the evaluation point is positioned. The source currents  $\mathbf{I}_s$  in the coil act on the magnetic subdomains  $\Omega_i$  (presenting the yoke which is non-linear). In the case of computation of superconducting magnets, the evaluation point is located inside the aperture of the magnet in the air domain. The magnetic field in the evaluation point comprises contributions of the iron yoke and the superconducting source currents. The magnetic domains may be of arbitrary shape.

is often denoted the "Neumann-boundary" and the tangential field vanishes, for example, on symmetry planes perpendicular to the field. These boundary conditions can be summerized as:

$$\mathbf{B} \cdot \mathbf{n} = -b \text{ on } \Gamma_B \quad (5.14)$$

and

$$\mathbf{H} \times \mathbf{n} = \mathbf{K} \text{ on } \Gamma_H, \quad (5.15)$$

where  $\mathbf{K}$  is a surface current distribution and  $b$  a fictitious magnetic charge density. The vector  $\mathbf{n}$  is the outer normal vector on the surface  $\Gamma$ , while  $\Gamma_B$  and  $\Gamma_H$  are disjoint parts of the entire boundary as shown in Fig. 5.4. The fictitious magnetic surface charge density can be used for the modeling of known magnetic flux distributions, for instance. In the application of the reduced vector potential, the known boundary conditions, given in the Eqs. (5.14) and (5.15) have to be expressed for the reduced vector potential (instead of the field vectors).

On any surface between two regions with different magnetic properties, the field quantities have to fulfil interface conditions: The continuity of the tangential component of  $\mathbf{H}$  and the

continuity of the normal component of the magnetic induction.

For 2D calculations, the vector potential has only one component  $\mathbf{A}_r = A_z(x, y)\mathbf{e}_z$  that can be set in  $z$ -direction. It therefore automatically satisfies the Coulomb Gauge and thus is unique, making any further gauging procedure unnecessary. In the program package ROXIE, the use of this ungauged reduced vector potential is implemented for the field calculations in the plane. It offers the possibility to separately calculate the excitation field due to the current in the coils and the reduced field due to the iron magnetization. Therefore it is possible to calculate the peak field in the coils with required high accuracy. For details on the reduced vector potential see [37], [67]. A description of the implementation into the ROXIE program can be found in [52], [69], for example.

## 5.6 Implementation and Conversion in ROXIE

The method used for the calculation of the magnetization of a superconducting filament/strand in the field computation program ROXIE considers the repercussion of the magnetic induction resulting from the induced persistent currents  $\mathbf{B}^{\text{PERS}}$ .

The structure of the iteration reads as follows:

$$\mathbf{B}^{(i-1)} \rightarrow \mathbf{M}^{\text{PERS},(i-1)} \rightarrow \mathbf{B}^{\text{PERS},(i-1)} \rightarrow \underbrace{\mathbf{B}^{\text{IRON},(i-1)}(\mathbf{B}^{\text{PERS},(i-1)})}_{\text{optional}} \rightarrow \mathbf{B}^{(i)},$$

and thus presents a fixed point iteration method:

$$\mathbf{B}^{(i)} = \mathbf{F}(\mathbf{B}^{(i-1)}) \quad \text{with } i \in \mathbb{N}.$$

The superscript index  $(i)$  denotes the actual iteration step and each strand is calculated separately. In a first step, the magnetic induction,  $\mathbf{B}^{(i-1)}$ , as a function of the actual  $(i-1)^{\text{th}}$  iteration step, according to its local strand position, is calculated. From this, the calculation of the induced persistent currents and the resulting strand magnetization  $\mathbf{M}^{\text{PERS},(i-1)}$  is possible, as is described in section 4.1. Also the magnetic induction  $\mathbf{B}^{\text{PERS},(i-1)}$  produced by the persistent currents, is calculated. The total field results from a superposition of the magnetic field from the source currents in the coil and the persistent current field. The outcome results in a change in the originally assumed field distribution.

Depending on the vicinity of iron parts (as the yoke or shims) and the state of saturation in the individual parts, it is necessary to consider the influence of the persistent currents on the field distribution inside the ferromagnetic parts in each iteration step by performing a re-calculation of the iron magnetization and the resulting field  $\mathbf{B}^{\text{IRON},(i-1)}(\mathbf{B}^{\text{PERS},(i-1)})$ .

The existence of very thin non-linear and highly permeable domains, in the aperture of a magnet, for example, may lead to a change in the local field distribution. This change then causes a change in the excitation field for the persistent currents and results in the production of unwanted multipoles. In such cases, the re-calculation of the iron magnetization by using the numerical solver a second time is inevitable in each step of the iteration.

The outline of the M(B)-iteration and the feed-back of the superconducting filament magnetization are shown in detail by means of a flow-chart in Fig. 5.5. The entities in the diagram are as follows:  $I_s$  presents the total current (source current) driven during the magnet cycle while  $I_n$  is the individual transport current in single strands.  $\mathbf{B}_{S,k}$  is the source field at the  $k^{\text{th}}$  strand position and is calculated by means of the Biot-Savart's Law.  $A_r$  is the  $z$ -component of the vector potential on the coupling boundary from the BEM-FEM coupling

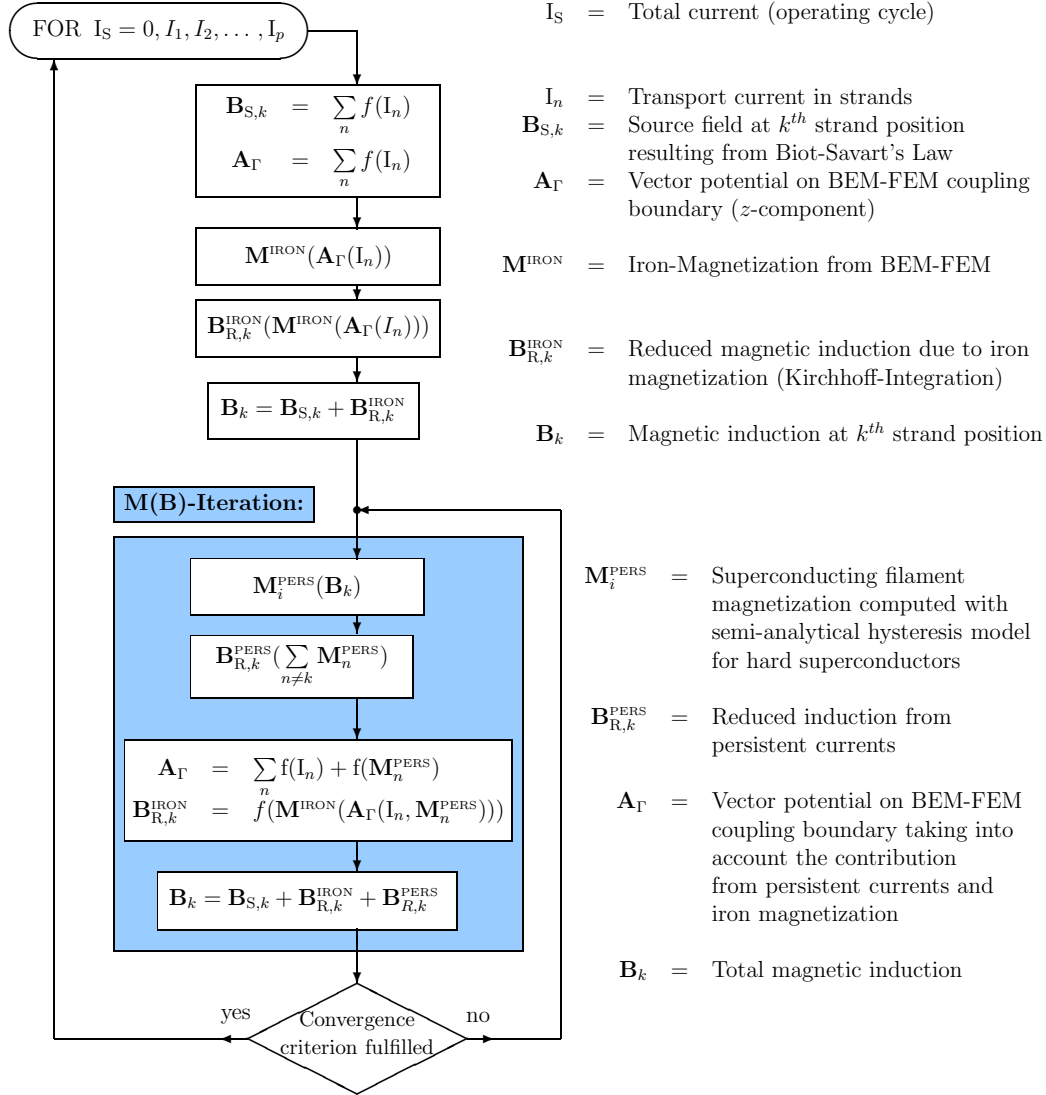


**Figure 5.5:** Algorithm for the calculation of persistent currents as incorporated in the field computation program ROXIE. The blue part shows the M(B)-Iteration to be carried out in order to consider the repercussion of the persistent current produced field on the externally applied field. The flow chart exemplary shows the interfacing with the BEM-FEM method. In the ROXIE program, the method is combined with a classical FEM method as well

method. From these vector potentials, the entity  $M^{\text{IRON}}$ , the magnetization arising from the surrounding ferromagnetic (iron) yoke is calculated. The magnetization is defined as the magnetic moment per unit volume.  $B_{R,k}^{\text{IRON}}$  denotes the reduced magnetic induction due to the iron magnetization and is computed by solving Kirchhoff's integrals. Hence, the magnetic induction,  $B_k$ , of the  $k^{\text{th}}$  strand position is obtained by superposing the source field and the reduced field arising from the iron magnetization.

The superconductor filament magnetization is calculated from the magnetization model.

This magnetization is the source of the reduced induction  $\mathbf{B}_{R,k}^{\text{PERS}}$ . The induced fields from the persistent currents are superimposed to the fields from the source currents, resulting in an updated vector potential  $A_{\Gamma}$  on the BEM-FEM boundary and a change in  $\mathbf{B}_k$ , the magnetic induction at the  $k^{\text{th}}$  strand position. Iterations with the source fields which are up-dated in this way are performed repeatedly until convergence is obtained.

### 5.6.1 The Iteration Function

The iteration function of the M(B)-iteration is given as a non-linear hysteresis function. The dependence of the superconductor magnetization on the externally applied field is only given indirectly, by means of the function for the critical current density  $J_c$ . For the calculation of the magnetization, the  $J_c$ -distribution is determined explicitly from the fit in the individual steps as is described in section 2.3. Therefore, the fulfillment of the Lipschitz Criterion cannot be proven for the complete calculation range. However, the Lipschitz Criterion is checked explicitly in each step of the iteration in the case the relaxation is used. The following expression is used for the point-wise testing of the Lipschitz constant:

$$\lambda = \frac{|\mathbf{B}^{(i)} - \mathbf{B}^{(i-1)}|}{|\mathbf{B}^{(i-1)} - \mathbf{B}^{(i-2)}|} < 1 \quad (5.16)$$

If the criterion is once violated<sup>2</sup> with  $\lambda \geq 1$ , the relaxation in the actual step is reversed and is not further used in the iteration steps. As long as the Lipschitz Criterion is fulfilled, the iterated values will be relaxed by applying the Eqs. (5.9) to (5.10).

### 5.6.2 Termination Criterion in ROXIE

The convergence is decided by the relative termination criterion given in Eq. (5.7). This procedure leads to numerical problems, if the iterated field values reach an interval close to zero. In this case, the termination criterion is immediately switched to the absolute criterion given in Eq. (5.8).

### 5.6.3 Local and Global Method of the Relaxation

The calculation of the induced magnetization in a superconducting coil of an accelerator magnet depends on the local field distribution and therefore on the position of the strand in the coil cross-section.

Figure 5.6 shows the distribution of the magnetic induction calculated for an excitation current of 600 A (left) and the amount of induced magnetization in the superconducting strands (right), resulting from the field distribution on the left-hand side. As can be seen from the plots, strands in the outer layer of the coil (close to the abscissa) experience lower fields (dark blue regions), whereas filaments in the inner coil layer are affected by a higher field (red and purple regions). However, during magnet up-ramp, the field variation is bigger in the outer coil layer since the low field regions (field drains) move outwards with increasing yoke saturation. It is also observed that even at nominal field there are filaments in the coil cross-section remaining still non-fully penetrated.

---

<sup>2</sup>A violation of the Lipschitz Criterion is no proof that the iteration with an applied relaxation method will not converge, whereas convergence is ensured as long as the criterion holds.

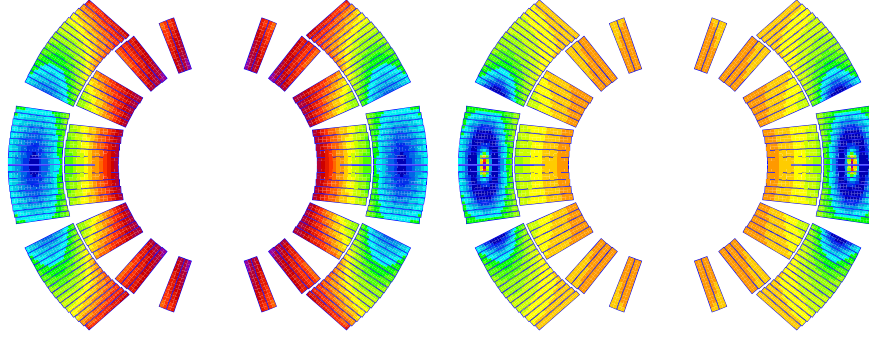


**Figure 5.6:** Left: Amount of magnetic induction inside the superconducting coil. Regions in blue indicate the low field region, whereas areas with high field levels are indicated in red. From the dipole geometry, two low field levels (field drains) exist in the coil cross-section. Right: Superconductor magnetization resulting from the magnetic induction. The magnetization is highest in the region of the field drains, as is indicated in red.

This means that for each strand an individual history has to be stored. The factor by which the field changes will also influence the convergence behavior in the calculation of the individual strands. Experience shows that in the iteration, some strands converge faster than others. In general, one can expect that the iteration of strands which experience low fields will converge considerably slower than those exposed to a high external magnetic induction. The intention of the local method is to make use of this behavior in order to save computing time.

### Local Method of Relaxation

The local method of relaxation makes use of a local convergence criterion which assumes that the convergence behavior of the individual strands is independent from each other. In this case, the single vector components of the applied magnetic induction  $\mathbf{B}$  of the  $N$  strands are treated independently as  $N$  scalar fixed point iterations and the relaxation method is applied locally on the strands:

$$k \in \mathbb{N} : B_i^{(i)} = F_i(B_i^{(i-1)}) \quad \text{with } i = 1 \dots N.$$

This relaxation factor is then calculated by means of Eq. (5.11).

At the end of each iteration step, some strands (number  $n$  of  $N$  existing strands in the cross-section) will show a local convergence, leaving a number of  $N - n$  remaining strands, for which the iteration still has to be carried out.

No further iterations are applied on strands which are locally convergent and total convergence is achieved in the case that all strands have shown a local convergence. The Lipschitz Criterion is tested for each iteration step. As already explained, the relaxation method is not applied on strands which violated the criterion once. The iteration is finished as soon as a convergence is achieved on all strands.

### Global Method of Relaxation

The global method of relaxation only uses one global convergence criterion. Instead of iterating and relaxing the applied field of the individual strands, the vector of the applied magnetic induction  $\mathbf{B}$  is relaxed by means of one relaxation factor. The relaxation factor is then calculated from Eq. (5.10).

### Starting the Relaxation

Another important question is at which iteration step the relaxation method should start. It will be shown in section 5.7.2 that the starting conditions have a certain influence on the convergence behavior of the fixed point iteration in the individual steps. A number of principles with different starting points have therefore been tested which are classified in the following list:

- **3/3–Method:**  
The relaxation factor is calculated and applied from step 3 on.
- **3/4–Method:**  
The relaxation factor is calculated from step 3 and applied from step 4 on.
- **4/4–Method:**  
The relaxation factor is calculated and applied from step 4 on.
- **4/5–Method:**  
The relaxation factor is calculated from step 4 and applied from step 5 on.

## 5.7 Test Results from the Relaxation Methods

### 5.7.1 Comparison of Local and Global Methods

All computations shown in this paragraph are based on a simple 1-in-1 dipole magnet consisting of the 6-block coil geometry, taken from the LHC main dipoles surrounded by a circular yoke with a 98 mm inner yoke radius. This simple geometry has been chosen in order to simplify the observation of the differences in the iteration methods. The nominal excitation current in the coil is set to 11800 A. The first investigation is a comparison between the global and the local relaxation methods. Figure 5.7 exemplary shows the 3/3-Method as,

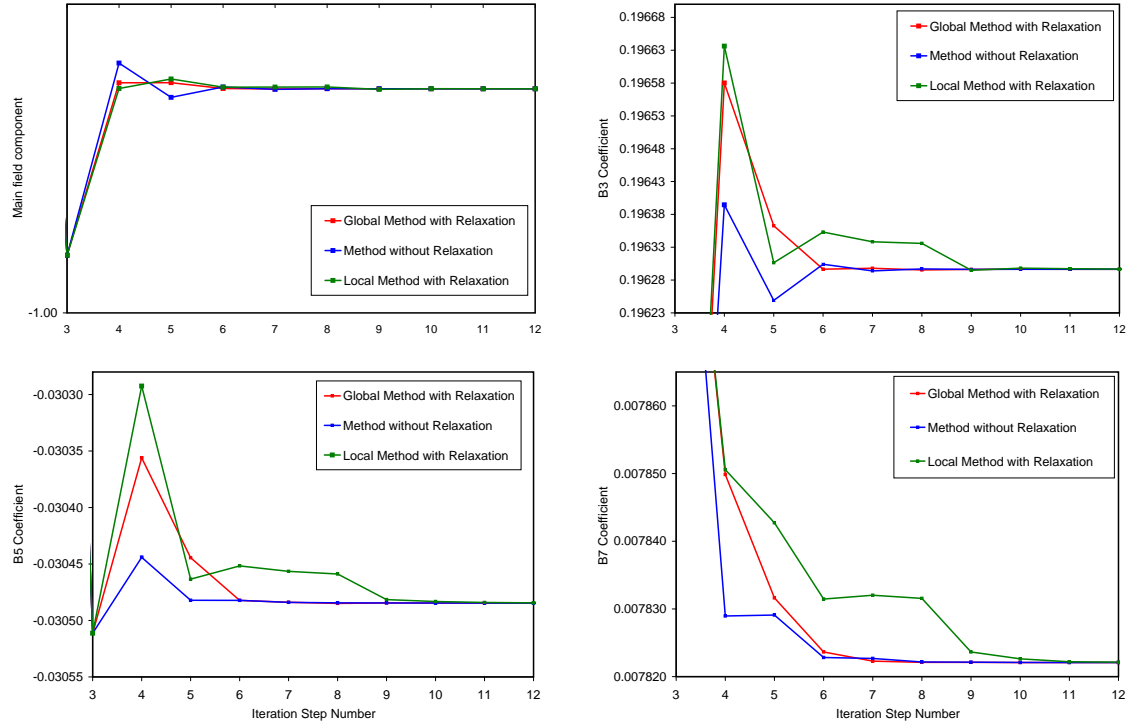


**Figure 5.7:** Comparison of the local relaxation method, the global relaxation method and the non-relaxed iteration for the lower order multipoles of an 1-in-1 dipole coil in a simple iron yoke. The results mainly demonstrate the stabilizing effect of the global method.

calculated for a small current factor of 0.001, corresponding to a source current of about 10 A. The presented results are typical and the other X/Y-Methods show a very similar behavior. As can be seen in the plots, two conclusions can be drawn from this: First of all, the global methods in general show a faster convergence behavior than the local methods for all calculated examples (compare the blue and the green curves in Fig. 5.7). Although the curves presented here do not show an effect of convergence acceleration, if compared with the non-relaxed iteration, this acceleration has been observed on more complicated magnet geometries. Secondly, it can be seen from the plots that the global relaxation method has a stabilizing effect on the oscillating behavior of the non-relaxed iteration (compare the blue and the red curves, also shown in Fig. 5.7). In the example presented, the stabilization mainly improved the convergence on the multipoles  $B_3$  and  $B_7$ . Due to the superior behavior of the



global methods during this investigation, the local methods are no longer considered.

### 5.7.2 Onset of the Relaxation

Various tests have been carried out in which the relaxation method was applied on the iteration for magnet calculation in order to stabilize and accelerate the convergence of the problem. However, since the induced fields produce a repercussion on the originally applied magnetic induction, a considerable field change takes place during the first steps of the iteration. It is therefore necessary to discuss in which step the relaxation method can be applied in a general and stable way.

It has been shown in section 5.4 that at least two iteration steps are mandatory in order to calculate the first relaxation factor. The earliest possible iteration step to apply the relaxation is therefore step number 3. Figure 5.8 shows the influence of the starting iteration step of the relaxation on the stabilization and the convergence of the multipole coefficients  $B_3$  and  $B_5$ . The naming convention follows the description given in section 5.6.3.

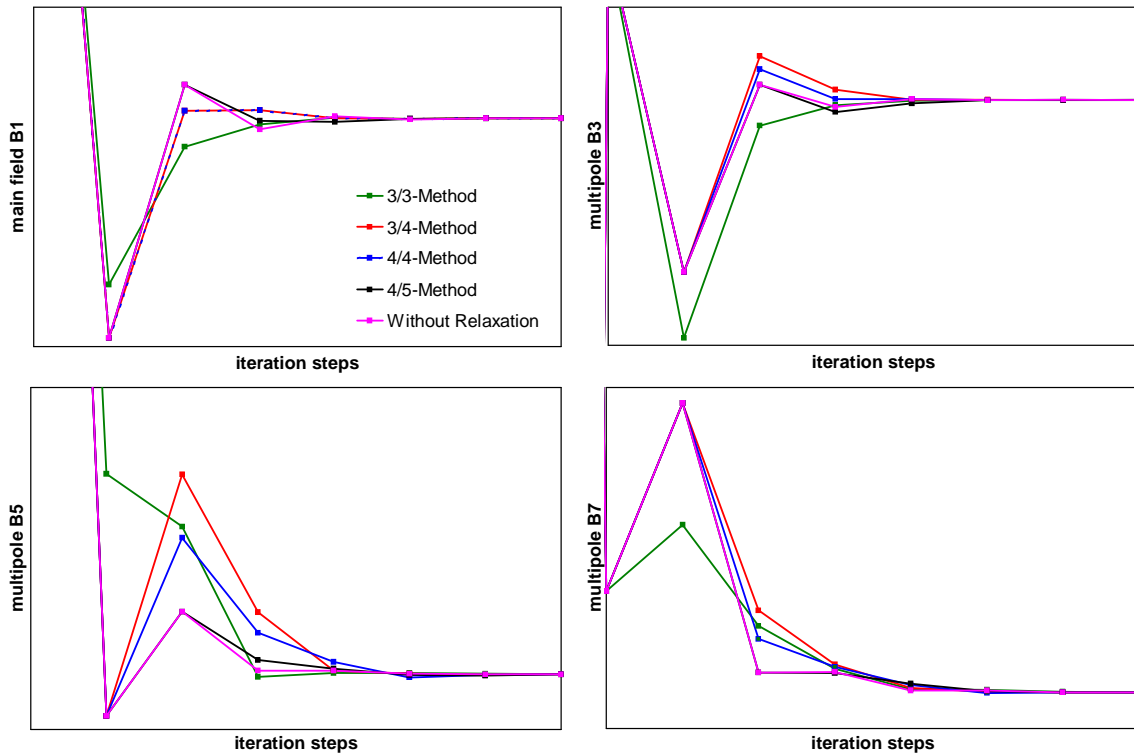


**Figure 5.8:** Influence of the onset of the relaxation on the stabilizing effect of the relaxation method. From the top left to the bottom right: main field component  $B_1$ , multipole coefficients  $B_3$ ,  $B_5$ , and  $B_7$ . All values are calculated at a reference radius of 17 mm.

As can be seen from the plots, the 3/3-Method (calculation of the relaxation factor and its application in the third step) has a stabilizing effect on the main field component and on the multipoles  $B_5$  and  $B_7$ , whereas the multipole coefficient  $B_3$  deteriorates at the onset of the relaxation method. The 3/4-Method and the 4/4-Method show little difference to the

3/3-Method. However, the 4/5-Method (calculation of the relaxation factor in step 4 and application in the fifth step) shows a weak stabilizing effect in the simple example of the 1-in-1 geometry from which the curves are taken. This effect has been observed to be strong mainly for more complicated geometries as for the two-in-one geometry of the LHC main dipole (introduced in section 6.3). Although the principle can also be seen in the simpler geometries, the gain here – in general – is smaller.

In addition to the stabilizing effect, a considerable acceleration of the convergence has been observed. Also this effect becomes especially important when the method is applied on more complicated magnet geometries that take a considerable amount of computational resources and usually run for more than one day (such as the LHC main dipole, or the nested magnets). In these cases, the iterations without any relaxation method have been terminated after 200 iteration steps when no convergence was achieved. This was the case for some calculations with extremely low source currents, when the induced persistent currents fully compensated, or even overcompensated, the applied field in the very first iteration steps. With no stabilization measure applied, these cases of very low source currents have also the tendency to destabilize and oscillate. Then, a stabilizing measure is inevitable to ensure the convergence. The 4/5-Method has shown a very good performance in these cases as well and is therefore considered the optimum of the compared principles.

At last the convergence velocity of the global methods is investigated. Therefore, the factor  $\lambda$ , given in Eq. (5.16) is interpreted as the decrease of the size of the iterating interval. In that sense, smaller values of  $\lambda$  indicate a higher convergence velocity. For the comparison of the methods, the geometrical average of all  $\lambda^{(k)}$ s during one current step have to be computed. Figure 5.9 shows the calculations for all current steps and for all compared global methods.

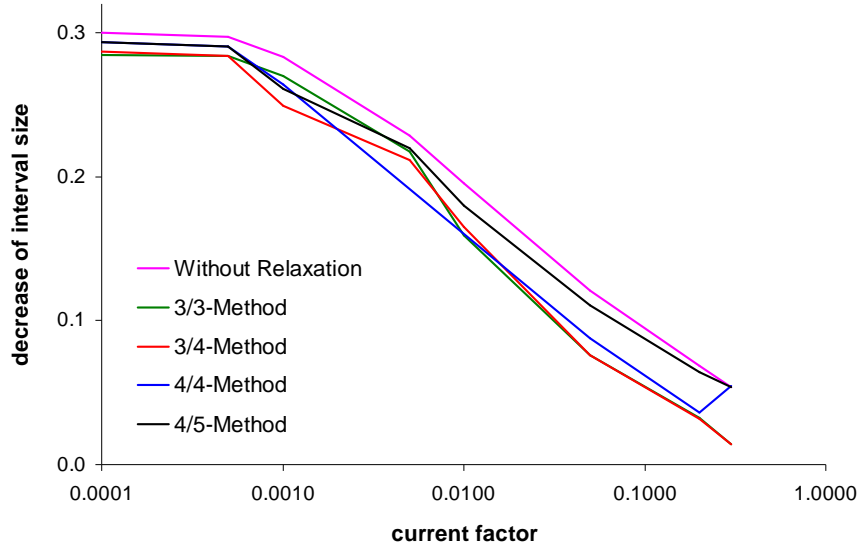


**Figure 5.9:** Comparison of the convergence velocity of the relaxation methods by the decrease of the interval size in the individual steps. The magenta curve shows the non-relaxed iteration method, here presented for the sake of completeness.

It can be seen from Fig. 5.9 that the non-relaxed iterations (magenta curve in this figure) is slower than the relaxed methods. An absolute comparison can be done by calculating

the convergence-step-weighted average of the interval decrease. From this investigation, the methods are ranked due to their convergence velocity:

$$3/4\text{-Method} > 3/3\text{-Method} > 4/5\text{-Method} > 4/4\text{-Method} > \text{non-relaxed methods}.$$

Although the 4/5-Method is not the fastest of the programmed relaxation methods, it has been implemented into the ROXIE program due to its superior feature with respect to stabilizing the convergence behavior.

## 5.8 Multipole Results with and without Repercussion

It has already been mentioned at the beginning of this chapter that the screening field of the induced superconductor magnetization influences the (originally) applied field and thus the resulting magnetization. By means of the above described iteration, it is possible to consider this repercussion. In general, it is observed that the influence of the repercussion on the induced magnetization in the superconducting coil and the field errors in the magnet aperture depend on the coil structure (which can be build out of one layer of coil blocks or several) and on the vicinity of the surrounding iron yoke. The effect is therefore less critical for the LHC main dipole, for example, where there are the stainless steel collars around the superconducting coil and this way the inner border of the ferromagnetic iron yoke is at a certain distance to the superconducting coil (see also Fig. 6.4).

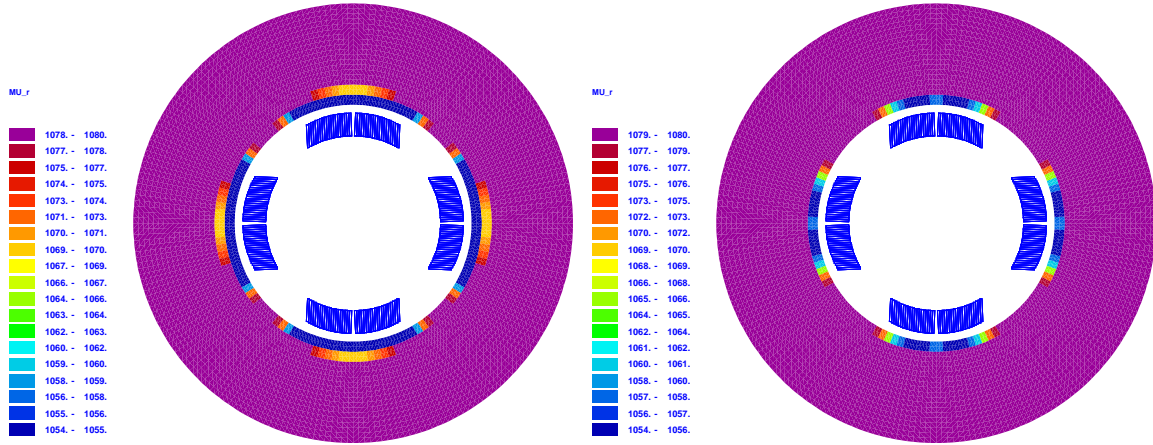


**Figure 5.10:** Cross-section of the MQTB magnet, a superconducting tuning quadrupole which has been developed at CERN for the LHC. The MQTB is a typical magnet geometry which is sensitive to the repercussion effect of the induced screening fields in the superconductors. The sensitivity results from the coil design which consists of only one layer and the vicinity of the surrounding iron yoke. The plot shows the  $\mu$ -distribution on the second up-ramp branch for a source current of 208 A. Left: The repercussion of the persistent current field is omitted; Right: The repercussion of the persistent current field is considered by iteration.

Figure 5.10 shows the cross-section of the coil of a so-called MQTB magnet in its surrounding yoke<sup>3</sup>. The MQTB magnet [70] has been developed at CERN for the LHC. It is a superconducting tuning quadrupole which is mounted into the main quadrupole cold mass. This magnet has been chosen here, since it is build from a one layered NbTi coil where the inner yoke radius is close to the outer radius of the coil. Thus, it presents a typical example of a magnet geometry which is very sensitive to the repercussion effect. The Figure 5.10 shows the  $\mu$ -distribution on the second up-ramp branch for a source current of 208 A. The plots present the influence of the persistent current field on the distribution of the yoke magnetization. The left plot is without any persistent current repercussion, whereas on the right-hand side, the persistent current influence is considered by means of an M(B)-iteration and an update of the yoke magnetization. Due to the quadrupole geometry, the lowest even order multipoles are the  $b_6, b_{10}, b_{14}, \dots$ , where only the multipoles  $b_6$  and  $b_{10}$  are known to be influenced by the persistent current effect (whereas the influence of the coil magnetization on the multipole  $b_{14}$  is considered to be negligible). The results for the multipole  $b_{14}$  and higher are therefore omitted here.

Figure 5.11 presents the calculated values for the lowest order multipole  $b_6$  versus the main field component. The plot shows a significant difference in the curves which are calculated with and without iteration (pink and blue curves), especially at low field. Also presented in the plot is the geometrical value of this magnet (green curve). The initial state curves are shown as dashed lines. The multipoles are determined during an up-down-up ramp cycle. As before in the case of the main dipole, which is presented at the beginning of this thesis, the geometric value stays fully reversible and the hysteresis in the calculated multipoles arises from the superconductor magnetization.

The values of the calculated multipole  $b_6$  are presented in table 5.1. It is in general observed that on the shielding branch (first up-ramp), the iterated values of the multipoles are lower than those which result when no iteration is applied, whereas on the trapping branch (first down-ramp) the iterated multipoles are higher. This is due to the effect of local field change which has already been observed in Fig. 5.1 at the beginning of this chapter. In the case shown here, the total field which is seen at each strand position in case the iteration is applied, is smaller than the values which result if only the first persistent current field is superimposed (without any further iteration). Consequently, the magnetization and thus the resulting field errors are higher (except on the initial state curve, where the magnetization rises according to the external field). As a result, the so-called 2M-value, which denotes the width of the magnetization curve for a certain field value, increases if an iteration is applied. The area which is encompassed by the magnetization curve enlarges, a feature which results, for example, in higher losses than those which are received without iteration (see section 7.4 for the loss determination).

Further, the differences between the calculation with and without iteration are biggest in the low field range, as expected, and reduce with increasing field strength. The calculated value of the multipole  $b_6$ , for example, amounts to 10.98 units without iteration, whereas with iteration, a  $b_6$  of 9.01 units is obtained, both determined for a field value of 0.140 T (see Fig. 5.11). In a higher field range, above approximately 0.8 T, the difference almost vanishes as can be seen from the plot in Fig. 5.11 and the values in the table 5.1.

Figure 5.12 shows the magnetization in the coil cross-section for low (about 0.14 T from

---

<sup>3</sup>Various test models exist of the MQT magnet with slight modifications, as for example, the use of different tuning shims in the coil cross-section or a change in the air gap between the coil and the inner yoke radius. The version chosen here is without any tuning shims and an air gap of about 3 mm.

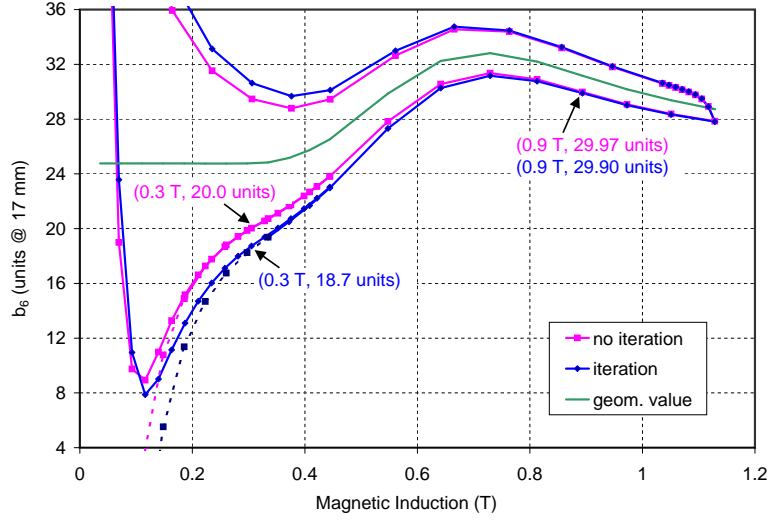


**Figure 5.11:** Calculated values for the lowest even order multipole  $b_6$  versus the magnetic induction in the magnet aperture. Pink curve: without applying the M(B)-iteration; Blue curve: The M(B)-iteration is applied. The green curve shows the geometric value, when no persistent currents are considered. The dashed lines result from the initial state curve.

**Table 5.1:** Multipole  $b_6$  calculated at 17 mm radius for the MQTB magnet. All values are taken from the second up-ramp cycle. The arrows indicate the highlighted values in Fig. 5.11

$I_{\text{source}}$	$ B $	Multipole $b_6$ in units of $10^{-4}$		
		geometric value	without iteration	after iteration
69.3	0.046	24.763	51.783	54.984
102.3	0.069	24.763	18.990	23.568
207.9	0.140	24.763	10.984	9.012
$\Rightarrow$ 452.1	0.305	24.764	20.029	18.732
590.7	0.399	25.562	22.385	21.464
660.0	0.445	26.524	23.818	23.035
$\Rightarrow$ 1485	0.894	31.170	29.972	29.896

a source current of 208 A) and intermediate field level (about 0.40 T from a source current of 591 A) in case the iteration is omitted (left side of Fig. 5.12) and with an iteration applied (right side of Fig. 5.12). As can be seen from the plots, a significant difference in the distribution of the magnetization in the cross-section occurs, when the iteration is applied. As expected, the difference is larger for the lower value of source current which is shown in the plots on the top of Fig. 5.12. However, the distribution of the magnetic induction in the coil cross-section shows very little change if the iteration is applied, even at low fields, as can be seen in Fig. 5.13. This results from the fact that the induced superconductor magnetization is extremely sensitive to even small field changes due to the steep slope of the  $J_c(B)$ -curve at low field. The  $J_c(B)$ -curve is shown in Fig. 2.9 of section 2.3. The small change in the

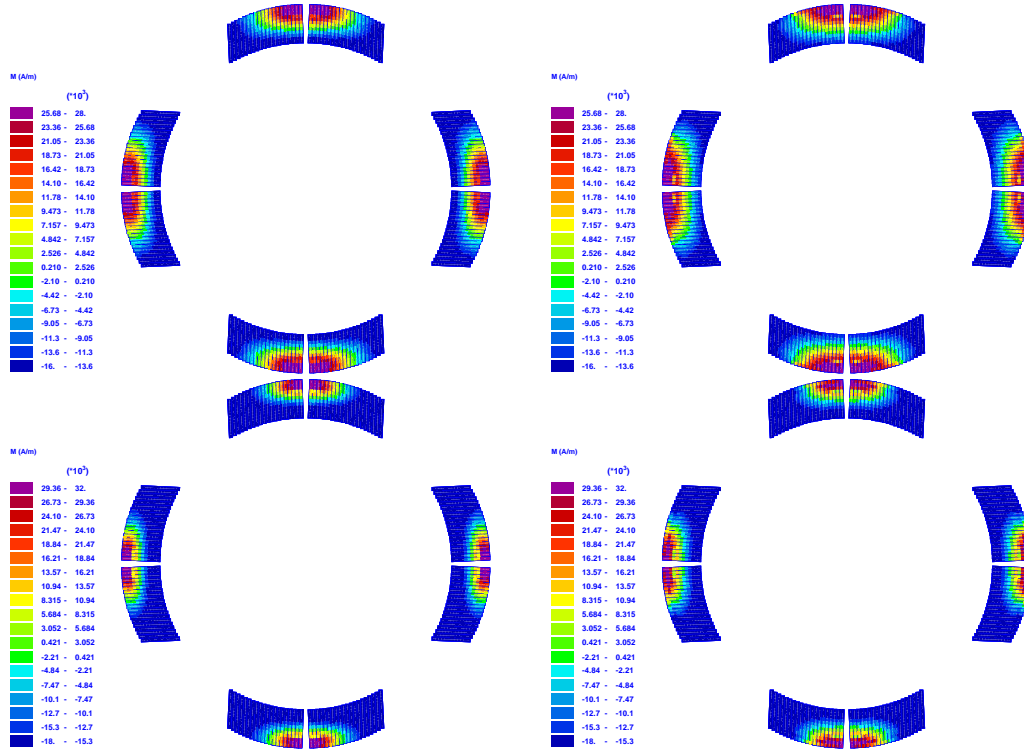


**Figure 5.12:** Magnetization in the coil cross-section of the MQTB magnet without and with the M(B)-iteration applied. Top: For a source current of 208 A; Bottom: For a source current of 591 A. The appropriate distributions of the magnetic induction according to the magnetization on the top is shown in Fig. 5.13. All values result from the second up-ramp cycle.

distribution of the magnetic induction in the coil cross-section is caused by the saturation effect which starts already at this very low field value and can also be observed in the distribution of the yoke magnetization in Fig. 5.10. Any saturation effect on the non-linear yoke can be considered as a change in the effective inner yoke shape and this way causes a slight change in the total field distribution. Following this reasoning, it is then also clear why magnet geometries which have the yoke in close vicinity to the superconducting coil are very sensitive to the field repercussion at low field levels. If the magnet geometry is such that there is a considerable distance between the coil and the inner yoke contour, the influence of the inner yoke shape is much smaller.

Note that the non-linear behavior of the multipole  $b_6$  for values of the magnetic induction above 0.4 T results from the saturation effect in the surrounding iron yoke structure. This feature is typical for magnet geometries with only a small air gap between the outer coil radius and the yoke.

Thus, the example of the MQTB magnet shows a strong influence due to the non-linear yoke features on the calculated field errors for all field levels. The plots very well illustrate the necessity of performing an M(B)-iteration and considering the repercussion of the persistent current field on the surrounding yoke. It has been observed that in the low field range, even

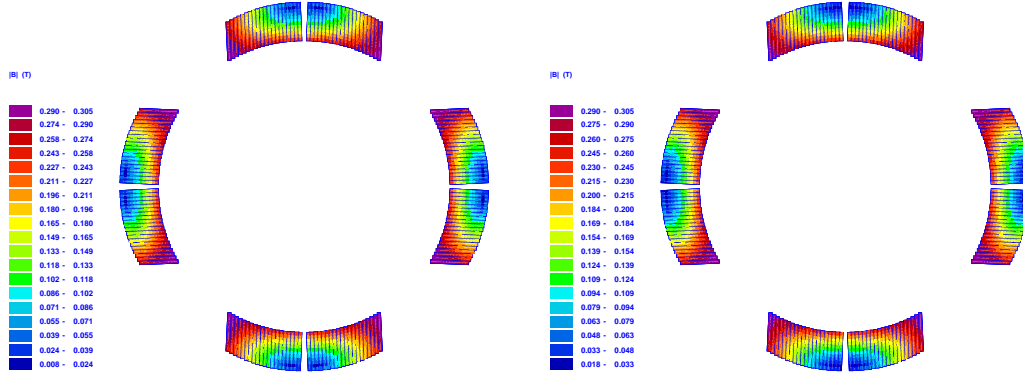


**Figure 5.13:** Cross-section of the coil of the MQTB magnet. The plot shows the distribution of the resulting magnetic induction without and with the M(B)-iteration applied for a source current of 208 A. Although only small changes can be observed in the B-distribution in the coil cross-section, the appropriate magnetization changes significantly (see Fig. 5.12, top).

small changes in the magnetic induction cause a significant change in magnetization and make an M(B)-iteration necessary if the persistent current induced field errors are to be determined correctly. At the intermediate and high field range, where the persistent current influence is smaller and vanishes, the saturation of the yoke increases and results in a change in the shape of the multipole curves.

It is now of interest to evaluate whether the field errors, calculated for this kind of magnet which possesses only a small air gap, could be determined with a comparable precision, in case the yoke is replaced by an iron yoke with constant permeability on which the imaging method is applied. This investigation is carried out in the next section.

### 5.8.1 The Limits of the Application of the Imaging Method

In order to consider the contribution of the iron yoke in magnet geometries, the non-linear area of the iron yoke in the simulation is sometimes replaced by an iron yoke with constant permeability which is then considered by means of the imaging method. The application of the imaging method is in principle possible if the inner yoke contour is perfectly round and only the resulting *fields in the magnet aperture* are of interest. However, no saturation effects in the yoke may occur, if this method is to be applied correctly, since local changes of the resulting field have to be considered, as has been shown in the last section, and cannot be determined by the imaging method.

By using the ROXIE program, a comparison has been carried out between the results of the iterated multipoles in case the influence of the yoke is calculated by the BEM-FEM method and in case the influence of the yoke is considered by the imaging method. Figure 5.14 shows again the calculated values for multipole  $b_6$  which are now determined by means of the imaging method (pink curve). For comparison, the plot also shows the result when the influence of the iron yoke is considered by means of the BEM-FEM method in the blue curve (already presented in Fig. 5.11). The green curve shows the geometric value. In all



cases, the iteration is applied. For the imaging method, a  $\mu$ -value of 1000 is assumed, which equals the  $\mu$ -value which has been given by the iron magnetization curve that is used by the BEM-FEM method at low field. As before, an up-down-up ramp is calculated. It can be

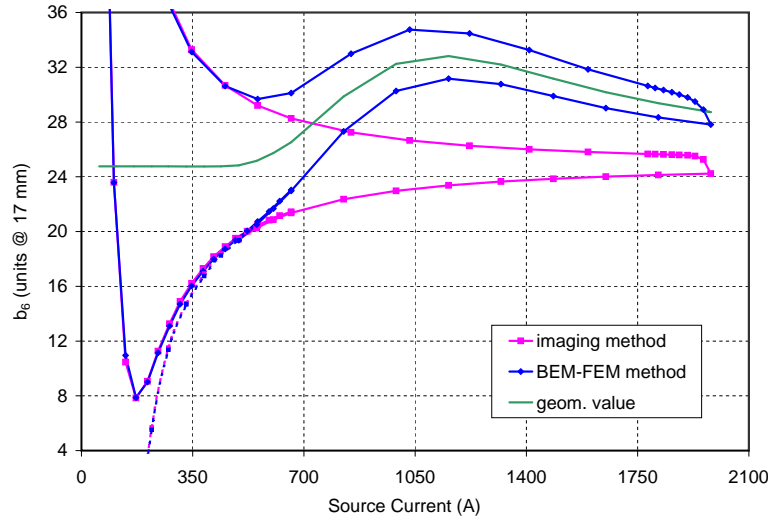


**Figure 5.14:** Calculated values for the lowest even order multipole  $b_6$  versus the source currents in the magnet coil. Pink curve: Imaging method is applied with a  $\mu$ -value of 1000; Blue curve: BEM-FEM method is applied. The green curve shows the geometric value, calculated with the BEM-FEM method, when no persistent currents are considered. The dashed lines result from the initial state curve. For all cases, an M(B)-iteration is carried out. The curves illustrate the significant difference between the methods which results from the saturation of the non-linear iron yoke.

seen from the two curves that a considerable difference between the calculated multipoles emerges. Depending on the region of interest, the deviation between the values is relatively small and amounts to about 0.2 units in  $10^{-4}$  (for a range of field values below 0.3 T). For higher fields, a deviation of 2 units up to 8 units (for a range of field values above 0.4 T) is observed. All values are determined at a 17 mm reference radius and are also given in table 5.2. Note, that the curves in Fig. 5.14 are plotted versus the source current instead the magnetic induction. This is due to the fact that the calculated values of the magnetic induction which result from the imaging method are considerably higher than those which result from the BEM-FEM calculation. The reason for this is that the contribution of the iron yoke reduces as soon as a saturation effect starts. A plot of the multipoles versus the magnetic induction could therefore be easily misleading. In addition, it can be said, that above a field value of approximately 0.35 T, the saturation effect dominates the multipole value and the results which are determined from the imaging method become very unprecise.



**Table 5.2:** Comparison of the multipole  $b_6$ , calculated for the case that the non-linear yoke is considered by means of the imaging method with the result when the yoke contribution is calculated from the BEM-FEM method. The multipole  $b_6$  is given in units of  $10^{-4}$  at 17 mm reference radius.

$I_{\text{source}}$	$ B $	Multipole $b_6$ in units of $10^{-4}$ for 17 mm reference radius.	
		from imaging method	from BEM-FEM method
69.3	0.0465600	56.208	54.984
171.6	0.1165500	7.844	7.869
310.2	0.2112900	14.893	14.694
452.1	0.3063200	18.902	18.732
521.4	0.3537100	20.020	20.037
590.7	0.4011000	20.833	21.464
660.0	0.4484800	21.444	23.035
1150.0	0.7852500	23.373	31.168
1320.0	0.8974900	23.652	30.769
1485.0	1.0097400	23.857	29.896
1980.0	1.3464500	24.234	27.812



## Chapter 6

# Field Calculations for the LHC Magnets

In this chapter, the results of field calculations which have been carried out for some LHC magnets, mainly the main dipole and quadrupole magnets, including the effect of superconductor magnetization, are presented. The calculation of the persistent current effects on the field quality of the LHC magnets offered the possibility to verify the magnetization model since plenty of measurements on magnets already have been carried out at CERN in the framework of the R&D program. This allowed the comparison of the measurements with the calculated values for various cable and magnet types. In this chapter, the LHC project and its magnet system is first briefly introduced. Then the calculated results are presented and discussed for the LHC main dipole, the LHC main quadrupole and a nested magnet for orbit correction which consists of two nested dipole coils where the inner coil is rotated by an angle of 90 degrees. The nested magnet is of special interest, since there the effect of the rotating fields can be observed.

### 6.1 The LHC Project

The Large Hadron Collider (LHC) project [1] is a superconducting particle accelerator that will provide proton-proton collisions, as well as collisions of lead ions. The aim of this collider is not only to produce a higher collision energy, but also a higher luminosity<sup>1</sup> than that of already existing hadron colliders. In order to recreate the conditions which existed in the universe just  $10^{-12}$  seconds after the “Big Bang”, LHC will provide proton-proton collisions with a center-of-mass energy of 14 TeV and a luminosity of  $10^{34}\text{cm}^{-2}\text{s}^{-1}$ . It will also provide heavy (Pb) ion collisions with a center-of-mass energy of more than 1000 TeV and a luminosity in excess of  $10^{27}\text{cm}^{-2}\text{s}^{-1}$ . Proton-proton colliders require two separate beam channels with fields that are equal in strength but opposite in orientations in order to bend particles that have identical electrical charge. Due to the limited space in the already existing LEP tunnel, a so-called two-in-one design was chosen for the LHC dipoles as well as for the main quadrupoles, where the two beam channels are incorporated into a common yoke structure and one single cryostat.

---

<sup>1</sup>The rate of interaction per unit cross-section.

## 6.2 Lattice and Magnet System

Figure 6.1 (right) shows the basic layout of the LHC accelerator which is divided into eight arc sections (so-called octants). The two beams cross from one beam pipe to the other at four points on the circumference and at those intersections, the physics experiments will be located: ALICE (*A Large Ion Collider Experiment*), ATLAS (*A Toroidal LHC ApparatuS*), LHC - B (*Large Hadron Collider Beauty experiment*) and CMS (*Compact Muon Solenoid*). The two high luminosity proton-proton experiments ATLAS and CMS are located in two new underground areas.

The four straight sections, where the beams do not cross, are used for machine utilities: Acceleration, beam cleaning and beam dump systems. The layout of octant four which contains the RF accelerating system is designed to allow the installation of an additional experiment in the future.

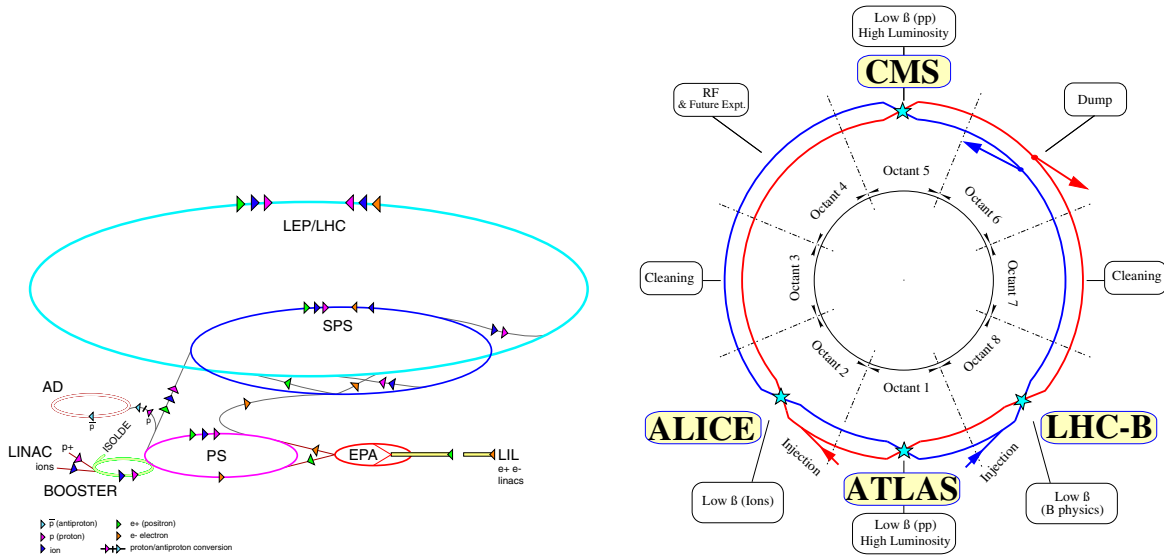


**Figure 6.1:** Left: Injector chain for the LHC. The LHC makes use of the already existing pre-accelerator chain of the LEP accelerator. Right: Layout of the LHC accelerator with the four physics experiments.

The LHC machine will make use of the existing injector chain which is also shown in Fig. 6.1 (left). The machine itself is subdivided in eight 2456 m long arcs that are built out of 23 cells, each formed of two identical half-cells. A half cell, as is shown in Fig. 6.2, comprises a bending/focusing configuration that is composed of three 14.2 m long twin-aperture main dipoles and a short straight section.

The use of superconducting magnets which operate in super-fluid helium below the temperature of 2 K will allow a guiding field of about 8.5 Tesla, i.e. proton beams to be stored at an energy of more than 7 TeV per beam.

The short straight section contains one 3.10 m long main quadrupole, a combined sextupole/dipole corrector, an octupole or a skew quadrupole or a trim quadrupole and a beam position monitor. Small 6-pole and 10-pole correctors are located at the ends of the main dipoles. The main dipoles and the main quadrupoles are all of twin-aperture (two-in-one aperture) design, where the two channels are incorporated into a single iron yoke and a

common cryostat. The other corrector magnets are installed independently for each beam.

The quadrupole is separated from the dipole string by 2.42 m. The separation between the dipoles is 1.46 m, including 520 mm for connections between the cryostats. In total, the LHC accelerator consists of 3444 superconducting magnet units, including 1232 main dipoles and 386 main quadrupoles. 4928 small correctors of the main dipoles have to be added, so in total there are about 8400 magnet units of different size and importance.

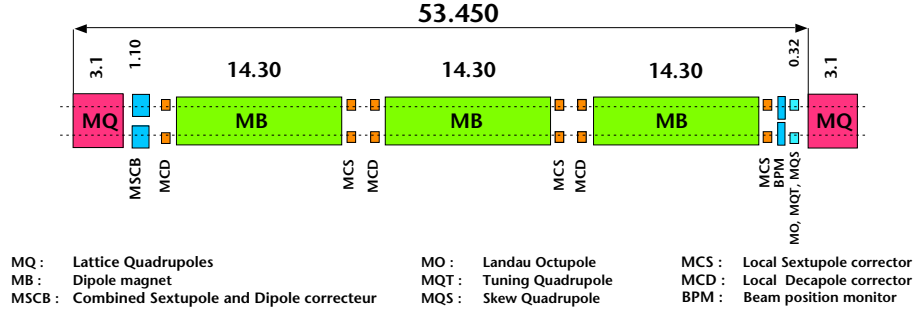


**Figure 6.2:** Sketch of an LHC halfcell containing three dipole bending magnets and various other magnets for beam focusing and field correction.

The characteristic features of the LHC dipole magnets are the high bending field in the aperture and the high stored energy. During the R&D phase, this features yielded a so-called short magnet model programme that includes the construction, test and measurement of several 1.3 m long magnet models and 10 m long dipole prototypes. At the same time, a test string of magnets is installed at CERN in order to test the basic machine halfcell and to confirm the feasibility of the project.

## 6.3 The LHC Main Dipole Magnet

As is explained in section 1.2, field errors in magnets are generally divided into random and systematic errors, where systematic errors arise from the coil geometry, for example. However, due to the existing symmetries, the field imperfections follow a simple pattern. The odd order normal multipoles  $b_3, b_5, b_7, \dots$  arise from contributions that respect the up-down and the left-right symmetry. Hence, these errors are mainly determined by misalignment or unprecise positioning of the conductors in the collared coil. In the case of the LHC main dipoles, an additional  $b_3$  component arises from the surrounding iron yoke due to the two-in-one design.

The even order multipoles  $b_2, b_4, b_6, \dots$  arise from contributions that do not respect a left-right symmetry. They are therefore mainly due to the shape and the positioning of the iron yoke and – in the case of the LHC dipole – of the iron insert.

In the final design of the LHC main dipole, the odd order multipoles (mainly the multipole  $b_3$ ) has been chosen to have non-zero values in order to compensate in the mean for the persistent current effect. This is why the geometric value of the multipole  $b_3$ , which is introduced and presented in section 1.2 as well, does not equal zero.

### 6.3.1 The Dipole Magnet Geometry

Figure 6.3 shows the cross-section of the two-in-one aperture dipole magnet in its cryostat. The coils of the LHC dipole magnets consist of two layers of 24 blocks in total, two on the outer and three on the inner coil layer of each quadrant. Both layers are connected in series and thus the current density in the cable of the outer layer is about 40% higher than in the cable of the inner layer. The coil is shaped in such a way as to make the best use of the superconducting material, while at the same time yielding the highest possible field homogeneity in the magnet aperture. Inside the coil aperture, the beam pipe (often also denoted as the cold bore) and a beam screen, with two small beam screen pipes, are positioned. They are indicated by the number 4 in Fig. 6.3, and can be seen in detail in Fig. 6.4. Since the beam pipe has to be kept free, the coil is wound on a winding mandrel with saddle-shaped endspacers in a so-called constant-perimeter coil end (see, for example, [8] for details on different coil ends).

After winding, the coil layers are polymerized in a mould in order to glue the turns firmly together and thus avoid coil positioning errors. The coil is then put into stainless steel collars and pressed together under a pressure of 120 MPa to keep its final shape. Collaring rods are inserted that lock the collars. These collars hold the coil in place and are enclosed by the iron yoke inside the shrinking cylinder. The shrinking cylinder is closed at the ends. This state of the assembly is called the cold mass and is indicated in red in Fig. 6.3. It encompasses all parts that are cooled by liquid helium.

Together, the collar, the iron yoke and the shrinking cylinder contribute a necessary azimuthal pre-compression in the coil in order to prevent conductor displacements arising in the coil under the action of electromagnetic forces. Even small movements of the coil have to be avoided since they result in a local energy rise which could make the magnet quench. A quench is the spurious transition of a magnet from superconducting to normal conducting state. A quench arises if the temperature in the conductor is too high or the local field intensity is above the critical field intensity. Therefore the origin of a quench usually is a magnetic or mechanical disturbance that heats a small region of the superconductor so that it becomes resistive. Current passing through this resistive region then generates additional Joule heat and raises the temperature of more material, leading to more heating and eventually the entire superconductor winding is driven normal. There are different possibilities to avoid a magnet quench, as, for instance, the already mentioned cryogenic stabilization. Others are explained in [8], for example, and therefore the discussion is omitted here.

The cold mass weights about 24 tons and is then mounted into a cryostat which also contains a support system, the cryogenic piping, a radiation insulation and a thermal shield. For electromagnetic field calculations it is sufficient to consider the structure including the cold mass whereas the influence of the outermost cryostat on the field in the aperture is negligible.

### 6.3.2 Technical Requirements

As already mentioned, superconducting coils for magnet design have become essential components of accelerators in order to reach the desired high field economically. The development of dipoles for higher and higher fields is a great incentive, with the consequence that the superconducting dipole magnets, which are the most important components of the accelerator from the cost point of view, have also become the most critical technology.

The main requirements for the superconducting magnets are:

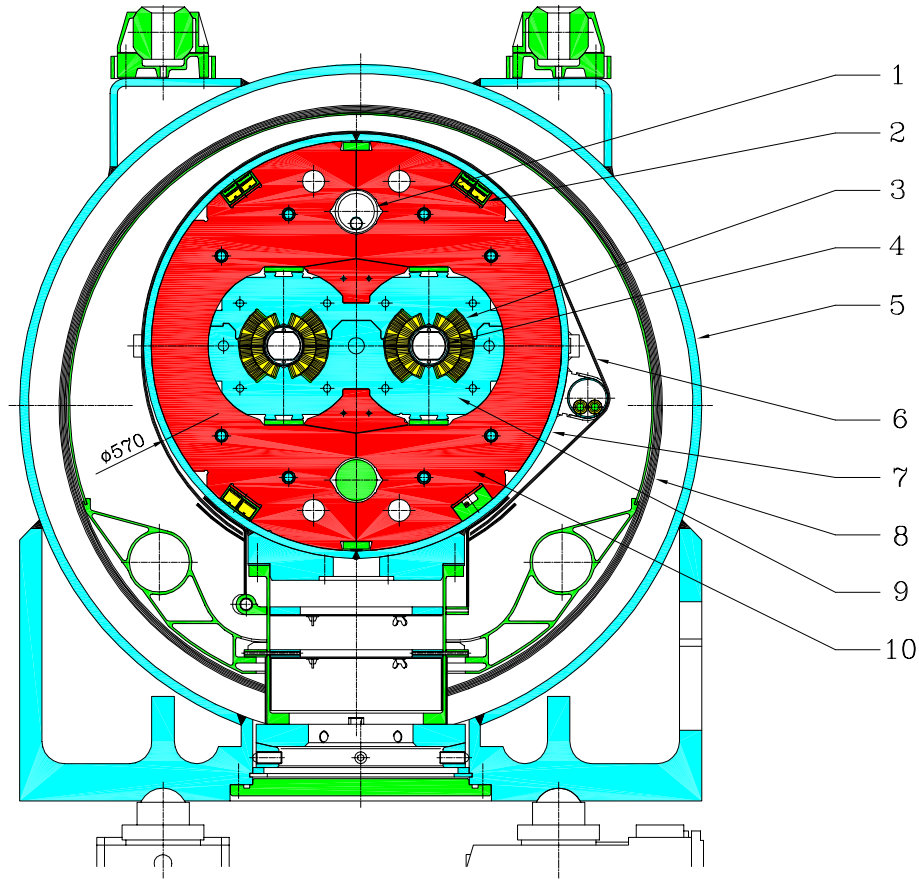


**Figure 6.3:** Cross-section of the LHC main dipole magnet in its cryostat.

Where

- |                                |   |
|--------------------------------|---|
| 1) heat exchanger pipe         | 5) cryostat                             |
| 2) bus bar (sc)                | 6) thermal shield                       |
| 3) superconducting coil        | 7) shrinking cylinder (He-vessel)       |
| 4) beam pipe surrounding       | 8) super-insulation                     |
| the beam screen with its       | 9) non-magnetic collar                  |
| two attached beam screen pipes | 10) iron yoke (ferromagnetic material). |

1. An extremely uniform field in the aperture both at injection field level as well as during the ramping of the magnets to the nominal field level, which means the presence of a large good field region over the aperture.
2. A field strength of about 8.3 Tesla, and
3. a sufficient quench margin.

In the framework of the short dipole model programme at CERN, 23 single aperture models and ten double aperture models have been built and tested at CERN since 1995. Additionally, seven 10 m long double aperture prototypes were industrially manufactured. The testing and measuring of the magnets has not only shown the feasibility of the project but has also offered an opportunity to compare the field calculations, resulting from the

different magnetization models, with the measured values.

The main parameters of the LHC dipole are listed in Table 6.1.

**Table 6.1:** Main parameters of the LHC dipole.

Operational field	8.36 T
Coil aperture	56 mm
Magnetic length	14.2 m
Distance between aperture axes	194 mm
Operating current	11800 A
Operating temperature $T_{\text{ref}}$	1.9 K

### 6.3.3 The Cables of the LHC Main Dipole and Quadrupole Magnets

For the LHC main dipole and quadrupole magnets, a Rutherford-type cable of trapezoidal shape is used as is shown already in Fig. 1.1 in the introduction of this thesis. The trapezoidal shape is chosen in order to give a good circular approximation when being put closely around the circular aperture of the magnet. However, the trapezoid is not sufficient to allow the cables to build up arc-segments. Therefore the coil layers are divided into individual blocks which are separated by copper wedges. Besides the cable properties, the radial position and angular alignment of the coil blocks can be used as design variables for the optimization of field errors arising from the coil.

For the manufacturing of the main dipole and quadrupole magnets, two different cables have been ordered in industry, where cable 1, consisting of 28 strands of 1.065 mm diameter is used for the inner layer coil of the LHC dipole (and for the main quadrupole). Cable 2 which is used for the outer layer of the LHC main dipole consists of 36 strands of 0.825 mm diameter. Therefore, the cables have the same height, but are different in width. The strands are made of thousands of superconducting NbTi filaments which are embedded in a copper matrix in order to stabilize the superconductor in case of a quench. This principle of current sharing is called cryogenic stabilization and is also described in chapter 1. The size of the filaments is aimed to keep as small as possible in order to reduce the magnetization effects. However, a reduction in diameter is limited by manufacturing possibilities as well as cost considerations. The cable is insulated with layers of polyimide film of 50.8  $\mu\text{m}$  thickness which is wrapped around the cable ‘edge-to-edge’ and an additional layer of 60.8  $\mu\text{m}$  thickness twisted longitudinally with a spacing of 2 mm. Table 6.2 gives the main cable data.

**Table 6.2:** Main cable data for the LHC main dipole and quadrupole magnets.

Number of filaments per strand (inner/outer layer)	8900/6500
Filament diameter (inner/outer layer)	7/6 $\mu\text{m}$
$B_{\text{ref}}(T_{\text{ref}})$ reference value of magnetic induction	
(inner/outer layer)	9/10 T
$J_c(5 \text{ T}, 4.2 \text{ K})$ reference value of critical current density	
(inner/outer layer)	3 kA/mm <sup>2</sup>
used in current fit function	



## 6.3.4 Results

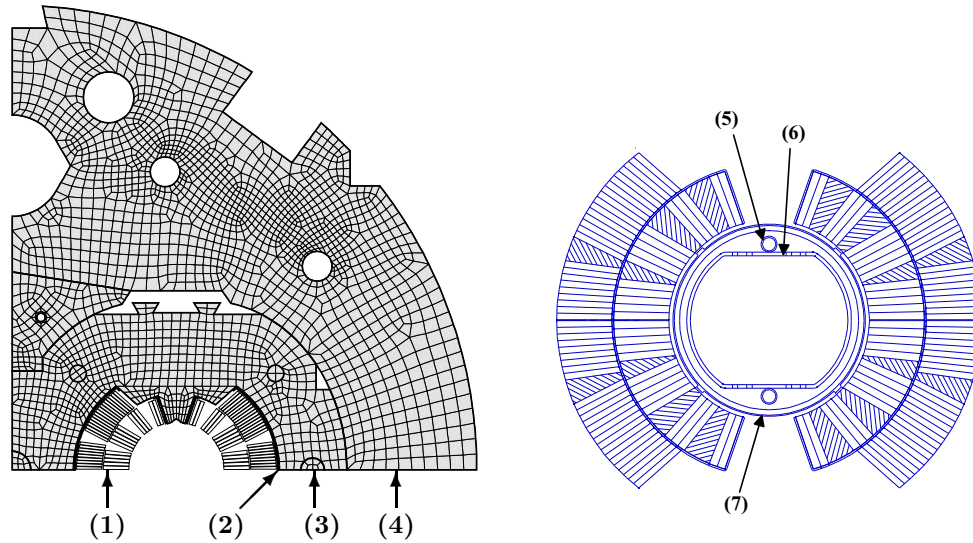


**Figure 6.4:** Left: ROXIE model of one quadrant of the LHC main dipole magnet geometry in finite elements for the application of the BEM-FEM method. The geometry includes the superconducting coil (1) in a ferromagnetic yoke structure (4) with stainless steel collars (3). The coil protection sheet (2) is mounted on the outer coil radius. Right: Geometry of the LHC main dipole coil including the vacuum tube (7) and the beam pipe (6) with the two cooling pipe tubes (5). The hatched areas indicate the copper wedges between the coil blocks.

Figure 6.4 (left) shows a ROXIE plot of the meshed structure of the LHC dipole consisting of the superconducting coil (1), the coil protection sheet (2), the stainless steel collars (3) and the ferromagnetic iron yoke (4). On the left-hand side of Fig. 6.4, the geometric model of the dipole coil including the vacuum beam pipe (7) and the beam screen (6) with the two beam screen tubes (5) is displayed.

The model shown here is prepared for the application of the coupled BEM-FEM method, where only the iron domains have to be meshed. All air domains (as the region above the outer yoke radius or the holes in the yoke structure) remain without a mesh. As already mentioned in chapter 5.5, in the ROXIE program all numerical solvers work in such a way that the coil geometry does not have to be modelled in finite elements.

In order to give an idea of the expected field distribution in the yoke cross-section of the LHC main dipole, Figure 6.5 shows the modulus of the magnetic induction in the first quadrant for the case of nominal field. The plot displays one half of the superconducting coil surrounded by the stainless steel collars and the non-linear iron yoke with the iron insert structure. The computed values for the odd lower order multipole  $b_3$  versus the main field are presented in Fig. 6.6 for an up-down ramp. In that plot, the dashed curve in blue shows the calculation without persistent currents, the so-called *geometric value*, when the multipole components are fully reversible. The continuous curve in red shows the calculation including

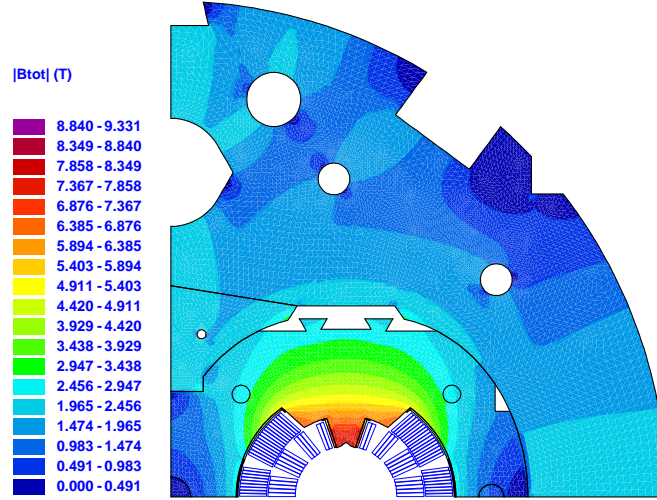


**Figure 6.5:** Modulus of the magnetic induction,  $|B|$ , of the first quadrant of the LHC main dipole cross-section, including the stainless steel collars, at nominal current.

the persistent current effect.

The geometric value should be constant during any ramp-cycle, since it – per definition – comes from the geometry that are the conductor positioning and the shape of the yoke.

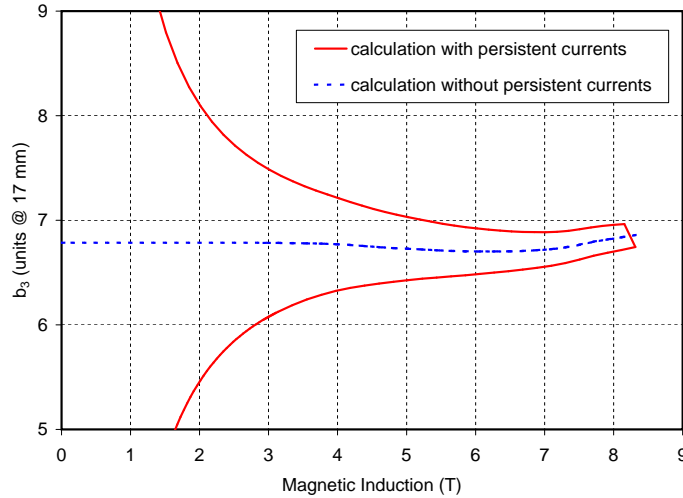


**Figure 6.6:** Multipole  $b_3$  calculated at 17 mm reference radius for an up-down-up ramp cycle on the non-initial state curve. Red curve: including persistent current effects; Dashed blue curve: results without persistent current calculation. When the persistent current effect is excluded from the calculation, the multipoles values show a fully reversible behavior.

However, both curves show a slight decrease in the interval of about 4 to 6.5 T as compared to a situation without iron saturation. Also, a slight slope upwards can be observed from

the dashed curve in Fig. 6.6 when the main field increases. Both variations are due to yoke saturation effects that change the magnetic field contribution from the iron material and thus influence the multipole behavior (starting from approx. 6 T on). It can also be seen that at high field level little influence of the coil magnetization remains: the shape of the red curve is following the dashed one, both during up- and down-ramp. Only the hysteresis effect which occurs due to a change in ramp direction, remains. Note, that the saturation influence is relatively small for the dipole geometry due to the distance between the outer coil radius and the ferromagnetic yoke. Saturation effects are observed to be much higher for magnet geometries on which the inner yoke contour is in close vicinity to the magnet coil (an effect which is already demonstrated in detail in section 5.8.1).

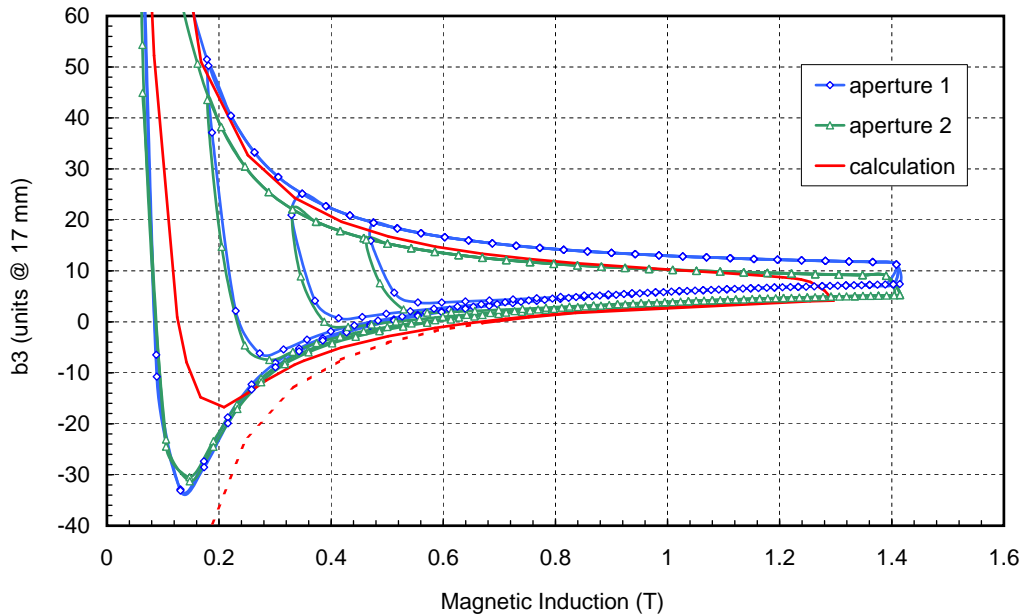


**Figure 6.7:** Comparison of the calculation of the odd lower order multipole  $b_3$  for the LHC main dipole magnet (determined at a reference radius of 17 mm and expressed in units of  $10^{-4}$ ). Blue curve: Measurement taken in the left aperture; green curve: Measurement taken in the right aperture; red curve: Calculation. The dashed red curve shows the calculated initial state curve for the sake of completeness (no measurements for the initial state curve presented). The measurements are taken for repeatedly up-down-up ramp cycles, whereas the calculation is carried out only for the major loop.

Figure 6.7 now shows a comparison of the calculated values of the multipole  $b_3$  at a reference radius of 17 mm and expressed in units of  $10^{-4}$  with measurements taken in both apertures (blue and green curves, respectively). This picture has already been presented in the introduction. As can be seen from the plot, there is a very good agreement between the measured and the calculated values. Both, the measurements and the calculations are taken for values of the magnetic induction below 1.6 T, which is the most interesting range, from the persistent current point of view. The deviation between the measurements taken in the left and right magnet aperture, respectively, are usually caused by little deformations of the coil or small errors in the cable positioning.

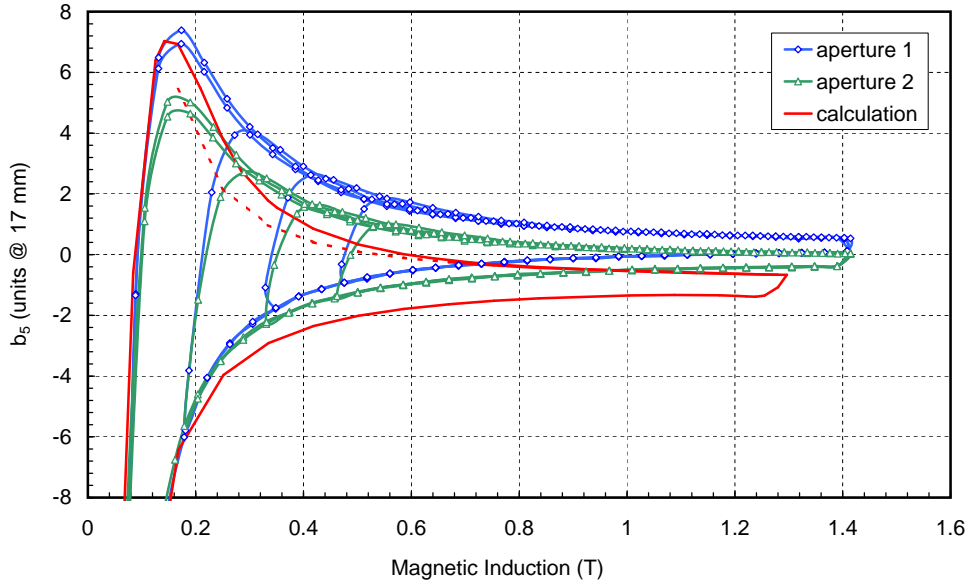


**Figure 6.8:** Comparison of the calculation and the measurements of the odd lower order multipole  $b_5$  for the LHC main dipole magnet (determined at a reference radius of 17 mm and expressed in units of  $10^{-4}$ ). Blue curve: Measurement taken in left aperture; green curve: Measurement taken in right aperture; red curve: Calculation. The dashed red curve shows the calculated initial state curve for the sake of completeness (no measurement for initial state curve presented). The measurements are taken for repeatedly up-down-up ramp cycles, whereas the calculation is carried out for the major loop, only.

The behavior of the lower odd order multipole  $b_5$  is shown in Fig. 6.8. Here as well, a very good agreement between the measured and the calculated values can be observed, although there is a bigger difference between the calculated and the measured values, compared to the difference for the  $b_3$  multipole. However, as can be seen from the plot by comparing the measurements taken in the left and the right magnet aperture, there also a considerable difference exists between the measurements of the two apertures. This is leading to the conclusion that there has been a noticeable deformation or cable position error in at least one of the coil cross-sections. This means that the coil cross-sections during the measurements are probably not identical with the cross-section which is taken for the calculation. Since the difference between the measured and the calculated value does not exceed the deviations between the two measured apertures, Fig. 6.8 presents a good result.

## 6.4 The LHC Main Quadrupole Magnet

The coils of the LHC main quadrupole magnets consist of two layers with 32 blocks in total, four on the outer and four on the inner coil layer of each quadrant. Both layers are connected in series. The coil is shaped in such a way as to make the best use of the superconducting material, while at the same time yielding the highest possible field gradient in the magnet aperture. Since the beam pipe has to be kept free, the coil is wound on a winding mandrel with saddle-shaped endspacers (in a similar way as is shown for the LHC main dipole coil) in a so-called constant-perimeter coil end (see for example, [8] for details on different coil ends).

In a similar way as for the LHC main dipole magnet, the coils are held in place by a stainless steel collar that is surrounded by the iron yoke inside the shrinking cylinder. The main quadrupole, however, has two separated collars (see Fig. 6.9 for the geometry, for example). In order to carry out the electromagnetic field calculations, it is sufficient to consider the structure including the cold mass whereas the influence of the outermost cryostat on the field in the aperture is negligible.

The cable of the LHC main quadrupole magnet is identical with the cable of the outer layer dipole cable which was discussed in detail in section 6.3.3, where the features of the dipole cable are shown.

### 6.4.1 Results

Figure 6.9 shows a ROXIE plot of the meshed structure of the quadrupole geometry consisting of the ferromagnetic iron yoke and the stainless steel collars. The model shown here is

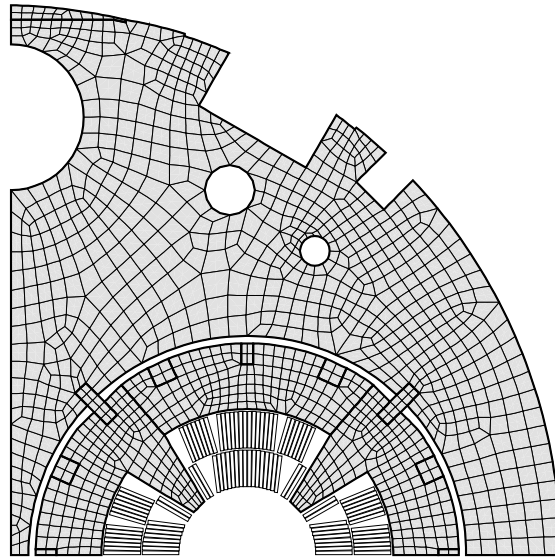


**Figure 6.9:** ROXIE model of one quadrant of the LHC main quadrupole magnet geometry in finite elements for application of the BEM-FEM method. The geometry includes the coil, the non-linear yoke structure and the stainless steel collars.

prepared for the application of the coupled BEM-FEM method, where only the iron domains have to be meshed. All air domains (as the region above the outer yoke radius or the holes

in the yoke structure) remain without a mesh. The coil geometry is not shown explicitly, but can be seen in Fig. 6.10, where the field distribution in the coil and the corresponding coil magnetization are plotted.

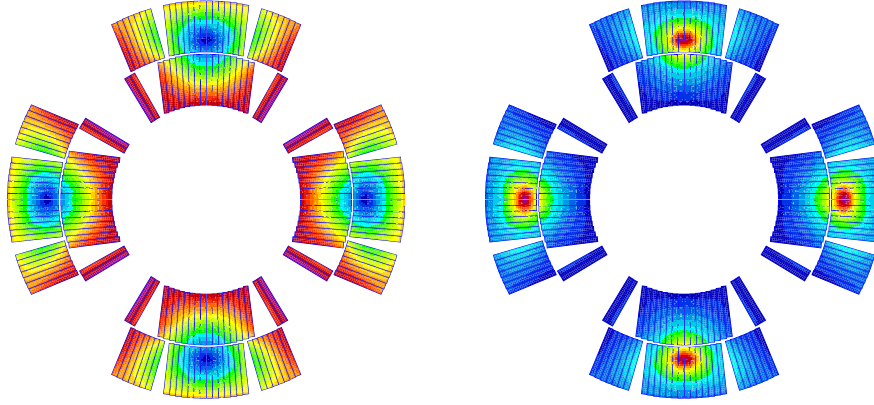


**Figure 6.10:** Left: Modulus of the magnetic induction,  $|B|$ , in the coil cross-section of the LHC main quadrupole magnet. Right: Coil magnetization resulting from the coil fields presented on the left-hand side. As can be seen from the plots, in case of a quadrupole geometry, four vortices (field drains) exist inside the coil geometry.

The dark blue regions in Fig. 6.10, left plot, indicate the low field areas (field drains), whereas in the red and magenta regions, the field is highest. On the right-hand side, the corresponding coil magnetization is shown. As expected, the plot of the magnetization shows an inverse behavior to the magnetic field in the cross-section. This results in a high magnetization value in the region of the field drains and a low magnetization in the high field areas.

In Figure 6.11, the values for the multipole  $b_6$  calculated at a reference radius of 17 mm and expressed in units of  $10^{-4}$  is presented. Also shown in this plot are the measurements taken at CERN. As can be seen from the curves, there is a good agreement between the measured and the calculated values. Both, the measurements and the calculations are presented for low field, only, since this is the interesting range from the persistent current point of view. The persistent current influence vanishes in the high field range, except for the non-reversibility of the superconductors arising from changes in the ramp direction, which is also the source of the hysteresis effect and remains in the curves. The measurements are taken for a repeatedly up-ramp cycle, whereas the calculation is carried out only for the major loop.

As can be seen from the curve, a small deviation by means of an off-set on the curve can be observed between the measured and the calculated data. As has already been explained in case of the LHC main dipole, such an offset is usually the result of a small conductor misplacement in the magnet cross-section. The shape of the curve, however, matches for the measured and calculated values. In order to illustrate this fact, the main quadrupole geometry has been re-calculated with a shift of  $0.5^\circ$  on the two conductors of the top inner block without applying any further optimization or inverse calculation. Figure 6.12 shows the calculated multipole  $b_6$  for an up-down-upramp cycle of the geometry after the shift is applied on the coil cross-section. For comparison, the measurement that has been shown in Fig. 6.11 already is presented as well. As can be seen from the pink curve of the calculated

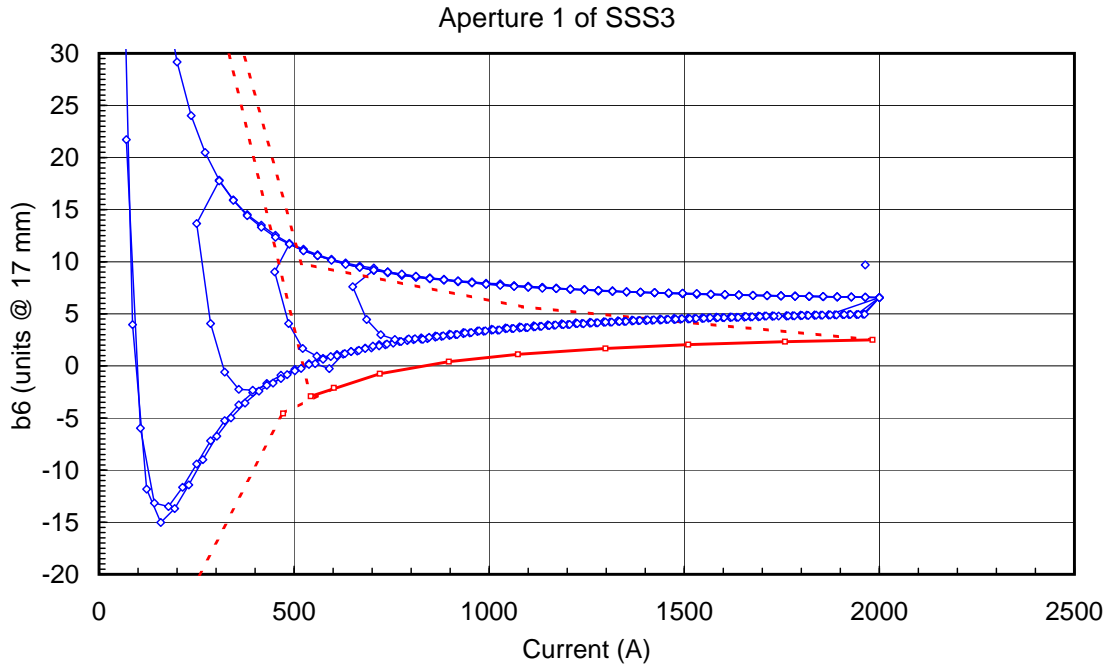


**Figure 6.11:** Comparison of the calculation of the even lower order multipole  $b_6$  for the LHC main quadrupole magnet (determined at a reference radius of 17 mm and expressed in units of  $10^{-4}$ ). Blue curve: Measurement taken in left aperture; red curve: Calculation. The dashed red curve shows the calculated initial state curve for the sake of completeness (no measurement for initial state curve presented) and the complete ramp loop. The measurements are taken for repeatedly up-down-up ramp cycles, whereas the calculation is carried out for the major loop, only. The continuous line is the operating area for the MQ magnet.

values, the geometrical value increased to about 6.5 units (which corresponds to an increase in the geometrical value of about 3 units compared to the results without the block shift, Fig. 6.11).

Though it cannot be claimed that this block shift is the exact source of the deviation between the measured and the calculated values that are presented in Fig. 6.11, it is a good illustration of the sensitivity of such a magnet geometry with respect to the conductor positioning. It also well illustrates the underlying task that is behind the calculation of magnet geometries in order to have an exact re-production of measured values. As has been already said before, concerning the calculation of persistent current effects, one is rather interested in the exact re-production of the *shape* of the measured curve, considering the shifts which are often observed of secondary interest.

In order to give also an idea of the field distribution in the yoke cross-section of the LHC main quadrupole, Figure 6.13 shows the modulus of the magnetic induction in the first quadrant of this magnet. The geometry includes the stainless steel collars.



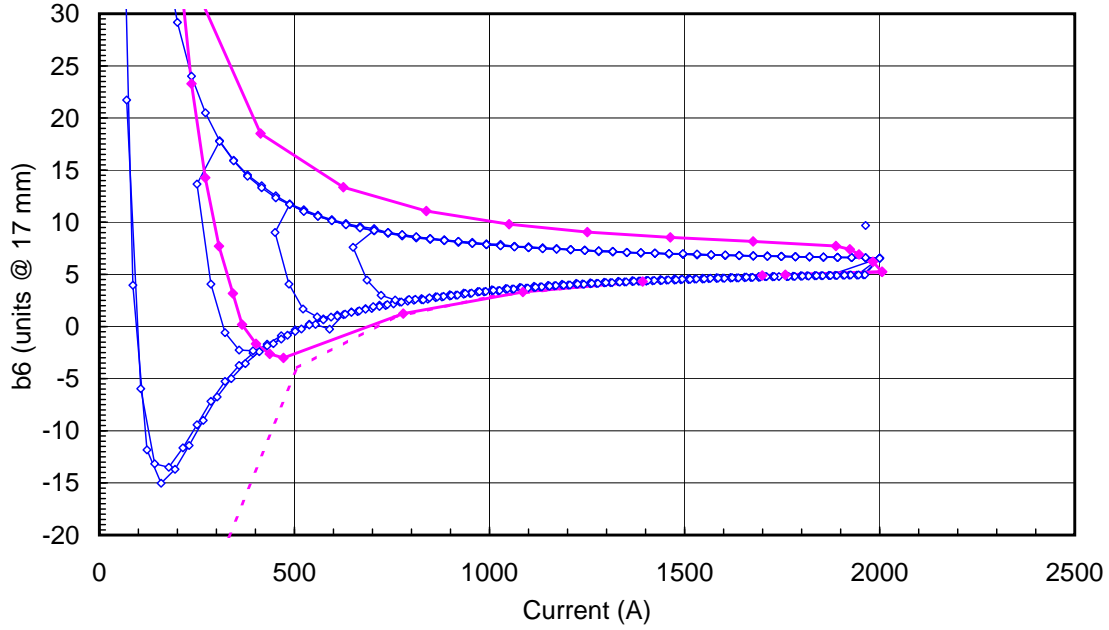


**Figure 6.12:** Comparison of the calculation of the even lower order multipole  $b_6$  for the LHC main quadrupole magnet (determined at a reference radius of 17 mm and expressed in units of  $10^{-4}$ ) with the measured value (blue curve). Here, the two conductors in the inner layer of the coil cross-section of the MQ magnet have been shifted angularly by  $0.5^\circ$ , producing a shift of the geometric value. The dashed line is the initial state curve (no measurements presented).

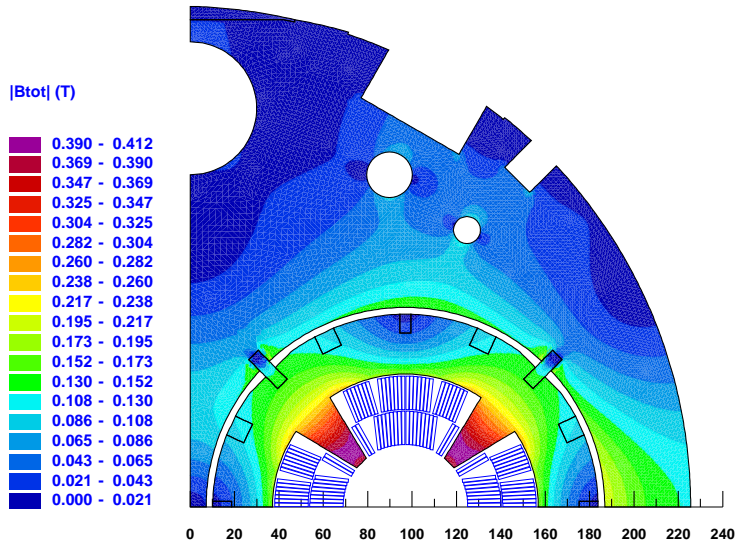


**Figure 6.13:** Modulus of the magnetic induction  $|B|$  of the first quadrant of the LHC main quadrupole cross-section including the stainless steel collars at low excitation current.



## 6.5 Calculation of the MCBX Orbit Corrector Magnet

It has been explained in detail in section 4.2 that the orientation of the magnetization that is produced by a filament in the case of an applied rotating field de-couples from the direction of the source field. It is therefore obligatory to consider the rotating field features for the calculation of the field errors in a superconducting magnet. In this section, these features will be illustrated by calculating a dipole orbit corrector magnet, the so-called MCBX magnet. The MCBX magnet is a superconducting single aperture (1-in-1) dipole corrector magnet which was designed at CERN. In total, 16 of these 0.6 m long dipole correctors are needed in the LHC ring for orbit correction.

The MCBX features two nested single-layer dipole coils which can be powered individually. The coil cross-section of this special magnet has already been shown in Fig. 4.17 in chapter 4, since it is an exemplary of a magnet which can be used for the production of rotating fields. The inner coil yields a vertical dipole field whereas the outer coil yields a horizontal dipole field. This way, by powering the layers individually with sine and cosine current patterns, a rotating field in the magnet aperture can be produced. Though the original objective of the MCBX magnet is beam orbit correction by providing an integrated dipole field of 1 Tm in any angular direction, it has been used here for the calculation of coil magnetization patterns in a magnet cross-section where the conductors are exposed to rotating fields.

The coils of the MCBX magnet are wound from a NbTi rectangular wire which is bound into a flat cable of 9 and 7 wires in the inner and the outer layer, respectively. The magnet is designed for an operating dipole field of 3.3 T per layer, operated at 1.9 K and an excitation current in the range of 360 to 600 A. The coil is incorporated into a circular iron yoke, the complete magnet design has been introduced in detail by Ang et al. [71] and is omitted here.

Powering this magnet in the above described current pattern of sine and cosine terms with an amplitude of about 110 A produces a dipolar field with any angle within the magnet aperture. The figures 6.5 and 6.5 show the coil cross-section of the MCBX magnet for different time steps. The yoke structure is not plotted. The actual time step is indicated in the left corner of each plot. On the left hand side of the Figs. 6.5 and 6.5, the resulting magnetic induction is shown whereas on the right hand side, the corresponding magnetization in the coils can be seen. The amount of the magnetization is illustrated by the colors following the legend. The orientation of the magnetization vectors can be seen from the small arrows plotted within the coil. In addition, for the magnetization plot, the orientation of the main field pattern which produces the magnetization is indicated by the black arrows inside the aperture. The coils are powered in such a way that the produced field in the magnet aperture rotates clock-wise

The purpose of these plots is to illustrate the fact that the orientation of the magnetization vectors in a coil cross-section (small arrows within the coil area) de-couple from the orientation of the main field (big arrows in the aperture of the coil) for the application of rotating fields.

The powering cycle is as follows:

1. Starting with time step 10, in which the outer coil is powered only, the field (left plot) is of dipolar type. The dark blue regions indicate the field drains (low field region). As can be seen, the inner coil is not powered, however, is exposed to the dipolar field which is produced by the outer layer. In the corresponding pattern of the coil magnetization shown on the right hand side, it can be seen that the magnetization is highest (red areas) in the regions where the source field is low (as expected). The amount of the induced magnetization can be interpreted by the color code in the legend; in addition, the orientation is shown by the small arrows which are plotted on top of the colored region. In the time step 10, the magnetization vectors are following the pattern of the source field (all opposite). It is now of interest to observe this pattern of the magnetization when the source field rotates.
2. In time step 20, the inner coil is powered also and the resulting magnetic field is obtained by superimposing the two contributions of the outer and the inner layer. Thus, the field has rotated clock-wise. The resulting field drains have moved accordingly inside the coil and the low field area enlarges on both coil layers. The bigger part of the low field area is located in the inner layer which is contributing a larger amount to the total field than the outer layer during this step. The corresponding magnetization pattern on the right hand side now shows the before-mentioned de-coupling of its vector orientation with respect to the field pattern. This can be best seen in the low field region (where the magnetization is highest, red area).
3. In time step 30, the field has further rotated clock-wise, the main contribution is coming from the outer coil layer, consequently the field drain is located there. For the magnetization vectors, the same principle which has already been observed in time step 20, repeats, showing a de-coupling of the magnetization vectors from the orientation of the source field. It is interesting to see here that the magnetization arrows do not recover their orientation in such a way that they oppose the source field although the source field now is back to almost a dipole type (as in the first plot, time step 10) with inverse sign.
4. In time step 40, the source field is rotated further, the two layers are powered with approximately equal strength, resulting in a field orientation of about  $270^\circ$ . It can be seen that the orientation of the magnetization vectors is fully de-coupled from the orientation of the source field vectors, their pattern becoming more complicated. Though the amount of magnetization stays highest in the low field region, the orientation is rectangular to the main field in the aperture and also does not oppose the local field pattern in this region.
5. In time step 55, the orientation of the source field is back to the starting value, however, due to the hysteresis in the magnetization, the orientation of the magnetization vectors still is in any direction, staying completely de-coupled from the vectors of the main (source) field.

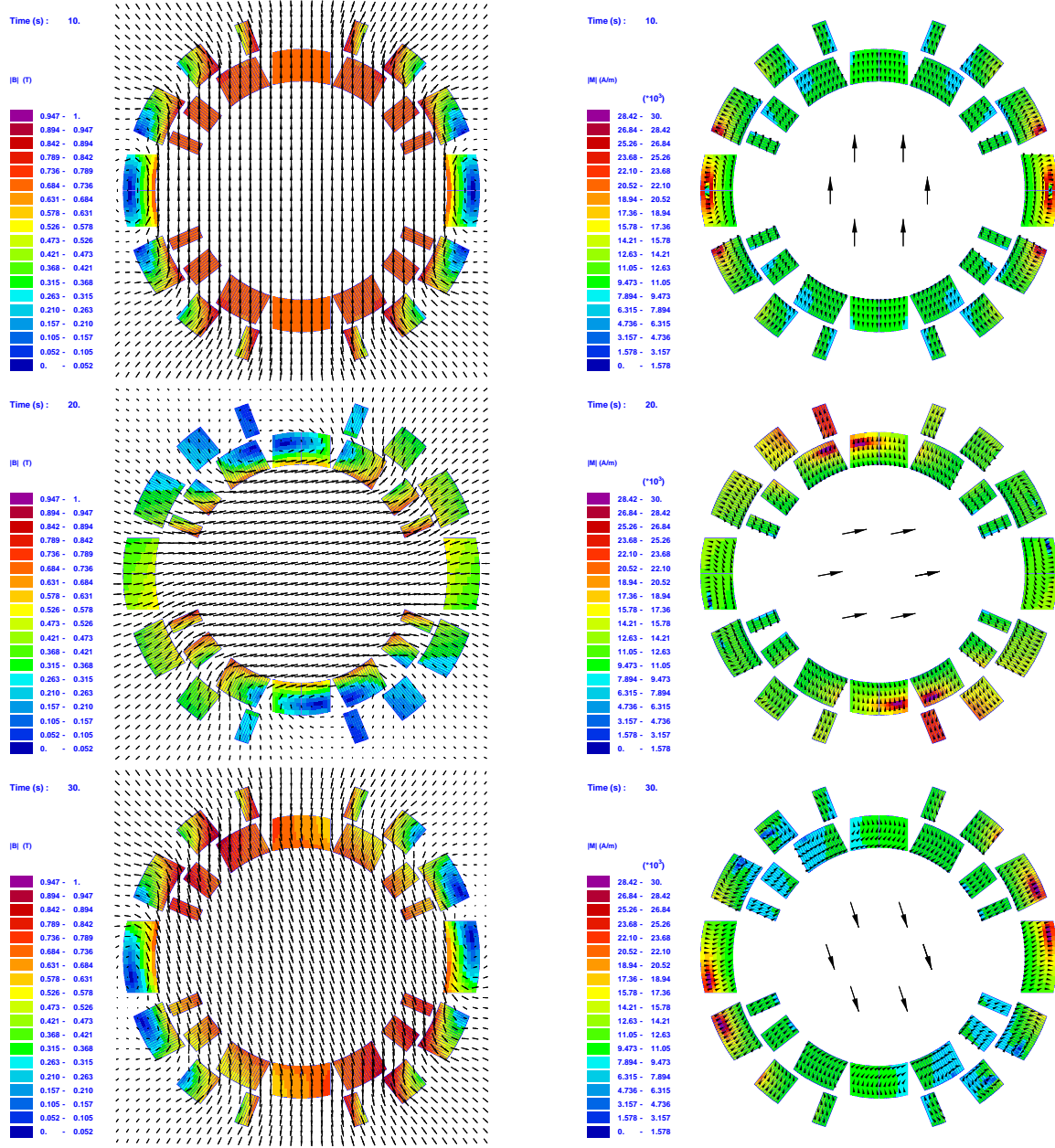


**Figure 6.14:** Coil cross-section of the superconducting MCBX magnet for various time steps in the rotating field case (time steps 10, 20, 30). Left: Magnetic induction in the cross-section; Right: Magnetization and orientation of the magnetization vectors in the coil. The arrows in the center of the right plots indicate the direction of the magnetic induction corresponding to the plot on the left side.

As a conclusion, it can be said that the magnetization within the cross-section of a superconducting coil that is exposed to rotating fields completely de-couples its orientation

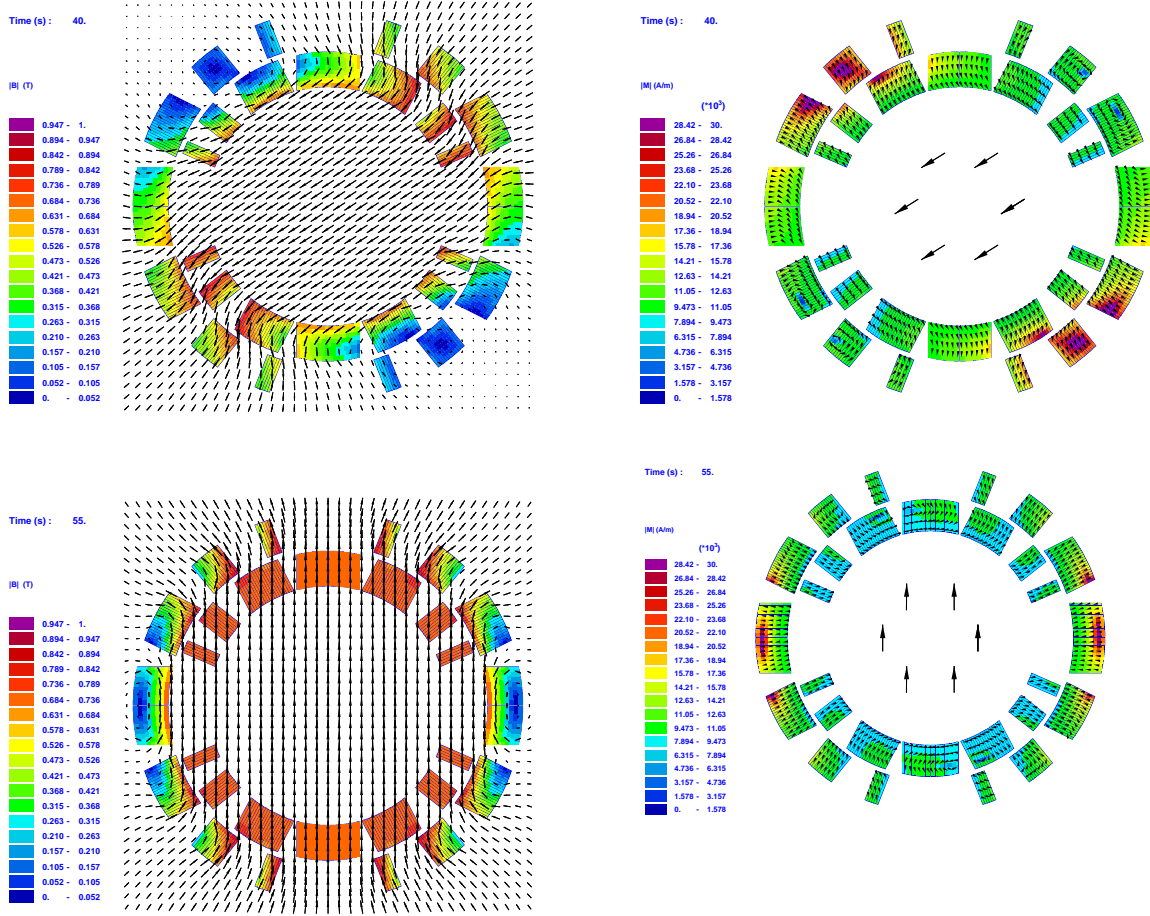


**Figure 6.15:** Coil cross-section of the superconducting MCBX magnet for various time steps in the rotating field case (time steps 40 and 55). Left: Magnetic induction in the cross-section; Right: Magnetization and orientation of the magnetization vectors in the coil. The arrows in the center of the right plots indicate the direction of the magnetic induction corresponding to the plot on the left side.

from that of the source field. As a consequence, the field errors which are resulting from such an induced magnetization have to be calculated by considering the local distribution of the magnetization and cannot be derived from the orientation of the main field component. Consequently, the calculation of field errors by applying a 1-dimensional magnetization model in such a magnet type as the MCBX will not result in a correct reproduction of the induced persistent current field errors.

## Chapter 7

# Field Errors from Persistent Currents

In chapter 6, the field errors in the LHC dipole and quadrupole magnet and the combined orbit corrector magnet including the errors due to the coil magnetization are calculated. In this chapter, some important features to be considered when calculating these field errors are explained. First, the determination of the value of an equivalent pair of replacement currents is shown for the magnetization of an LHC strand at low field. A replacement of a magnetic moment  $\mathbf{m}$  is possible in the far-field region of a field calculation. Then, the calculation of the vector potential which results from a magnetic moment in the plane is shown. Expressions for the multipoles are derived and also for the magnetic field in the vicinity of such a magnetized strand are given .

### 7.1 Multipole Expansion from the Magnetic Moment

Usually, the field quality in the aperture of a magnet is expressed by the Fourier coefficients of the series expansion of the radial main field component [72]. In this section the multipole expansion resulting from the source of a magnetic moment  $\mathbf{m}$  is derived. The general theory of Fourier series expansion is described in appendix A.2.

In order to compare the amount of persistent currents that have to be expected within a coil which is driven by a certain transport current, the following example can be exercised: For far-field calculations which are carried out in a reasonable distance to the magnetic source, the magnetic moment per unit length  $l$  of a strand with cross-section  $A$ ,  $\mathbf{m}/l = A\mathbf{M}$ , can be substituted by a small dipole of (replacement) line-currents with the strength  $-I_s$  and  $I_s$ . This pair of line-currents is separated by a distance  $S$  and oriented perpendicular to the direction of the magnetic moment. The magnetic moment of such a single dipole  $m/l = I_s S$  must equal the magnetic moment which arises from persistent currents. Therefore the replacement currents read:

$$I_s = \frac{MA}{S}, \quad (7.1)$$

where the distance between the currents,  $S$ , can be chosen to be the strand diameter.

A strand taken from the LHC main dipole cable has a diameter of 1.065 mm and therefore a cross-sectional area of approximately  $A = 0.9 \text{ mm}^2$ . In the case of low fields, the cable cross-section carries a transport current of about 500 to 1000 A. Consequently, a substitute current

of about 6.65 A (maximum value) at low field level ( $\approx 0.7$  T) is received for such a strand which compares to about 20 A of transport current in each strand. This equivalent pair of line currents can then be used for the calculation of field errors resulting from the superconductor magnetization.

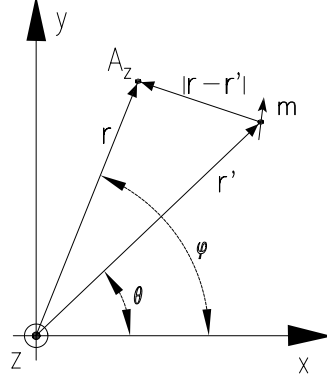


**Figure 7.1:** Coordinate system for the calculation of the magnetic vector potential  $\mathbf{A}$  from the magnetic moment  $\mathbf{m}$ .

However, it is also possible to receive the (persistent current) induced field errors directly from the vector potential which is calculated at an evaluation point  $\mathbf{r}$  while the magnetic moment is given at a source point  $\mathbf{r}'$ , as indicated in Fig. 7.1. The derivation starts from the expression for the magnetic vector potential:

$$\mathbf{A}(\mathbf{r}) = -\frac{\mu_0 \mathbf{m}(\mathbf{r}') \times (\mathbf{r} - \mathbf{r}')}{4\pi |\mathbf{r} - \mathbf{r}'|^3} = \frac{\mu_0 \mathbf{m}(\mathbf{r}')}{4\pi} \times \nabla_r \frac{1}{|\mathbf{r} - \mathbf{r}'|} = -\frac{\mu_0 \mathbf{m}(\mathbf{r}')}{4\pi} \times \nabla_{r'} \frac{1}{|\mathbf{r} - \mathbf{r}'|},$$

which holds in three dimensions and

$$\mathbf{A}(\mathbf{r}) = -\frac{\mu_0 \mathbf{m}(\mathbf{r}')}{2\pi} \times \nabla_{r'} \ln \frac{|\mathbf{r} - \mathbf{r}'|}{a} \quad (7.2)$$

which holds for two-dimensional problems, respectively. Here,  $|\mathbf{r} - \mathbf{r}'|$  indicates the distance between the source- and evaluation point whereas  $a$  is an arbitrary reference distance.

The logarithmic term can be expressed from the particular solution of Poisson's Equation as:

$$\ln \frac{|\mathbf{r} - \mathbf{r}'|}{a} = \ln \frac{R}{a} = \frac{A_z}{-\frac{\mu_0 I}{2\pi}}, \quad (7.3)$$

so that the vector potential reads:

$$\mathbf{A}(\mathbf{r}) = -\frac{\mu_0 \mathbf{m}(\mathbf{r}')}{2\pi} \times \nabla_{r'} \left( \frac{A_z}{-\frac{\mu_0 I}{2\pi}} \right). \quad (7.4)$$

The distance between the source point and the evaluation point  $R$ , used in Eq. (7.3), can be expressed by means of the Cosine Law to be:

$$R^2 = r^2 + r'^2 - 2rr' \cos(\varphi - \theta)$$

and rewritten as [9]:

$$R^2 = r'^2 \left(1 - \frac{r}{r'} e^{i(\varphi-\theta)}\right) \left(1 - \frac{r}{r'} e^{-i(\varphi-\theta)}\right).$$

Thus, the logarithmic expression reads:

$$\ln\left(\frac{|\mathbf{r} - \mathbf{r}'|}{a}\right) = \ln\left(\frac{r'}{a}\right) + \frac{1}{2} \ln\left(1 - \frac{r}{r'} e^{i(\varphi-\theta)}\right) + \frac{1}{2} \ln\left(1 - \frac{r}{r'} e^{-i(\varphi-\theta)}\right).$$

Applying the Taylor Series expansion of  $\ln(1 - x)$  which for  $|x| < 1$  (here:  $r < r'$ ) reads<sup>1</sup>:

$$\ln(1 - x) = - \sum_{n=1}^{\infty} \frac{1}{n} x^n,$$

the expression for the magnetic vector potential results in:

$$\frac{A_z}{-\frac{\mu_0 I}{2\pi}} = \ln\left(\frac{r'}{a}\right) - \sum_{n=1}^{\infty} \frac{1}{n} \left(\frac{r}{r'}\right)^n \cos(n(\varphi - \theta)). \quad (7.5)$$

Now applying the Nabla operator in cylindrical coordinates<sup>2</sup> on Eq. (7.5) yields:

$$\nabla_{r'}\left(\frac{A_z}{-\frac{\mu_0 I}{2\pi}}\right) = \frac{1}{r'} \left[ \left(1 + \sum_{n=1}^{\infty} \left(\frac{r}{r'}\right)^n \cos(n(\varphi - \theta))\right) \mathbf{e}_{r'} - \sum_{n=1}^{\infty} \left(\frac{r}{r'}\right)^n \sin(n(\varphi - \theta)) \mathbf{e}_{\theta} \right].$$

Introducing this result in Eq. (7.4) and solving the cross-product yields

$$\mathbf{A}(\mathbf{r}) = \frac{\mu_0}{2\pi r'} \mathbf{e}_z \left[ -m_{r'} \sum_{n=1}^{\infty} \left(\frac{r}{r'}\right)^n \sin(n(\varphi - \theta)) - m_{\theta} \left(1 + \sum_{n=1}^{\infty} \left(\frac{r}{r'}\right)^n \cos(n(\varphi - \theta))\right) \right].$$

For the evaluation of the Fourier Series expansion, the radial field component of the magnetic induction  $B_r(r_0)$  at a defined reference radius  $r_0$  is needed (see appendix A.2).

Since  $B_r(r_0, \varphi) = \frac{1}{r_0} \frac{\partial A_z}{\partial \varphi}$ , one can apply the trigonometric identities<sup>3</sup> and in this way express the radial component of the magnetic induction to:

$$\begin{aligned} B_r(r_0, \varphi) &= \frac{\mu_0}{2\pi r_0 r'} \left[ -m_{r'} \sum_{n=1}^{\infty} \left(\frac{r_0}{r'}\right)^n n (\cos n\varphi \cos n\theta + \sin n\varphi \sin n\theta) \right. \\ &\quad \left. + m_{\theta} \sum_{n=1}^{\infty} \left(\frac{r_0}{r'}\right)^n n (\sin n\varphi \cos n\theta - \cos n\varphi \sin n\theta) \right], \\ &= \frac{\mu_0}{2\pi r_0 r'} \left[ \sum_{n=1}^{\infty} n \left(\frac{r_0}{r'}\right)^n (-m_{r'} \cos n\theta - m_{\theta} \sin n\theta) \cos n\varphi \right. \\ &\quad \left. + \sum_{n=1}^{\infty} n \left(\frac{r_0}{r'}\right)^n (-m_{r'} \sin n\theta + m_{\theta} \cos n\theta) \sin n\varphi \right]. \end{aligned}$$

<sup>1</sup>The condition  $r < r'$  is always fulfilled when calculating a magnet structure, since the multipoles are calculated inside the magnet aperture.

<sup>2</sup>The Nabla operator in the cylindrical coordinate system which is applied here reads:  $\nabla_{r'} = \frac{\partial}{\partial r'} \mathbf{e}_{r'} + \frac{1}{r'} \frac{\partial}{\partial \theta} \mathbf{e}_{\theta}$ . No  $z$ -component is necessary due to the calculation in the plane.

<sup>3</sup> $\sin(n\varphi - n\theta) = \sin n\varphi \cos n\theta - \cos n\varphi \sin n\theta$ ,  $\cos(n\varphi - n\theta) = \cos n\varphi \cos n\theta + \sin n\varphi \sin n\theta$ .

Finally the multipole coefficients resulting from the magnetic moment can be expressed as:

$$\begin{aligned} A_n &= \frac{\mu_0}{2\pi} \frac{r_0^{n-1}}{r'^{n+1}} n(m_{r'} \cos n\theta + m_\theta \sin n\theta) , \\ B_n &= \frac{\mu_0}{2\pi} \frac{r_0^{n-1}}{r'^{n+1}} n(m_{r'} \sin n\theta - m_\theta \cos n\theta) . \end{aligned}$$

As is also explained in the appendix A.2, the values  $B_n$  are denoted as the normal and the values  $A_n$  as the skew components of the field while  $b_n$  are the normal relative and  $a_n$  the skew relative field components, all given at a reference radius  $r_0$ . The latter are dimensionless and usually expressed in units of  $10^{-4}$ .

As an example of the contribution of the strand magnetization to field errors in the LHC dipole coil, the resulting  $B_3$  field component in the coil cross-section evaluated at 17 mm reference radius is shown in Fig. 7.2. The left plot shows the harmonic  $B_3$  resulting from the transport currents and the right plot the same harmonic resulting only from the persistent currents.

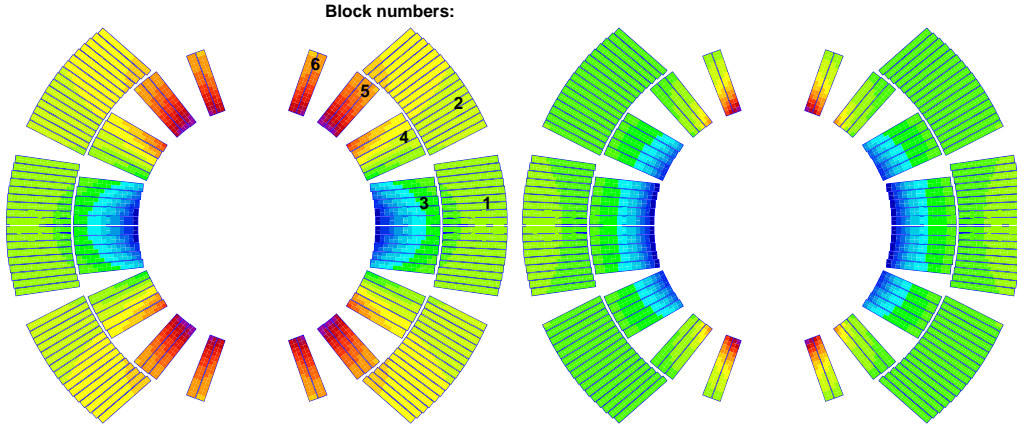


**Figure 7.2:** Left: Contribution of the source current to the  $B_3$  field component; Right: Contribution of the strand magnetization to the  $B_3$  field component. The calculation has been carried out at 17 mm reference radius for a very low source current of 12 A in the coil.

The regions in the coil cross-section of high contribution to  $B_3$  are represented by the dark red and mauve coloured areas, whereas the regions in green contribute little to the total  $B_3$ . The demonstration of such a field error distribution in the coil cross-section for individual multipoles is of interest since it allows to identify which region of the coil acts as the source of a certain unwanted multipole.

The coil blocks can now be arranged in such a way that the multipoles resulting from the coil geometry are minimized, if only the source currents are considered. However, a comparison of the two plots shows, that the  $B_3$  component from persistent currents arises mainly from the coil block number 6 (top block in the inner coil layer), whereas in the case of source currents, block number 5 dominates. From this, it can be concluded that it is not possible to fully suppress the persistent current induced  $B_3$  component by means of changing the design of the coil cross-section in such a way that the total persistent current induced  $B_3$  component is canceled out by the  $B_3$  component which is arising from source currents.



## 7.2 Resulting Field of Neighboring Strands

In order to determine the resulting magnetic induction at a certain strand position, the initially applied magnetic induction has to be superimposed with the inductions arising from the induced persistent currents of all other strands. However, Eq. (7.1) may not be applied on strands in the immediate vicinity of the evaluation point, since the substitute current loop  $I_s$  only produces an approximate, and not a pure, dipole field in the near-field region<sup>4</sup>. Hence, also the magnetic induction has to be determined from the magnetic moment  $\mathbf{m}$ .

Starting from Eq. (7.2) in the 2D plane, the magnetic induction at the evaluation point  $\mathbf{B}(\mathbf{r})$  results from  $\mathbf{A}(\mathbf{r})$  by  $\mathbf{B} = \nabla \times \mathbf{A} = -\mathbf{e}_z \times \nabla A_z$ , since  $\mathbf{A}$  only has a component in the  $z$ -direction. In contrary to the determination of the multipoles shown in section 7.1, the gradient of the logarithmic function has to be evaluated and reads in cylindrical coordinates:

$$\nabla_{r'} \ln(|\mathbf{r} - \mathbf{r}'|) = -\mathbf{e}_r' \frac{r_0 \cos(\varphi - \theta) - r_i}{|\mathbf{r} - \mathbf{r}'|^2} + \mathbf{e}_\theta \frac{r_0 \sin(\theta - \varphi)}{|\mathbf{r} - \mathbf{r}'|^2},$$

and in cartesian coordinates, respectively:

$$\nabla_{r'} \ln(\sqrt{(x - x')^2 + (y - y')^2}) = -\frac{1}{(x - x')^2 + (y - y')^2} ((x - x') \mathbf{e}_x + (y - y') \mathbf{e}_y).$$

Thus, the vector potential given in Eq. (7.2) and the resulting magnetic induction in cartesian coordinates read:

$$A_z(x, y) = \frac{\mu_0}{2\pi} \frac{m_x(y - y') - m_y(x - x')}{(x - x')^2 + (y - y')^2},$$

$$B_x(\mathbf{r}) = \frac{\mu_0}{2\pi} \left[ \frac{m_x}{(x - x')^2 + (y - y')^2} + \frac{2(m_y(x - x') - m_x(y - y'))(y - y')}{((x - x')^2 + (y - y')^2)^2} \right] \quad (7.6)$$

and

$$B_y(\mathbf{r}) = -\frac{\mu_0}{2\pi} \left[ -\frac{m_y}{(x - x')^2 + (y - y')^2} + \frac{2(m_y(x - x') - m_x(y - y'))(x - x')}{((x - x')^2 + (y - y')^2)^2} \right] \quad (7.7)$$

The vectors  $\mathbf{r}, \mathbf{r}'$  are the position vectors of the evaluation point and source point, respectively and in cartesian coordinates read  $\mathbf{r} = \sqrt{x^2 + y^2}$  and  $\mathbf{r}' = \sqrt{x'^2 + y'^2}$ . According to Fig. 7.1, the Eqs. (7.6) and (7.7) denote the resulting field components at the position  $\mathbf{r}$  from one strand with the induced superconductor magnetization  $\mathbf{M}(\mathbf{r}')$  at the position  $\mathbf{r}'$ . For the evaluation of the contribution of the complete coil, the contribution of all strands has to be calculated from the sum of the individual strand fields.

It has to be emphasized that the replacement of the strand/filament magnetizations by an equivalent pair of line currents will cause not only a numerical problem for the field solver since per definition the distance of separation of the currents in the pair should go to zero (whereas the value of the substitute current strives to infinity). Moreover, the calculation is simply incorrect in the near field region of the current pair and therefore the derivation of the expressions presented above is inevitable. Figure 7.3 shows the evaluation of the harmonic analysis of the resulting magnetic induction in the direct vicinity of an arbitrarily chosen strand.<sup>5</sup> It can be seen from the plot that the source currents are producing a pure dipole field

<sup>4</sup>It is clear from the definition of the magnetic dipole that an ideal dipole field will be received only if the encircled area  $A$  in the equation of the dipole moment  $\mathbf{m} = I \mathbf{A}$  approaches the null value, whereas the application implies a finite substitute area, however small.

<sup>5</sup>The direct vicinity is the position of the next strand in the cable, for example.

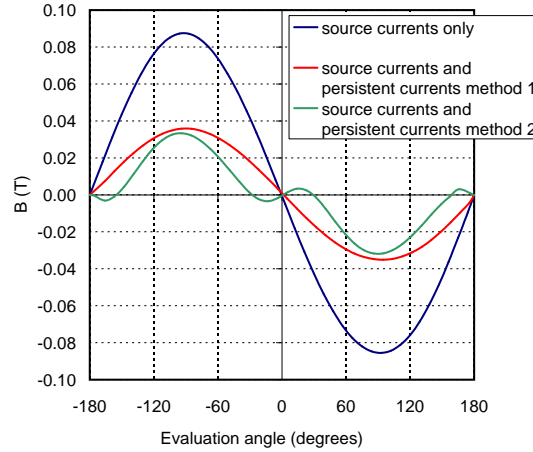


**Figure 7.3:** Harmonic analysis of the resulting magnetic induction of one strand evaluated in its direct vicinity. Blue curve: source currents only; Red curve: source currents and persistent currents; Green curve: Source currents and persistent currents where the screening field is calculated from an equivalent pair of substitute line currents.

(blue curve) which is damped (but stays dipolar!) if the persistent current effect is calculated by means of the method 1, i.e. following the Eqs. 7.6 and 7.7 (red curve). Applying the method of an equivalent pair of line currents is, however, producing a field harmonic which is not dipolar anymore (green curve); instead higher order multipoles are artificially introduced. The method is therefore inappropriate for the calculation of field errors in the aperture of a superconducting magnet.

### 7.3 Influence of the Ramp Cycle on the Induced Field Errors

In order to keep the orbit of the particles in a circular accelerator stable with increasing particle energy, the bending field of the main dipole magnets has to increase accordingly. This increase in field strength is called ramping of the magnets and the ramping pattern is called a ramp cycle. Figure 7.4 shows the ramp cycle for the LHC main dipole magnets. The total ramp cycle usually differs from the final *operating cycle* of the magnet – the LHC main dipoles, for instance, are ramped up to a high field and then down again, before in the second up-ramp branch, the beam is injected and the actual operating cycle starts. This pre-cycle is carried out to bring all the magnets in a defined state for both, the iron and the superconductor magnetization that, in addition, is identical for each individual magnet (a random pattern of magnetization histories along the beam trajectory is unwanted).

Now, the magnetization of each strand strongly depends on the history seen by the superconductor and hence on the applied ramp cycle. This means that for a magnet, the chosen ramp cycle influences the resulting total field errors at injection field level as well as the variation  $\Delta b_n$  during the operating interval<sup>6</sup>. In fact, the actual variation is mainly determined by the turning point at which the low field in the down-ramp branch ends and the applied field

<sup>6</sup>When calculating the multipole variation for a certain magnet without persistent currents, no variation in the operating cycle for different ramp cycles occurs. The ramping is fully reversible.

increases again (the so-called low field turning point, see also Fig. 7.4). At low field the strong increase of the critical current density results in an equally strong rise in the superconductor magnetization and from this also in an increase of the persistent current induced field errors. The value of the low field turning point is therefore of significance concerning the persistent current pattern and has to be chosen with caution. In this context, one also has to consider that the local field being experienced by the individual strands varies considerably depending on their position in the coil cross-section. This is due to the distribution of the applied field in the coil cross-section from which each strand will see its own ramp cycle and assume its own history.

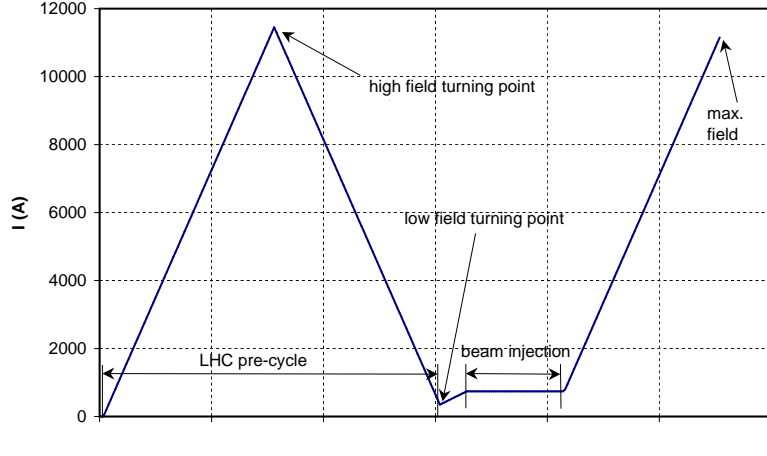


**Figure 7.4:** Actual scheduled current ramp cycle of the LHC main dipole magnet. After one pre-ramp without beam, the beam is injected at low field of the second up-ramp branch. For the calculation of the field errors in the magnet's aperture resulting from persistent currents, the low field turning point is of importance.

The effect of the value of the low field turning point is illustrated by the calculation of different ramp cycles with varying values of the low field turning being calculated exemplary for the geometry of an LHC main dipole coil. The dipole coil is incorporated into a 1-in-1 iron yoke structure with a circular inner yoke radius of 98 mm. This easy geometry has been chosen in order to simplify the recognition of the observed effects and shows the effect without loss of generality. The calculations resulted in a change of the slope of the multipole components. The graphs in Figure 7.5 show the influence of a change in ramp cycle on multipole  $b_3$  versus the source current in the coil. In Figure 7.5 (left), the complete ramp cycle as a function of the value of the low field turning point, for three different turning points is presented. The change occurs in the interval of  $I = [500, 1000]$  A of the operating cycle (the framed yellow box on the second up-ramp branch). Figure 7.5 (right) presents this interval for the same turning points of B(0A), B(350A) and B(500A) (the plot corresponds to the yellow box). Also shown in Fig. 7.5 is the curve for the turning point of B(600A). The presented values can also be found in table 7.1

As can be seen from the plots in Fig. 7.5 and from table 7.1, the multipole variation of  $b_3$  increases with decreasing values of the low field turning point and a maximum in variation is reached for the turning point at zero field. From this result, it is therefore recommendable to choose the turning point at a current as high as possible in order to reduce the variation,  $\Delta b_3$ ,

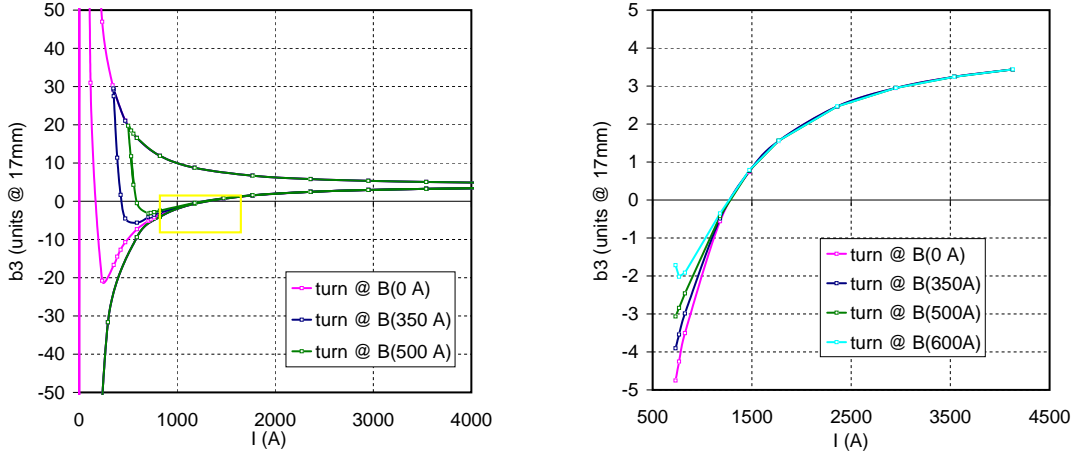


**Figure 7.5:** Left: Hysteresis curve of multipole  $b_3$  calculated at 17 mm reference radius versus the source current in the coil. The curves show the dependence of the  $b_3$ -hysteresis on different low field turning points in the second up-ramp branch. The yellow box indicates the interval where the change in the  $b_3$ -values occurs. Right: Variation of  $b_3$  on the second up-ramp branch in the interval of  $I = [500, 1000]$  A.

$I_{\text{turn}}$	$B_{\text{turn}}$	$b_3$	$b_3$	$\Delta b_3$	$b_5$	$b_5$	$\Delta b_5$
		$B_{\text{main}} \approx 0.5 \text{ T}$	$B_{\text{main}} \approx 3 \text{ T}$		$B_{\text{main}} \approx 0.5 \text{ T}$	$B_{\text{main}} \approx 3 \text{ T}$	
1	0.0004	-4.753	3.438	8.191	0.249	-0.819	1.067
350	0.2547	-4.161	3.439	7.599	0.484	-0.819	1.303
400	0.2906	-3.903	3.439	7.342	0.529	-0.819	1.348
448	0.3256	-3.602	3.439	7.041	0.584	-0.819	1.403
500	0.3632	-3.197	3.439	6.636	0.669	-0.819	1.488
602	0.4368	-0.984	3.439	4.423	0.754	-0.819	1.573

**Table 7.1:** Multipoles  $b_3$  and  $b_5$  calculated at 17 mm radius for low field levels and for  $B \approx 3 \text{ T}$  as a function of the low field turning point in the LHC operating cycle.

on the multipole  $b_3$ . However, it can also be seen that the gain in reducing the multipole variation of  $b_3$  by changing the ramp-cycle is limited. A pay-off can be observed in the multipoles, since the measures to reduce the variation of multipole  $b_3$  cause an increase in the variation of multipole  $b_5$ . Moreover, for low field turning points, above  $\approx 550 \text{ A}$ , the onset of the  $b_3$  curve is increasing again and the reduction in the variation will partially be lost with further increase. Considering the multipole  $b_5$  in this example, a deterioration can already be observed for values of  $I_{\text{turn}}$  above 400 A. The higher order multipoles (not shown) are hardly influenced by the value of the current at the turning point.

Thus, considering also the behavior of multipole  $b_5$ , a relative optimum can be found for the geometry considered here by setting the low field turning point at a source current of about 550 A.

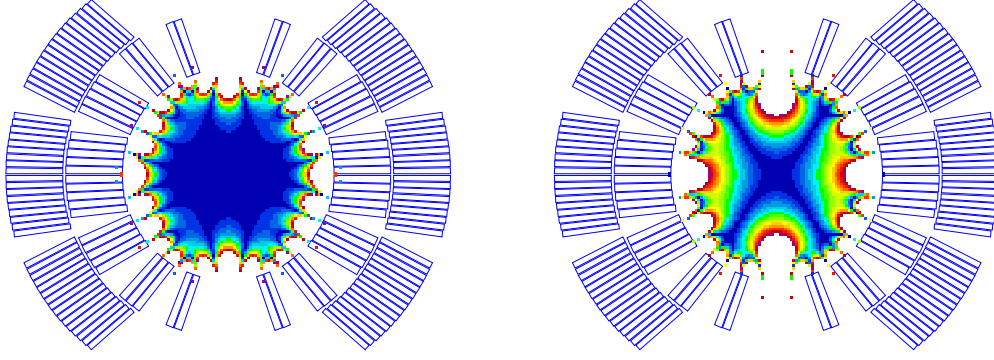


**Figure 7.6:** Field quality in the aperture of the main dipole coil at a field level of about 0.5 T (main field component). Left: Low field turning point at B(350 A); Right: Low field turning point chosen at B(0 A). The dark blue region indicates the homogeneous field region (the so-called good field region).

Figure 7.6 shows the calculated field quality in the aperture of the main dipole coil. As already explained, the coil is placed in a circular iron yoke structure with a 98 mm inner yoke radius for this simulation. The plots show the distribution of the field homogeneity in the magnet aperture and are therefore a measure of the dynamic beam aperture. The dark blue region is denoted as good field region in which the field homogeneity is at its maximum. Consequently, the size of the dark blue region desired to be as large as possible. The total deviation is calculated from

$$\left| 1 - \frac{B_y}{B_{\text{nom}}} \right| \begin{cases} < 0.1 \cdot 10^{-4} & \text{dark blue area} \\ > 2 \cdot 10^{-4} & \text{white areas} \end{cases}$$

Both field quality plots are determined at a main field component of 0.5 T, received after different low field turning points in their ramp cycles. In the left plot, the low field turning point is chosen at B(350 A), resulting in a satisfyingly good field region for low excitation fields. The right plot shows the field quality as received after setting the low field turning point to B(0 A). As can be seen from the plot, a strong reduction of the size of the good field region is the result in this case. The plots clearly illustrate the influence of the value of the low field turning point on the field quality, for instance, at injection field level.

## 7.4 Hysteresis Losses in Strands

Hysteresis losses occur in each filament of the superconducting coils in accelerator magnets. They are a major source of energy dissipation and have to be considered when calculating the heat load of the cryogenic plant. The source of the hysteresis are the pinned flux vortices, which cannot move out of the material freely, but are trapped inside the superconductor. They are then the source of a hysteresis of the magnetic induction inside the filament, as well as the cause of a hysteresis in the filament magnetization. The loss calculation in superconductors is similar to the loss calculation in ferromagnetic samples. Energy may be stored inductively in the current pattern in the superconductor during a field cycle. The energy loss of a magnet can then be calculated by means of an integration over the magnetization of each filament

during the magnet cycle. In general, the energy loss of one filament  $p$  is given by:

$$Q_p^{\text{hyst}} = \oint \frac{1}{\mu_0} M_p(B_p(\mathbf{r})) d\mathbf{B}, \quad (7.8)$$

where  $\mathbf{r}$  denotes the position of the filament in the magnet cross-section and  $B_p(\mathbf{r})$  is the local field which is experienced by the considered filament. The energy loss is given in  $\frac{\text{Ws}}{\text{m}^2}$ . Finally, the total hysteresis loss is calculated as the sum of the losses of all filaments:

$$Q^{\text{hyst}} = \sum_p Q_p^{\text{hyst}},$$

where  $p$  denotes the filament number.

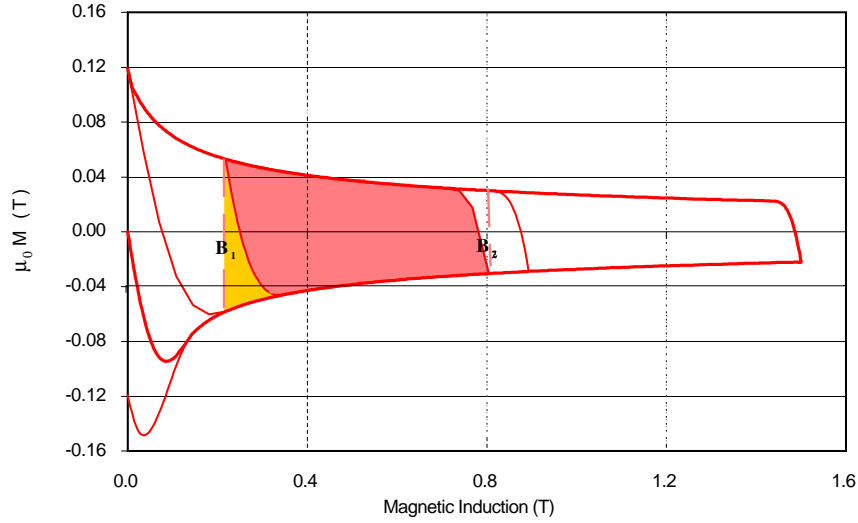


**Figure 7.7:** Hysteresis loss calculation for a superconducting filament. For the loss calculation, a closed cycle has to be calculated, excluding the yellow area which may not be part of the integration.

The loss integral formula, Eq. (7.8), is only correct if the integration is carried out along a closed cycle, as indicated by the closed integral loop. Contrary to expressions often given in literature, it is not sufficient to integrate the first quadrant of the  $M(B)$ -curve and multiply the outcome with a symmetry factor (for example two in case of an up-down-up ramp cycle from  $0T \rightarrow \text{maximum field} \rightarrow 0T$  or four in case of an up-down-up ramp cycle also covering the negative range). The reason for that is the unsymmetry of the magnetization curve. However, depending on the operating cycle, a symmetry with respect to the ordinate axis is a good assumption in case the cycle does not include the initial state curve. As shown in Fig. 7.7, a loop from  $B_1$  to  $B_2$  encompasses the red area, however, the yellow area may not be part of the integration and has to be subtracted from the total calculated losses. The dissipated power, given in watts, results from the total loss per cycle time (given in seconds):

$$P_h = \frac{Q^{\text{hyst}}}{\text{cycletime}}.$$

The dissipated power is calculated in watts. For the LHC superconducting dipole, during one complete up-down-upramp cycle up to injection field level, the energy loss has been calculated to  $Q^{\text{hyst}} = 281.9 \text{ Ws/m}$ .

Thus, the dissipated power results to:

$$P_h = 281.9 \frac{\text{Ws}}{\text{m}} \underbrace{14.7\text{m}}_{\text{magneticlength}} / 20\text{min} = 3.5\text{W}$$





## Chapter 8

# Compensation of Persistent Current Induced Multipole Errors

As has been shown in the chapters 6 and 7, persistent current effects in the coils of superconducting accelerator magnets are a source of unwanted multipoles and a multipole hysteresis. The resulting deterioration in field quality is most critical at low field levels, since then the particle beam is injected and at the same time, the persistent current influence is at its maximum. In the case of the LHC dipoles, the persistent current induced field errors reduce to a negligible amount for higher fields. However, for corrector magnets, which are powered in several up-down-up ramps, not only the induced currents persist, but also the hysteresis on the multipoles can be a problem. It has also been shown in section 7.3 that the persistent currents influence the setting of the ideal ramp cycle for the LHC main dipoles, for instance.

In this chapter, a practical application of the developed Nested Ellipse Model is presented. The model is used to calculate a reduction and partial compensation of the persistent current induced field errors by means of different compensation principles. A main part of this chapter is taken by compensations with ferromagnetic shims in various shapes and positions which are inserted into the magnet cross-section. Also, the compensation by means of an insertion of passive (non-powered) superconducting shims or rods is investigated. This methods have partially been introduced in [73] and [74]. In any case, the main idea behind these compensations is, to add materials which only react on the applied field at low field levels, since the persistent current effect vanishes for higher fields. Thin, ferromagnetic shims will saturate at high field and then behave almost linear, whereas non-powered superconductors behave in the same way as the powered ones, from the persistent current point of view. This means, the induced currents in the superconductors are highest at low fields. Therefore, both principles (ferromagnetic shims and passive superconductors) are mainly active at the low field range and thus qualify for persistent current compensations.

All compensation principles which are presented here, are intrinsic solutions which means, that they could be incorporated from start on into the magnet design process. These compensations could than be a means to reduce the necessary field strength of the corrector magnets which are attached, for example, to the LHC main dipoles in order to correct for the persistent current induced field errors.

## 8.1 Ferromagnetic Coil Protection Sheet

One possible solution for a partial compensation of the persistent current multipole errors has been found for the LHC superconducting dipoles by making a part of the so-called coil protection sheets (CPS) from ferromagnetic material. Non-magnetic coil protection sheets, consisting of different layers of the same material, have originally been foreseen in the magnet design in order to protect the coil against damages from the surrounding stainless steel collars.

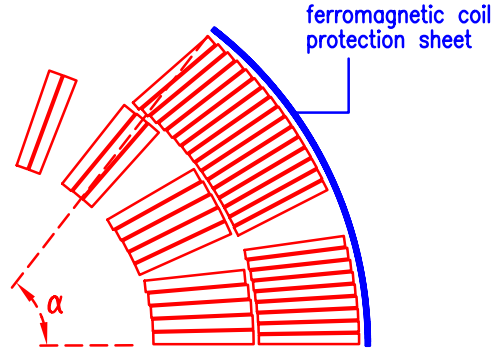


**Figure 8.1:** Ferromagnetic part of the coil protection shield as it has been used in a compensation study in one of the short models of the LHC main dipole.

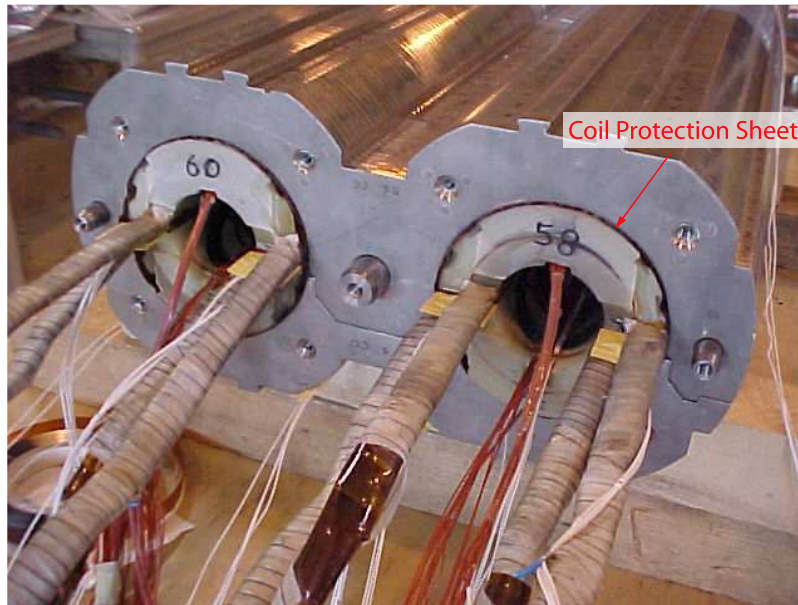


**Figure 8.2:** Picture of the LHC main dipole coils in the common stainless steel collar, including the ferromagnetic coil protection sheet (indicated by the red arrow). This 1.5 m long test magnet has been constructed and studied at CERN.

It has to be emphasized here that the aim was to compensate for the *variation* in the odd order multipoles  $b_3$  and  $b_5$ , rather than affect the *absolute value*. This is due to the fact that multipole variations are much more difficult to correct by adjusting the coil geometry, for example, than constant offsets which show up on the multipole curves during a complete powering cycle. Changes in the average multipole value can be corrected by small shifts of coil blocks in the final design version of a magnet. A shift of one degree, applied on the uppermost coil block on the inner layer of an LHC dipole coil, for example, results in about one unit of constant multipole  $b_3$ , calculated at 17 mm reference radius. The ideal case is, if there is no multipole variation versus excitation at all in the magnet.

An experimental verification of the compensation principle has been carried out at CERN in one of the short model dipole magnets. The compensation for the persistent current effects consists of changing one layer of the CPS from non-magnetic stainless steel to iron sheets with a very low content of impurities (99.99% pure Fe). Figure 8.1 shows the first quadrant of the LHC main dipole coil with the ferromagnetic part of the coil protection sheet which is mounted on the outer coil radius between the coil and the collars (see also Fig. 8.2). The angle  $\alpha$  of the magnetic part of the shield has been chosen to  $52^\circ$  from mechanical necessities: The coil protection shield has to fully cover the outer coil shape.

In table 8.1, the calculated and measured values of this test magnet is presented. It can be seen from these numbers that the insertion of the ferromagnetic coil protection sheet results in a significant reduction of variation in all lower order multipoles.

**Table 8.1:** Expected variation in relative multipole errors  $\Delta b_n$  including persistent currents (in units of  $10^{-4}$  determined at 17 mm reference radius). A compensation has been calculated by means of a ferromagnetic coil protection sheet for a range of 0.6 – 1.6 T.

CPS	Calculated Values		Measured Values	
	no	yes	no	yes
$\Delta b_2$	0.001	0.041	0.277	0.142
$\Delta b_3$	5.721	3.632	5.981	1.370
$\Delta b_4$	0.002	0.003	0.007	0.018
$\Delta b_5$	0.721	0.337	1.076	0.036

The difference, and the resulting change, in the calculated multipole  $b_3$  for geometries with and without the ferromagnetic CPS compared with measurements taken at CERN are shown in Fig. 8.3. As already shown in section 4.1.9, it is important to calculate a full up-down-up ramp cycle of the magnet in order to achieve simulation data for an LHC operating cycle that can be compared to the measurements. The LHC dipoles will be ramped up from about 0.6 T (injection field) to about 8.5 T (nominal field). Injection field level indicates the value, when the particle beam is injected into the accelerator. Following the increasing energy of the beam, the magnetic field in the bending magnets rises linearly to their nominal field value. For the calculations, an interval up to 1.6 T has been considered. This interval is sufficient, since the relative field errors due to the persistent current effect vanishes for higher fields (except for the hysteresis, which remains). In this range, the calculated curves show a reduction in the non-linearities of the multipole  $b_3$  of about 60 % (while the variation of multipole  $b_5$  can be reduced to about 50 % of its original value). Except for small deviations

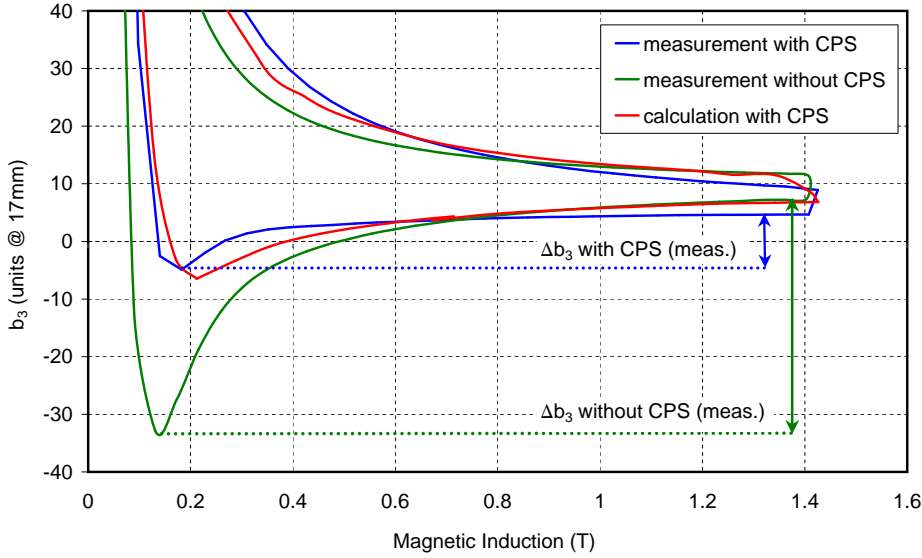


**Figure 8.3:** The odd lower order multipole  $b_3$  determined at 17 mm reference radius compared with measurements from the test magnet, with and without the magnetic coil protection sheet, respectively. The aim of the ferromagnetic coil protection sheet is to reduce the variation  $\Delta b_n$  of the lower order multipoles in the LHC main dipoles.

between calculated and measured values, the curves well validate the partial compensation of the sheet, since the compensative effect, as well as the curve shapes, are fully reproduced. The measurements give an even more optimistic picture: According to the values presented in table 8.1, the variation of multipole  $b_3$  could be reduced from 5.981 units in  $10^{-4}$  (without the CPS) to a value of 1.370 units in  $10^{-4}$  at a reference radius of 17 mm.

It should be mentioned here, that in case of a dipole magnet, the odd lower order multipoles  $b_3$  and  $b_5$  are contradictory in their values: An improvement in the values of multipole  $b_3$  (or its variation) is usually coupled to a deterioration of the multipole  $b_5$  (or its variation, respectively). This inherent behavior is also illustrated in the next section and means a restriction in the compensation capabilities of the CPS.

### 8.1.1 Investigating the Sheet Covering Angle

In this section, the investigation of small changes in the covering angle of the ferromagnetic part of the coil protection sheet,  $\alpha$ , are presented (see Fig. 8.1 for the position of the angle). It is expected that even small angular changes should result in a considerable change in the odd lower multipoles  $b_3$  and  $b_5$ , since from the point of coil symmetries, geometrical changes in the angular range of  $50^\circ$  are known to be a source of variation of these multipoles. Table 8.2 shows the computed values at different angles.

As can be seen from the plots in Fig. 8.4, the covering angle of the ferromagnetic coil protection sheet has a certain influence on the lower order multipoles. Although it is shown in the last section that a ferromagnetic coil protection sheet with a covering angle of  $52^\circ$  (which is used for the test model) resulted in a considerable reduction of the variation of the

**Table 8.2:** Expected relative multipole errors including persistent current contribution in units of  $10^{-4}$  calculated at 17. mm reference radius for different angles of the ferromagnetic coil protection sheet.

	Coil protection sheet in ferromagnetic material					
	$\alpha = 44.68^\circ$			$\alpha = 46.34^\circ$		
	injec. field	nominal field	vari. $\Delta b_n$	injec. field	nominal field	vari. $\Delta b_n$
$b_2$	-2.943	-3.178	0.909	-2.941	-3.177	0.906
$b_3$	10.848	8.300	2.721	10.094	8.304	2.200
$b_4$	0.080	-0.013	0.111	0.080	-0.013	0.111
$b_5$	-0.820	-0.905	0.130	-0.955	-0.917	0.104
$b_6$	0.002	-0.002	0.005	0.002	-0.002	0.005
$b_7$	0.171	0.632	0.461	0.183	0.632	0.449

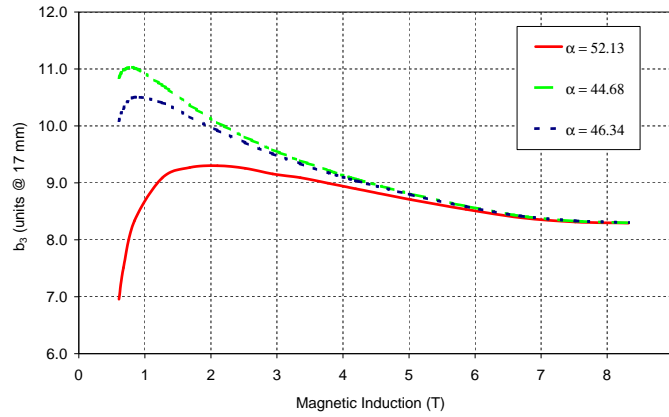


**Figure 8.4:** Odd lower order multipole  $b_3$  versus the magnetic induction as a function of the covering angle of the ferromagnetic part of the coil protection sheet (CPS) on the superconducting coil. The ferromagnetic part of the CPS reduces the variation on  $b_3$  and  $b_5$ . A comparison of the plot with Fig. 8.5 also illustrate the contradictory dependence in the multipole variation of these two multipoles: Geometrical changes which cause a reduction of the variation of multipole  $b_3$  at the same time increase the variation of multipole  $b_5$ .

multipoles<sup>1</sup>, it can be seen from the plots, that the value of  $52^\circ$  is not optimal. Note, that the plots cover the whole LHC excitation range up to about 8.4 T. As can be seen from the plots, a covering angle of around  $46^\circ$  (dark blue dashed curve) seems to be the best choice for a reduction of both multipoles. This result has been obtained after optimization of the objectives  $\Delta b_3 \rightarrow \min$  and  $\Delta b_5 \rightarrow \min$ .

<sup>1</sup>For the test magnet, a change in the covering angle was not an option, since the coil protection sheet has to fully cover the superconducting coil, and the stainless steel collars should not be modified in order to have an easy and inexpensive test possibility. In general, however, the size of the angle can be optimized.

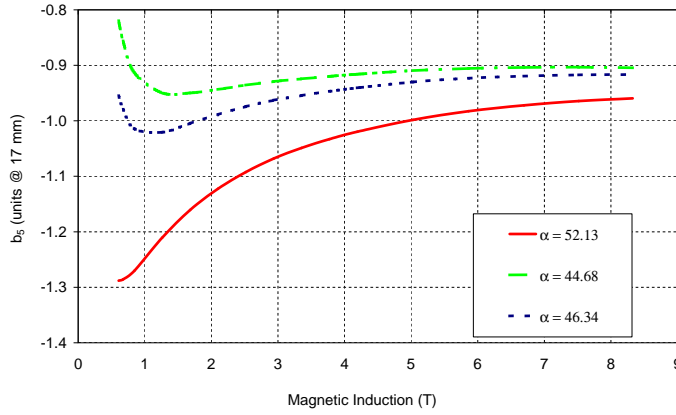


**Figure 8.5:** Odd lower order multipole  $b_5$  versus the magnetic induction as a function of the covering angle of the ferromagnetic part of the coil protection sheet (CPS) on the superconducting coil. The ferromagnetic part of the CPS reduces the variation on  $b_3$  and  $b_5$ .

In Figure 8.5, where  $b_5$  is presented, it can also be seen, that a reduction of the angle from  $52^\circ$  to approximately  $44^\circ$  yields an overcompensation of this multipole, which is indicated by the change of the curve shape. The same behavior can be expected for the multipole  $b_3$  in case the angle is reduced even further.

### 8.1.2 Tuning Possibility by Varying the Sheet Thickness

The use of ferromagnetic coil protection sheets of slightly different thicknesses offers a tuning possibility for the series magnet coils and can compensate deviations in multipole components arising from different magnetization [75] in the cables of the different cable manufacturers for the LHC.

Figure 8.6 shows the multipole  $b_3$  versus the magnetic induction as a function of the thickness of the ferromagnetic CPS. In all the presented cases, the covering angle is held at  $52^\circ$ . The computed multipole values are shown in table 8.3.

**Table 8.3:** Expected relative multipole errors including persistent current contribution in units of  $10^{-4}$  calculated at 17. mm reference radius for different thicknesses of a ferromagnetic part replacing a part of the already existing coil protection sheet.

	Coil protection sheet in ferromagnetic material								
	0.4 mm thick			0.5 mm thick			0.6 mm thick		
	injec. field	nominal field	multipole variation	injec. field	nominal field	multipole variation	injec. field	nominal field	multipole variation
$b_2$	-2.964	-3.163	0.921	-2.937	-3.157	0.914	-2.916	-3.152	0.871
$b_3$	5.259	7.974	3.297	6.957	8.293	2.344	8.654	8.611	1.506
$b_4$	0.080	-0.012	0.111	0.080	-0.012	0.111	0.079	-0.012	0.111
$b_5$	-1.062	-0.949	0.156	-1.288	-0.959	0.328	-1.511	-0.969	0.542
$b_6$	0.002	-0.001	0.005	0.002	-0.001	0.005	0.002	-0.001	0.005
$b_7$	0.244	0.634	0.390	0.241	0.633	0.392	0.237	0.632	0.394

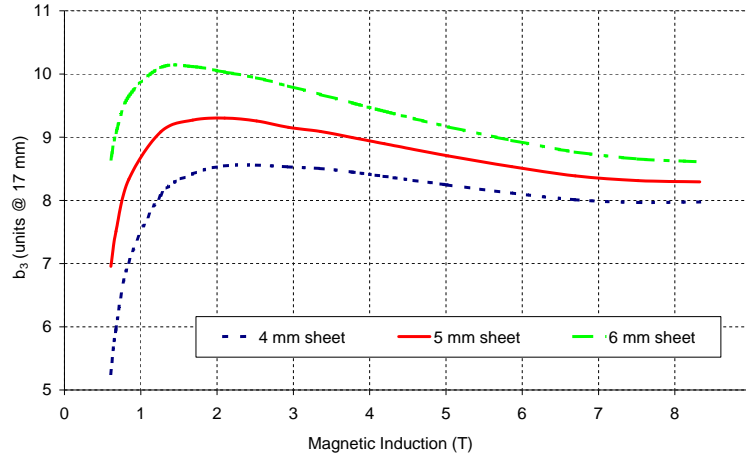


**Figure 8.6:** Influence of sheet thickness variation on multipole  $b_3$  during LHC up ramp cycle (for 0.4 mm, 0.5 mm and 0.6 mm). The coil protection sheet is partially made of ferromagnetic iron sheets (99.99% pure Fe). Multipoles in units of  $10^{-4}$  calculated at 17 mm reference radius.

As can be seen from the curves in Fig. 8.6, the range of tuning possibilities by varying the thickness of the ferromagnetic part of the CPS covers about 1.8 units in  $10^{-4}$  for the multipole  $b_3$ : The increase of the sheet thickness reduced the value of the multipole variation from a  $\Delta b_3$  of 3.297 units to 1.506 units (all calculated at a reference radius of 17 mm). At the same time, the even lower order multipoles see relatively little changes (see table 8.3). It can also be seen in the plot in Fig. 8.6 that the average value of the multipole  $b_3$  shows a slight increase (shift to higher values). This is due to the additional magnetic material which is added to the original geometry, when the ferromagnetic coil protection sheet is inserted. As has already been explained in the introduction to this chapter, a curve shift can easily be compensated by a slight change in the final coil geometry of a magnet. It can therefore be concluded, that the variation of the thickness of the ferromagnetic part of the CPS offers an additional tuning possibility for magnet design purposes.

## 8.2 Influence of a Ferromagnetic Sheet Inside the Magnet Aperture

Another easy to realize and effective method of a partial compensation of the persistent current effect is to add a thin ferromagnetic layer on the outer radius of the already existing cold bore. The cold bore denotes the beam pipe cylinder which contains the vacuum in the magnet (see Fig. 6.3 in chapter 6.3.1, for instance). The ferromagnetic layer can easily be added by a sputtering process, for example, or by means of a thin metallic foil to be glued on the outer cold bore radius. The sheet thickness in this case should be in the range of some micrometers as is shown in Fig. 8.7.

Table 8.4 shows the calculated values for different thicknesses of the sputtered sheet on the outer cold bore radius. As before in the case of the ferromagnetic coil protection sheet, an interval range up to 1.6 T has been considered. The objectives were again a reduction of

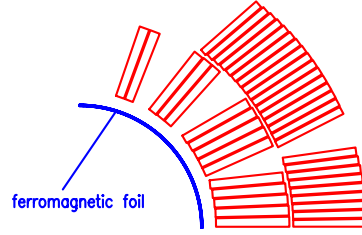


**Figure 8.7:** 1st quadrant of the LHC dipole coil with ferromagnetic sheet which can be used for a partial compensation of persistent current induced multipole errors.

**Table 8.4:** Expected relative multipole variation including the persistent current contribution in units of  $10^{-4}$ , calculated at 17. mm reference radius. The values are determined for an LHC dipole magnet with a cold bore and a sputtered ferromagnetic layer of various thicknesses attached to the outer cold bore radius. In the left column, the calculated values for the LHC dipole without a sputtered layer are presented for comparison.

	Without sputtered layer	Calculated multipole variation		
		With sputtered layer of ferromagnetic material on the outer cold bore radius		
		40 $\mu\text{m}$ thick	50 $\mu\text{m}$ thick	60 $\mu\text{m}$ thick
$b_2$	0.0006	0.034	0.005	0.002
$b_3$	5.7207	1.124	0.055	1.187
$b_4$	0.0021	0.050	0.018	0.035
$b_5$	0.7206	1.337	1.821	2.334
$b_6$	0.0004	0.005	0.011	0.011
$b_7$	0.2826	0.581	0.788	1.000

the variation of the odd lower order multipoles  $b_3$  and  $b_5$ . It can be seen from the values that the sputtered layer only partially fulfills these objectives, since it improves the variation of the odd lower order multipoles  $b_3$ , however, causes an increase on the multipole  $b_5$ . Here, the before mentioned contradictory behavior of these two multipoles can be seen. A thickness of the sputtered layer of 40  $\mu\text{m}$  causes a reduction of the variation on multipole  $b_3$  of about 4.75 units from 5.72 to 0.97 units, whereas at the same time the multipole  $b_5$  increases from about 0.72 units to more than one unit. This result repeats with increasing thickness of the ferromagnetic layer. For thicknesses above approximately 50  $\mu\text{m}$ , also the variation of multipole  $b_3$  increases again.

Figure 8.8 shows the calculated objectives  $b_3$  and  $b_4$  resulting from the geometry which includes a ferromagnetic layer of 40  $\mu\text{m}$  thickness. The dashed curves in the plot show the complete ramp cycle, whereas the part of the actual operating cycle is drawn in continuous lines. It is expected, that the values for the multipoles which are calculated for a main field component of around 1.5 T do not differ significantly from the multipoles at nominal field. As can be seen from the curves, the variation of this two multipoles is reduced considerably.

Compared with the results from the ferromagnetic coil protection sheet, the sputtered



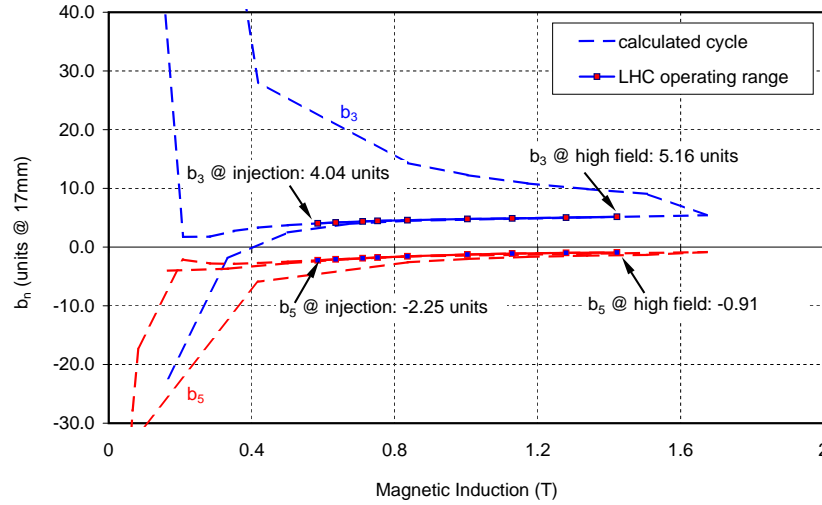


**Figure 8.8:** Odd lower order multipoles  $b_3$  and  $b_5$  calculated at a reference radius of 17 mm, including a ferromagnetic layer of  $40\ \mu\text{m}$  thickness inside the magnet aperture.

layer on the cold bore has the advantage that the circular symmetry of the cold bore can be exploited. Thus, no unwanted multipoles are induced by this change in the magnet cross-section. In addition, the cold bore is centered with a high precision in the magnet aperture and therefore no ill-positioning with respect to the up/down or the left-right symmetry has to be expected. However, the trade-off between the multipole variations of  $b_3$  and  $b_5$  show up in a relatively strong way, in this case and thus present a real flaw for this compensation measure.

As a conclusion, it can be said that a sputtered layer of ferromagnetic material on the existing cold bore of the LHC main dipoles can be considered a simple possibility to intrinsically partially compensate unwanted persistent current induced field harmonics, in case the layer can be produced sufficiently thin.

### 8.3 Ferromagnetic Shims Inside the Superconducting Cable

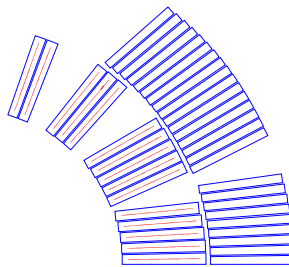


**Figure 8.9:** First quadrant of the LHC dipole coil with ferromagnetic sheet which can be used for a partial compensation of persistent current induced multipole errors.

A compensation by means of thin ferromagnetic shims inserted into the cable of the inner layer of the coil (as indicated in Fig. 8.9) has been calculated. These shims are centered inside the keystone cables and have a thickness of 0.1 mm. They can be included during the cable production process and are then an easy to realize method of compensation.

As before for the shims in the magnet aperture, a complete up-down-up ramp cycle for the LHC main dipole coil has been determined. Although a compensation takes place, the calculated results were not satisfying for application in magnets with NbTi cables, since the calculation of the multipoles and the multipole variation including these shims showed a strong overcompensation of the persistent current effect. The compensatory effect of the ferromagnetic shims yields in an increase of multipole  $b_3$  to 37.4 units at injection field level and 8.8 units at nominal field level, respectively. All calculations are carried out at a reference radius of 17 mm. A reduction in the radial size of the shims can be done in principle, however could lead to difficulties with a precise shim centering inside the cable. It has therefore not been considered. This method of inserting ferromagnetic shims inside the cable cross-section can be interesting for cables made of Nb<sub>3</sub>Sn superconductor material. Nb<sub>3</sub>Sn magnets are currently studied in order to provide magnetic fields up to 11-15 T. The idea of passive correction by means of thin shims in the cable has already been proposed by Green [33] or Kashikin [36], for example. Commercially available Nb<sub>3</sub>Sn superconductors allow for a higher critical current density than NbTi superconductors. This, however, also increases the induced magnetization at low field levels. In addition, due to their production process, these Nb<sub>3</sub>Sn strands have a larger filament diameter of about 10-15  $\mu\text{m}$  compared to 6-7  $\mu\text{m}$  of a NbTi strand. The magnetization of a filament scales linear with its filament diameter. The insertion of thin ferromagnetic strips in the cable could therefore be a viable method to reduce the total magnetization in the cable.

## Chapter 9

# Conclusion

In the framework of this thesis, it has been shown, that the critical current density is one of the most important parameters with respect to the calculation of coil magnetization effects. Its dependence on the local field value and the field distribution in the cross-section of a superconducting coil heavily influences the computed field and the resulting error.

The purpose of this thesis is to develop a new model for the superconducting filament magnetization and incorporate it into the ROXIE program for the calculation of field errors and the design optimization of superconducting accelerator magnets.

Most of the currently available magnetization models for superconductors calculate the magnetization from field maps in the magnet cross-section. The repercussion of the screening field produced by the superconductor is not considered and the magnetization is usually determined from a measurement by means of a curve fit. The models are usually restricted to a change of a homogeneous external field.

For the calculation of superconducting accelerator magnets, these approaches are not satisfying with respect to the determination of the persistent current influence with the required preciseness. Therefore, a filamentary superconductor magnetization model has been developed which calculates the *continuous course of the magnetic field* inside the filament by means of a differential approach. Expressions are given for the magnetization of superconducting filaments and coil magnetizations are calculated. The derived solution is exact in  $B_{\text{screen}} = 0$  within the current-free core of the filament.

The magnetization model is implemented into the source code of the CERN field computation program ROXIE. This allows the combination of the superconductor model with advanced numerical field solvers and thus the calculation of the persistent current effects in superconducting magnets.

Several magnet types which are used for the LHC accelerator which is currently under construction at CERN have been calculated by using this model. Measurements taken at CERN verified well the calculated field errors in this magnets.

The LHC main dipole magnet has been used exemplary and, after the determination of the persistent current induced field errors in this magnet, different methods are computed for (passive) partial compensation by means of ferromagnetic parts to be inserted into the magnet cross-section. One method of partial compensation of the persistent current induced field errors has been tried on a 1.5 m long test dipole magnet. There, a part of the existing coil protection sheet has been replaced by a ferromagnetic layer. This magnet has been measured at CERN and confirmed the compensatory effect which has been calculated.

The following conclusions can be drawn:

1. A filamentary superconductor model should be such as to consider the non-fully penetrated state of the superconductor. It has been shown during the calculation of the LHC main dipole, for example, that a part of the total number of filaments stays non-fully penetrated even if the main field in the magnet aperture reaches its maximum of about 8.5 T. These filaments are located in the low field areas in the coil cross-section. The number and position of these low field areas depend on the magnet type (dipole, quadrupole, etc.), however, at low field, the (locally) induced currents are highest and thus the non-fully penetrated state should be considered in order to get a reliable prediction of the expected field errors.
2. A hysteresis model to be combined with the magnetization model is recommended in order to allow the calculation of arbitrary ramp cycles. It is shown for the LHC dipole, that the choice of the ramp cycle influences the field error at injection field level. In the case of loss calculations, a hysteresis model is inevitable for a precise determination of losses due to hysteresis and superconductor magnetization.
3. For the determination of persistent current induced field errors in superconducting accelerator magnets, each superconductor model has to be combined with numerical field solvers in order to enable the user to consider saturation effects during magnet ramp. It has been shown that the use of the imaging method as a replacement of the non-linear iron magnetization is in the general case not sufficient for the calculation of the magnet cross-section.
4. The calculated field from the induced current distribution has to be fed back and added to the originally applied field. It has been shown, that the repercussion of the persistent current field has to be considered. This is easiest done by an  $M(B)$ -iteration. Depending on the magnet geometry, it is sufficient to include the source field in the coil into the iteration. In case of highly non-linear domains in the vicinity of the superconducting coil, however, also the contribution to the total field of these magnetic domains has to be part of the iteration, since they can be the source of field variations which influence the induced persistent currents.
5. Partial compensation of the persistent current induced field errors can intrinsically be achieved by ferromagnetic parts which are added to the magnet cross-section. The use of the superconductor model allows the incorporation of these ferromagnetic compensation parts into the design process of a magnet. Optimization algorithms can be used in order to obtain the best compensatory effect on different multipoles.

As an outlook on continuing subjects, an interesting investigation which has not been part of this thesis is the incorporation of the strain- and temperature dependence of the critical current density, which has been mentioned in chapter 3, for instance.

Also, the influence of the coil ends for a complete three dimensional field calculation and its effect on the local superconductor magnetization is an interesting topic which is not covered in this thesis.

Finally, the calculation of the current coupling between the individual strand and the influence on the coil magnetization should be investigated. A model which considers this current coupling on the level of the individual strands or the superconducting cables could

easily be combined with the filamentary superconductor model which has been developed in the framework of this thesis.



# Appendix A

## A.1 The RRR-Value of Normal Conductors

Not only the superconductors behavior, but also the electrical resistivity  $\rho$ , of the normal conducting stabilizing matrix material of a superconducting strand, depends on the temperature and on the applied magnetic induction. The electrical resistivity is usually expressed in terms of the residual resistivity ratio (RRR):

$$\text{RRR} = \frac{\rho(273.15\text{K})}{\rho(4.22\text{K})} \Big|_{B=0 \text{ T}} \quad (\text{A.1})$$

which defines the ratio of the resistivity of the material at zero degrees Celsius to the resistivity measured at the boiling point of helium (4.22 K) in zero magnetic field<sup>1</sup>.

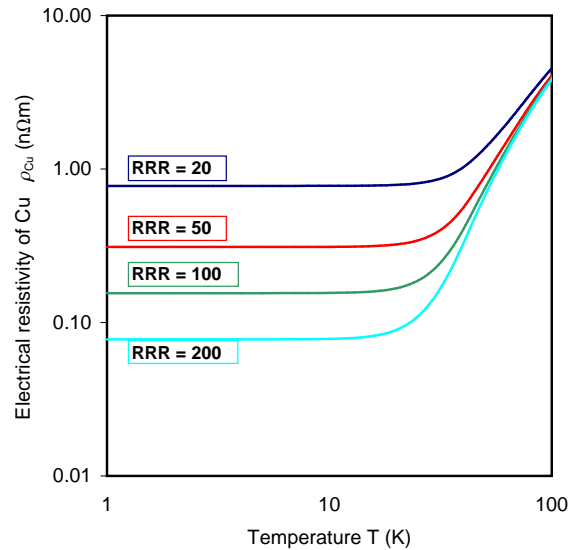


**Figure A.1:** Temperature dependence of the electrical resistivity of Copper  $\rho_{\text{Cu}}$  as a function of the residual resistivity ratio RRR.

Figure A.1 shows the electrical resistivity of copper,  $\rho_{\text{Cu}}$ , versus the temperature  $T$  for different values of RRR. The presented curves are received by means of a fit function, following [76].

<sup>1</sup>The given definition of the RRR-value is the standard, also for practical reasons. Often it is given as the ratio between the resistivity at room temperature and the resistivity at operating temperature. Note, that for Cu, this definition implies an error of about 15 %.

In general, the electrical resistivity of metals with impurities can be described by:

$$\rho = \rho_l + \rho_i, \quad (\text{A.2})$$

where  $\rho_l$  denotes the resistivity due to the collision of conduction electrons with the atoms in the lattice. This is often denoted as the intrinsic resistivity, since it is a characteristic of a certain material.  $\rho_l$  dominates at room temperature, but since the interaction of the electrons with the atoms goes to zero with decreasing temperature, the entity  $\rho_l$  vanishes in this limit and below approximately 20 K, the electrical resistivity is dominated by  $\rho_i$ , which is then denoted the residual resistivity. The residual resistivity depends on the amount of impurities and lattice defects of the metal and scales linearly with the concentration of impurities (the higher the impurity and lattice defects amount, the lower the RRR-value). Therefore, the purity of a material is also a measure of the thermal conductivity and the purity is often expressed in terms of its RRR-value.

$\rho_i$  results from the interaction of the conduction electrons with the impurities in the material. It gets independent of the temperature in the case where the concentration of impurities in the metal is small [5].

A commercially pure copper wire has an RRR of about 50 to 500 [76]. In the case of very high purity copper that is well annealed, a RRR value of around 2000 is reached. The cables for the LHC main dipoles and quadrupoles have to fulfill the condition of a RRR above 70. For aluminum, values between 5 to 10 times higher are usually observed. The residual resistivity is strongly affected by the magneto-resistivity effects. This yields to a  $\rho$  as given in Eq. (A.2). For superconducting material, the RRR is defined by using a  $\rho$ -value for temperatures  $T$  above  $T_c$ .



## A.2 Fourier Expansion of the Radial Field Component

Since the radial component of the magnetic induction  $B_r$  is a function with the period  $2\pi$ , it is generally possible to expand  $B_r$  into trigonometric functions. Assuming that the field component  $B_r(r, \varphi)$  is known at a reference radius  $r = r_0$ , the Fourier expansion of the magnetic field reads:

$$B_r(r_0, \varphi) = \frac{A_0(r_0)}{2} + \sum_{n=1}^{\infty} B_n(r_0) \sin n\varphi + A_n(r_0) \cos n\varphi, \quad (\text{A.3})$$

where  $A_0 = 0$ ,  $A_n$  and  $B_n$  are the coefficients of the cosine and sine terms, calculated by:

$$A_n(r_0) = \frac{1}{\pi} \int_{-\pi}^{\pi} B_r(r_0, \varphi) \cos n\varphi d\varphi \quad (\text{A.4})$$

$$B_n(r_0) = \frac{1}{\pi} \int_{-\pi}^{\pi} B_r(r_0, \varphi) \sin n\varphi d\varphi \quad \text{for } n \geq 1. \quad (\text{A.5})$$

For the superconducting LHC magnets at CERN, the reference radius is chosen to be 17 mm, which corresponds to approximately 2/3 of the magnet aperture. If the field components are related to the main field component  $B_N$ , the units of dipole component is found for  $N=1$ , the units of quadrupole component for  $N=2$ , etc. after normalization:

$$B_r(r_0) = B_N(r_0) \sum_{n=1}^{\infty} b_n(r_0) \sin n\varphi + a_n(r_0) \cos n\varphi. \quad (\text{A.6})$$

The values  $B_n$  are denoted<sup>2</sup> the normal and the values  $A_n$  the skew components of the field, while  $b_n$  are the normal relative and  $a_n$  the skew relative field components at a reference radius  $r_0$ . The latter are dimensionless and are usually given in units of  $10^{-4}$ .

In terms of magnet design, this means that the magnetic field is characterized by the sequence of harmonic coefficients  $b_n$  and  $a_n$ . For reasons of symmetry of the main component in the two-in-one design of the LHC main dipoles, the even terms  $b_2, b_4, b_6, \dots$  have different signs in the two apertures, whereas the odd order multipoles  $b_3, b_5, b_7, \dots$  have the same sign.

---

<sup>2</sup>Note that in this denotation is not unique. In the USA, for example, it is inversely and the  $A_n$  are denoted as the normal whereas the values  $B_n$  are denoted the skew components of the field.

### A.3 The Thermodynamic Potential of Superconductors

It is known from thermodynamics that each thermodynamic system can be unequivocally described by means of its thermodynamic potential, the so-called Gibbs-functions. However, the problem is how to choose an appropriate Gibbs-function and the corresponding set of independent variables for a certain system. Following [41], the Gibbs-function is chosen at will to  $G(T, p, B)$  where the independent variables of the function denote the temperature  $T$ , the pressure  $p$  and the magnetic induction  $B$ . The Gibbs-function then reads:

$$dG = -S dT + V dp - m dB \quad (\text{A.7})$$

with  $S$  := the entropy  
 $V$  := the volume  
 and  $m$  := the magnetic moment.

The Gibbs-function has to fulfill additional constraints in order to reproduce the well-known features of superconductors. If the pressure is assumed to be stable and the applied magnetic induction to be constant (but not necessarily zero), the only remaining independent variable is the temperature and the following conclusions can be drawn:

- From experiments, it is known that the superconducting phase is stable for temperatures  $T < T_C$ , hence the value of the Gibbs-function of the superconducting state  $G_s(T = \text{const.})$  is smaller than the value for the normal conducting state  $G_n(T = \text{const.})$ , if  $T < T_C$ :

$$G_s < G_n \text{ for } T < T_C.$$

- Two phases of a system are in equilibrium if their Gibbs-functions have the same value, therefore:

$$G_s = G_n \text{ for } T = T_C.$$

- An applied magnetic induction above the critical value makes the superconducting state unstable, hence:

$$G_s > G_n \text{ for } T > T_C.$$

- If the superconductor is in the normal conducting phase, the Gibbs-function is independent of the magnetic field, therefore:

$$G_n(B) - G_n(B = 0) = 0 \text{ for } T > T_C.$$

- The determination of  $B_c$  at various temperatures yields:

$$G_s(B) - G_s(B = 0) = - \int_0^B m dB \text{ for } T = \text{const.},$$

where  $m$  denotes the magnetic moment due to the field  $B$ .

From these conditions, an expression for the free energy difference between the normal and the superconducting state is deduced:

$$G_n(T) - G_s(T) = - \int_0^{B_c(T)} m \, dB. \quad (\text{A.8})$$

From the definition of the magnetization  $M$  as the magnetic moment  $m$  per volume  $V$ , a relation between the Gibbs-function and the magnetization can be derived, saying that the area under the magnetization curve yields the difference in the Gibbs-functions (this is often denoted as the free energy difference):

$$G_n - G_s = -V \int_0^{B_c} M \, dB, \quad (\text{A.9})$$

where  $V$  indicates the sample volume.

From this, the magnetization is easily derived as shown in Fig. 2.4 for Type I superconductors and in Fig. 2.7 for Type II superconductors. A Type I superconductor macroscopically exhibits an ideal diamagnetism, where the magnetic susceptibility  $\chi = -1$ . In the case that the sample has the volume  $V_s$  and is shaped in such a way that the demagnetization factor can be neglected, the magnetization  $M$ , multiplied with the permeability of free space  $\mu_0$  is inversely proportional to the applied field for values below the critical field  $B_c$ , and reads  $M = \chi \frac{B}{\mu_0} = -\frac{B}{\mu_0}$ . The expression for the free energy difference results in:

$$G_n - G_s = -\frac{V_s}{\mu_0} \int_0^{B_c} B \, dB = \frac{1}{2} \frac{V_s}{\mu_0} B_c^2. \quad (\text{A.10})$$

In this case, the sample volume is considered to be constant, which is a good approximation for a Type I superconductor, since the London penetration depth is in the order of some hundreds of Å [77] and the volume, de facto, stays the same.

However, for a Type II superconductor, the superconducting volume reduces considerably when flux tubes with a normal conducting core penetrate the material. This process is non-linear and renders the shape of the  $M(B)$ -curve for the interval  $B_{c1} < B < B_{c2}$ , as is indicated in Fig. 2.7.

## A.4 Using the Hypergeometric function

The hypergeometric function,  ${}_2F_1$  which is applied in the Nested Ellipse Model has three input parameters  $a, b$  and  $c$  and one functional argument  $z$ . The hypergeometric function is no intrinsic FORTRAN-function, however, can generally be expressed by means of the Gamma-function,  $\Gamma$ . The Gamma-function is available in most FORTRAN libraries. From the Eqs. (4.47), (4.48), it can be seen that the hypergeometric function is only used for real input values  $z$  from the interval of  $(-\infty, 1]$ . Following [57], the hypergeometric function reads in terms of the Gamma-function:

$${}_2F_1(a, b, c, z) = 1 + \frac{\Gamma(c)}{\Gamma(a)} \sum_{x=1}^{\infty} (-1)^x \binom{-b}{x} \frac{\Gamma(a+x)}{\Gamma(c+x)} z^x. \quad (\text{A.11})$$

The expression is valid for input values  $|z| < 1$ . This results for the case of interest, when the parameters  $a = 1/2, b = 3/4$  and  $c = 3/2$ , in:

$${}_2F_1\left(\frac{1}{2}, \frac{3}{4}, \frac{3}{2}, z\right) = 1 + \frac{\Gamma(\frac{3}{2})}{\Gamma(\frac{1}{2})} \sum_{x=1}^{\infty} (-1)^x \binom{-3/4}{x} \frac{\Gamma(x + \frac{1}{2})}{\Gamma(x + \frac{3}{2})} z^x \quad (\text{A.12})$$

$$= 1 + \frac{1}{2} \sum_{x=1}^{\infty} (-1)^x \binom{-3/4}{x} \frac{\pi^{1/2}}{\Gamma(x + \frac{3}{2})} (2x-1)! \left(\frac{z}{2}\right)^x \quad (\text{A.13})$$

The hypergeometric function is convergent for the considered interval of  $|z| < 1$ . The special case of  $z = 0$ , where  ${}_2F_1(a, b, c, 0) = 1$  is included in Eq. (A.12). The use of the  $\Gamma$ -function has the additional advantage that the  $\Gamma$ -function  $\Gamma(x)$  converges for all arguments  $x > 0$  [78] (whereas the hypergeometric function only converges for certain intervals, which are then to be indicated). In Eq. (A.12), the following features of the  $\Gamma$ -function are used (all expressions taken from [78]):

$$\Gamma\left(\frac{3}{2}\right) = \frac{1}{2} \sqrt{\pi}, \quad \Gamma\left(\frac{1}{2}\right) = \sqrt{\pi}, \quad \Gamma\left(x + \frac{1}{2}\right) = \frac{1 \cdot 3 \cdot 5 \dots (2x-1)}{2^x} \Gamma\left(\frac{1}{2}\right).$$

The term  $\binom{-b}{x}$  denotes the binomial coefficient for real numbers  $b$  and integers  $x$  and is defined as:

$$\binom{-b}{x} = \begin{cases} \frac{b(b-1)(b-2) \dots (b-x+1)}{x!} & \text{if } x > 0 \\ 1 & \text{if } x = 0. \end{cases}$$

Following again [78], the hypergeometric function can be expressed by a linear transformation formula which is valid for values of  $z < -1$  as:

$${}_2F_1(a, b, c, z) = (1-z)^{-a} {}_2F_1\left(a, c-b, c, \frac{z}{z-1}\right), \quad (\text{A.14})$$

where the value of the hypergeometric function with the argument  $\frac{z}{z-1}$  can then be obtained from Eq. (A.11). In the application of Eq. (A.14), it has been observed, that the programmed solution became increasingly unprecise for higher values of  $|z|$  in the negative range. The interval has therefore been splitted at the value of  $z = -20$ , making use of the following relation:

$${}_2F_1(a, b, 2b, z) = \left(\frac{1}{2} + \frac{1}{2}\sqrt{1-z}\right)^{-2a} {}_2F_1\left(a, a-b + \frac{1}{2}, b + \frac{1}{2}, \left(\frac{1-\sqrt{1-z}}{1+\sqrt{1-z}}\right)^2\right).$$

This relation can be applied since  $c = 2b$ . The hypergeometric function with the function argument of  $(\frac{1-\sqrt{1-z}}{1+\sqrt{1-z}})^2$  can then be evaluated by using the Eq. (A.11).

The expressions given above have been used in FORTRAN, when the hypergeometric function has been programmed.



# Bibliography

- [1] The LHC study group. *The Yellow Book, LHC, The Large Hadron Collider - Conceptual Design*. CERN/AC/95-5(LHC), Geneva, 1995.
- [2] Klaus Wille. *Physik der Teilchenbeschleuniger und Synchrotronstrahlungsquellen*. Teubner Studienbücher, Reihe Physik, Stuttgart, 1992.
- [3] Reed et. al. *Materials at Low Temperatures*. Institute of Physics Publishing, Institute of Physics, London, 1998.
- [4] P.F. Chester. Superconducting Magnets (*Article*). In *Reports on Progress in Physics*, London, 1967. Institute of Physics and the Physical Society.
- [5] Bernd Seeber (ed.). *Handbook of Applied Superconductivity*, volume 1. Institute of Physics Publishing, Philadelphia, 1998.
- [6] Martin N. Wilson. Seminar on Superconducting Magnets for Accelerators, held at GSI, Darmstadt, April 2001.
- [7] Z. Ang et al. Results of Magnetic Field Measurements in the MBP2N1 (15 m) Dipole. CERN Report, MTA-IN-2000-10, 2000.
- [8] Martin N. Wilson. *Superconducting Magnets*. Monographs on Cryogenics, Oxford University Press, New York, 1983.
- [9] K.-H. Mess, P. Schmüser, and S. Wolff. *Superconducting Accelerator Magnets*. World Scientific Publishing Co., New Jersey, 1996.
- [10] Charles P. Bean. Magnetization of Hard Superconductors. In *Physical Review Letters*, volume 8, pages 250–253, 1962.
- [11] Charles P. Bean. Magnetization of High Field Superconductors. In *Review of Modern Physics*, volume 36, pages 31–39, 1964.
- [12] Chung-yeung Pang. *Losses in Type II Superconducting Wire Due to Alternating and Rotating Fields*. PhD Thesis, M.I.T., Boston, 1980.
- [13] Robin A. Hartmann. *A Contribution to the Understanding of AC Losses in Composite Superconductors*. PhD Thesis, University of Twente, Twente, 1989.
- [14] Y.B. Kim, C.F. Hempstead, and A.R. Strnad. Critical Persistent Currents in Hard Superconductors. In *Physical Review Letters*, volume 9, page 306ff, 1963.

- [15] K.V. Bhagwat and P. Chaddah. Magnetization Curves for a Hard Superconductor Sample in the Shape of a General Ellipsoid. In *Physica C*, number 190, pages 444–452, 1991.
- [16] K.V. Bhagwat and P. Chaddah. Hysteretic Loss in Hard Superconductor Samples with Non-zero Demagnetization Factor. In *Physica C*, number 166, pages 1–8, 1990.
- [17] K.V. Bhagwat and P. Chaddah. Flux penetration in Spheroid Samples - Critical State Model With Field-dependent Critical Current Density. In *Physica C*, number 224, pages 155–167, 1994.
- [18] K.V. Bhagwat and P. Chaddah. Flux penetration in Thin Superconductor Films With Field-dependent Critical Current Density. In *Physica C*, number 280, pages 52–60, 1997.
- [19] Yuriy N. Zhilichev. Hysteresis of Superconducting Cylinder in Transverse Magnetic Field. In *IEEE Transactions on Applied Superconductivity*, volume 10, pages 1657–1661, 2000.
- [20] Ernst Helmut Brandt. Superconductors of Finite Thickness in a Perpendicular Magnetic Field: Strips and Slabs. In *Physical Review B*, volume 54, pages 4246–4264, 1996.
- [21] Leonid Prigozhin. The Bean Model in Superconductivity: Variational Formulation and Numerical Solution. In *Journal of Computational Physics*, number 129, pages 190–200, 1996.
- [22] M. Haverkamp et al. Penetration of an External Field Change into a Saturated Superconducting Filament. CERN Internal Note no. LHC-MTA-IN-2001-164, 2001.
- [23] M. Haverkamp et al. Penetration of an External Field Change with Arbitrary Angle into a Saturated Superconducting Filament. In *EUCAS 2001, 5th European Conference on Applied Superconductivity*, Denmark, 2001.
- [24] Markus Haverkamp. PhD Thesis, University of Twente. To be published.
- [25] Rob Wolf. Remanent Fields in Multipoles Due to Superconductor Magnetisation. CERN Report, ISR-MA/RW/cb, 1974.
- [26] Rob Wolf. Persistent Currents in LHC Magnets. In *IEEE, Transactions on Magnetics*, volume 28, pages 374–377, 1992.
- [27] H. Brück et al. Field Distortions from Persistent Currents in the Superconducting HERA Magnets. In *Zeitschrift für Physik C, Particles and Fields*, volume 44, pages 385–392, 1989.
- [28] M. Pekeler et al. Coupled Persistent-Current Effects in the HERA Dipoles and Beam Pipe Correction Coils. Desy Report no. 92-06, Hamburg, April 1992.
- [29] Michael A. Green. Residual Fields in Superconducting Magnets. In *4th International Conference on Magnet Technology*, pages 339–346, Upton, 1972.
- [30] Michael A. Green and R.M. Talman. Correction of the Field in the SSC Dipoles Using Superconductor on the Wedges. In *IEEE Transactions on Magnetics*, volume 24, pages 823–826, 1988.



- [31] Michael A. Green et al. Correction of Magnetization Sextupole in One-Meter Long Dipole Magnets Using Passive Superconductors. In *2nd International Industrial Symposium on the Super Collider (IISSC)*, Miami Beach, 1990.
- [32] M.A. Green et al. Measurements of Passive Correction of Magnetization Higher Multipoles in One Meter Long Dipoles. In *IEEE Transaction on Magnetism*, volume 27, pages 1989–1992, 1991.
- [33] Michael A. Green. Ferromagnetic Material in the Superconductor and its Effect on the Magnetization Sextupole and Decapole in the SSC Dipoles at Injection. In *3rd Annual International Industrial Symposium on the Super Collider (IISSC)*, Atlanta, 1991.
- [34] V.V. Kashikhin and A.V. Zlobin. Correction of Coil Magnetization Effect in Nb<sub>3</sub>Sn High Field Dipole Magnet Using Thin Iron Strips. FERMILAB Internal Report no.TD-99-048, 1999.
- [35] V.V. Kashikhin and A.V. Zlobin. Comparison of Correcting Capability of Passive Correctors Based on a Thin Pipe and Thin Strips. FERMILAB Internal Report no.TD-99-049, 1999.
- [36] V.V. Kashikhin and A.V. Zlobin. Correction of the Persistent Current Effect in Nb<sub>3</sub>Sn Dipole Magnets. In *IEEE Transactions on Applied Superconductivity*, volume 11, page 2058ff, 2001.
- [37] Oszkár Bíró, Kurt Preis, and Christian Paul. The Use of a Reduced Vector Potential Formulation for the Calculation of Iron Induced Field Errors. In *Proceedings to the 1st International ROXIE Users Meeting and Workshop*, Geneva, 1998.
- [38] Stefan Kurz and Stephan Russenschuck. The Application of the BEM-FEM Coupling Method for the Accurate Calculation of Fields in Superconducting Magnets. In *Electrical Engineering - Archiv für Elektrotechnik*, volume 82, pages 1–10, Berlin, 1999.
- [39] Terry P. Orlando and Kevin A. Delin. *Foundations of Applied Superconductivity*. Addison Wesley Publishing Company, Reading, Massachusetts, 1991.
- [40] J. F. Shackelford. *Introduction to Materials Science for Engineers*. Maxwell MacMillan International Editions, New York, 1992.
- [41] Werner Buckel. *Supraleitung*. VCH Verlagsgesellschaft mbH, Weinheim, 1990.
- [42] A. Modinos. *Quantum Theory of Matter*. Wiley Books, New York, 1995.
- [43] Charles Kittel. *Introduction to Solid State Physics, 7th ed.* Wiley Books, 1996.
- [44] Essman U. and H. Träuble. The Direct Observation of Individual Flux Lines in Type II Superconductors. In *Physics Letters*, volume 24 of A, 1967.
- [45] L. Cooley, P. Lee, and D. Larbalestier. Conductor Processing of Low  $T_c$  Materials: The Alloy Nb-Ti. To be published.
- [46] David Larbalestier. Superconducting Materials Suitable For Magnets. Academic Training Lectures at CERN, January 2002.

- [47] J. W. Ekin. Strain Scaling Law for Flux Pinning in NbTi, Nb<sub>3</sub>Sn, Nb-Hf/Cu-Sn-Ga, V<sub>3</sub>Ga and Nb<sub>3</sub>Ge. In *IEEE Transactions on Magnetics*, volume 17, pages 658–661, 1981.
- [48] M. S. Lubell. Empirical Scaling Formulas for Critical Current and Critical Field for Commercial NbTi. In *IEEE Transactions on Magnetics*, volume 19, pages 754–757, 1983.
- [49] L. T. Summers et al. A Model for the Prediction of Nb<sub>3</sub>Sn Critical Current as a Function of Field, Temperature, Strain, and Radiation Damage. In *IEEE Transactions on Magnetics*, volume 27, pages 2041–2044, 1991.
- [50] Luca Bottura. A Practical Fit for the Critical Surface of NbTi. In *16th International Conference on Magnet Technology*, Florida, 1999.
- [51] S. Le Naour et al. Magnetization Measurements on LHC Superconducting Strands. In *Applied Superconductivity Conference*, Palm Springs, 1998.
- [52] Stephan Russenschuck. *ROXIE: Routine for the Optimization of Magnet X-Sections, Inverse Field Calculation and Coil End Design*. CERN, Geneva, 1999.
- [53] C. Völlinger M. Aleksa, S. Russenschuck. Calculation of Persistent Currents in Superconducting Magnets. *Physical Review, Special Topics: Accelerators and Beams, IEEE, New York*, 2000.
- [54] J.H. Coupland. Equations and Formulae for Magnetis with Air Cored Windings of 'Saddle Coil' Type. Rutherford Laboratory Report RHEL/R 203, 1970.
- [55] I.N. Bronstein et al. *Taschenbuch der Mathematik, 4. überarbeitete und erweiterte Auflage der Neubearbeitung*. Verlag Harri Deutsch, Frankfurt/Main, 1999.
- [56] I.D. Mayergoyz. *Mathematical Models of Hysteresis*. Springer Verlag, New York, Berlin, Heidelberg, 1991.
- [57] A. Kratzer and W. Franz. *Transzendente Funktionen*. Akademische Verlagsgesellschaft, Leipzig, 1960.
- [58] A. den Ouden, H.H.J. ten Kate, and W.A.J. Wessel. Development of Improved Powder-in-Tube Nb<sub>3</sub>Sn Conductors for Application in Accelerator Magnets, 2000.
- [59] M Acri, C.-H. Denarié, R. Matet, L. Oberli, and J.-L. Servais. Critical Current Measurements of Superconducting Wires Supplied by the UMZ Factory, 1992.
- [60] Sandrine Le Naour and Rob Wolf. Results of the Magnetization Measurements on Strands for the Series Production LHC Main Dipoles and Quadrupoles, 2001.
- [61] Robert Schaback and Helmut Werner. *Numerische Mathematik*. Springer Verlag, Berlin, Heidelberg, 1993.
- [62] Willi Törnig and Peter Spellucci. *Numerische Mathematik für Ingenieure und Physiker*, volume I. Springer Verlag, Berlin, 1988.
- [63] Stefan Kurz, Joachim Fetzner, and Günther Lehner. A novel iterative algorithm for the nonlinear BEM-FEM coupling method. In *IEEE Transactions on Magnetics*, volume 33, pages 1772–1775, 1997.

- [64] Ioan Florea Hăntilă and Gabriel Grama. An Overrelaxation Method for the Computation of the Fixed Point of a Contractive Mapping. In *Rev. Roum. Sci. Techn. - Electrotechn. et Energ.*, number 27, pages 395–398, Bucarest, 1982.
- [65] Joachim Fetzner. *Die Lösung statischer und quasistationärer elektromagnetischer Feldprobleme mit Hilfe der Methode der finiten Elemente und der Randelementmethode, Dissertation, TU Stuttgart*. Number 192. VDI Verlag, Reihe Elektrotechnik, Düsseldorf, 1996.
- [66] H. R. Schwarz. *Methode der finiten Elemente*. Teubner Studienbuchverlag, Stuttgart, 1984.
- [67] Oszkár Bíró and Kurt Preis. On the Use of the Magnetic Vector Potential in the Finite Element Analysis of Three-Dimensional Eddy Currents. In *IEEE Transactions on Magnetism*, volume 25, 1989.
- [68] Stefan Kurz and Stephan Russenschuck. Different Approaches for Accurate Magnetic Field Computation in Superconducting Magnets Using BEM-FEM Coupling. In *fehlt, fehlt, fehlt*.
- [69] Stephan Russenschuck. *Numerical Field Calculation for the Design of Superconducting Magnets - Conception, Optimization, Inverse Problems*. Postdoctoral Thesis (Habilitation), Wien, 1999.
- [70] M. Allitt et. al. Development of Superconducting Tuning Quadrupole Corrector (MQT) Prototypes for the LHC. In *17th International Conference on Magnet Technology, Geneva*, 2002.
- [71] Z. Ang, L. Bottura, A. Ijspeert, M. Karppinen, and L. Walckiers. Magnetic Performance of First Low-B Dipole Corrector Prototype, MCBX. In *6th European Particle Accelerator Conference, Stockholm, Sweden*, 1998.
- [72] Stephan Russenschuck. Field Quality in Accelerator Magnets. In *Proceedings to the 1st International ROXIE Users Meeting and Workshop*, Geneva, 1998.
- [73] C. Völlinger S. Russenschuck. Compensation of the Persistent Current Multipoles in the LHC Dipoles by Making the Coil Protection Sheet from Soft Magnetic Material. *CERN LHC Project Note no. 228*, 2000.
- [74] C. Völlinger M. Aleksa, S. Russenschuck. Compensation of Magnetization Effects in Superconducting Accelerator Magnets. In *IEEE Transactions on Applied Superconductivity*, volume 12, 2002.
- [75] Rob Wolf and Sandrine Le Naour. The Expected Persistent Current Field Errors in the LHC Main Dipole and Quadrupole, 2000.
- [76] *Properties of Copper and Copper Alloys at Cryogenic Temperature*. United States, National Institute of Standards, 1992.
- [77] H. Brechna. *Superconducting Magnet Systems*. Springer Verlag, Berlin, Heidelberg, New York, 1973.
- [78] Milton Abramowitz and Stegun Irene A. *Handbook of Mathematical Functions*. Dover Publications, Inc., New York, 1972.



# Modellierung der Supraleiter-Magnetisierung zur numerischen Berechnung von Feldfehlern in Beschleunigermagneten

## Zusammenfassung der Dissertation in Deutscher Sprache

Zur Beschleunigung schwerer geladener Teilchen mit Hilfe von modernen Teilchenbeschleunigern werden ungewöhnlich starke Magnetfelder benötigt, um die Teilchen auf einer Kreisbahn zu halten. Diese hohen Magnetfeldstärken sind nur mit supraleitenden Magneten erzeugbar, wobei die Spulen der supraleitenden Magneten aus sog. Typ II Supraleitern hergestellt werden. Befinden sich solche Typ II Supraleiter in einem magnetischen Feld, werden – ähnlich dem Prinzip der Wirbelströme in einem herkömmlichen Leiter – Ströme in den Supraleitern induziert, die die Feldqualität in der Apertur eines supraleitenden Magneten empfindlich stören. Im Gegensatz zu Strömen in normalleitenden Materialien, klingen diese supraleitenden Ströme aufgrund des nicht vorhandenen Widerstands im Supraleiter nicht ab. Sie werden deshalb häufig als *supraleitende Dauerströme* bezeichnet und sind die Ursache einer (induzierten) Supraleitermagnetisierung.

Im Rahmen dieser Dissertation wurde ein makroskopisches Model zur Bestimmung der induzierten Magnetisierung eines dünnen supraleitenden Zylinders aus Typ II supraleitendem Material entwickelt, wenn dieser sich einem äusseren magnetischen Feld ausgesetzt sieht. Das Model berücksichtigt die Abhängigkeit der induzierten Stromdichte vom externen Feld sowie der lokalen Feldverteilung im Querschnitt des Supraleiters. Zur Bestimmung der Magnetisierung ist für das Model, neben geometrischen Daten wie des Radius des supraleitenden Zylinders, nur ein einziger Parameter, die sogenannte kritische Stromdichte  $J_c$  erforderlich.

Im häufigsten Fall der Magnetfeldberechnung, wie sie typischerweise bei den Dipolmagneten auftritt, wird nur ein eindimensionales Magnetisierungsmodel benötigt, bei dem ausschliesslich eine eindimensionale (homogene) Feldänderung in der Ebene berücksichtigt werden muss. Im allgemeinen Fall beliebiger Magnetgeometrien wird der Supraleiter jedoch einem sich drehenden Feld beliebiger Richtungsänderung in der Ebene ausgesetzt, was zu einem veränderten Induktionsverhalten und damit zu einer unterschiedlichen Magnetisierung führt. Für den zweiten Fall wurde das Magnetisierungsmodel zur Berücksichtigung von Drehfeldern erweitert, so dass beliebige Feldänderungen möglich sind.

Die Rückwirkung der induzierten Magnetisierung auf das ursprünglich angelegte Feld wird mit Hilfe eines Iterationsverfahrens nach dem Prinzip der Fixpunkt-Iteration berücksichtigt. Ein Relaxationsverfahren beschleunigt die Konvergenz und erhöht die Stabilität der Iteration. Die bei einer Änderung des äusseren Feldes auftretende Hysterese ist Teil des Magnetisierungsmodells und wird somit vollständig erfasst.

Das Model wurde implementiert in das Feldberechnungsprogramm ROXIE, das am CERN zur Berechnung und Optimierung der Felder supraleitender Magnete entwickelt wurde. Die Kombination des Supraleiter-Modells mit dem Feldberechnungsprogramm ROXIE erlaubt die Berechnung kompletter Magnetgeometrien, da das ROXIE Programm moderne Algorithmen zur numerischen Feldberechnung unter Verwendung unterschiedlicher Finite-Elemente Verfahren, besitzt. Diese numerischen Methoden sind erforderlich, um die nicht-linearen Materialien, die beim Bau supraleitender Magnete verwendet werden, in der Berechnung zu berücksichtigen (wie z.B. das Magnetjoch, gefertigt aus ferromagnetischem Material).

Die Gültigkeit des Supraleiter-Modells wurde anhand verschiedener supraleitender Mag-

nete, wie sie beim LHC-Projekt am CERN eingesetzt werden, getestet. Dazu wurden die Feldfehler des supraleitenden Dipols und des supraleitenden Quadrupols berechnet und mit Messungen verglichen. In beiden Fällen zeigten die berechneten Werte eine sehr gute Übereinstimmung mit den Werten aus den Messungen.

Zur Kompensierung dieser (unerwünschten) Feldfehler aus der supraleitenden Spulenmagnetisierung wurden verschiedene passive Kompensierungsmethoden unter Verwendung von ferromagnetischem Material berechnet. Als passive Kompensierung bezeichnet man Methoden, die eine intrinsische, also aus der Magnetgeometrie entstehende Kompensierung darstellen. Eine solche Kompensierungsmethode, die Verwendung eines teilweise ferromagnetischen Spulen-Schutzschildes wurde anhand des Modells eines supraleitenden Dipolmagneten am CERN getestet und die Feldfehler gemessen. Die Messungen wurden mit den berechneten Feldfehlern verglichen und zeigten ebenfalls eine sehr gute Übereinstimmung. Der aufgrund der Berechnungen vorhergesagte Kompensierungseffekt konnte anhand dieser experimentellen Messung verifiziert werden.

## Acknowledgements

The work presented in this thesis has been carried out in the framework of the Doctoral Student Programme at CERN in the LHC-ICP group. I am most grateful to my supervisor at CERN, Dr. Ing. habil. Stephan Russenschuck, head of the section MF (Magnetic Field Calculation) in the ICP group, for his support, for fruitful discussions and for giving me the opportunity to carry out this thesis work.

I would also like to thank the members of the scientific board of the examination of my doctorate, Prof. Dr. Ing. Heino Henke, Chair of Theoretical Electrical Engineering at the Technical University of Berlin and Prof. Dr. Lucio Rossi from the University of Milan and Head of the MMS group at CERN for giving support and suggesting unconventional solutions to all unforeseen problems. Further, I wish to give acknowledgements to Dr. Martin Aleksa from CERN for the teamwork in the ICP-MF section and for being available for numerous discussions and to Bernhard Auchmann and Markus Heneka for doing programming works.

I am also very grateful to Lisa Hall MSc, currently at the University of Newcastle, and to Elisabet Molin, currently at KTH in Stockholm, for patiently correcting my English. Further I want to express my gratitude to Ir. Ans Pardons and Dr. Christoph Schäfer from CERN for all their patience and for keeping the spirits up.

I very much appreciated the work in the ICP group and want to thank all my colleagues for the pleasant atmosphere during my stay.

